The University of Wisconsin

The Graduate School

MEASUREMENT OF THE POSITRON-PROTON NEUTRAL CURRENT DEEP INELASTIC SCATTERING DOUBLE DIFFERENTIAL CROSS SECTION AT HIGH Q^2

A Thesis in

Physics

by

Haibo Zhang

Submitted in Partial Fulfillment
of the Requirements
for the Degree of

Doctor of Philosophy

February 1998

Abstract

The neutral current deep inelastic scattering differential cross sections $d\sigma/dQ^2$ and $d^2\sigma/dxdQ^2$ are measured for $Q^2 > 200$ Gev^2 using 46.1 pb^{-1} of e^+p interactions at 300 GeV center-of-mass energy collected at the Hera collider using the Zeus detector during 1994-1997.

Contents

List of Figures

List of Tables

Chapter 1

Introduction

1.1 Historical Review

The traditional goal of particle physics has been to identify what appear to be structureless units of matter, and to understand the nature of the forces acting between them. The expectation is that the smallest units of matter should interact in the simplest possible way, and that there is a deep connection between the basic units of matter and the basic forces. The joint matter/force nature of the inquiry is illustrated by Thomson's discovery of the electron and Maxwell's theory of the electromagnetic field, which together mark the birth of modern particle physics.

In 1911 Ernest Rutherford in his experiment of scattering α particles off a target of gold foil, demonstrated that what was once believed to be the smallest element in nature–the atom, consists of electrons and a central core–nucleus, which is much smaller than the atom itself. It was a big step forward in the human understanding of nature.

In the 1930s, the neutron was discovered by Chadwick [1] and then nuclear fission was discovered, which again consolidated the concept that nucleus is made of protons and neutrons, which can be reconfigured and regrouped to form nuclei of other atoms. Enrico Fermi and his group successfully realized the first man-made self-sustained nuclear chain reaction in Chicago Pile One at University of Chicago. It was another revolution in modern particle physics.

In the 1960s, with modern accelerators reaching higher and higher energies, experiments in the Deep Inelastic Scattering (DIS) seemed to indicate that proton has substructures, which can be conceived as being built up of smaller constituents, the quarks. Two distinct groups of particles were identified: the baryons, of which the proton and neutron are the prime examples, are built up of three quarks; while the mesons, of which the pion is an example, consists of a quark and an anti-quark. Many new particles were discovered in that period.

The weak interaction, one of the four interactions in nature, was explained in Fermi's original theory of nuclear beta decay [2]. In this theory, the interaction was a point interaction between the four participating particles(in neutron decay $n \rightarrow p + e^- + \bar{\nu_e}$). In other words, there was no need for a field, because there is no effect to be propagated between one point and another. Fermi's theory worked well up to center-of-mass energy $\sqrt{s} \sim 10^2$ GeV, but it produced a cross section that diverges with increasing center-of-mass energy of the interaction, i.e. $\sigma \propto \frac{G_F}{4\pi} s$ (G_F being the Fermi constant of weak interactions), an unphysical result if $\sqrt{s}$ is allowed to increase indefinitely. The Weinberg-Salam-Glashow theory [3] emerged in the 1960s as the worthy successor to Fermi's theory. In this theory, electromagnetism and the weak force are combined in a non-trivial way. The weak field acquires *quanta*

- the W and Z bosons - which are more than 80 times as massive as the proton. In addition, *neutral current reactions* such as $\nu + p \rightarrow \nu + p+$ (neutral hadrons) are predicted, as well as a fourth (charmed) species of quark. Observation of all these things has established the Weinberg-Salam-Glashow theory as the accepted theory of weak interactions, electromagnetic and weak interactions are now unified.

This thesis will mainly deal with *neutral current* of the electroweak interactions mentioned above. More detail is explained in the next few sections.

1.2 Gauge Theory

Over a century ago, Faraday, Maxwell and others developed the theory of electromagnetic interaction, culminating in Maxwell's paper [4] of 1864. Today Maxwell's theory still stands. Moreover, Maxwell's electromagnetism theory, when suitably merged with quantum mechanics, gives us, *quantum electrodynamics* or *QED* , which has achieved great success in particle physics. The crucial thing about electromagnetism is that it is a theory in which the *dynamics* (the behaviour of the forces) is intimately related to a *symmetry* principle - or 'transformation' - which is applied to the objects in the theory such that the physical laws look the same after the operation. Such symmetrics are usually called *invariances* of the laws. A distinction that is vital to the understanding of interations is that between a *global* invariance and a *local* invariance. In a global invariance the same transformation is carried out at all space-time points: it has an 'everywhere simultaneous' character. In a local invariance different transformations are carried out at different individual space-time points. In general, a theory that is globally invariant will not be invariant under locally varying transformations. The particular local invariance relevant to electromagnetism is the *gauge invariance* of Maxwell's equations: in the quantum form of the theory this property is directly related to an invariance under local *phase transformations* of the quantum fields. A generalized form of this phase invariance also underlies the theories of the weak and strong interations. For this reason they are all known as 'gauge theories'.

1.2.1 The Gauge Principle

Let us take an example to show the gauge principle. For a charged particle in an electromagnetic field, the Schrödinger equation has the form:

$$[(1/2m)(-i\nabla - \mathbf{qA})^{\mathbf{2}} + \mathbf{qV}]\psi = \mathbf{i}\partial\psi/\partial\mathbf{t} \tag{1.1}$$

where A is the magnetic vector potential and V is the electric potential, q the electric charge, then under the combined transformation:

$$\mathbf{A} \rightarrow \mathbf{A}' = \mathbf{A} + \nabla\chi \tag{1.2}$$

$$V \rightarrow V' = V - \partial\chi/\partial t \tag{1.3}$$

$$\psi \rightarrow \psi' = e^{iq\chi}\psi \tag{1.4}$$

where χ is any scalar function of space-time 4-coordinates. Then the Schrödinger equation has the same form for the primed variables, this is the gauge invariance.

Now we want to reverse the argument: we shall start by demanding that our theory is invariant under the *space-time-dependent phase transformation*

$$\psi(\mathbf{x},\mathbf{t}) \rightarrow \psi'(\mathbf{x},\mathbf{t}) = \mathbf{e}^{\mathbf{iq}\chi(\mathbf{x},\mathbf{t})}\psi(\mathbf{x},\mathbf{t}) \tag{1.5}$$

We can demonstrate that such a phase invariance is not possible for a free theory, but rather requires an *interacting* theory, involving a (4-vector) field whose interactions with the charged particle are precisely determined, and which undergoes the transformation:

$$\mathbf{A} \rightarrow \mathbf{A}' = \mathbf{A} + \nabla\chi \tag{1.6}$$

$$V \rightarrow V' = V - \partial\chi/\partial t \tag{1.7}$$

when $\psi \rightarrow \psi'$. The demand of this type of phase invariance will then have dictated the form of the interaction - this is the basis of the *gauge principle* . A vector field such as A^{μ}, introduced in order to gurantee local phase invariance, is called a 'gauge field'. The principle that the interaction should be so dictated by the phase (or gauge) invariance is called the *gauge principle* : it allows us to write down the wave equation for the interaction directly from the free particle equation.

1.2.2 Cross Section for two-particle scattering

Consider the general two-body process $1 + 2 \rightarrow 3 + 4$. It can be shown from first principle (Aitchison and Hey, ch5, p144) that the cross section of this scattering is given by

$$d\sigma = P_{fi} \frac{V^2}{2E_1 \cdot 2E_2 \mid \mathbf{v} \mid} \frac{V}{(2\pi)^3} \frac{d^3p_3}{2E_3} \frac{V}{(2\pi)^3} \frac{d^3p_4}{2E_4} \tag{1.8}$$

where V is the volume, p_i and E_i are the momentum and energy of particle i, $\mathbf{v}$ is the relative velocity between incoming particle 1 and 2, and P_{fi} is the transition rate per unit volume between initial and final state, which is defined by

$$P_{fi} = \mid \mathcal{A}_{fi} \mid^2 / VT \tag{1.9}$$

where $\mathcal{A}_{fi}$ is the transition amplitude between initial and final states, V is the volume and T is the time of interaction. The transition amplitude is defined by[1]

$$\mathcal{A}_{fi} = -i \int d^4x \phi_f^* \hat{V} \phi_i \tag{1.10}$$

where ϕ_i and ϕ_f are the initial and final state free particle solutions, $\hat{V}$ is the interacting potential.

For electron and hadron interaction, using Dirac equation for electron and the γ matrices algebra, the above cross section eqn 1.8 can be reduced to

$$d\sigma \sim L_{\mu\nu} W^{\mu\nu} \tag{1.11}$$

[1]chapter 9 of Bjorken and Drell (1964)

i.e. it factorises into the product of a 'lepton tensor' $L_{\mu\nu}$ involving all the Dirac algebra

$$L_{\mu\nu} = 1/2 \sum_{s} \sum_{s'} \bar{u}(k', s') \gamma_{\mu} u(k, s) \bar{u}(k, s) \gamma_{\nu} u(k', s') \tag{1.12}$$

and a 'hadron tenson' $W^{\mu\nu}$ for the hadron vertex

$$W^{\mu\nu} = (p + p')^{\mu} (p + p')^{\nu} \tag{1.13}$$

where k, s are the electron momentum and spin, p is the hadron momentum.

After the Dirac algebra is worked out, the final *lepton tensor* may be written

$$L_{\mu\nu} = 2[k'_{\mu} k_{\nu} + k'_{\nu} k_{\mu} + (q^2/2) g_{\mu\nu}] \tag{1.14}$$

where $q^2 = (k - k')^2$. The tensor $L_{\mu\nu}$ is important since it appears not only in elastic scattering, but also in the calculation of inelastic electron scattering cross sections.

1.3 Deep Inelastic Scattering

At large momentum transfers there is very little elastic scattering: inelastic scattering, in which there is more than just the electron and proton in the final state, is much more probable. The simplest inelastic cross section to measure is the so-called 'inclusive' cross section, for which only the final electron is observed. This is therefore a sum over the cross section for all the possible hadronic final states: no attempt is made to select any particular state from the hadronic debris created at the proton vertex. This process can be represented by the diagram of Figure **??**, assuming that the one-photon exchange amplitude dominates.

The 'blob' at the proton vertex indicates our ignorance of the detailed structure: X indicates a sum over all possible hadronic final states. The assumption of one-photon exchange, which is known experimentally to be a very good approximation, means that, as in last section eqn 1.11, the cross section can factorise into a leptonic tensor contracted with a tensor describing the hadron vertex

$$d\sigma \sim L_{\mu\nu} W^{\mu\nu}(q,p) \tag{1.15}$$

The lepton vertex is well described by QED and takes the same form as eqn 1.14. For the hadron tensor, we must deduce its general structure by invariance arguments. We will only consider unpolarized scattering and therefore perform an average over the initial proton spins. The sum over final states, X, includes all possible quantum numbers for each hadronic state with a total momentum p'. For an inclusive cross section, the final phase space involves only the scattered electron. Moreover, since we are not restricting the scattering process by picking out any specific state of X, the energy k' and the scattering angle θ of the final electron are now independent variables. The relation

$$p' = p + q \tag{1.16}$$

leads to

$$p'^2 = M^2 + 2p \cdot q + q^2 \tag{1.17}$$

where M is the proton mass. In this case, the invariant mass of the hadronic final state is a *variable*

$$p'^2 = W^2 \tag{1.18}$$

and is related to the other two scalar variables

$$p \cdot q = M\nu \tag{1.19}$$

$$q^2 = -Q^2 \tag{1.20}$$

by the condition

$$2M\nu = Q^2 + W^2 - M^2 \tag{1.21}$$

Making use of Lorentz invariance and current conservation and also keeping in mind that for inclusive inelastic scattering there are now two independent scalar variables ν and Q, we can show by working out the Dirac algebra again (Aitchison and Hey, chapter 7, p221) with the conventional definition of the proton structure functions W_1 and W_2:

$$\begin{aligned} W^{\mu\nu}(q,p) &= (-g^{\mu\nu} + q^\mu q^\nu/q^2)W_1(Q^2,\nu) + \\ & [p^\mu - (p\cdot q/q^2)q^\mu][p^\nu - (p\cdot q/q^2)q^\nu]M^{-2}W_2(Q^2,\nu) \end{aligned} \quad (1.22)$$

Early fixed target lepton scattering experiments have provided a powerful tool to study the structure of the proton. These experiments contributed to the development of quark-parton model needed to explain the proton structure function. A series of electron scattering experiments at Stanford Linear Accelerator Center (SLAC) begun in late 1967 eventually led to the acceptance of the quark-parton model. The measured cross section showed little dependence with momentum transfer at fixed x, the fractional momentum of the proton carried by the struck quark. This means that for large enough energy transfer, the electrons bounce backwards quite abundantly, just as Geiger and Marsden's α particles did, suggesting proton contains 'hard' constituents. This indicated a scattering from a point-like object.

1.3.1 Cross Section of DIS

Combining lepton tensor eqn 1.14 and hadron tensor eqn 1.22, also inserting the usual flux factor together with the final electron phase space leads to the following expression for the inclusive differential cross section for inelastic electron-proton scattering

$$d\sigma = (\frac{4\pi\alpha}{q^2})^2 \frac{1}{4[(k\cdot p)^2 - m^2M^2]^{1/2}} 4\pi M L_{\mu\nu} W^{\mu\nu} \frac{d^3k'}{2\omega'(2\pi)^3} \tag{1.23}$$

In terms of 'laboratory' variables, neglecting electron mass effects, this yields

$$\frac{d^2\sigma}{d\Omega dk'} = \frac{\alpha^2}{4k^2 sin^4(\theta/2} [W_2 cos^(\theta/2) + 2W_1 sin^2(\theta/2)] \tag{1.24}$$

Here $cos\theta$ and k' are independent variables for inelastic scattering, we can change variables from $cos\theta$ and k' to Q^2 and ν, assuming azimuthal symmetry for the unpolarized cross section. We have

$$Q^2 = 2kk'(1 - cos\theta) \tag{1.25}$$

$$\nu = k - k' \tag{1.26}$$

so that

$$\frac{d^2\sigma}{dQ^2 d\nu} = \frac{\pi\alpha^2}{4k^2 sin^4(\theta/2)} \frac{1}{kk'} [W_2 cos^2(\theta/2) + 2W_1 sin^2(\theta/2)] \tag{1.27}$$

We can use another set of variables, namely

$$x = \frac{Q^2}{2M\nu} \tag{1.28}$$

and

$$y = \frac{\nu}{k} \tag{1.29}$$

which is invariant and represents the fractional energy transfer in the 'lab' frame.

1.3.2 Bjorken Scaling

One might expect W_1 and W_2 to be complicated functions of ν and Q^2, reflecting the complexity of the inelastic scattering process. However, in 1969 Bjorken predicted that in the 'deep inelastic region' – large ν and Q^2, but Q^2/ν finite – there should be a very simple behavior. He predicted that the structure functions should scale, i.e. become functions not of Q^2 and ν independently but only of their ratio Q^2/ν [5]. It was the verification of approximate 'Bjorken scaling' that led to the development of the modern quark parton model.

Bjorken proposed the following 'scaling hypothesis' in the limit

$$\left.\begin{array}{r} Q^2 \to \infty \\ \nu \to \infty \end{array}\right\} \; with\ x = Q^2/2M\nu\ \ fixed \tag{1.30}$$

the structure functions scale as

$$MW_1(Q^2, \nu) \to F_1(x) \tag{1.31}$$

$$\nu W_2(Q^2, \nu) \to F_2(x) \tag{1.32}$$

if we assume spin-1/2 quarks as the point-like partons, then

$$2xF_1(x) = F_2(x) \tag{1.33}$$

This relation between F_1 and F_2 is called the Callan-Gross relation [6]. The physical origin of this relation is best discussed in terms of virtual photon total cross sections for transverse ($\lambda = \pm 1$) virtual photons and for a longitudinal/scalar ($\lambda = 0$) virtual photon contribution.

1.3.3 The quark parton model

How can the scaling be understood? Feynman [7] gave an intuitive explanation in terms of elastic scattering from free pointlike constituents of the nucleon, which he dubbed 'partons'. The essence of the argument lies in the *kinematics of elastic scattering of electrons by pointlike partons:* At high Q^2 and ν it is intuitively reasonable that the virtual photon is probing very short distance and time scales within the proton. In this situation, the photon interacts with small (pointlike) constituents within the proton, which carry only a certain fraction y of the proton's energy and momentum. Over the short time scales involved in the transfer of a large amount of energy ν, the struck constituents can be treated as effectively free. We then have the idealised elastic scattering process shown in Figure 1.1.

If we regard the proton as a collection of partons off which the virtual photon scattered elastically, then the deep inelastic scattering cross-section is the incoherent sum of these individual cross-sections. The kinematics of the elastic scattering for the partons leads directly to a relation between Q^2 and ν and hence to the observed

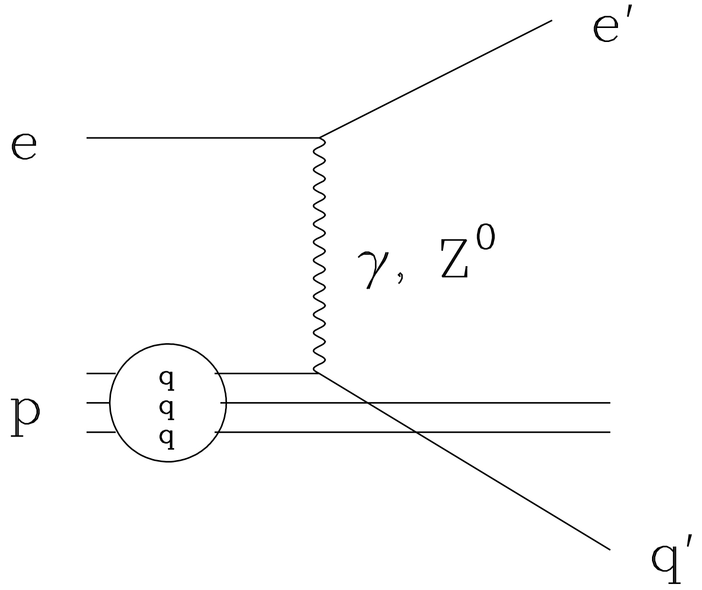

Figure 1.1: A classic example of Photon-Parton interaction

scaling behavior. The original discussion of the parton model took place in the infinite-momentum frame of the proton, in this case the Bjorken x variable was just the fraction of the proton's momentum carried by the elastically scattered parton, and the size of this cross-section was proportional to the probability $q_i(x)$ of finding a quark of type i and momentum xP in the proton.

We now proceed a stage further with the idea that the 'partons' *are* quarks (and antiquarks). If we assume that the photon only couples to these objects, then we can have

$$F_2^{ep}(x) = x\{\frac{4}{9}[u(x) + \bar{u}(x)] + \frac{1}{9}[d(x) + \bar{d}(x) + s(x) + \bar{s}(x)] + ...\} \tag{1.34}$$

where $u(x)$ is the probability distribution for u quarks in the proton, $\bar{u}(x)$ for u antiquarks and so on. The full power of the quark parton model lies in the fact that the same distribution functions appear, in different combinations, for neutron targets, and in the analogous scaling functions for deep inelastic scattering with neutrino and antineutrino beams. To relate the distribution of u and d quarks in a neutron to the distributions in a proton, we can use I-spin invariance

$$u^p(x) = d^n(x) \equiv u(x) \tag{1.35}$$

$$d^p(x) = u^n(x) \equiv d(x) \tag{1.36}$$

Hence the scaling function for en scattering may be written

$$F_2^{en}(x) = x\{\frac{4}{9}[d(x) + \bar{d}(x)] + \frac{1}{9}[u(x) + \bar{u}(x) + s(x) + \bar{s}(x)] + ...\} \tag{1.37}$$

The quark distribution inside the proton and neutron must satisfy some constraints. Since both proton and neutron have strangeness zero, we have a *sum rule* (treating only u, d and s flavors from now on)

$$\int_0^1 dx[s(x) - \bar{s}(x)] = 0. \tag{1.38}$$

Similarly, from the proton and neutron charges we obtain two other sum rules:

$$\int_0^1 dx\{\frac{2}{3}[u(x) - \bar{u}(x)] - \frac{1}{3}[d(x) - \bar{d}(x)]\} = 1 \tag{1.39}$$

$$\int_0^1 dx\{\frac{2}{3}[d(x) - \bar{d}(x)] - \frac{1}{3}[u(x) - \bar{u}(x)]\} = 0. \tag{1.40}$$

These are equivalent to the sum rules

$$\int_0^1 dx[u(x) - \bar{u}(x)] = 2 \tag{1.41}$$

$$\int_0^1 dx[d(x) - \bar{d}(x)] = 1 \tag{1.42}$$

which are, of course, just the excess of u and d quarks over antiquarks inside the proton. One can gain further insight if we introduce the idea of 'valence' quarks (those of the elementary constituent quark model) and 'sea' quarks ($q\bar{q}$ pairs created virtually). Then, in a proton, the u and d quark distribution would be parametrised by the sum of valence and sea contributions

$$u = u_V + q_S \tag{1.43}$$

$$d = d_V + q_S \tag{1.44}$$

while the antiquark and strange quark distributions are taken to be pure sea

$$\bar{u} = \bar{d} = s = \bar{s} = q_S \tag{1.45}$$

where we have assumed that the 'sea' is flavor-independent. Such a model replaces the six unknown functions now in play by three, and is consequently more predictive. We then have:

$$\int_0^1 dx\ u_V(x) = 2 \tag{1.46}$$

$$\int_0^1 dx\ d_V(x) = 1 \tag{1.47}$$

An important sum rule emerges from above as the fractional momentum carried by quark i. This is the *momentum sum rule*

$$\int_0^1 dx\ x[u(x) + \bar{u}(x) + d(x) + \bar{d}(x) + s(x) + \bar{s}(x)] = 1 - \varepsilon \tag{1.48}$$

where ε is interpreted as the fraction of the proton momentum that is not carried by quarks, but carried by gluons. By combining the information got by using neutrino and anti-neutrino beams (charged weak current exchange) with the experiments using electrons and muons and by varying the target, the various quark probability distributions could be isolated. The u and d valence quarks were consistent with vanishing at $x = 0$ and $x = 1$ while the sea-quarks tended to populate the small-x region. Furthermore it became clear that the quarks carried only roughly one-half the proton's momentum.

In the parton model, the unpolarized neutral-current cross-section can be written [8]:

$$\begin{aligned}
\frac{d^2\sigma(e^{\pm}p)}{dxdQ^2} &= \frac{2\pi\alpha^2}{xQ^4}\left[Y^+F_2(x,Q^2) \mp Y^- xF_3(x,Q^2) - y^2F_L(x,Q^2)\right], \qquad (1.49)\\
Y^{\pm} &= 1 \pm (1-y)^2\\
F_2 &= \sum_{flavor}[xq(x,Q^2) + x\bar{q}(x,Q^2)]A_f(Q^2)\\
xF_3 &= \sum_{flavor}[xq(x,Q^2) - x\bar{q}(x,Q^2)]B_f(Q^2)
\end{aligned}$$

where $q(x, Q^2)$ and $\bar{q}(x, Q^2)$ are the quark and anti-quark distribution functions and the top (bottom) sign is for positrons (electrons). A_f and B_f include photon and Z boson terms:

$$\begin{aligned}
A_f(Q^2) &= q_f^2 - 2q_f v_e v_f P_z + (v_e^2 + a_e^2)(v_f^2 + a_f^2)P_z^2\\
B_f(Q^2) &= -2q_f a_e a_f P_z + 2v_e a_e v_f a_f P_z^2\\
P_z &= \frac{1}{4\sin^2\theta_W \cos^2\theta_W}\frac{Q^2}{Q^2 + M_Z^2}\\
v_i &= T_i^3 - 2q_i \sin^2\theta_W\\
a_i &= T_i^3
\end{aligned}$$

where T^3 is the weak isospin ($+1/2$ for u,ν, $-1/2$ for d,ℓ) and θ_W is the electroweak mixing angle. The longitudinal structure function F_L is expected to be small in the kinematic region studied in this thesis and is neglected. This thesis will deal with the measurement of e^+p double-differential cross-section and the extraction of the structure function $xF_3(x, Q^2)$ at $Q^2 > 200$ GeV^2.

Chapter 2

ZEUS at HERA

This chapter provides an overview of the HERA accelerator, located at the Deutsches Elektronen Synchrotron (DESY) laboratory in Hamburg, Germany, and the ZEUS experiment, one of the four experiments at HERA.

2.1 The HERA Accelerator

HERA is the world's only ep collider. Beams of electrons[1] with energy 27.52 GeV collide with beams of protons at 820 GeV, resulting in a center of mass energy ($\sqrt{s}$) of 300 GeV - an order of magnitude higher than for previous fixed-target lepton-nucleon experiments. There are four experiments at HERA, two collider experiments, ZEUS and H1, and two fixed-target experiments, Hermes and HERA-B. Some HERA design parameters are summarized in Table 2.1.

A diagram of the HERA accelerator is shown in Figure 2.1. A linear accelerator accelerates electrons to 500 MeV before injection into the DESY II ring, where

[1] In this chapter and thereafter, electron is used to mean either a positron or an electron.

Parameter	Electron	Proton	Units
Nominal Energy	30	820	GeV
Energy Range	10 - 33	300 - 820	GeV
Injection Energy	14	40	GeV
Filling time	15	20	min
No. of particles	0.8×10^{13}	2.1×10^{13}	
Circulation current	58	160	mA
Magnetic field	0.165	4.65	T

Parameter		Units
Tunnel length	6336	m
No. of bunches	200	
No. of bunch buckets	220	
Time between crossings	96	ns
Crossing angle	0	mrad
ep CM energy	314	GeV
Luminosity	1.5×10^{31}	$\mathrm{cm}^{-2}\mathrm{s}^{-1}$

Table 2.1: Some HERA design parameters

they are then accelerated to 7 GeV, before being transfered into the PETRA ring. PETRA collects 210 electron bunches, which are accelerated to 14 GeV, upon which time they are injected into the main HERA ring for acceleration to the nominal beam energy.

Protons are obtained from an H^- ion source, and accelerated to 50 MeV in a linear accelerator. From the linac, they are sent to HERA III, where they are stripped of electrons, and accelerated to 7.5 GeV. At this point they are injected into the PETRA ring, which collects 210 bunches and accelerates these to 40 GeV before injection into HERA. The protons are injected first.

To maintain the protons in their orbit, a bending field of 4.65 T is required, which necessitates superconducting magnets. The lower energy electron beam can be maintained with conventional magnets operating at a magnetic field of 0.165 T.

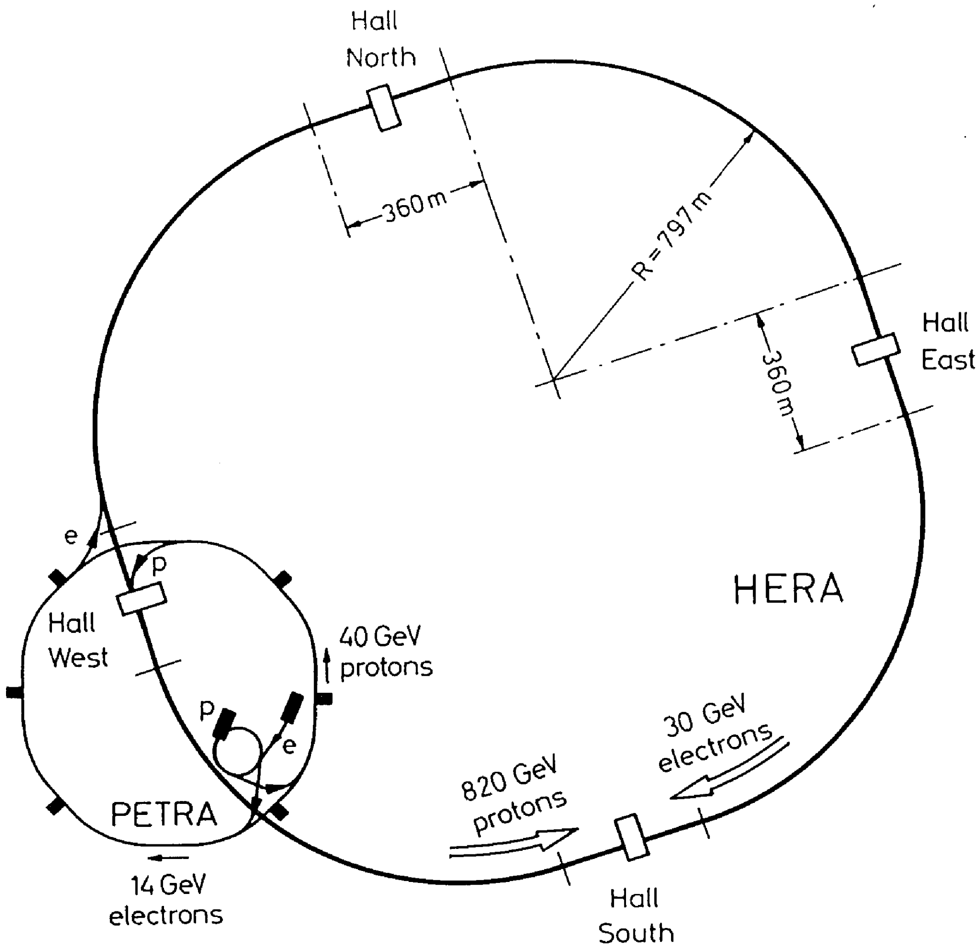

Figure 2.1: The HERA accelerator.

To accelerate and maintain the electron beams, which suffer considerable losses due to synchrotron radiation around the ring, superconducting RF cavities are used, operating at a frequency of 500 MHz. The protons, which lose significantly less energy to radiation, being more massive, can be maintained with conventional cavities. For acceleration, the cavities operate at 52 MHz, which is increased to 208 MHz to tighten up the beam after the protons have reached full energy.

HERA began operations in 1992 and with each year HERA performance has improved dramatically. In 1994, HERA began operations with electrons. After a short e^- run, HERA switched to positrons which significantly improved electron beam lifetimes. The e^+ running remained ever since.

In addition to the $e^{\pm}p$ colliding bunches, HERA delivered pilot bunches, either unpaired protons or electrons, as well as empty bunches for the study of backgrounds. The HERA delievered luminosity, ZEUS on tape luminosity, colliding bunches, pilot bunches information are listed in Table 2.1.

Table 2.2: HERA Luminosity and Running information.

Year	Type	HERA delievered Luminosity (pb^{-1})	ZEUS on tape Luminosity (pb^{-1})	colliding bunches	e pilot bunches	p pilot bunches	days of running
1994	e^-p	1.08	0.41	153	15	15	60
1994	e^+p	5.11	3.30	154	14	17	100
1995	e^+p	12.30	7.30	174	15	6	210
1996	e^+p	17.16	11.26	175	15	5	160
1997	e^+p	36.35	27.94	176	18	5	240

2.2 The ZEUS Experiment

This section focuses only on the components important to this analysis. Other details of the experiment can be found in [9].

The ZEUS detector, located in HERA's South Hall, was constructed by over 450 physicists from 12 countries. The ZEUS detector, is shown in Figures 2.2 and 2.3.

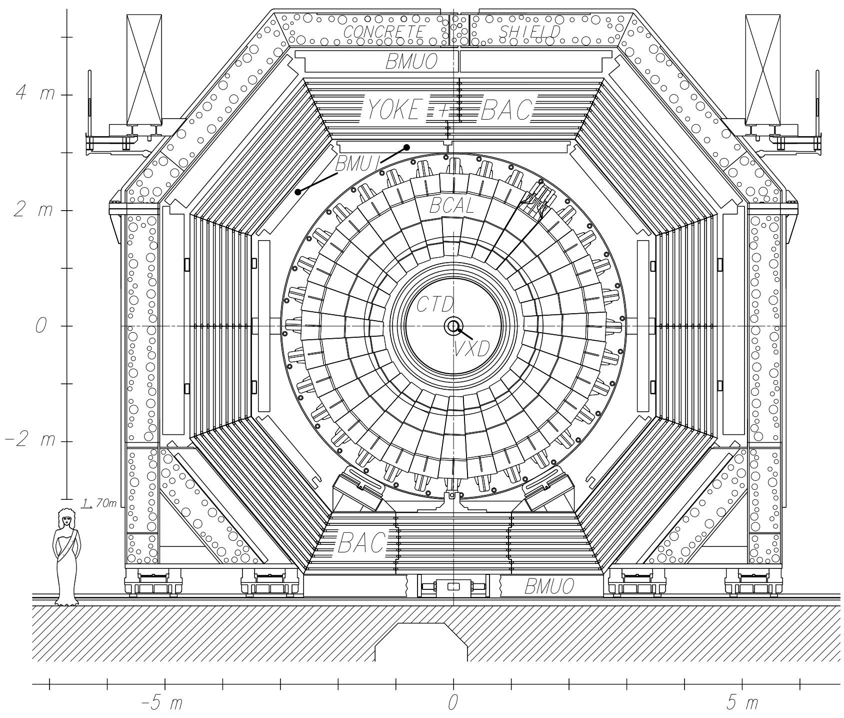

Figure 2.2: The ZEUS detector (end view)

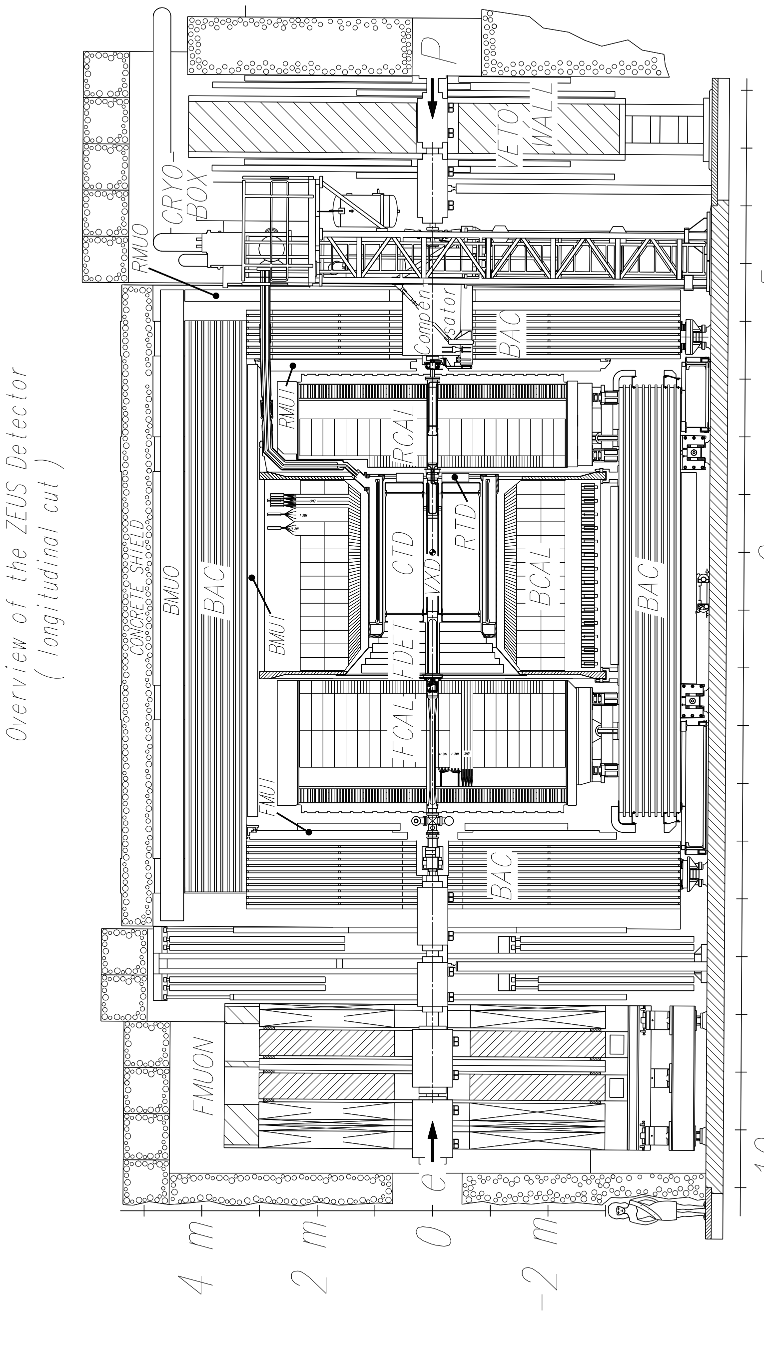

Figure 2.3: The ZEUS detector (side view)

2.2.1 ZEUS Coordinates

ZEUS uses a right-handed coordinate system. The origin, $x = y = z = 0$, is defined to be at the nominal ep interaction point. The $+z$ direction is defined to be along the proton direction (this is also referred to as the 'forward' direction). The $+x$ direction is defined to be inwards, towards the center of the HERA ring, $+y$ is therefore up. Angles are defined in the following way: θ is the polar angle from the $+z$ axis; ϕ is the azimuthal angle from $+x$. r is the distance from the beam axis, $r = \sqrt{x^2 + y^2}$.

2.2.2 The Central Tracking Detector

Charged particles are measured in the Central Tracking Detector (CTD), which is made of up 9 superlayers, each with 8 sense wires. The CTD has an outer radius of 86 cm, and is surrounded by a superconducting solenoid, producing a 1.43 T magnetic field. The active length of the CTD is 2.05 m, covering an angular range of $15^o < \theta < 164^o$.

Of the 9 CTD superlayers, 5 ('axial' superlayers) are parallel to the beam axis. The remaining 4 ('stereo' superlayers) have a small angle, approximately 5^o to the beam, to allow reconstruction of track positions along the z axis. The z position can also be reconstructed from the CTD's 'z-by-timing' electronics, which determine the position of a hit from the time difference of the pulses at opposite ends of the sense wires. As the resolution from the 'z-by-stereo' is significantly better, z-by-timing information is not used, except in tracks too short for a reliable z-by-stereo measurement. Only z-by-timing is used in the CTD First Level Trigger.

CTD resolutions for vertex reconstruction were 190 μm in the $r\phi$ plane, $\sim$4.5 cm for z-by-timing and $\sim$2 mm for z-by-stereo. Momentum resolution for 90^o tracks passing through all 9 superlayers was $\frac{\sigma(p_T)}{p_T} = 0.005p_T \oplus 0.016$, where p_T is expressed in units of GeV/c.

2.2.3 The Calorimeter

The ZEUS calorimeter covers over 99.8% (99.5%) of the solid angle in the forward (rear) hemisphere. The only openings are 20x15 cm^2 holes [2] in the forward and rear sections for the beampipe, and the cracks between forward and barrel calorimeter, and between barrel and rear calorimeter.

The calorimeter is divided into 3 sections. The forward calorimeter (FCAL) covers the angular region $2.2^o < \theta < 39.9^o$, the barrel calorimeter (BCAL) covers from $36.7^o < \theta < 129.1^o$, and the rear calorimeter (RCAL) covers from $128.1^o < \theta < 176.5^o$. The calorimeters are further subdivided longitudinally into electromagnetic (EMC) and hadronic (HAC) sections, which are themselves divided into cells. The typical size of a cell is 5x20 cm^2 in the FCAL and BCAL EMC sections, 10x20 cm^2 in the RCAL EMC and 20x20 cm^2 in the HAC sections. Each cell is composed of layers of depleted uranium alternating with scintillator, read out by two wavelength shifter to photomultiplier tubes. The relative pulseheight in the two PMTs, located on opposite sides of the cell, improves the position measurement for energy deposits within a cell. It is often convenient to consider groups of cells, called towers. These consist of 4 EMC cells (2 in the RCAL), together with the HAC cells directly behind them. In the RCAL, there is only a single HAC layer, in the FCAL and BCAL there

[2] Before 1995, the hole is 20x20 cm^2.

are 2.

The ZEUS calorimeter is a sampling, compensating calorimeter. In a sampling calorimeter, the active material (solid scintillator) is sandwiched between layers of inactive material (depleted uranium). The advantage of a sampling calorimeter is that showers can be fully contained in a small region due to the dense inactive material. This advantage comes with a price - most of the shower energy is lost in the inactive material, which degrades detector resolution. A compensating calorimeter is one with an equal response to electromagnetic and hadronic showers. This is accomplished by adjusting the thickness of the absorber and active layers in the EMC and HAC sections, and use of DU as absorber.

The ZEUS calorimeter has an energy resolution of $18\%/\sqrt{E}$ for electromagnetic showers, $35\%/\sqrt{E}$ for hadronic showers [10], with E expressed in units of GeV. The response for electromagnetic and hadronic showers is equal to within 5%. The position resolution for electrons is approximately 1 cm. The time resolution for a cell is better than $1.5/\sqrt{E} \oplus 0.5$ ns [11].

2.2.4 Veto Detectors

By definition, an ep event occuring at the nominal interaction point has a time $t = 0$. In addition to ep events, there is a high rate of background events, due mainly to interactions between the proton beam and residual gas in the beampipe (these interactions are referred to as p-gas or, together with e-gas, as beamgas events). p-gas events which occur near the interaction point will have a time signature similar to ep events. p-gas events which occur upstream of the detector will have a time much earlier than events at the nominal interaction point, and can be vetoed at the FLT. ZEUS has 3 detectors for rejection of out-of-time backgrounds, the SRTD, the C5 counter, and the veto wall.

On the face of the RCAL, located around the RCAL beampipe, is the Small-angle Rear Tracking Detector (SRTD). The SRTD is composed of 272 1 cm wide, 0.5 cm thick and either 24 or 44 cm long scintillators, arranged in two planes, covering a region 68x68 cm^2 (with a 20x15 cm^2 hole for the beampipe). The role of the SRTD at the First Level Trigger (FLT) is to reject out of time backgrounds. Because of its location inside the calorimeter, nearest to the interaction point, this is particularly important, as the SRTD will detect background events missed by the veto detectors further upstream. Details of the SRTD other functions can be found in [12].

The C5 counter consists of 4 scintillator counters surrounding the beampipe at $z = -315$ cm. p-gas events will have a C5 time 21 ns earlier than events at the nominal IP.

The Veto Wall is located further upstream, at $z = -7.5$ m. It is an 8 m wide, 9.07 m high, 87 cm thick wall of iron, covered on both sides by a layer of scintillator. The role of the veto wall is to reject muons created in far upstream p-gas interactions.

2.2.5 The Luminosity Monitor

Luminosity is determined from the hard bremsstrahlung process, $ep \rightarrow ep\gamma$. The cross section for this process is given by the Bethe-Heitler equation [13]:

$$\frac{d\sigma_{BH}}{dk} = 4\alpha r_e^2 \frac{E'}{kE}\left(\frac{E}{E'} + \frac{E'}{E} - \frac{2}{3}\right)\left[\ln\left(\frac{E_p E E'}{m_p m_e k}\right) - \frac{1}{2}\right], \tag{2.1}$$

where k, E, E' and E_p are the photon, incident electron, scattered electron and proton energies, respectively, m_p and m_e are the proton and electron masses, α is the fine structure constant, and r_e is the classical radius of the electron. To measure this process, the luminosity monitor detects both the photon and the scattered electron in coincidence. Electrons with energies in the range 14-19 GeV and angles $\theta < 0.5$ mrad hit the electron detector, a lead-scintillator sampling calorimeter, located at $z = -35$ m. Photons are detected in the photon calorimeter, consisting of a carbon filter to shield against synchrotron radiation, an air-filled Čerenkov detector to reject electrons, and a lead-scintillator sampling calorimeter.

2.2.6 The ZEUS Trigger System

The high bunch crossing rate (an event every 96 ns), together with the high backgrounds of 30 kHz, and the wide variety of interesting physics processes require a sophisticated, state-of-the-art trigger. ZEUS uses a 3 level trigger scheme, with each level having access to more information, and therefore capable of a more sophisticated discrimination than the previous. In addition to the 3 online trigger levels, further data reduction is achieved offline as the data are reconstructed. Each major component has its own First Level Trigger and Second Level Trigger.

The First Level Trigger (FLT) has access to only a limited amount of component data, such as simple energy sums, number of isolated electrons, number of isolated muons, times from the veto components, and number of CTD tracks, in order to handle every bunch crossing (a rate of 10MHz). Data from the components are pipelined for 5 μsec until a decision at the first level can be made. The FLT decision is based on information from component processors, and subject to 64 separate criteria. Upon a global FLT accept, pipelined data are readout by the second level trigger. As the rate of FLT accepts is low, for 1994-1997 typically around 300$\sim$600 Hz, deadtime is negligible. A detailed description of the Cal FLT is in the next section.

The Second Level Trigger (SLT) has access to all the data from the components, but as it must be capable of handling input rates of up to 1 kHz, it is not capable of performing the full reconstruction, so only a limited analysis is possible. Component SLT processors, all transputers, analyze the data, and the results of component second level triggers are sent to the global SLT processor. Upon a global SLT accept, data are sent to the Event Builder (EVB). A rate reduction at the second level of a factor of 10 is required to prevent deadtime at the third level.

The EVB gathers component data for events passing the SLT and assembles the complete information for use by the Third Level Trigger (TLT). The TLT runs on a farm of SGI workstations, running a slightly reduced version of the offline reconstruction code. The TLT decisions are based on the requirements of the physics analysis groups, as opposed to more general event characteristics at the previous levels. Events passing the TLT, which again must reduce the incoming data by a factor of 10, are written to tape.

Data on tape are run through the full ZEUS reconstruction package at a later time. The ZEUS reconstruction code is run on a pair of fast SGI Challenge machines, and processes the data into a format more usable for physics analysis. The format is the DST (Data Summary Tape) format, based on criteria from the physics analysis groups. The DST format reduces the data to a more manageable size before being written to disk for use in analysis. The overview of the ZEUS trigger system is shown in Figure 2.4.

2.2.7 The Calorimeter First Level Trigger

The Calorimeter First Level Trigger (CFLT) utilizes a pipelined architecture to provide trigger data for a global first level trigger decision 5 microsec after each beam crossing, occurring every 96 nsec. The charges from 13K phototubes are summed into 1792 trigger tower pulseheights which are digitized by flash ADC's. The digital values are linearized, stored and used for sums and pattern tests. Summary data is forwarded to the Global First Level Trigger for each crossing 2 microsec after the crossing occurred. The CFLT identifies charged and neutral current, photoproduction, and exotic physics events while rejecting beam gas background using three different approaches. They are: (i) detection of isolated electrons and muons using pattern analysis logic, (ii) identification of patterns of energy deposits obtained from local energy sums, and (iii) recognition of characteristic deposits of total transverse and missing transverse energy. It also provides information on the electromagnetic and hadronic energy deposited in various regions of the calorimeter. The CFLT is currently keeping the experimental trigger rate around 300$\sim$400 Hz.

The CFLT has to make each step of its calculations, including digitization of the PMT pulse, at a rate of 96 ns in order to keep up with the incoming data. However, in order to reduce the amount of electronics, cables, and crate backplane required, the data is at several points multiplexed in time, so that many elements of the system run at rates up to 83 MHz.

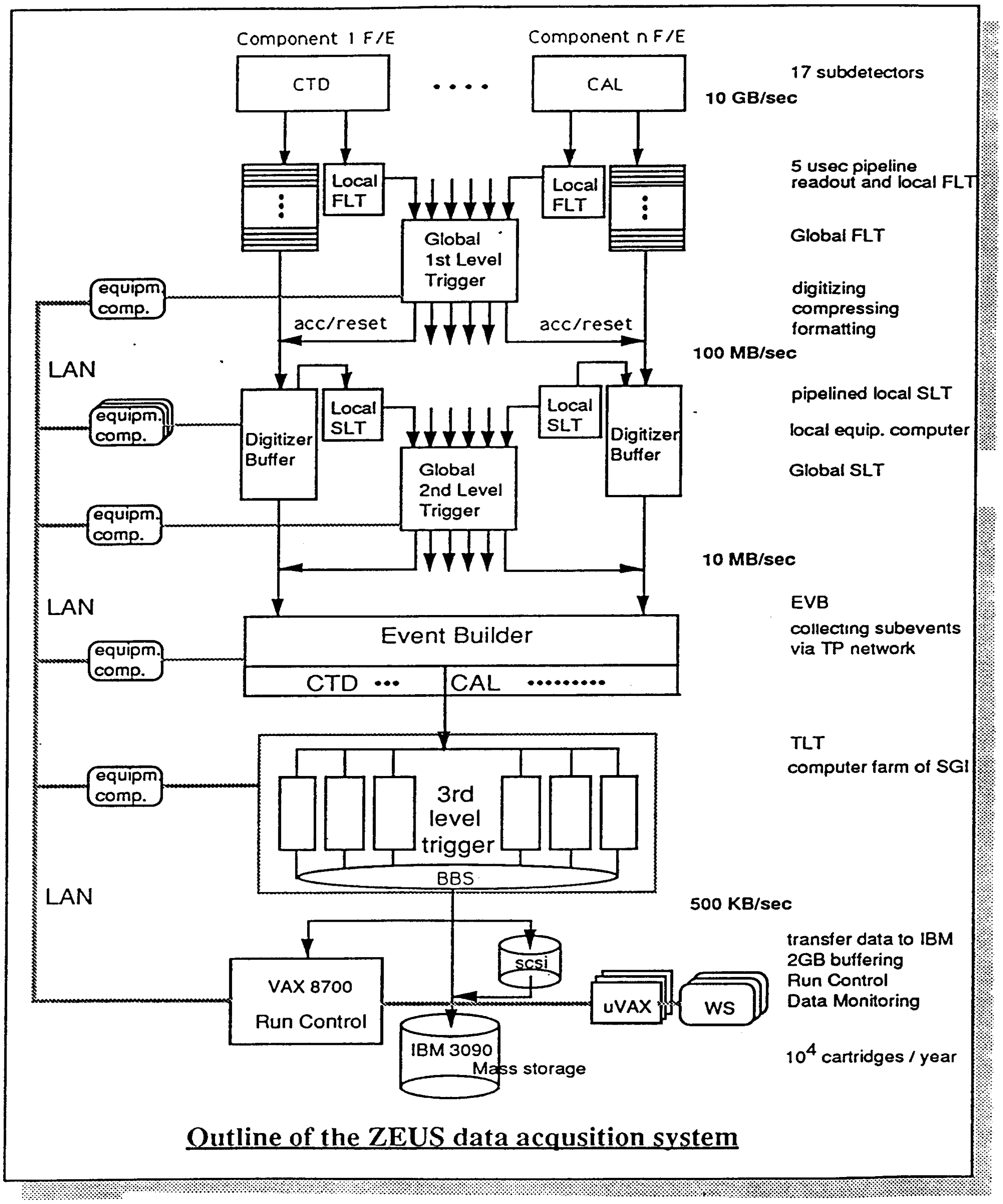

Figure 2.4: The overview of ZEUS trigger system. Shown are the central components crucial to the ZEUS trigger and data acquisition.

The organization of the CFLT is shown in Figure 2.5.

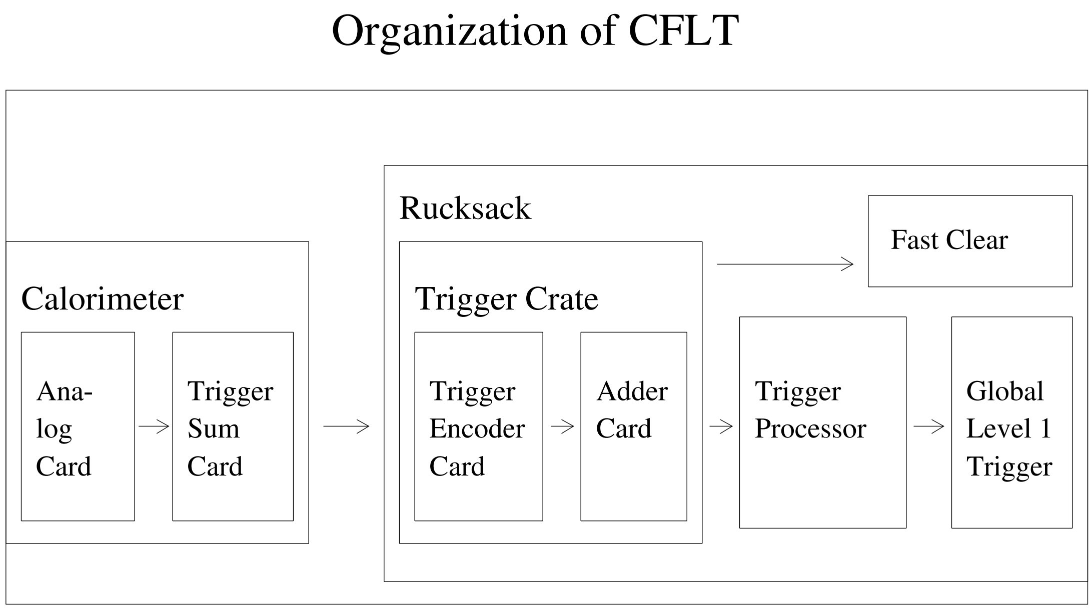

Figure 2.5: The organization of CFLT. Schematic diagram showing the basic components of Calorimeter First Level Trigger System.

The first element of the CFLT is the Trigger Sum Card (TSC), which is mounted on the detector next to the Front End Cards (FEC). The FECs are the first step in the calorimeter data acquisition chain. Each FEC accepts pulses from up to 12 photomultiplier tubes (PMT) and passes 5% of sums of up to 4 PMTs to the TSC. The TSC receives eight inputs, four left and four right phototube sum signals. These are integrated and summed for each left and right pair, and the baseline restored quickly after the integration. The TSC, having shaped the signal, sends it as a differential signal down 60 m of shielded twisted pair cable to the electronics house, where it enters the Trigger Encoder Card (TEC) for digitization.

After digitization the TEC linearizes, pedestal corrects, and zero suppresses the energy. It also tests whether the energy is consistent with electromagnetic minimum ionizing particle or a quiet tower. The corrected energy is used to calculate subregional E, E_t, E_x and E_y. These values are fed into adder trees, which sum values for towers of the same type (EMC or HAC). The partial sums from each TEC are sent to the Adder Card which completes the summation of E, E_t, E_x and E_y for a single region (which consists 56 trigger towers). The linearized energy for each channel is also placed in a FIFO. The data at the head of the FIFO is sent to Fast Clear (which is a component in the trigger system to request an abort on the current processing if its own processing thinks so) via the Adder Card upon receipt of a trigger. EMC and HAC data from the same tower are also used to address a memory lookup table which determines which of six thresholds the trigger tower energy has passed. The same table determines if there is an electron candidate in that tower. Threshold level, electron candidate, minimum ionizing particle, and quiet tower information are all forwarded to the Adder Card.

The Adder Card sends control signals and clocks out to the TECs on the backplane. It collects FIFO data from the TECs and sends them to the Fast Clear upon receipt of a trigger, and continues the summing of E, E_t, E_x and E_y. It determines, from the tower energy thresholds, the energies in programmable subregions of the 56-tower region. The Adder Card histograms the number of towers in the region which reached each threshold, and finds the number of isolated muons and electrons in the region. This information is sent from the Adder Cards in the 16 trigger crates (which can also be called the 16 pre-processors) to the CFLT processor. The physical CFLT crate overview is shown in Figure 2.6.

The Calorimeter First Level Trigger Processor (CFLTP) does the final trigger calculations with data from the Adder Cards and ships these results to the Global First Level Trigger for the final trigger decision. The CFLTP is composed of 8 Input Cards, 10 Algorithm Cards, 4 Output Cards and One Communication Card. It calculates the total E, E_t, E_x, E_y, electromagnetic and hadronic energy, compares region boundaries to calculate the number of isolated electrons and muons, and computes regional EMC, HAC and total energies, particularly around the beam-pipe region where the beam-gas background is greatest. The CFLTP produces information on the global and regional status of the calorimeter trigger. It counts the total number of isolated muons and isolated electrons. These sums are made by first adding all of the contained isolated muons and electrons. The edge muons and electrons are matched up with the appropriate neighboring 56-trigger tower region. If the adjoining edge is quiet or has an isolated edge electron or muon in it, a single isolated electron or muon is included in the sum. If the adjoining edge is neither quiet nor contains an isolated muon or electron, the isolated muon or electron is not counted. The summary of all this information is transmitted to the GFLT for each 96 ns crossing.

The ZEUS Calorimeter First Level Trigger system has operated reliably, beautifully and up to design in 6 data-taking runs at HERA, and has accumulated 46 pb^{-1} integrated luminosity of physics data, at a 200 Hz output rate. It consistes of a 1792 channel system contained in 16 modified VME crates with 14 TECs and 2 Adder Cards, followed by a powerful Trigger Processor in a custom-backplane crate that analyzes 5 GBybes/sec data. The system makes extensive use of memory lookup tables so that thresholds, EM/HAC ratios, geometric factors, dead/noisy channel switchoff, calibration and subregion definitions are programmable. This

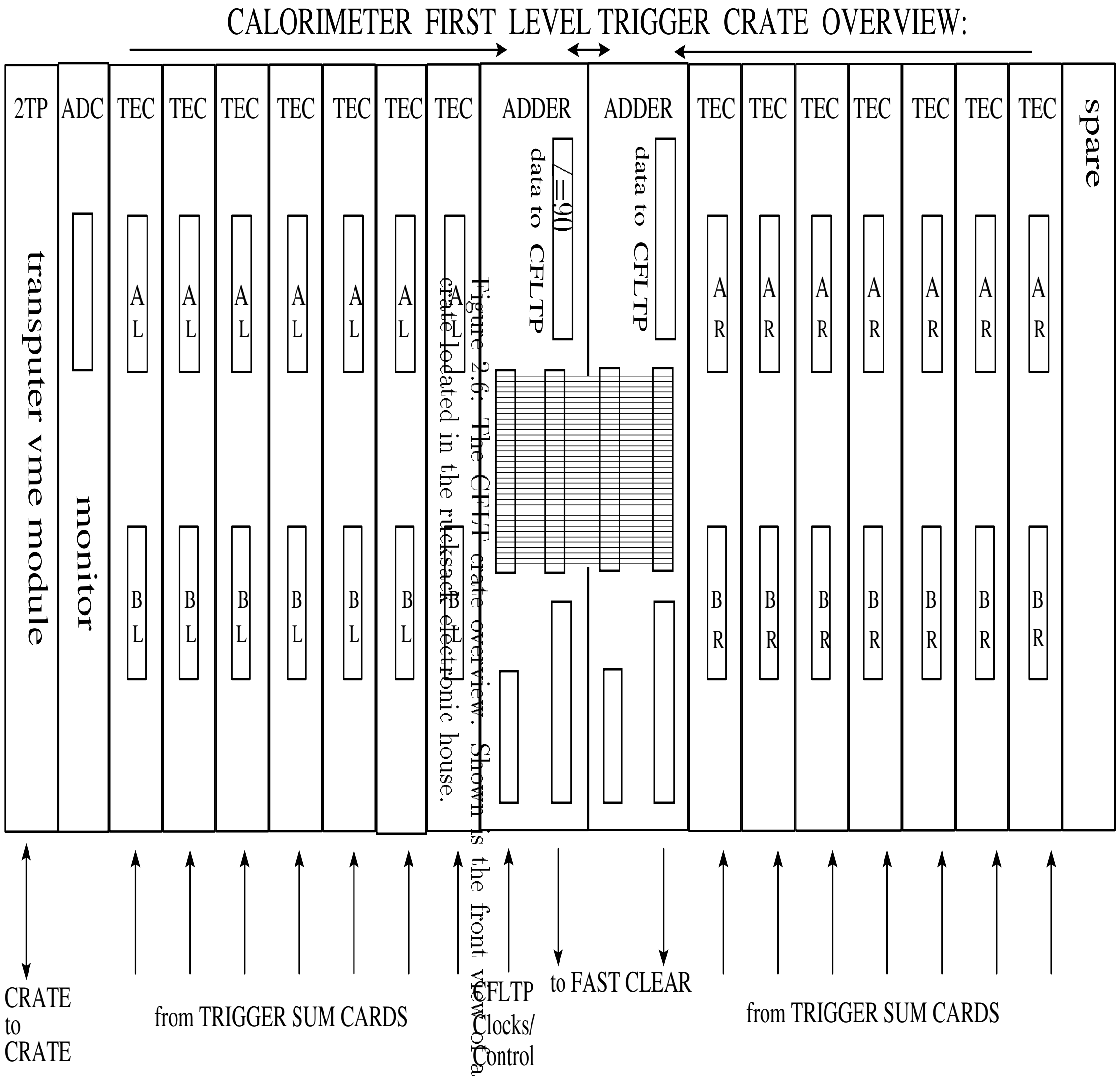

Figure 2.6: The CFLT crate overview. Shown is the front view of a typical CFLT crate located in the rucksack electronic house.

flexibility has proven very useful and has enabled frequent changes in configurations to accomodate changing physics requirements.

Chapter 3

EM Electron Finder

The Neutral Current analysis depends on the technique of lepton finding. In order to find an electron, one needs an algorithm (finder) to search for the electron in a neutral current event. There already exist at ZEUS several electron finders, namely, Repond finder, Sinistra, Exotics, etc. So why do we want to construct a new one? The answer lies in the limitations of other electron finders and also on the differences of the physics involved. For instance, Sinistra was fine tuned to optimize the electron finding efficiency and purity for low Q^2 DIS neutral current physics analysis. It also based its tuning on the Monte Carlo samples, which may or may not describe the data in the best possible way. Further, the other electron finders do not incorporate the valuable tracking information in their algorithm. This is understandable because at low Q^2, the electron generally misses the CTD acceptance region, electron tracks from CTD reconstruction may not exist at all. Background level from photoproduction processes can be controlled without introducing electron tracking requirement, due to dominant cross sections at low Q^2.

For high Q^2 neutral current DIS physics analysis, it is a different story. Here the electrons are usually in the BCAL, or the outer portions of FCAL and RCAL, where the CTD tracking acceptance is high. Incorporating tracking information makes the electron finding more accurate, it also reduces the photoproduction background even further. At high Q^2, the physics cross section is much lower than that at low Q^2, so background levels from photoproduction and low Q^2 DIS are a big concern. Based on these considerations, EM electron finder was designed to have the best performance for high Q^2 neutral current DIS physics analysis.

EM electron finding algorithm utilizes electron profiles (attributes) in the calorimeter and electron tracking in the CTD, a probability parameter is assigned to each of those profiles. The final electron finding is determined by a grand probability parameter which is a functional combination of those individual probability parameters.

3.1 Features of the new finder EM

- Use Cell Island algorithm instead of regular Island algorithm to do calorimeter clustering. The calorimeter is read out in terms of cell energies. A particle, however, may leave energy in a number of cells. There must be some consistent way of associating cells with objects likely to be deposited by a single particle. This analysis uses the concept of islands to make that association. A regular island is built in the following way. Cell energies are first summed into tower energies. The calorimeter is then scanned for local energy maxima - towers with no neighbor (neighbors include diagonally bordering towers) of higher energy. These become the seeds for the islands. Towers that are not local maxima are associated with the adjacent tower of highest energy. If this is not a maximum, the process continues until the local maximum is found. An island consists of all the towers, however remote, pointing to a single seed. Its energy is the sum of the energies of all the component towers. An energy weighted average position of all cells building the island is taken to be the island position. The difference between cell island and regular island is that for cell island, neighbors don't include diagonally bordering towers, neighbors have to physically touch each other in order to be counted as neighbors. This design is to avoid problems found in other electron finders where a huge blob consisting more than 50 cells is recognized as an electron. An electron is highly unlikely to have a shower that big.

- Parameterize NC DIS data in BCAL and RCAL, DIS Monte Carlo in FCAL. Unlike other electron finders, which use MC events to fine-tune the parametrisation to get best efficiency and purity, EM uses neutral current DIS data events to do the parametrisation in BCAL and RCAL. Since there are only a few data events with a scattered electron in FCAL, EM has to rely on MC to do the same thing in FCAL. Using data sample iteratively to tune the EM finder can avoid bias, introduced in the MC based finder if the MC sample does not describe the data very well.

- Integrate Tracking and Isolation. Calorimeter energy - CTD track match and calorimeter energy isolation are important ways of reducing backgrounds (fake electrons). As stated earlier, without tracking or isolation requirement, background levels can not be easily controlled. Here track-matching and isolation requirement are components of EM finder itself, a part in a big picture.

- Modular - one can easily add additional detectors (Presampler + HES +

SRTD). EM finder has room for future improvement as the ZEUS detector expands, so that it can be competitive and remain state-of-the-art.

- User can switch off probability components (e.g. no Isolation or Track match). This is convenient for different physics purposes. For instance, people who wish to pursue prompt photon physics do not want to find electrons, they want to find photons, which should not have a track pointing to the electromagnetic cluster. However, in this thesis no such switch off is done for obvious reason.

3.1.1 Variables parameterized

The following variables were parameterized as components of EM electron finding algorithm.

- HAC energy fraction of the electron cluster. This is a good indicator of whether the object is electron or hadron. For an electron candidate, the value of HAC energy fraction is close to 0.

- Fractional energy leakage of the cluster outside the two highest energy modules. Electromagnetic shower is much narrower than hadronic shower, large leakage indicates broader shower.

- Fractional energy leakage of the cluster outside the two highest energy cell rows. Same argument as above, but in the perpendicular direction to above.

- Background energy inside 0.8 $\eta\phi$ cone around the electron, indicating isolation. Background energy is the energy inside that cone, but not associated with the cells of electron candidate cluster. The smaller this background energy, more isolated the candidate is, and more likely the candidate is an electron, except for electromagnetic radiation events.

- $\theta_{CAL} - \theta_{CTD}$. The difference between the θ angle of the electron candidate measured by calorimeter, and the θ angle of the matched track measured by CTD. It indicates how good the match is.
- $\phi_{CAL} - \phi_{CTD}$. The difference between the azimuthal ϕ angle of the electron candidate measured by calorimeter, and the ϕ angle of the matched track measured by CTD. Same indication as above.
- $1/P_{CTD} - 1/E_{CAL}$. The difference between the inverse energy of the electron candidate in the calorimeter, and the inverse momentum of the matched track in the CTD. It indicates whether the match is good, provided that the EM cluster is due to a single particle.

Each variable is assigned a probability P, which is determined in the following subsection. For n variables we will have corresponding $P_1, P_2, ..., P_n$, with those n individual probabilities we can make a grand probability by:

$$GrandProb = F(P_1 \cdot P_2 \cdots P_n) \tag{3.1}$$

where function $F()$ transforms the product of n independent numbers each uniformly distributed between 0 and 1, into a single number uniformly distributed between 0 and 1. That is the ideal case. The variables in EM finder may not be independent variables, but they can be regarded as nearly so. The biggest correlation is found to be between the last two variables, namely, $\phi_{CAL} - \phi_{CTD}$ and $1/P_{CTD} - 1/P_{CAL}$. The correlation is below 0.2, all other correlations are very small.

EM finder has built-in algorithm to choose the correct electron if multiple candidates are found by the following way:

$$DrakeProb = GrandProb \cdot 1/Q^4 \cdot f(P_tFake, P_tTrue) \tag{3.2}$$

where $f(P_tFake, P_tTrue)$ is a probability function, depending on the P_t of the fake electron and P_t of the true electron which are determined by neutral current DIS MC. The highest $DrakeProb$[1] candidate is chosen to be the true electron. This algorithm has since drawn some criticism from people who think the $1/Q^4$ factor is artificially introduced without foundation. The answer to that point is this: suppose two electron candidates are found with roughly equal Grand Probability, one is a low Q^2 electron, the other a high Q^2 electron, which one do you choose? It is sensible to choose the low Q^2 one because of the dominance ($\propto 1/Q^4$) of the low Q^2 cross section over high Q^2 cross section. This does not mean this algorithm will always make the right decision. So the P_t factor is also added in because high Q^2 electron tends to have a higher P_t and higher P_t electron tends to be a true electron. High Q^2 electron gets back some compensation.

[1]Named after the great explorer Sir Francis Drake, who once remarked, "There must be a beginning to any great matter, but the continuing unto the end until it be thoroughly finished, yields the true glory"

3.2 Explanation of Electron-finding Algorithm

The preselection was done by applying Cell-Island algorithm on 93, 94 and 95 neutral current DIS data sample[2]. Interest was given to $Q^2 > 200\,\mathrm{GeV}^2$ events sample. Then the following 7 variables were parameterized. For each variable being parameterized, no limit was applied to its value but certain limits were applied on the remaining 6 other variables to make the sample clean of photoproduction background, and to introduce as little bias as possible.

To parameterize those variables, the following standard cuts were applied:

- Apply Cell-Island routine to form electron clusters.
- $E - P_z > 40\,$Gev to cut off most of the photoproduction backgrounds.
- $\not{P}_t/\sqrt{E_t} < 3$ to get rid of most of cosmic rays.
- $0 < DCA < 5$ cm to require track-CAL matching, where DCA is the distance of the closest approach between CTD track and electron cluster in the calorimeter.
- $0.5 < P_{CTD}/E_{CAL} < 2.$ to require momentum-energy match in CTD and CAL.
- $Bgd < 2.$GeV, where Bgd is the energy inside the electron 0.8 $\eta\phi$ cone but not belonging to electron cells.

The cuts for all 7 different variables are listed in Table 3.2.

[2]The EM finder was developped before 96 data was available

Table 3.1: EM finder variables parametrisation cuts. A "Yes" means the standard cut in the left column is applied, a "No" means that standard cut is not applied, a paranthesis with numbers in it means the standard cut in the left column is changed to the values in that paranthesis.

	fHAC	X_{size}	$d\theta$	$d\phi$	dInvP	fMdl	fCel	Bgd
$E - P_z > 40$	Yes	Yes	Yes	Yes	Yes	Yes	Yes	Yes
$\not{P}_t/\sqrt{E_t} < 3$	Yes	Yes	Yes	Yes	Yes	Yes	Yes	Yes
$0 < DCA < 5$	Yes	Yes	(0,20)	(0,20)	(0,20)	Yes	Yes	Yes
$0.5 < P_{CTD}/E_{CAL} < 2$	Yes	Yes	(0,4)	(0,4)	(0,4)	Yes	Yes	Yes
$Bgd < 2.$ GeV	Yes	Yes	Yes	Yes	Yes	Yes	Yes	No
$fHAC < 0.1$	No	Yes	No	No	No	No	No	No
Cell-Island	Yes	Yes	Yes	Yes	Yes	Yes	Yes	Yes

- $fHAC$: HAC fraction of the energy of the electron candidate.
  - First an event distribution of $fHAC$ was obtained, here the distribution was taken in four different cases because a little care is needed. We know the fact that if the electron is closer to the crack between two modules, the electron is more likely to get a bigger HAC energy fraction, so those electrons having different distances to the module edge should not be treated on an equal footing. They were taken in different categories of:
    - $Dmedg < 0.7$cm.
    - $0.7 < Dmedg < 1.4$cm.
    - $1.4 < Dmedg < 2.1$cm.
    - $Dmedg > 2.1$cm.

    where $Dmedg$ is the distance to the module edge.
  - For each category, the probability is computed as:

$$P(fHAC) = \frac{\int_{fHAC}^{\infty} f(x) \cdot dx}{\int_0^{\infty} f(x) \cdot dx} \tag{3.3}$$

where $f(x)$ is the distribution of variable $fHAC$. $f(x)$ is plotted in Figure 3.1 for BCAL electrons, Figure 3.2 for RCAL electrons and Figure 3.3 for FCAL electrons, the majority of the events have HAC fraction equal to zero, which are not shown in the plots, their probability is calculated by:

$$P(fHAC = 0) = \frac{1 + N_0/N}{2} \tag{3.4}$$

where N_0 is the number of events with $fHAC = 0$, and N is the total number of events.

– Finally the $P(x)$ distribution was fitted with a smooth function which then became the parameterization of $fHAC$. The bigger the value of this function, the more likely it is an electron candidate. Same procedure was applied for all the other variables.

- Z_{size}: The physical size of the BCAL electron in the z direction. The physical size of an electron in a particular direction was calculated in the following way, it applies to physical size in any of x, y, z direction:

$$\langle X^{\mu} \rangle = \frac{\sum_{i=1}^{nCell} [X_i^{\mu} \cdot E_i]}{\sum_{i=1}^{nCell} E_i} \tag{3.5}$$

$$X_{size}^{\mu} = \sqrt{\frac{\sum_{i=1}^{nCell} \left[\left(X_i^{\mu} - \langle X^{\mu} \rangle \right)^2 \cdot E_i \right]}{\sum_{i=1}^{nCell} E_i}} \tag{3.6}$$

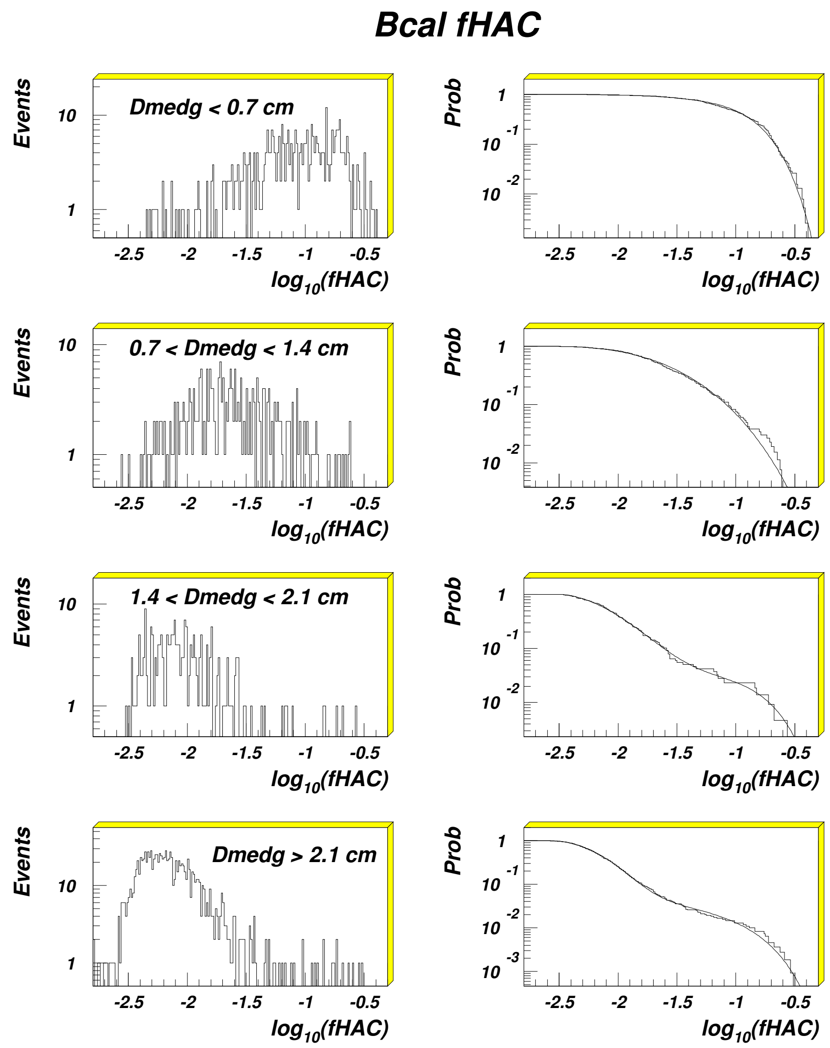

Figure 3.1: Distribution and Probability function of Bcal electron in terms of $fHAC$, the HAC fraction of the electron cluster energy, in four different categories. Here the horizontal axis is taken as the $log_{10}fHAC$. The histogram is the data and the curve is the fit to the data.

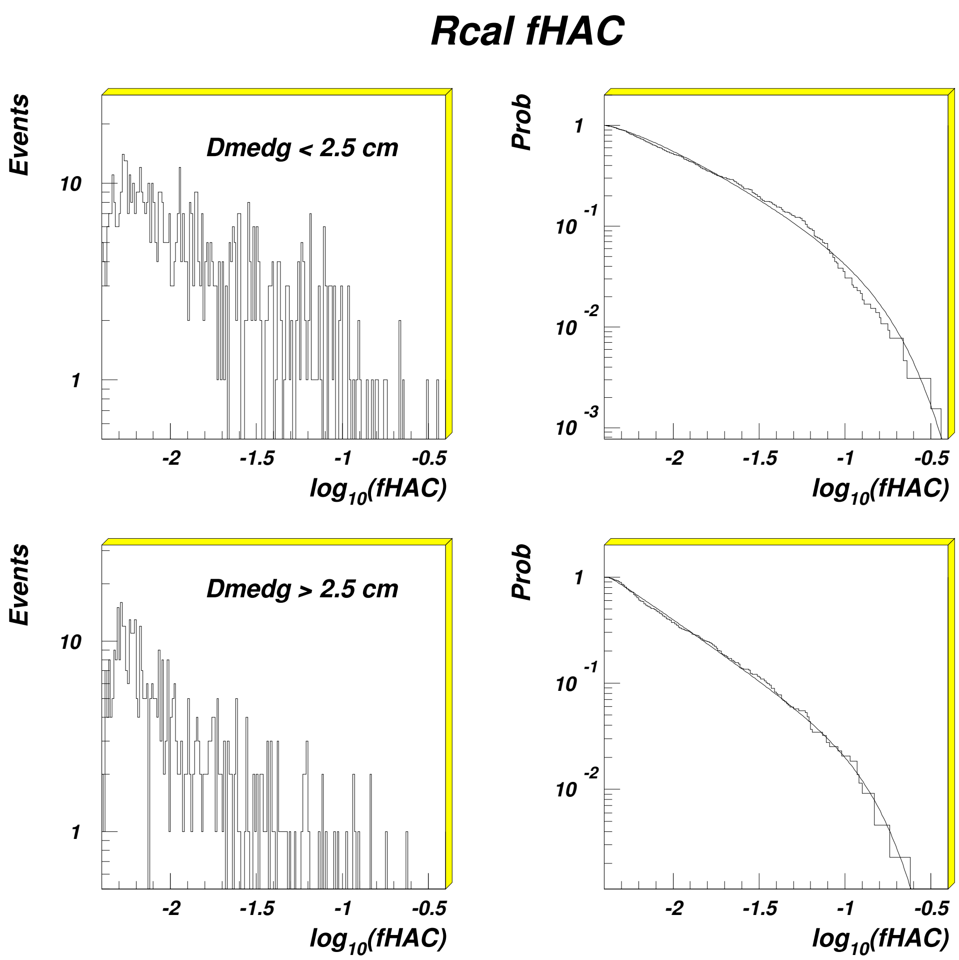

Figure 3.2: Distribution and Probability function of Rcal electron in terms of $fHAC$, the HAC fraction of the electron cluster energy, in two different categories. Here the horizontal axis is taken as the $log_{10}fHAC$. The histogram is the data and the curve is the fit to the data.

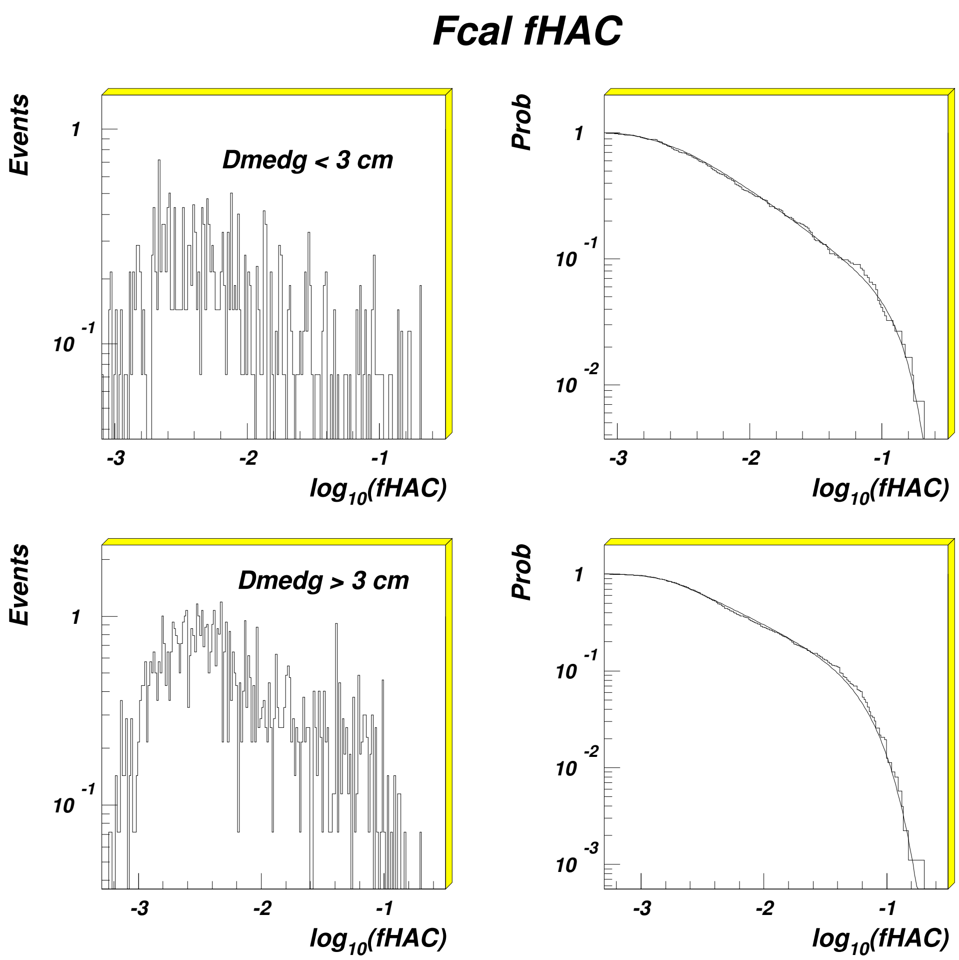

Figure 3.3: Distribution and Probability function of Fcal electron in terms of $fHAC$, the HAC fraction of the electron cluster energy, in two different categories. Here the horizontal axis is taken as the $log_{10}fHAC$. The histogram is the data and the curve is the fit to the data.

where $\mu = 1, 2, 3$ correspond to x, y, z coordinates, X_i^μ is the position of the ith cell, $\langle X^\mu \rangle$ is the electron position calculated by doing a cell energy-weighted average over the cell center position. X_{size}^μ is the size of the electron in x, y or z direction.

To parameterize Z_{size}, the standard preselection cuts as stated in the beginning of this section were applied, plus an extra requirement $fHAC < 0.1$ to get a more pure sample. The Z_{size} distribution for BCAL electron is shown in Figure 3.4.

- $R\phi_{size}$: The physical size of the BCAL electron in $R\phi$ projection. It was calculated as:

$$R\phi_{size} = \sqrt{\left(X_{size} \cdot \sin\phi\right)^2 + \left(Y_{size} \cdot \cos\phi\right)^2} \tag{3.7}$$

  To parameterize $R\phi_{size}$, the same standard preselection cuts were applied. The distribution was then integrated to obtain probability function for $R\phi_{size}$. Both distribution and probability are shown in Figure 3.5.

- X_{size}: The physical size of the RCAL or FCAL electron in x direction. The same standard preselection cuts were applied to get the distribution of X_{size} and then the probability function. They are shown in Figure 3.6 for RCAL electrons and Figure 3.7 for FCAL electrons.

- Y_{size}: The physical size of the RCAL or FCAL electrons in y direction. The same standard preselection cuts were applied. we know the fact that if the electron is closer to the crack (tower edge) between two towers, the electron shower is more likely to spread wider, thus having a larger Y_{size}. So those

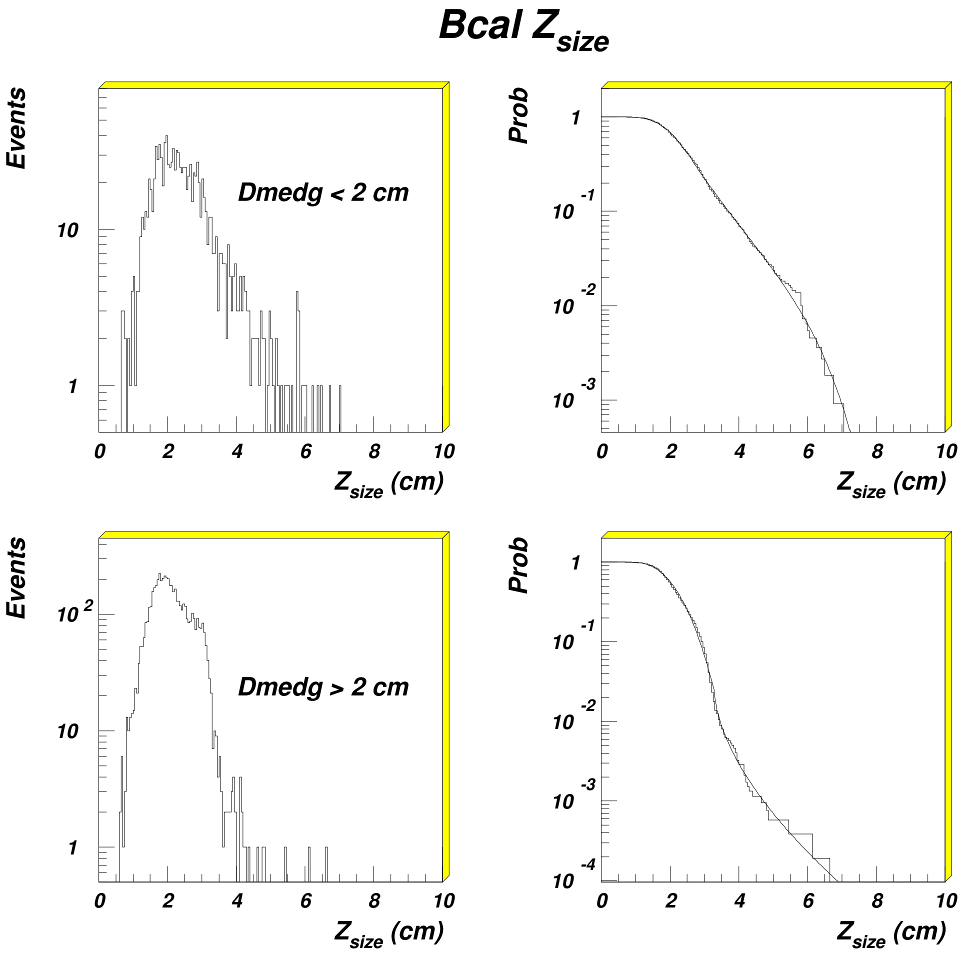

Figure 3.4: Distribution and Probability function of Bcal electron in terms of Z_{size}, the physical size of the electron in z direction, in two different categories. The histogram is the data and the curve is the fit to the data.

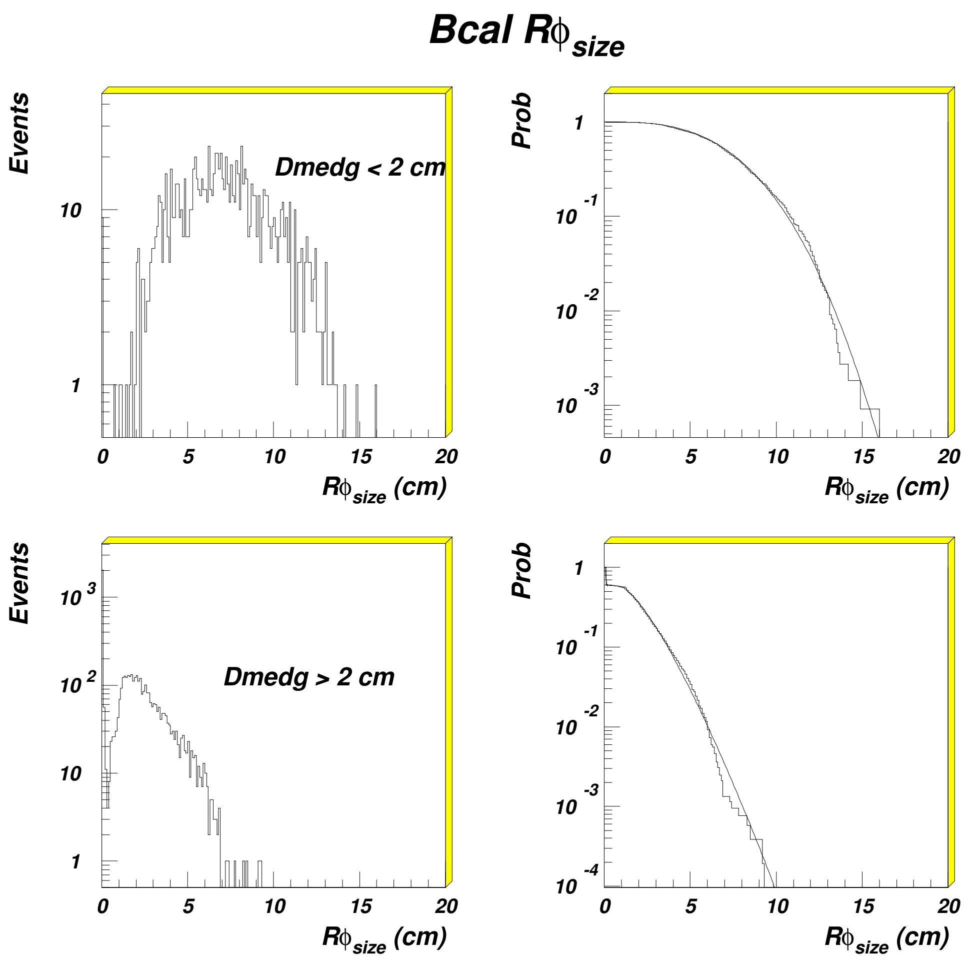

Figure 3.5: Distribution and Probability function of Bcal electron in terms of $R\phi_{size}$, the physical size of the electron in $R\phi$ direction, in two different categories. The histogram is the data and the curve is the fit to the data.

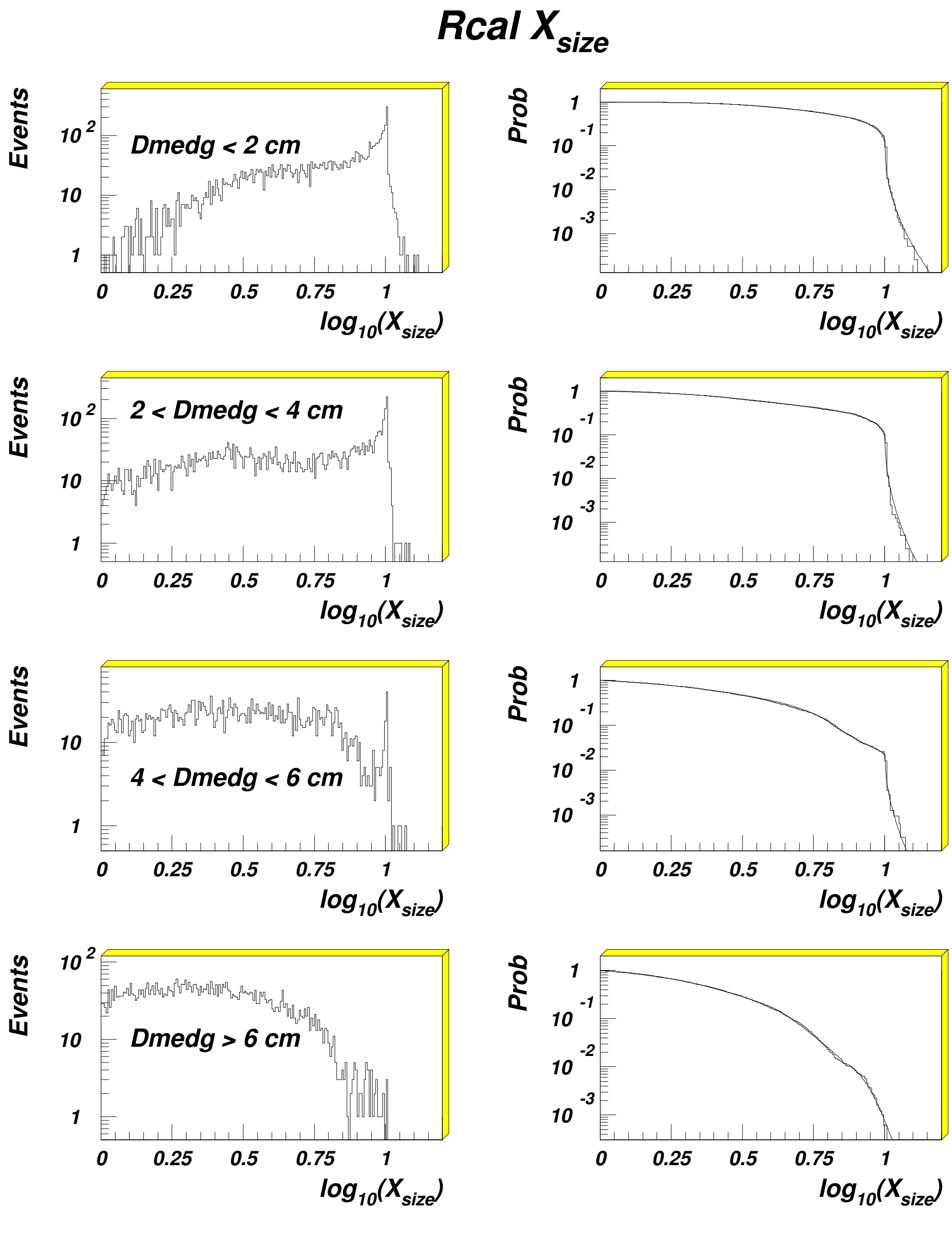

Figure 3.6: Distribution and Probability function of Rcal electron in terms of X_{size}, the physical size of the electron in x direction, in four different categories. The histogram is the data and the curve is the fit to the data.

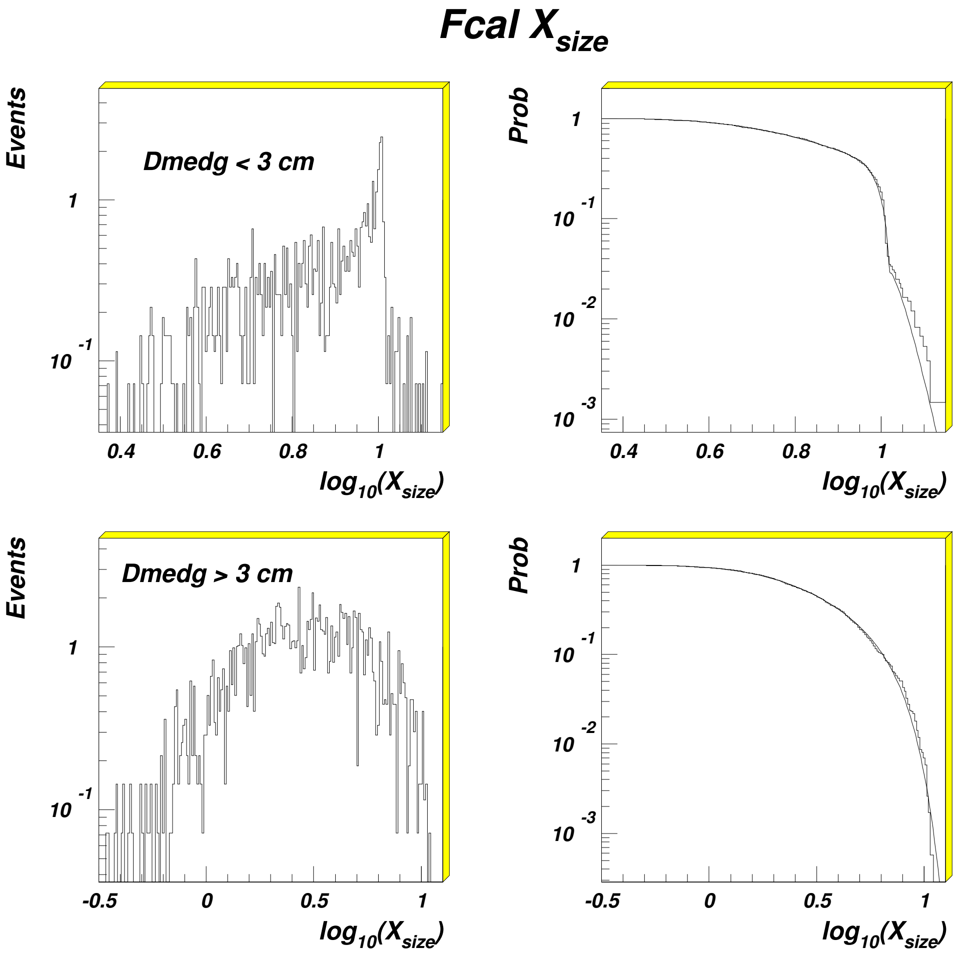

Figure 3.7: Distribution and Probability function of Fcal electron in terms of X_{size}, the physical size of the electron in x direction, in two different categories. The histogram is the Monte Carlo and the curve is the fit to the Monte Carlo.

electrons having different distances to the tower edge should not be treated on an equal footing. If they are treated on the same footing, one electron will have a larger probability over another electron simply because it is farther away from the tower edge than the other one, even though their other properties are the same. So they are put in the different categories of:

- $Dtedg < 3cm$.
- $Dtedg > 3cm$.

$Dtedg$ being the distance to the tower edge. The integration was done separately for the two categories. The RCAL electron is shown in Figure 3.8 and FCAL electron is shown in Figure 3.9.

- dθ: $\theta_{CAL} - \theta_{CTD}$, the difference of electron polar angle θ measured by calorimeter and the polar angle of the matching track measured by CTD. The cuts listed in Table 3.2 were applied.

  - We use the mean value of $d\theta$, ranging from -1 to 1 radian, $\langle d\theta \rangle$ and the rms, $\sigma_{d\theta}$ to define:

$$d\Theta = \frac{\mid d\theta - \langle d\theta \rangle \mid}{\sigma_{d\theta}} \tag{3.8}$$

  - The probability for each calorimeter was then calculated:

$$P(d\Theta) = \frac{\int_{d\Theta}^{\infty} f(x) \cdot dx}{\int_{0}^{\infty} f(x) \cdot dx} \tag{3.9}$$

They are shown in Figure 3.10 for BCAL, Figure 3.11 for RCAL, and Figure 3.12 for FCAL.

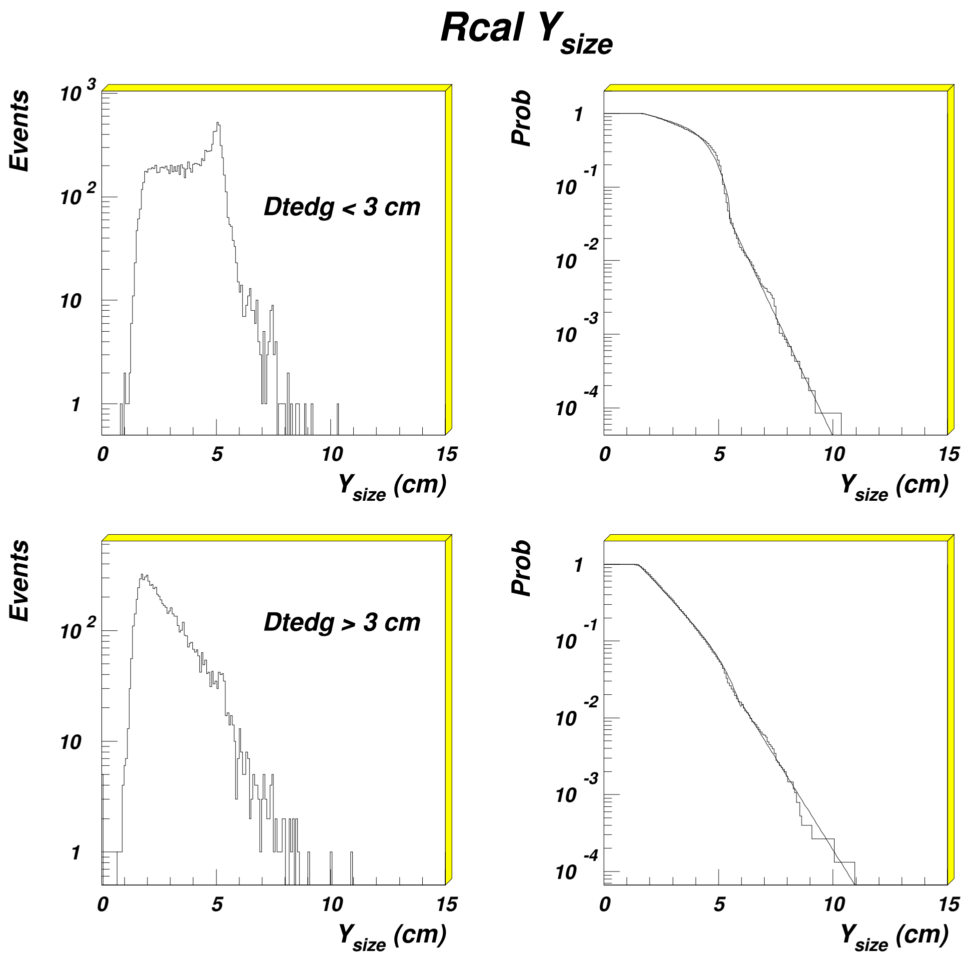

Figure 3.8: Distribution and Probability function of Rcal electron in terms of Y_{size}, the physical size of the electron in y direction, in two different categories. The histogram is the data and the curve is the fit to the data.

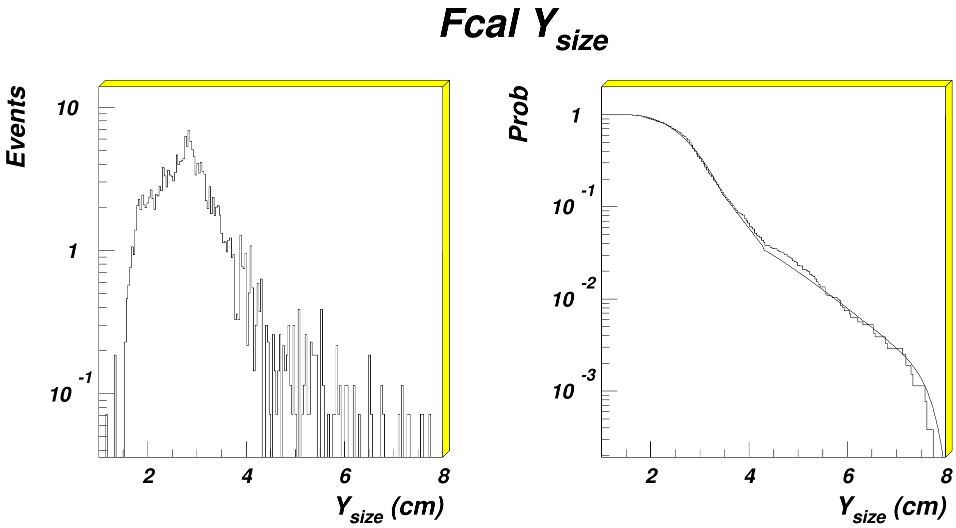

Figure 3.9: Distribution and Probability function of Fcal electron in terms of Y_{size}, the physical size of the electron in y direction. The histogram is the Monte Carlo and the curve is the fit to the Monte Carlo.

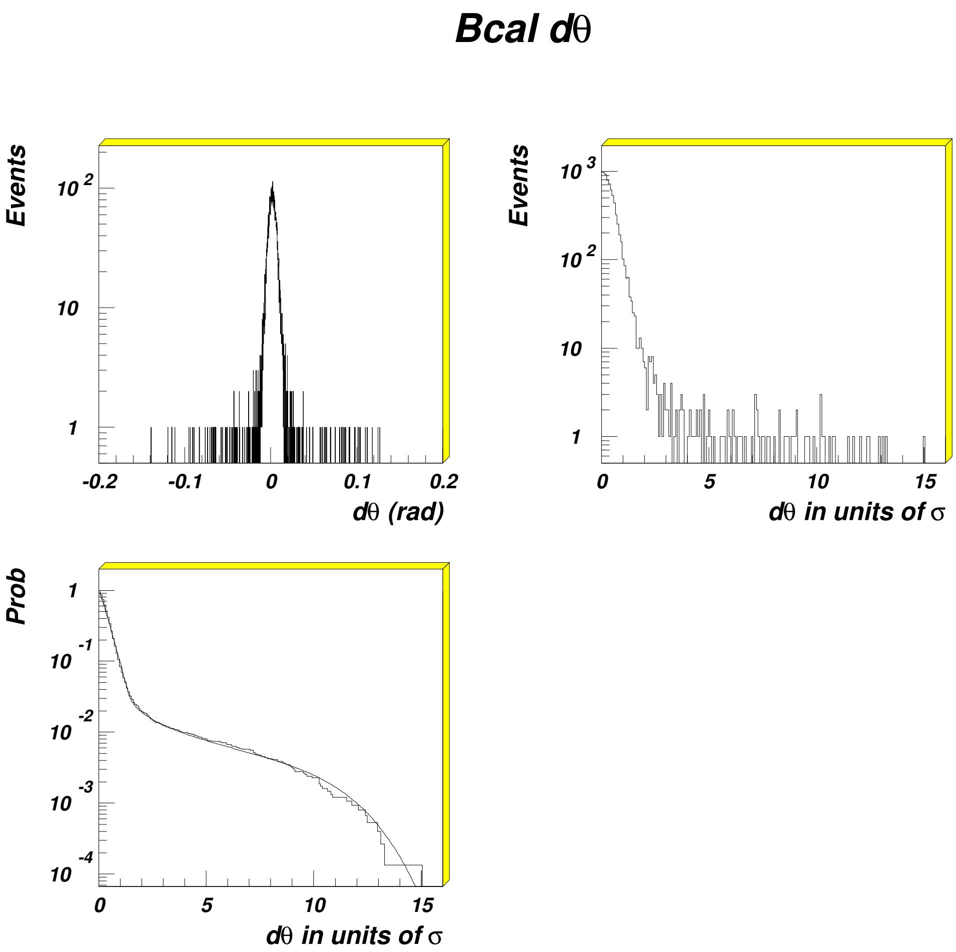

Figure 3.10: Distribution and Probability function of Bcal electron in terms $d\Theta$, the difference between polar angle measured by calorimeter and that by CTD. The histogram is the data and the curve is the fit to the data. Note that the horizontal units have been converted to CTD polar angle resolution in the last two plots.

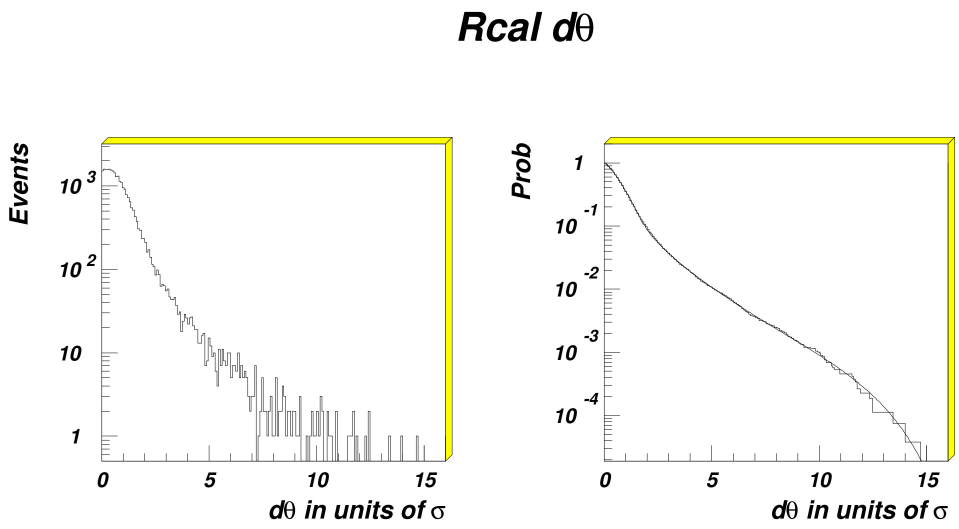

Figure 3.11: Distribution and Probability function of Rcal electron in terms $d\Theta$, the difference between polar angle measured by calorimeter and that by CTD. The histogram is the data and the curve is the fit to the data. Note that the horizontal units have been converted to CTD polar angle resolution.

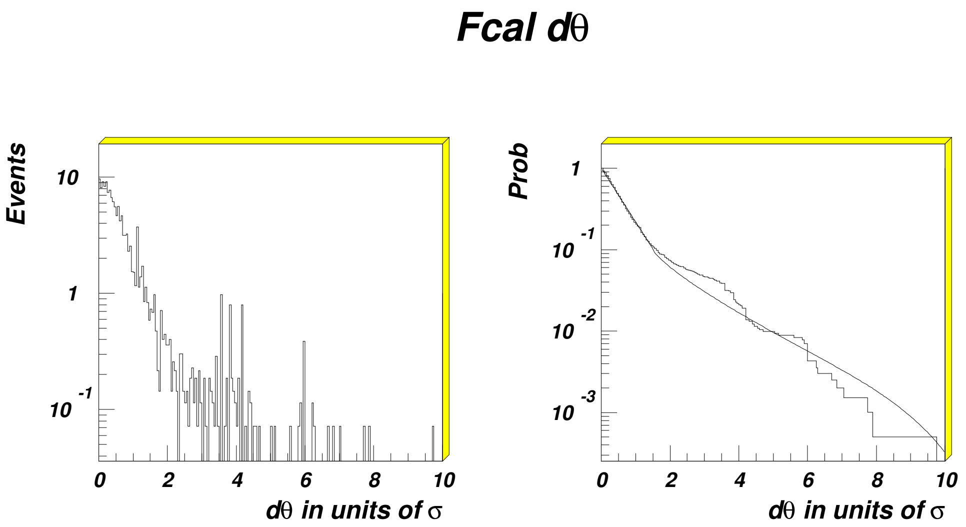

Figure 3.12: Distribution and Probability function of Fcal electron in terms $d\Theta$, the difference between polar angle measured by calorimeter and that by CTD. The histogram is the MC and the curve is the fit to the MC. Note that the horizontal units have been converted to CTD polar angle resolution.

- dϕ: The difference of electron azimuthal ϕ angle measured by calorimeter and the ϕ angle of the matching track measured by the CTD. The cuts listed in Table 3.2 were applied.

  – We use the mean value of $d\phi$, ranging from -1 to 1 radian, $\langle d\phi \rangle$ and the rms, $\sigma_{d\phi}$ to define:

  $$d\Phi = \frac{\mid d\phi \mid}{\sigma_{d\phi}} \tag{3.10}$$

  Since positively-charged particles and negatively-charged particles necessarily bend in different directions, $d\phi$ will be asymmetric about 0. Therefore $d\phi$ was multiplied by the electric charge of the particle, and distributions were put in two different categories with $d\phi > 0$ and $d\phi < 0$.

  The distribution and probability function $P(x)$ are shown in Figure 3.13 for BCAL, Figure 3.14 for RCAL, and Figure 3.15 for FCAL.

- dInvP: The difference of the reciprocal of electron energy measured in the calorimeter and the curvature of the electron track as measured by the CTD.

  $$dInvP = \frac{1}{P_{CTD}} - \frac{1}{E_{CAL}} \tag{3.11}$$

  To parameterize this variable, the preselection cuts as stated in Table 3.2 were applied.

  From the event distribution of $dInvP$, ranging from -1 to 2, $\langle dInvP \rangle$, the mean value of $dInvP$, was determined, and also σ_{dInvP}, the rms of $dInvP$. A new variable called $\Delta InvP$ was defined:

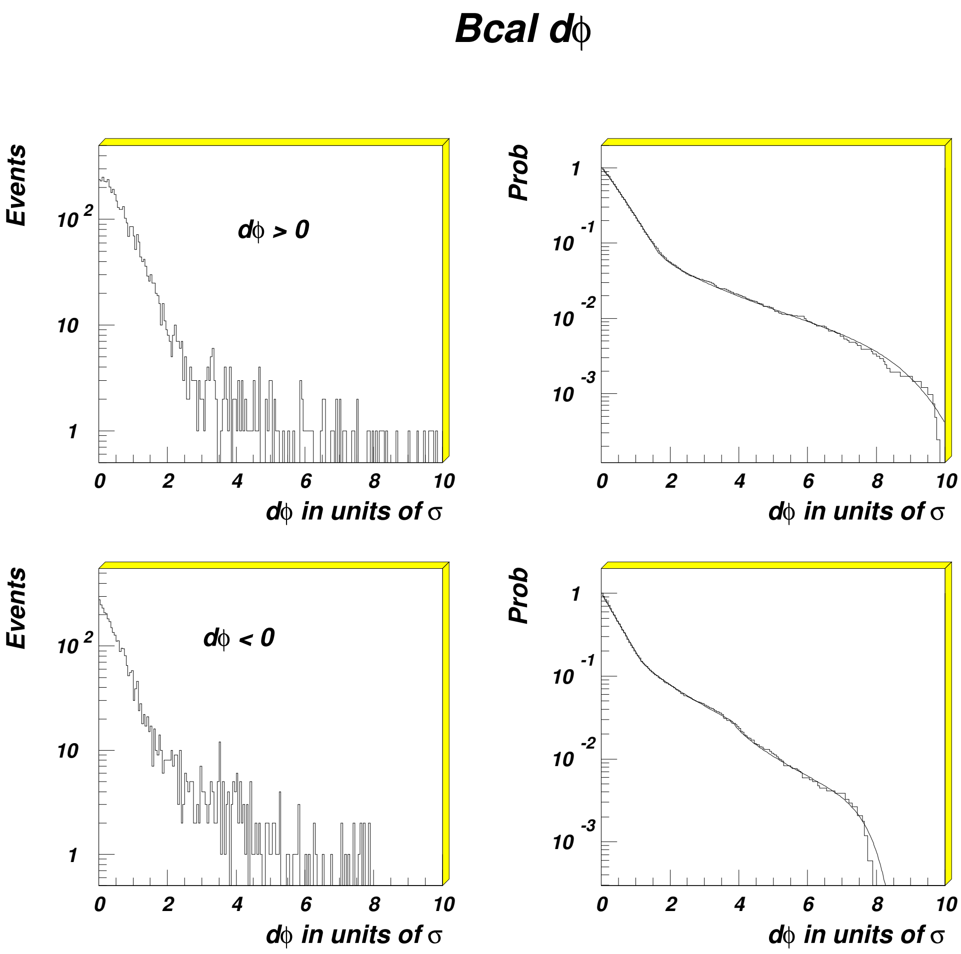

Figure 3.13: Distribution and Probability function of Bcal electron in terms $d\phi$, the difference between azimuth angle measured by calorimeter and that by CTD. The histogram is the data and the curve is the fit to the data. Note that the horizontal units have been converted to CTD azimuth angle resolution.

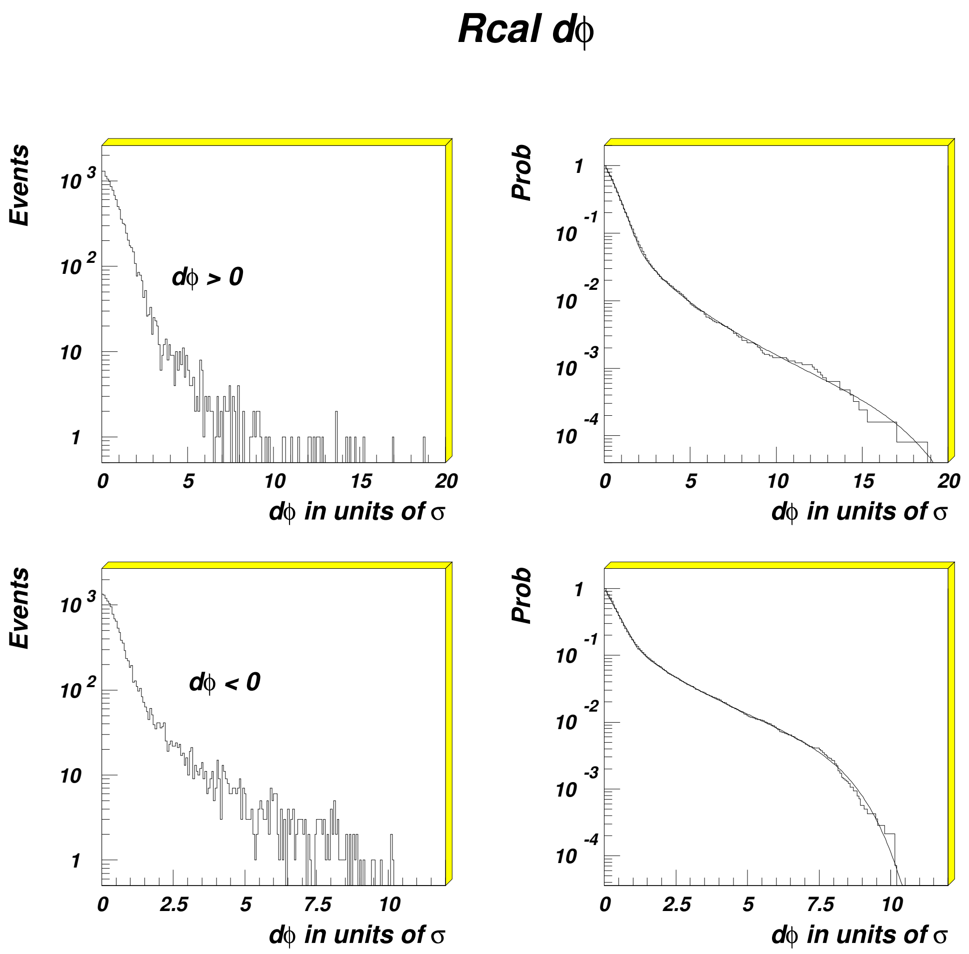

Figure 3.14: Distribution and Probability function of Rcal electron in terms $d\phi$, the difference between azimuth angle measured by calorimeter and that by CTD. The histogram is the data and the curve is the fit to the data. Note that the horizontal units have been converted to CTD azimuth angle resolution.

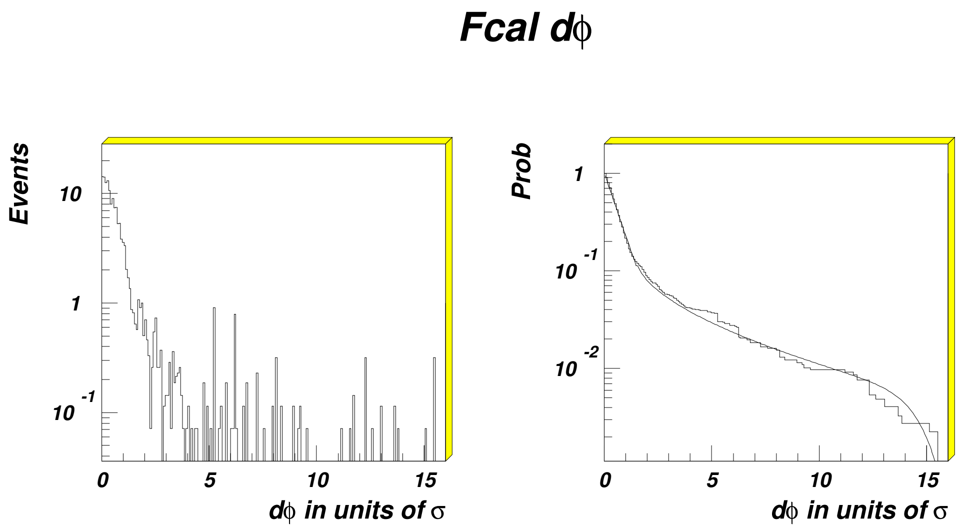

Figure 3.15: Distribution and Probability function of Fcal electron in terms $d\phi$, the difference between azimuth angle measured by calorimeter and that by CTD. The histogram is the MC and the curve is the fit to the MC. Note that the horizontal units have been converted to CTD azimuth angle resolution.

$$\Delta InvP = \frac{\mid dInvP \mid}{\sigma_{dInvP}} \tag{3.12}$$

Then same technique was employed on event distribution of $\Delta InvP$, to determine probability distribution P(x).

Event distribution and probability function $P(x)$ are shown in Figure 3.16 for Bcal, Figure 3.17 for Rcal, and Figure 3.18 for Fcal.

- Bgd: The peripheral background energy around the electron cluster, i.e. the energy inside the electron cone but which does not belong to electron cells.

  The standard cuts as stated in Table 3.2 were applied, but without any cut on Bgd itself, to get event distribution of Bgd. Then the same integration technique was employed to obtain probability function of this variable.

$$P(Bgd) = \frac{\int_{Bgd}^{\infty} f(x) \cdot dx}{\int_{0}^{\infty} f(x) \cdot dx} \tag{3.13}$$

  The event distribution and probability function are shown in figure 3.19 for BCAL, Figure 3.20 for RCAL, and Figure 3.21 for FCAL.

- fMdl: The fractional energy leakage outside the two highest energy modules in the electron cluster. This variable is defined:

$$fMdl = 1. - E_1(highest) - E_2(secondhighest) \tag{3.14}$$

  where E_i is the ith highest energy module's energy fraction in the electron cluster. The standard cuts as stated in Table 3.2 were applied for this variable.

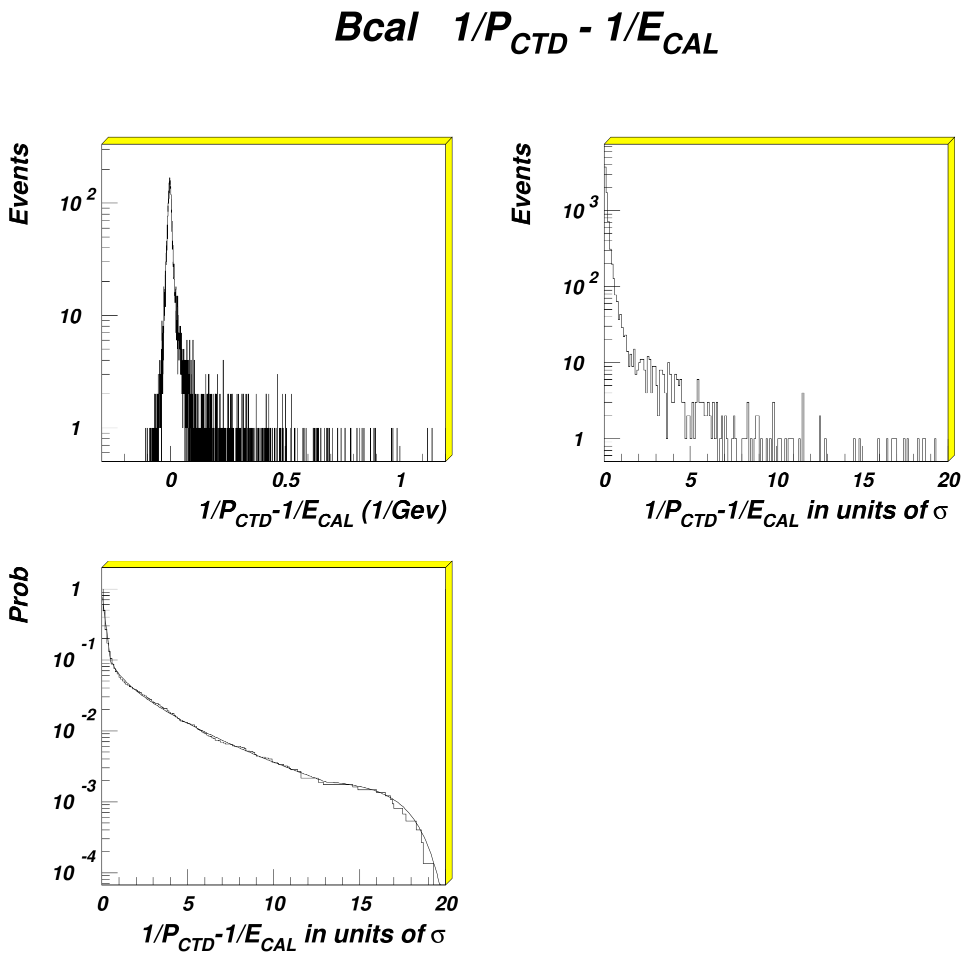

Figure 3.16: Distribution and Probability function of Bcal electron in terms $dInvP$ ($=1/P_{CTD} - 1/E_{CAL}$), the difference of the reciprocal of electron energy measured in the calorimeter and the curvature of the electron track as measured by the CTD. The histogram is the data and the curve is the fit to the data. Note that the horizontal units have been converted to CTD curvature resolution in the last two plots.

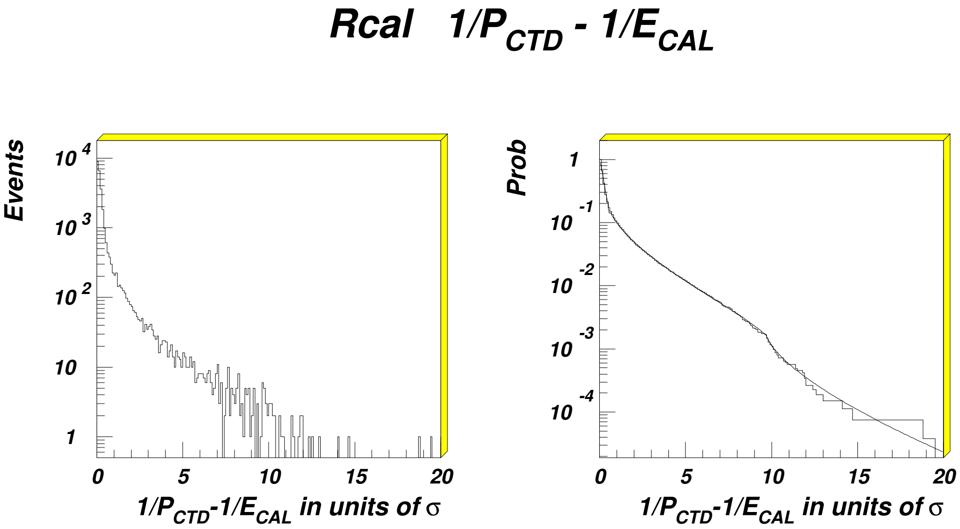

Figure 3.17: Distribution and Probability function of Rcal electron in terms $dInvP$ ($=1/P_{CTD}-1/E_{CAL}$), the difference of the reciprocal of electron energy measured in the calorimeter and the curvature of the electron track as measured by the CTD. The histogram is the data and the curve is the fit to the data. Note that the horizontal units have been converted to CTD curvature resolution.

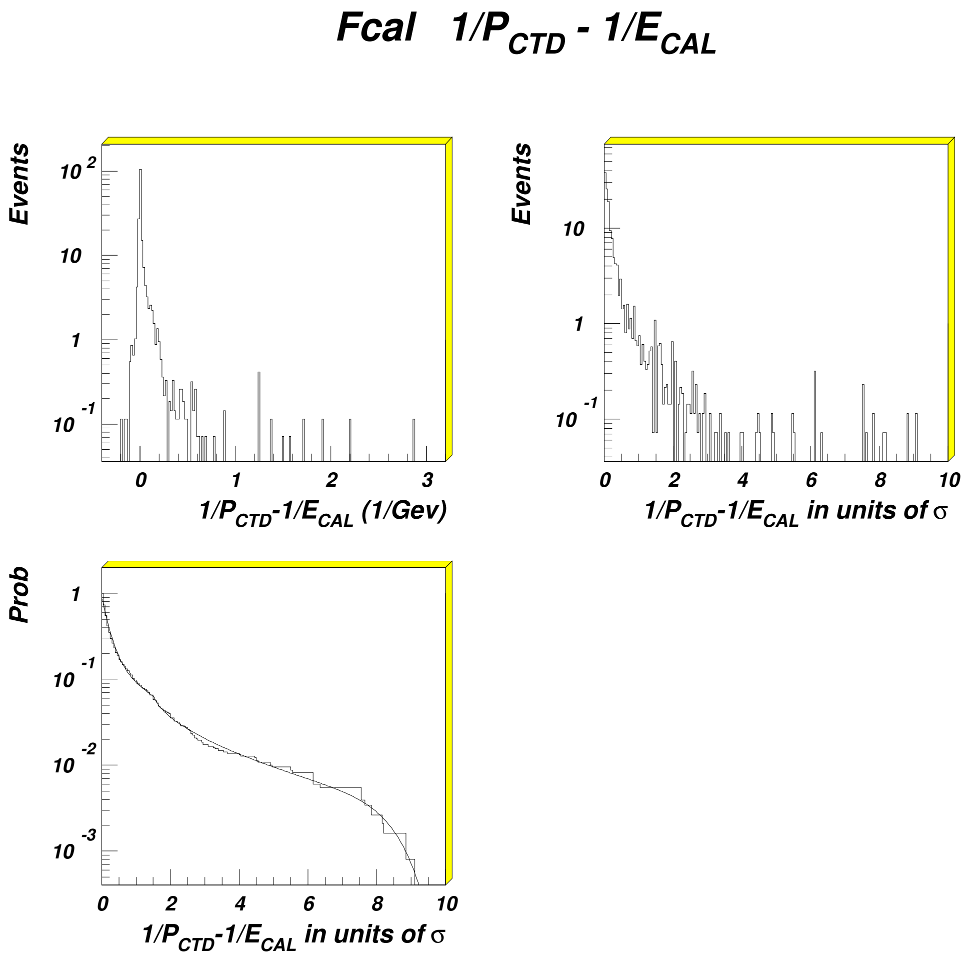

Figure 3.18: Distribution and Probability function of Fcal electron in terms $dInvP$ ($=1/P_{CTD} - 1/E_{CAL}$), the difference of the reciprocal of electron energy measured in the calorimeter and the curvature of the electron track as measured by the CTD. The histogram is the MC and the curve is the fit to the MC. Note that the horizontal units have been converted to CTD curvature resolution in the last two plots.

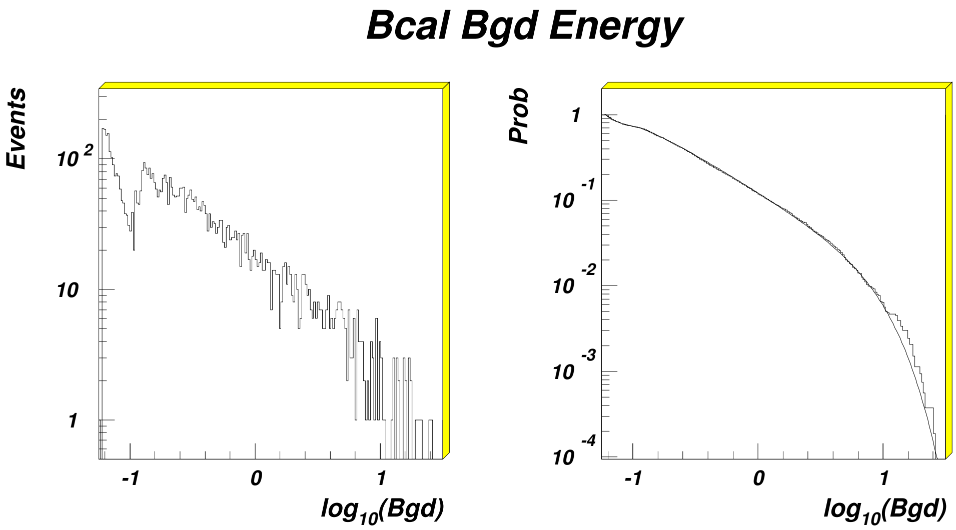

Figure 3.19: Distribution and Probability function of Bcal electron in terms Bgd (Background), the peripheral background energy around the electron cluster, i.e. the energy inside the electron cone but which does not belong to electron cells. It is a measure of isolation. The histogram is the data and the curve is the fit to the data. Note that the dip at about 100 MeV is due to the calorimeter noise suppression. The horizontal unit is in log scale.

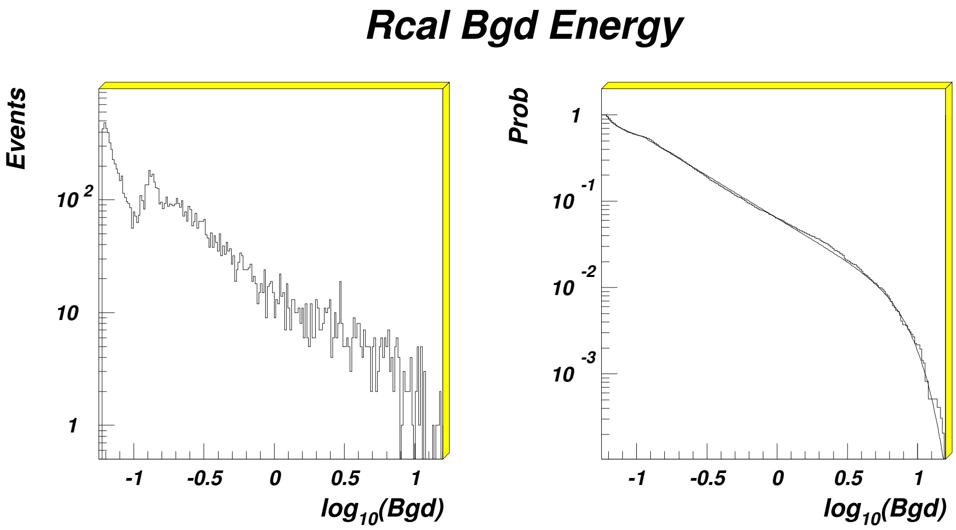

Figure 3.20: Distribution and Probability function of Rcal electron in terms Bgd (Background), the peripheral background energy around the electron cluster, i.e. the energy inside the electron cone but which does not belong to electron cells. It is a measure of isolation. The histogram is the data and the curve is the fit to the data. Note that the dip at about 100 MeV is due to the calorimeter noise suppression. The horizontal unit is in log scale.

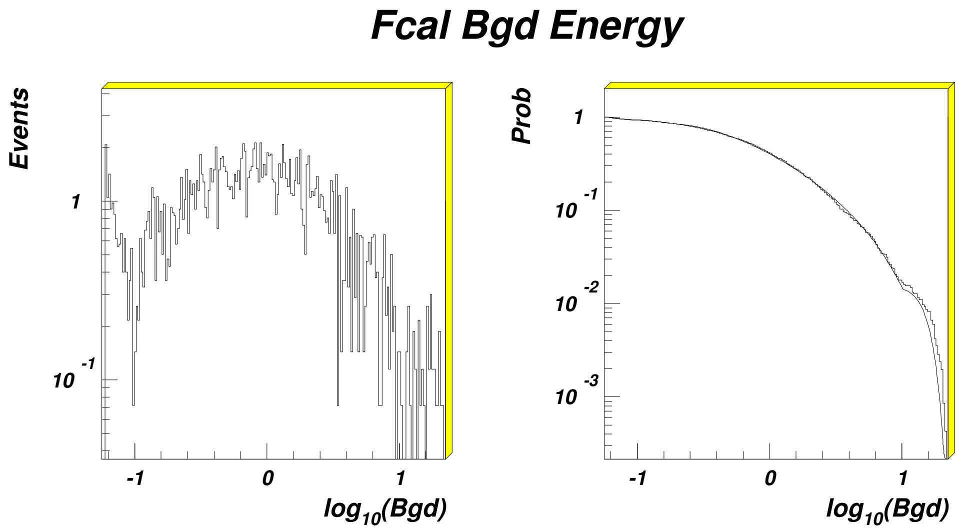

Figure 3.21: Distribution and Probability function of Fcal electron in terms Bgd (Background), the peripheral background energy around the electron cluster, i.e. the energy inside the electron cone but which does not belong to electron cells. It is a measure of isolation. The histogram is the MC and the curve is the fit to the MC. Note that the dip at about 100 MeV is due to the calorimeter noise suppression. The horizontal unit is in log scale.

The event distribution and probabilty fuction are shown in Figure 3.22 for BCAL, Figure 3.23 for RCAL, and Figure 3.24 for FCAL.

- fTwr: The fractional energy leakage outside the two highest energy tower rows perpendicular to module direction in the electron cluster. It is defined:

$$fTwr = 1. - E_1(highest) - E_2(secondhighest) \tag{3.15}$$

where E_i is the ith highest energy tower row's energy fraction in the electron cluster. The standard cuts as stated in Table 3.2 were applied for this variable. This variable is valid only for FCAL and RCAL, not for Bcal because of the calorimeter geometry. The event distribution and probability function are shown in Figure 3.25 for RCAL and Figure 3.26 for FCAL.

- fCel: The fractional energy leakage outside the two highest energy cell rows perpendicular to module direction in the electron cluster. It is defined:

$$fCel = 1. - E_1(highest) - E_2(secondhighest) \tag{3.16}$$

where E_i is the ith highest energy cell row's energy fraction in the electron cluster. The standard cuts as stated in Table 3.2 were applied for this variable. The event distribution and probability function are shown in Figure 3.27 for BCAL, Figure 3.28 for RCAL, and Figure 3.29 for FCAL.

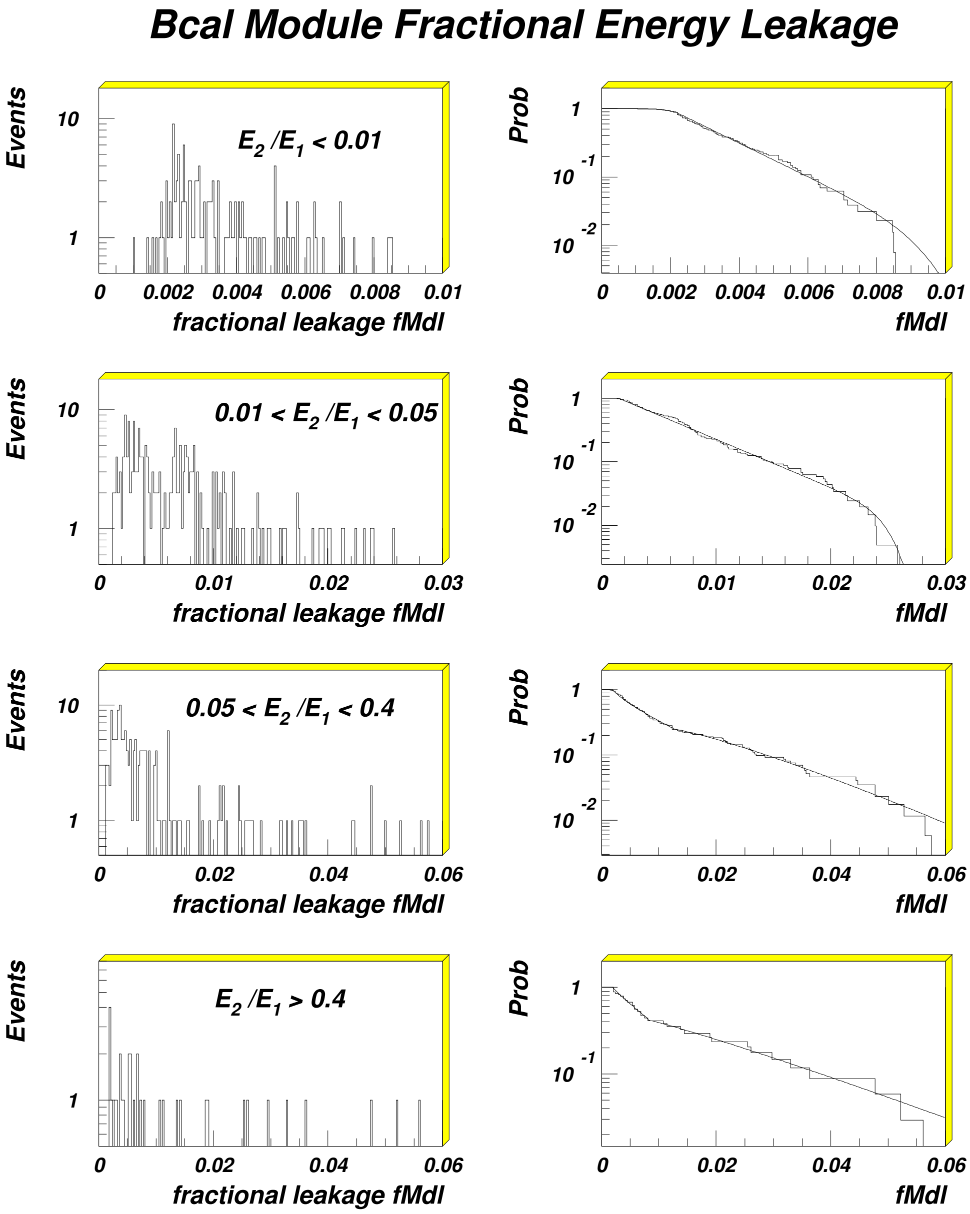

Figure 3.22: Distribution and Probability function of Bcal electron in terms $fMdl$, the fractional energy leakage outside the two highest energy modules in the electron cluster. It is a measure of electron shower size. The histogram is the data and the curve is the fit to the data. Note that there are four different categories according to the value E_2/E_1, the ratio of second highest module energy over highest module energy.

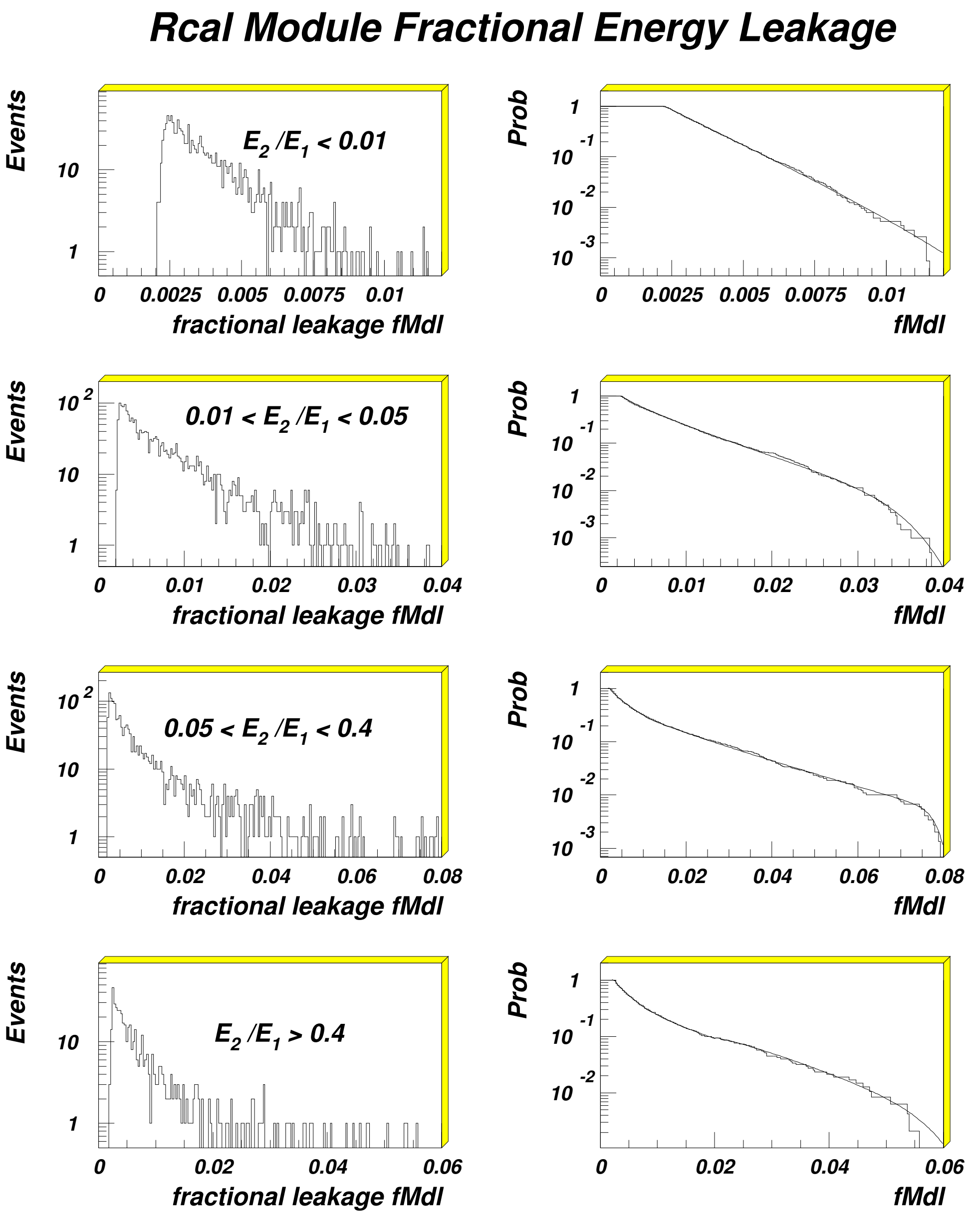

Figure 3.23: Distribution and Probability function of Rcal electron in terms $fMdl$, the fractional energy leakage outside the two highest energy modules in the electron cluster. It is a measure of electron shower size. The histogram is the data and the curve is the fit to the data. Note that there are four different categories according to the value E_2/E_1, the ratio of second highest module energy over highest module energy.

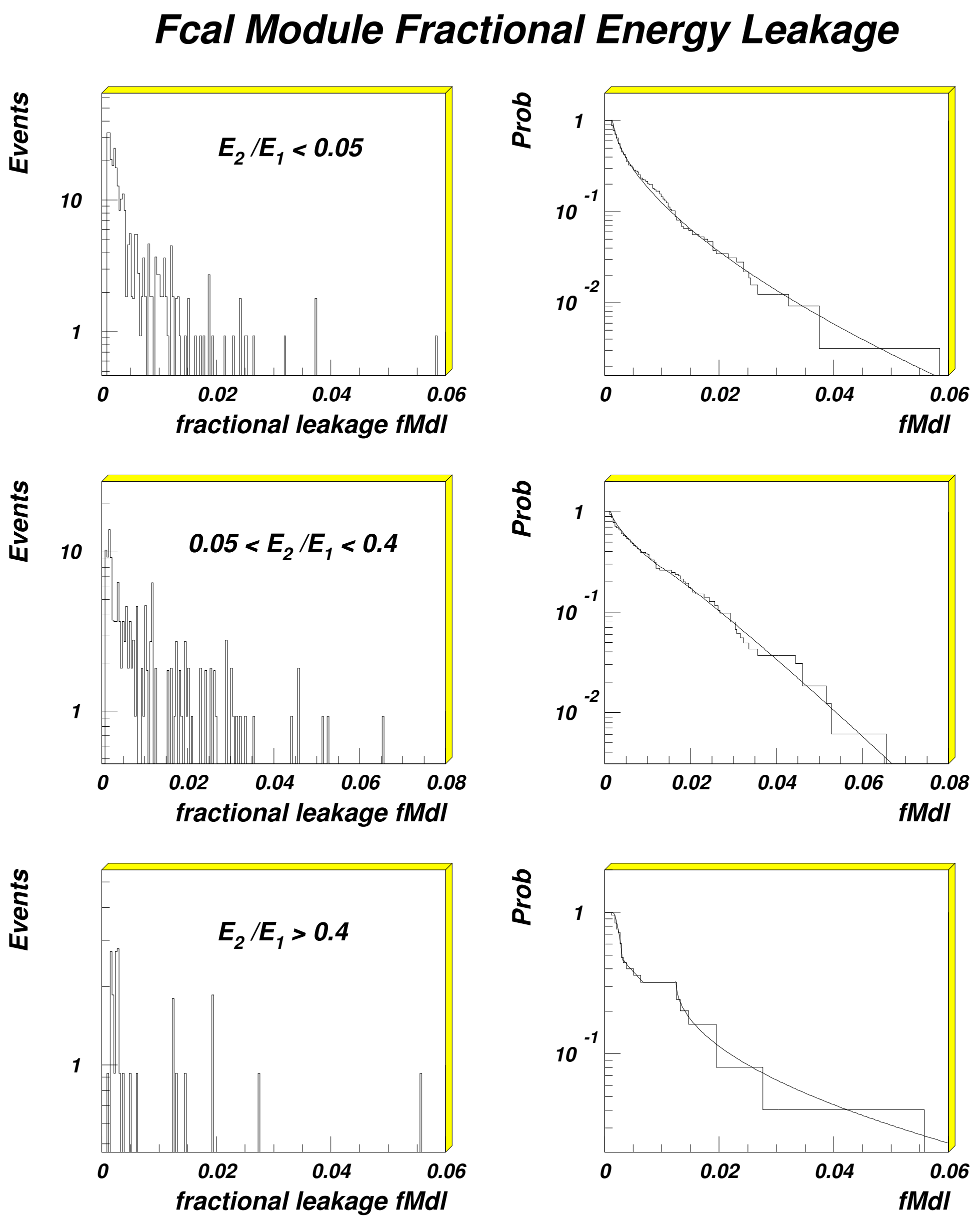

Figure 3.24: Distribution and Probability function of Fcal electron in terms $fMdl$, the fractional energy leakage outside the two highest energy modules in the electron cluster. It is a measure of electron shower size. The histogram is the MC and the curve is the fit to the MC. Note that there are three different categories according to the value E_2/E_1, the ratio of second highest module energy over highest module energy.

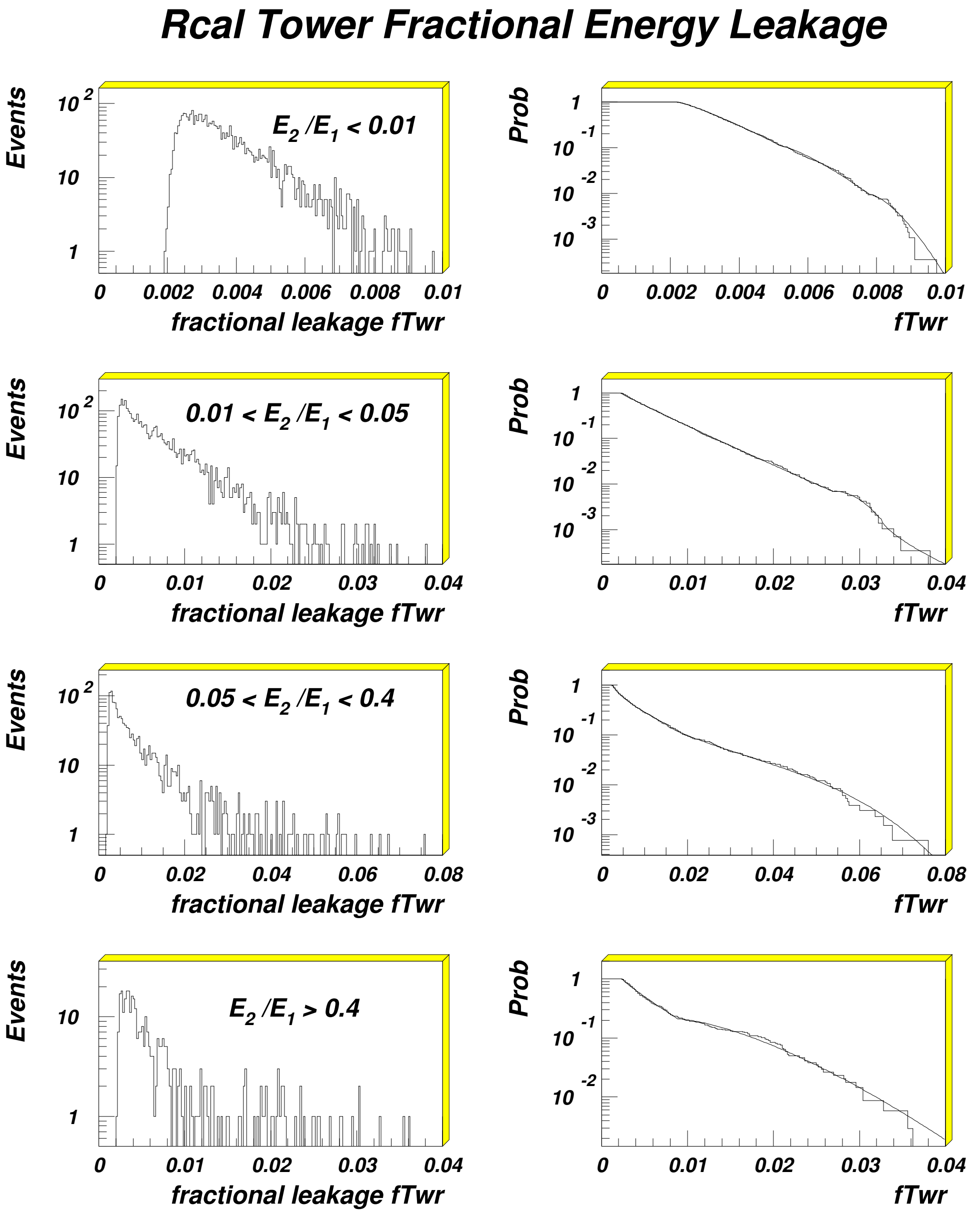

Figure 3.25: Distribution and Probability function of Rcal electron in terms $fTwr$, the fractional energy leakage outside the two highest energy tower rows perpendicular to module direction in the electron cluster. It is a measure of electron shower size. The histogram is the data and the curve is the fit to the data. Note that there are four different categories according to the value E_2/E_1, the ratio of second highest tower row energy over the highest tower row energy.

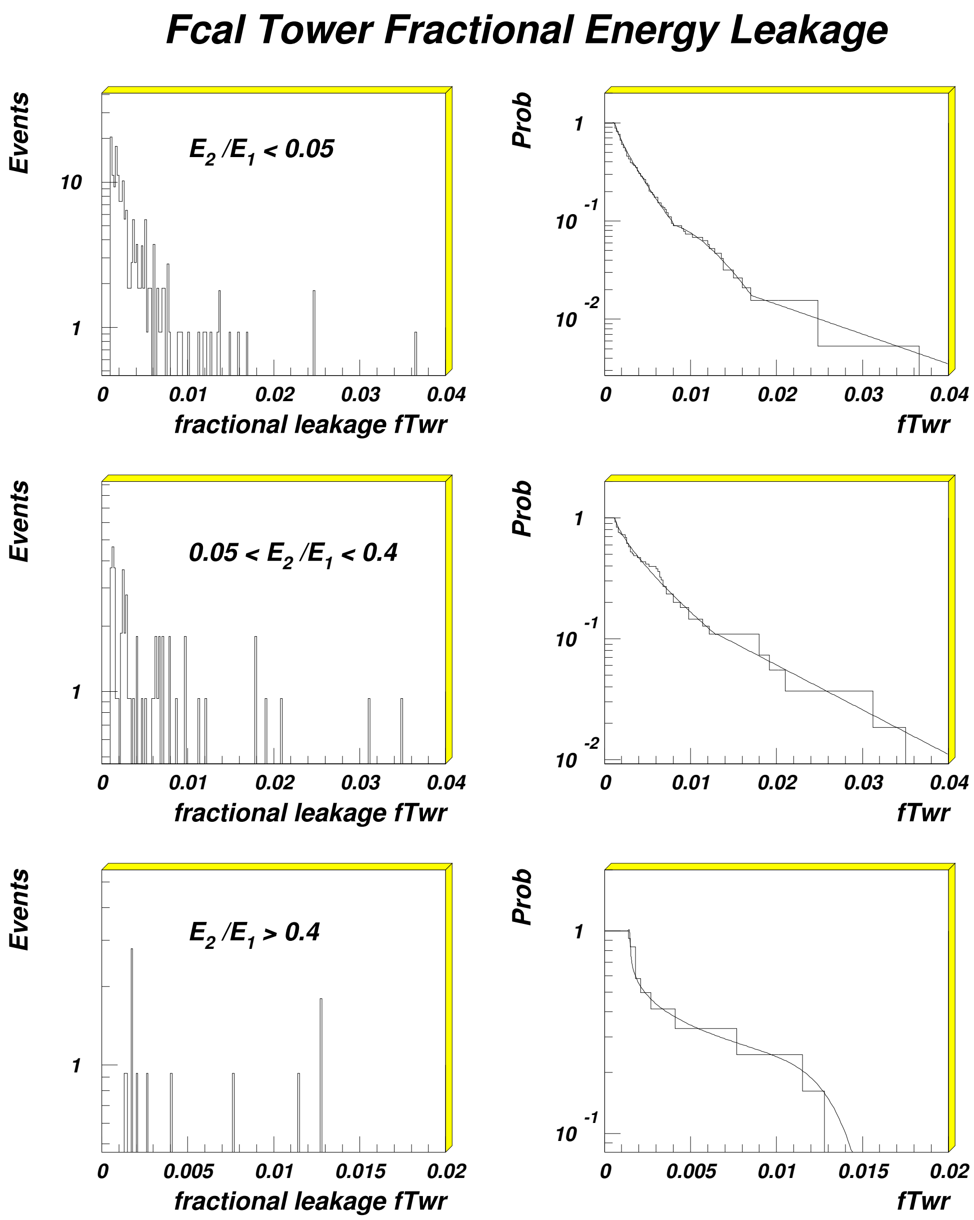

Figure 3.26: Distribution and Probability function of Fcal electron in terms $fTwr$, the fractional energy leakage outside the two highest energy tower rows perpendicular to module direction in the electron cluster. It is a measure of electron shower size. The histogram is the MC and the curve is the fit to the MC. Note that there are three different categories according to the value E_2/E_1, the ratio of second highest tower row energy over the highest tower row energy.

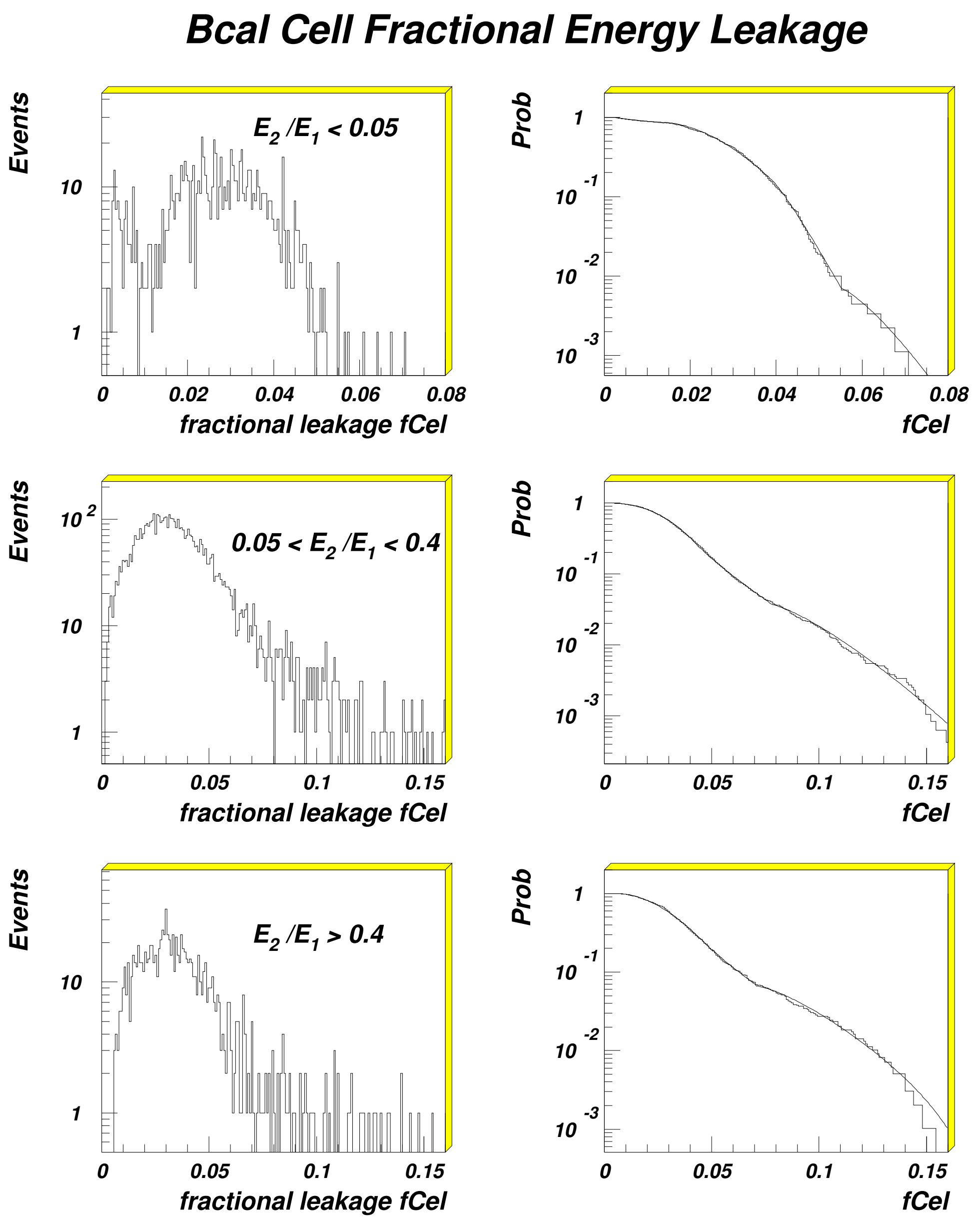

Figure 3.27: Distribution and Probability function of Bcal electron in terms $fCel$, the fractional energy leakage outside the two highest energy cell rows perpendicular to module direction in the electron cluster. It is a measure of electron shower size. The histogram is the data and the curve is the fit to the data. Note that there are three different categories according to the value E_2/E_1, the ratio of the second highest cell row energy over the highest cell row energy.

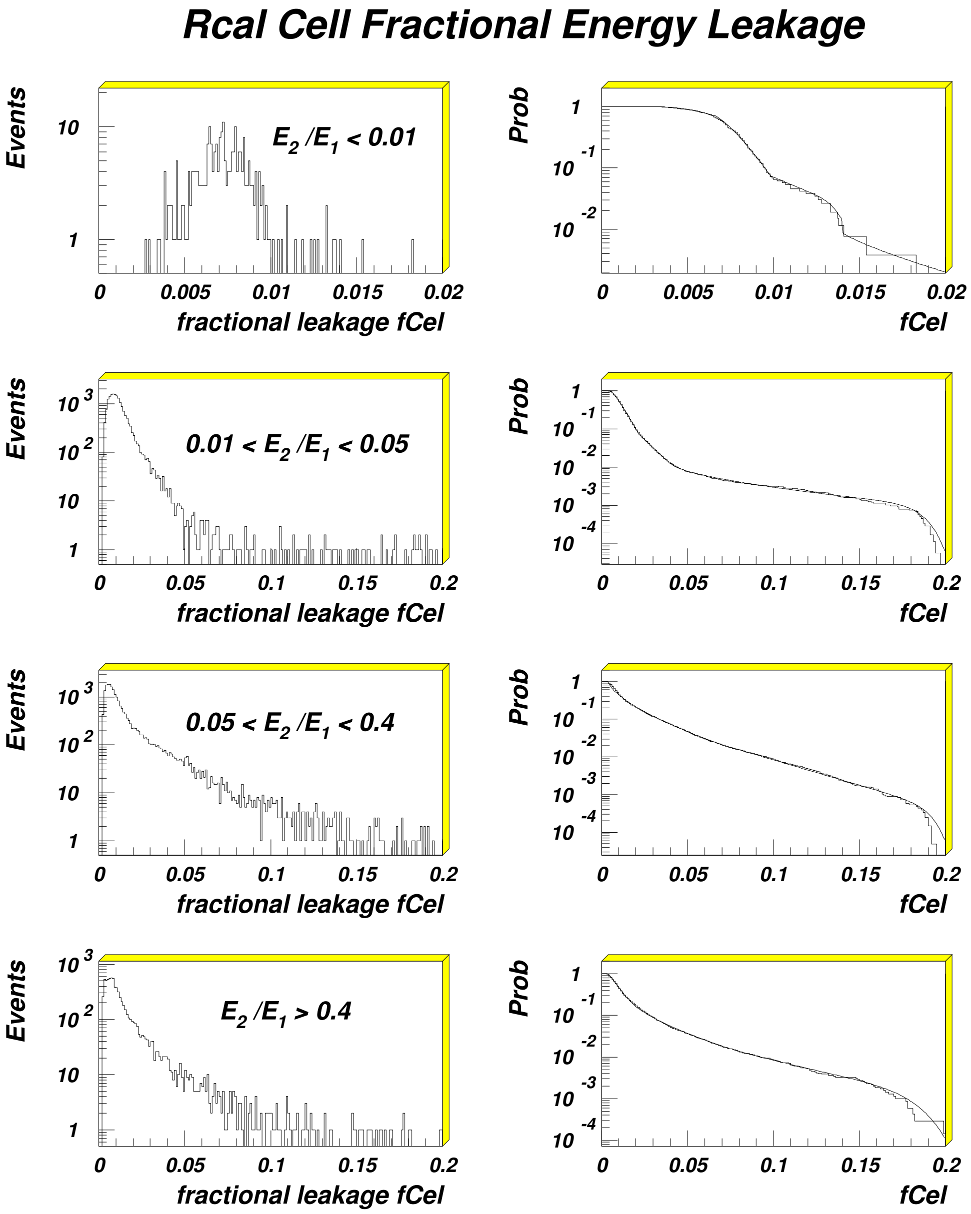

Figure 3.28: Distribution and Probability function of Rcal electron in terms $fCel$, the fractional energy leakage outside the two highest energy cell rows perpendicular to module direction in the electron cluster. It is a measure of electron shower size. The histogram is the data and the curve is the fit to the data. Note that there are four different categories according to the value E_2/E_1, the ratio of the second highest cell row energy over the highest cell row energy.

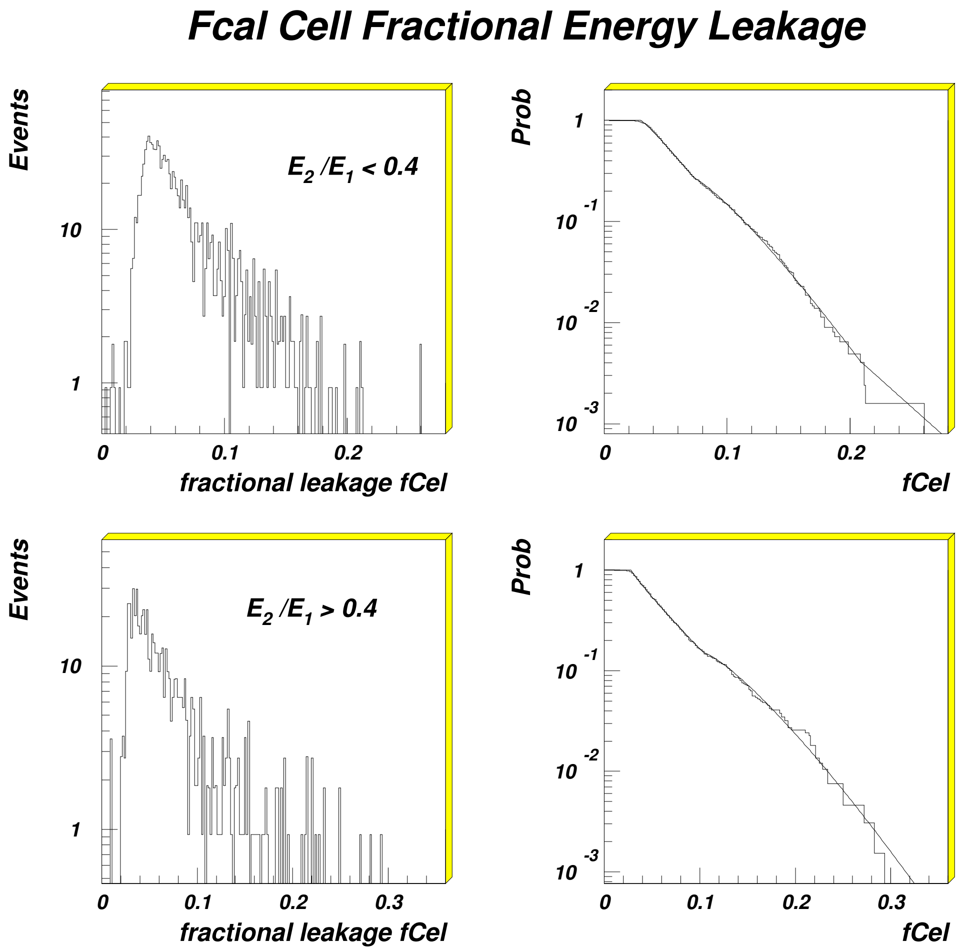

Figure 3.29: Distribution and Probability function of Fcal electron in terms $fCel$, the fractional energy leakage outside the two highest energy cell rows perpendicular to module direction in the electron cluster. It is a measure of electron shower size. The histogram is the MC and the curve is the fit to the MC. Note that there are two different categories according to the value E_2/E_1, the ratio of the second highest cell row energy over the highest cell row energy.

3.2.1 The probabilities of FCAL electrons

The determination of a likely FCAL electron is constructed as the product of 7 probability functions. High Q^2 DIS Monte Carlo instead of data was used to parameterize the 7 variables simply because there was not enough statistics for FCAL electrons in the data. The samples used were $Q^2 > 100$ Gev^2, $Q^2 > 300$ Gev^2, $Q^2 > 400$ Gev^2, $Q^2 > 1000$ Gev^2, and $Q^2 > 5000$ Gev^2 Monte Carlo. Cell-Island algorithm plus the RCAL probability functions[3] were applied to find FCAL electrons in the Monte Carlo sample, then we require the found FCAL electron candidates to match the Monte Carlo FCAL true electrons. Once the clean FCAL Monte Carlo electrons sample was obtained, the same technique as was used for the parameterization of BCAL and RCAL electrons was again employed on FCAL variables.

3.2.2 Choosing the correct candidate

To choose the correct candidate from multiple candidates[4], the candidate with the greatest $DrakeProb$ as defined by the following was chosen:

$$DrakeProb = GrandProb \cdot 1/Q^4 \cdot f(P_t Fake, P_t True) \tag{3.17}$$

where $GrandProb$ is the product of 7 probability functions, and $f(P_t Fake, P_t True)$ is yet another probability function determined from neutral current DIS MC, this probability function takes into account the P_t of the candidate. Since for the Monte

[3]RCAL probabilities were used here because FCAL variables have not yet been parameterized at this stage.

[4]It happens sometimes

Carlo, the P_t of fake electron and P_t of the true electron were known, the following variable can thus be parameterized:

$$P_tFactor = log_{10}\frac{P_tFake}{\sqrt{P_tTrue^2+1}} \tag{3.18}$$

$P_tFactor$ and its integrated distributions are shown in Figure 3.30. True electron tends to have a larger P_t than fake electrons. This fact was exploited in the selection scheme. For each candidate, first we make the hypothesis that this candidate is the true electron, its P_t is taken as P_tTrue, while other candidates are hypothesized as fake electrons, the highest P_t of the fake ones is taken as P_tFake. So, each candidate has its own probability function $f(P_tFake, P_tTrue)$ along with $GrandProb$ and Q^2. Therefore, each candidate has its own $DrakeProb$ as calculated in Eqn 3.17. The candidate with the highest $DrakeProb$ is chosen as the *correct* candidate.

3.3 Summary of EM finder probability functions

We have constructed 7 probability functions (quality factors) for EM finder. One can in principle make a complicated function out of those 7 probability functions to maximize the probability for true NC DIS scattered electrons, and to minimize the probability for fake electrons from other physics processes like photoproduction. We simply choose to multiply those 7 probability functions together as the *zero*th order approximation. Future improvements can be anticipated.

The product of those 7 probability functions is called $GrandProb$. The user can choose either the highest $GrandProb$ candidate or highest $DrakeProb$ candidate

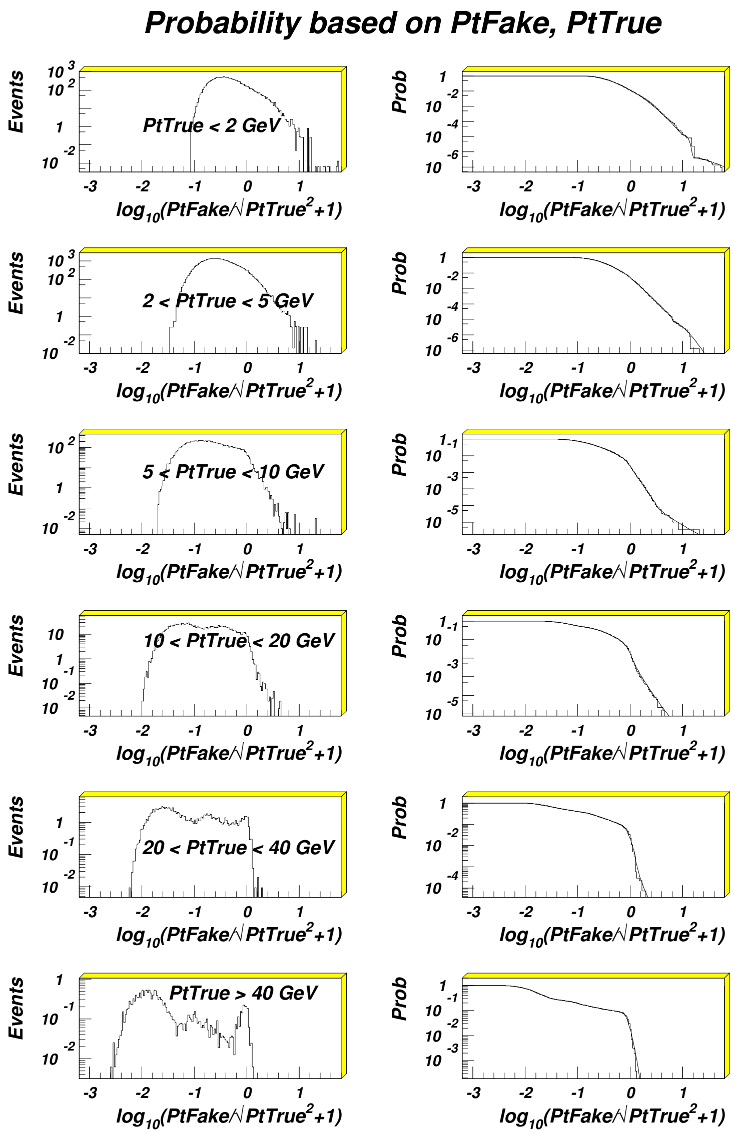

Figure 3.30: Another Probability function factor from $f(P_tFake, P_tTrue)$, in situation where multiple candidates were found. It depends on the P_t of those candidates, based on Monte Carlo studies. One can see fake electron tends to have a lower P_t. Note that there are six different categories according to P_tTrue, the P_t of the true scattered electron.

(stated in the last section) as the DIS scattered electron. The selection of highest *DrakeProb* candidate is the default [5] selection scheme.

3.4 Performance of EM electron finder

To check the efficiency and mistake rate of EM electron finder, high Q^2 DIS Monte Carlo event samples, Photoproduction MC, and low Q^2 DIS event samples were tested. For high Q^2 MC, $Q^2 > 100$ GeV^2, $Q^2 > 300$ GeV^2, $Q^2 > 400$ GeV^2, $Q^2 > 1000$ GeV^2 and $Q^2 > 5000$ GeV^2 samples were used.

We define:

$$efficiency = \frac{No.\ of\ electrons\ found\ that\ also\ match\ true\ MC\ electrons}{total\ No.\ of\ DIS\ MC\ events} \tag{3.19}$$

$$mistake\ rate = \frac{No.\ of\ electrons\ found\ that\ DONOT\ match\ true\ MC\ electrons}{total\ No.\ of\ DIS\ MC\ events} \tag{3.20}$$

$$null\ rate = \frac{No.\ of\ events\ where\ no\ electron\ found}{total\ No.\ of\ DIS\ MC\ events} \tag{3.21}$$

match is defined as that the $\eta\phi$ angular separation between the candidate and the true electron is less than 0.15 radian. Those three indicators of our EM electron

[5] Studies show selecting candidates according to *DrakeProb* has a better performance than using *GrandProb*. However, the effect is marginal.

finder were compared to that of Repond[6] finder and Sinistra95[7]. The comparisons are shown in Figure 3.31 for efficiency, and Figure 3.32 for mistake rate and null rate.

For the low Q^2 DIS MC, the fake electron rate cross sections is plotted in pb for the three electron finders. They are shown in Figures 3.33.

For the Photoproduction MC, the background (which mimics the DIS scattered electron) cross sections is plotted in pb for the three electron finders. They are shown in Figures 3.34.

Finally, fake high Q^2 electron cross sections from low Q^2 DIS and from photoproduction are added together, and are shown vs efficiency, for the three electron finders, in Figure 3.35.

From all the three indicators that EM finder seems better than the other two electron finders. EM finder has high efficiency, and low background contamination. But there is still room for further improvement. This thesis analysis uses the EM electron finder developed above.

[6]Repond was the early default ZEUS electron finder developed by Jose Repond.
[7]Sinistra95 was the 95 default ZEUS electron finder based on neural network.

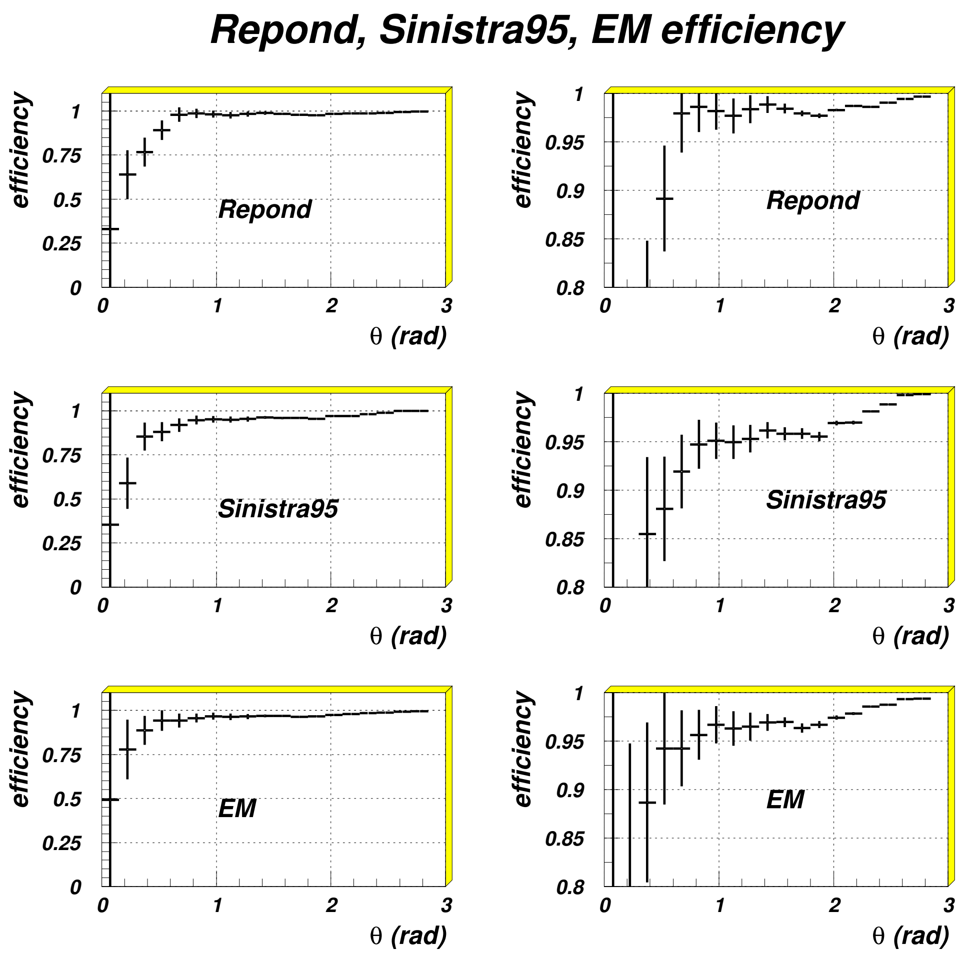

Figure 3.31: Efficiency comparison between three electron finders, Repond, Sinistra95 and EM. Note that the left column has a scale from 0. to 1.; while the right column has a scale from 0.8 to 1., a zoom of left column.

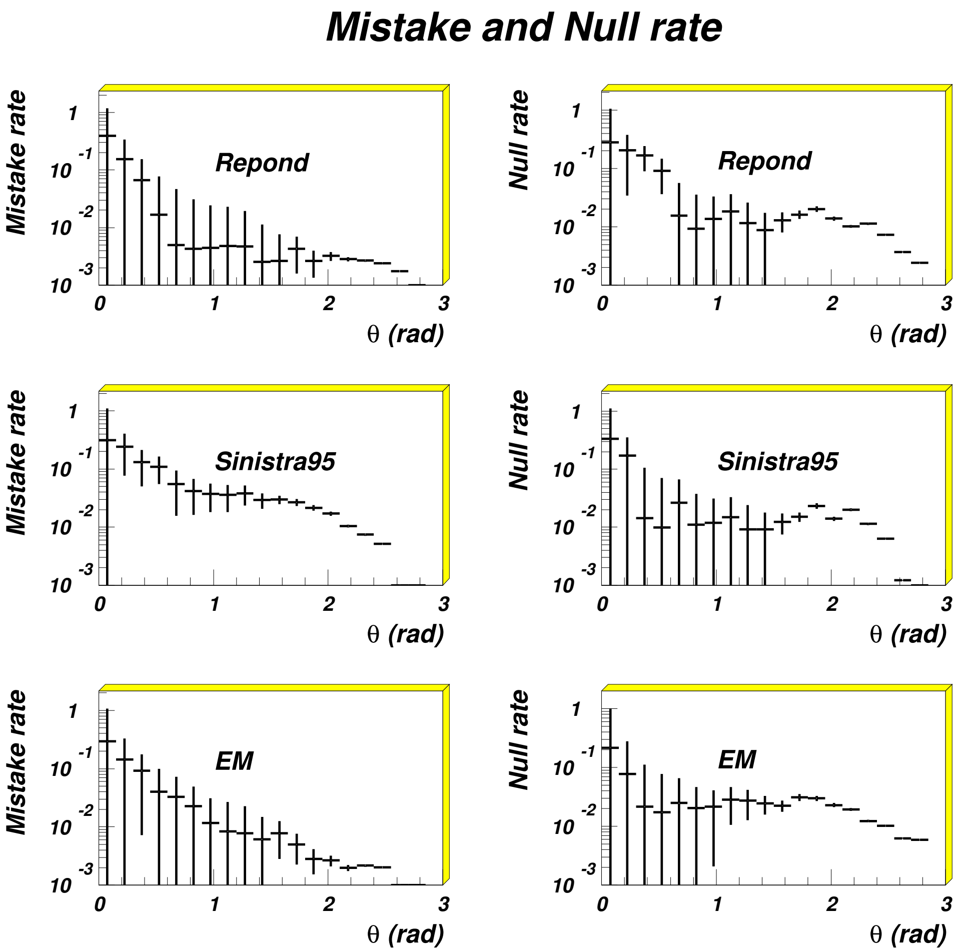

Figure 3.32: Mistake rate and null rate comparison between three electron finders, Repond, Sinistra95 and EM. Note that the left column is mistake rate; while the right column is null rate

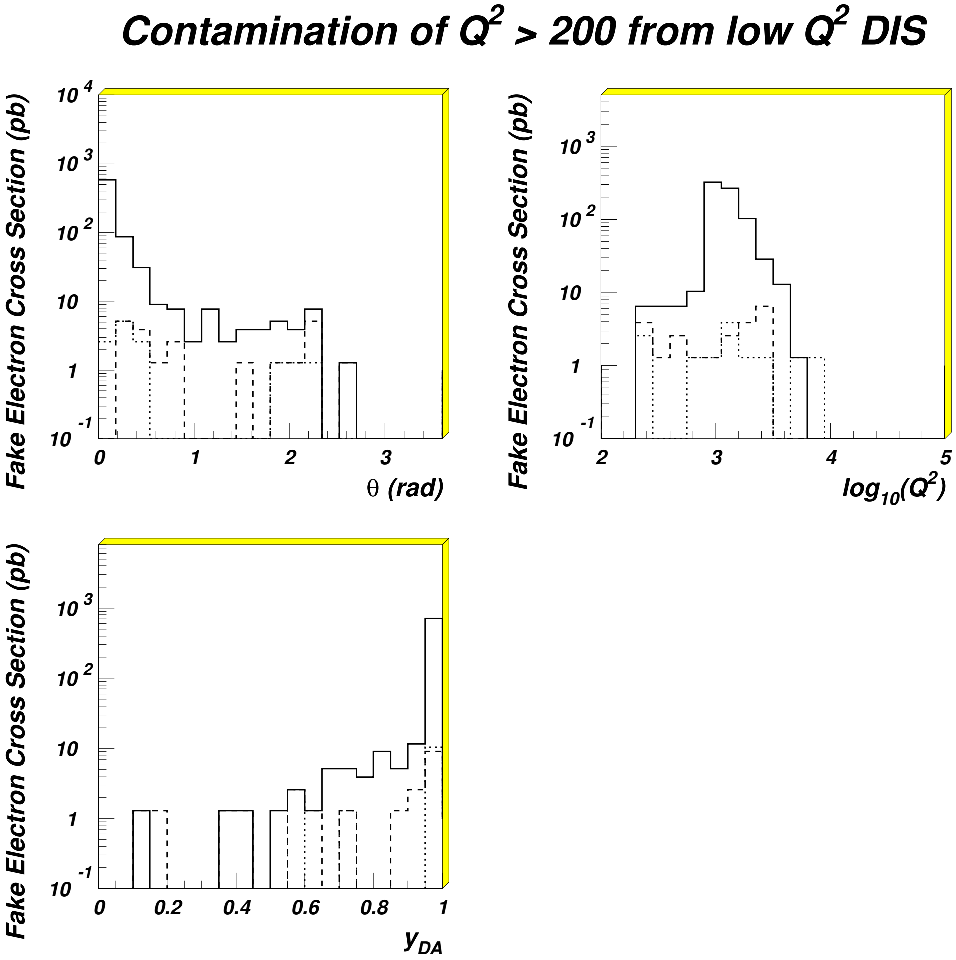

Figure 3.33: Cross section (pb) of contamination from low Q^2 DIS for the three electron finders. The solid line is Repond finder, the dashed line is Sinistra95, the dotted line is EM finder.

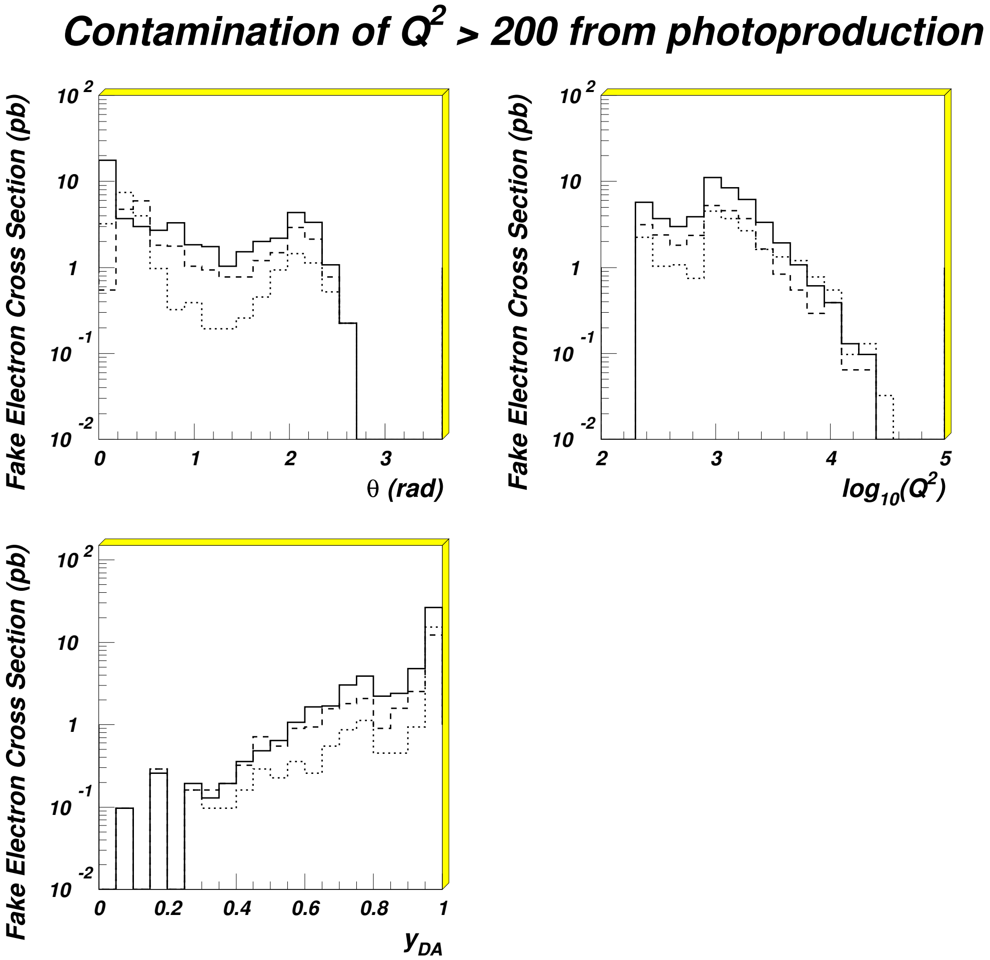

Figure 3.34: Cross section (pb) of contamination from photoproduction for the three electron finders. The solid line is Repond finder, the dashed line is Sinistra95, the dotted line is EM finder.

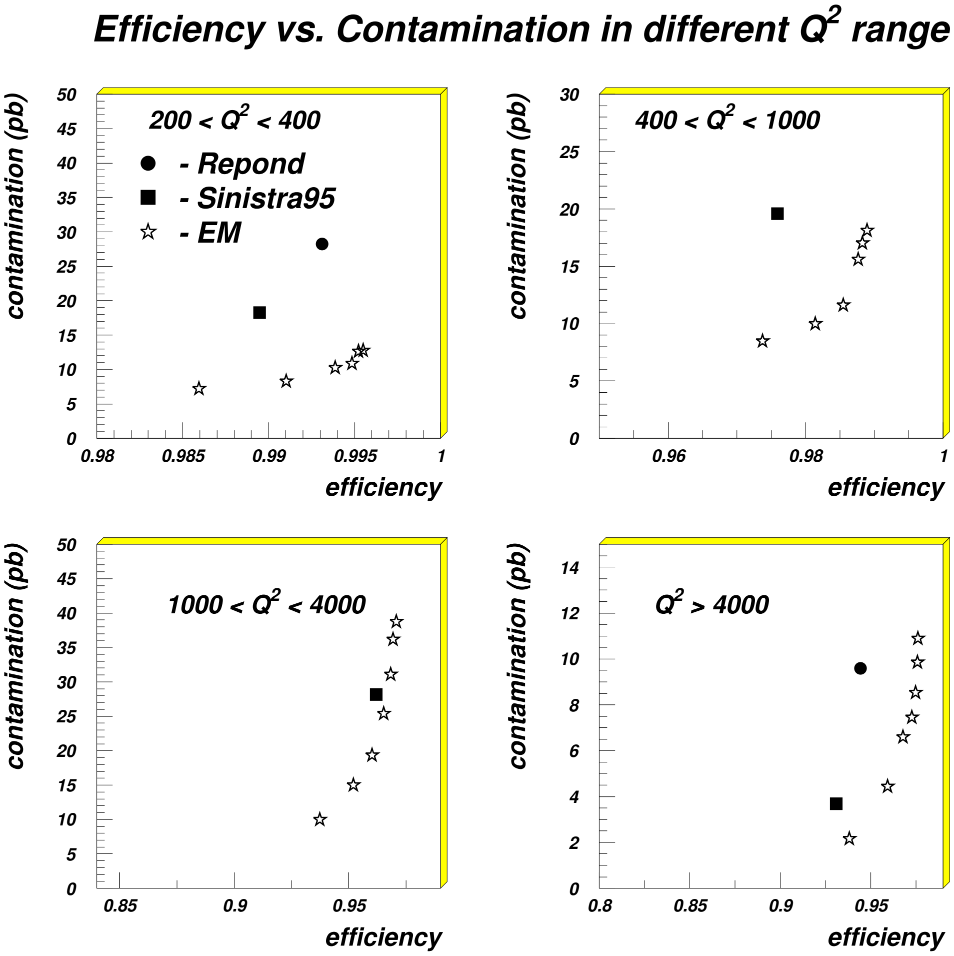

Figure 3.35: Fake cross section (pb) of contamination from both low Q^2 DIS and photoproduction vs efficiency for the three electron finders. The solid circle is Repond finder, the solid square is Sinistra95, the open star is EM finder. For EM finder a series of points corresponding to different probability cuts were shown, for Repond and Sinistra95 the default recommended probability cut was used, corresponding to one point on the plot.

Chapter 4

Event Selection

This analysis uses e^+p data collected with the ZEUS detector in 1994, 1995, 1996 and 1997 nominal vertex ($V_z \approx 0$) runs, with a total integrated luminosity of 49.8 pb^{-1} on tape. Of the luminosity provided by HERA, not all is available for analysis. For instance, it takes some time to set up the detector at the start of each HERA physics run. Furthermore, some runs have detector problems and should not be used for analysis. This analysis uses the collaboration approved EVTAKE[1] sample, augmented by EXOTAKE [2] (designed by high Q^2 exotics physics group) sample, which are deprived of such problem runs. After this reduction, the total luminosity used in this analysis is 46.1 pb^{-1}.

4.1 The Trigger Selection

This analysis begins with the non-prescaled neutral current DIS (NC DIS) trigger. This set of trigger criteria is described below.

[1]EVTAKE rejects runs with CTD/CAL/magnet/luminosity-detector off.

[2]EXOTAKE rejects runs with more than 4 holes in F/B/Rcal or more than 7 holes in total.

4.1.1 The NC DIS First Level Trigger

The First Level Trigger accepts events which may have electron candidates in the calorimeter. To this end, Exotics group First Level Trigger was designed to search for an isolated electron in the calorimeter or to sufficient EMC energy deposit. One of the following criteria must be satisfied:

- BEMCE(4776) * gTRK or
- BCAL IsoE * gTRK, or
- RCAL IsoE * REMCE(2032), or
- EMCE(14968), or
- (CAL(14968) or EMCE(10068) or BEMCE(3404) or REMCE(2032)) * gTRK or
- FCAL IsoE[3]

The subtrigger BEMCE(4776) requires a minimum sum of 4776 MeV of energy deposited in the BCAL EMC section. gTRK requires a good track in the CTD. Subtrigger REMC(2032) requires a minimum sum of 2032 MeV of electromagnetic energy in the RCAL, excluding the towers immediately surrounding the beampipe from the sum. Around the beampipe, the background rate from events surviving the VETO detector is too high, and a more sophisticated trigger must be used instead. The IsoE (isolated electron) trigger selects events with a electron-like energy

[3]Implemented only in 96, 97

deposit, surrounded by quiet regions with little energy deposit. Specifically, there must be at least one, but no more than four connected towers consistent with the following energy deposit, namely $E_{EMC} > 2.5$ GeV and either $E_{HAC} < 0.512$ GeV or $\frac{E_{EMC}}{E_{HAC}} > 3$. The towers surrounding the electron towers must be 'quiet', i.e. $E_{EMC} < 2.5$ GeV and $E_{HAC} < 1.$ GeV. It was found early in the run that background rates were still high with this trigger, so a further requirement was made that the total EMC energy in the beampipe region be at least 3750 MeV (REMCTh(3750)) in addition to the IsoE requirement. Subtrigger EMCE(14968) requires a minimum sum of 14968 MeV of electromagnetic energy in the calorimeter. All 6 subtriggers have the timing vetoes from the 3 VETO detectors applied to reject out-of-time backgrounds.

4.1.2 The NC DIS Second Level Trigger

At the second level trigger, calorimeter timing is used to reject background events. This is very powerful even after the application of first level vetoes. An event is rejected if it meets one of the following:

- $|t_{RCAL}| > 8$ ns, or
- $|t_{FCAL}| > 8$ ns, or
- $|t_{FCAL} - t_{RCAL}| > 8$ ns, or
- $|t_{GLOBAL}| > 10$ ns.

Here t_{FCAL} and t_{RCAL} are energy weighted average times of energy deposits in the forward and rear calorimeters, and t_{GLOBAL} is an average over the entire calorimeter.

Recalling that physics events should have a time $t \approx 0$, these timing cuts will only veto events occuring meters away from the nominal interaction point, or events arising from outside the main beam bunch, in a satellite bunch. The veto on t_{RCAL} is mainly for the rejection of p-gas events, with e-gas rejected by the FCAL time. Taking the difference, $t_{FCAL} - t_{RCAL}$ serves to remove events which may have passed the two vetoes independently. Background originating from cosmic muons can be rejected by splitting the BCAL into an upper and a lower half, and vetoing events if

- $t_{UP} - t_{DOWN} < -10$ ns.

Fake triggers due to sparking in the photomultiplier tubes are removed if they satisfy:

- No cells have both PMTs with $E > 200$ MeV, and
- A single PMT has $E > 2.0$ GeV.

Additional requirements are made on calorimeter transverse energy and $E - P_z$. Specifically, one of the following must be true:

- $E_t > 10$ GeV and $E - P_z + 2E_{lumi-\gamma} > 25$ GeV, or
- $E_t[-1ir] > 10$ GeV and $E - P_z + 2E_{lumi-\gamma} > 25$ GeV, or
- $E_t[-1ir] > 15$ GeV and $E - P_z > 28$ GeV, or
- $E_t[-2ir] > 16$ GeV and $E - P_z > 34$ GeV, or

For the identification of DIS events, the quantity $E - P_z$ is invaluable. ZEUS defines $+z$ as being along the proton direction, so an event will have $E - P_z = 2E_e$. In a DIS event, the scattered electron is observed in the detector, so the observed $E - P_z$ should be close to $2E_e$. Energy lost into the FCAL beamhole will carry little $E - P_z$ as, since it is forward, its P_z momentum component will be nearly equal to the energy. Events with an initial state radiated photon will lose energy through the rear beamhole, and therefore have a somewhat lower $E - P_z$, so the cut imposed, is well away from the expected $2E_e$. As opposed to DIS events, in photoproduction and p-gas events the electron escapes undetected. For these events, $E - P_z \approx 0$, and they are rejected by the lower cut. Values of $E - P_z > 2E_e$ are unphysical, and can only arise from such 'events' as PMT sparking, and overlays, where 2 separate interactions occur during a single crossing. $E_t[-1ir]$ means total E_t but excluding 1st FCAL inner ring where big jets activities result in large E_t. Likewise, $E_t[-2ir]$ sums total E_t but excluding 1st and 2nd FCAL inner ring. E_t requirement was designed to guarantee some activities in the calorimeter thus making the triggered event interesting.

4.1.3 The NC DIS Third Level Trigger

The Third Level Trigger has the full, integrated detector information, while the First and Second Levels only have limited or component-by-component information. At the TLT, $E - P_z$ can be calculated with the full information, using the luminosity monitors's photon calorimeter energy to handle initial state radiated photons, and using the observed event vertex to calculate the P_z component; while Second Level Trigger, without access to the integrated information, was restricted to assuming

$x_{VTX} = y_{VTX} = z_{VTX} = 0$. The following cut is imposed at the TLT:

- $E - P_z > 32$ GeV, and
- not beam-gas vertex, and
- electron (Local, Repond, Sinistra or EM) $E_e > 10$ GeV and $\max(Q^2_{da}, Q^2_{el}) > 200$ GeV^2

While a cut on $E - P_z$ implies finding a electron in the detector, a more straightforward method is to look for the electron itself. The TLT runs 4 electron finders, Local, Repond, Sinistra and EM. These finders use a variety of criteria, such as total EMC energy, $\frac{E_{EMC}}{E_{HAC}}$, shower depth, and shower radius, to determine whether an energy deposit is likely to be an electron. Q^2 cut emphasizes the high Q^2 analysis nature.

4.1.4 The DST Selection

The DST selections used in this analysis, are the following:

- DST bit 32
- DST bit 43

DST bit 32, the Neutral Current bit, requires:

- $E - P_z > 28$ GeV

- Standard Timing
- A electron with energy > 4 GeV
- $E_t > 10$ GeV
- Not a spark

DST bit 43, the hotline bit, requires:

- bit 32
- Good vertex.
- $35 < E - P_z < 70$ GeV

  and
- $Q^2_{DA} > 160$ GeV^2 and $y_{el} < 0.95$, or
- $E[\theta > 150] < 5$ GeV and $E_t > 20$ GeV

Again, DST bit selection emphasizes high Q^2 nature directly with a Q^2 cut, or indirectly requiring little activity in the backward direction with $E[\theta > 150] < 5$ GeV.

4.2 Event Selection

Event selection for high Q^2 events must emphasize background rejection for two reasons: the low cross-section and the position of the electrons in the BCAL and

FCAL where photons from hadronic jets can be found. The strategy for coping with background is to supplement the calorimeter electron identification with tracking and to require the electrons to be isolated. The remaining cuts are kept simple to limit systematic errors and simplify their estimation.

To be selected, each event must:

- Not belong to shifted vertex runs.
- Be pre-selected with DST bit 32 and bit 43.
- Belong to the list of good events in EVTAKE augmented with EXOTAKE.
- Contain an isolated electron of at least 10 GeV.
- For $\theta_e > 15°$ the electron must have a matching track, otherwise the electron must have $p_t > 25$ GeV.
- Have $\delta = E - p_z > 35$ GeV.
- Have a vertex with $-50 < VtxZ < 50$ cm.
- Not appear to be a Compton or low Q^2 event.
- Have $p_T/\sqrt{E_T} < 3.0$ GeV$^{-1/2}$.

Details are described below. The event samples and their luminosities are listed in Table 4.2. Of the events selected, only those with $Q^2_{DA} > 200$ GeV are used for this analysis.

After DST selection, calorimeter noise is reduced using the standard ZEUS noise suppression routine.

Table 4.1: Event samples and their Luminosity.

Year	Type	Luminosity (pb^{-1})
1994	e^+p	2.88
1995	e^+p	6.22
1996	e^+p	10.71
1997	e^+p	26.59

Electrons, the primary characteristic of neutral-current events, are identified using the EM finder program. A cut of 10 GeV (Figure 4.1) in energy is applied to reduce background and to avoid low energy electrons whose selection efficiency may be difficult to simulate.

To avoid electron misidentification from photons in the hadron jet, each electron is required to be isolated. To determine if the electron is isolated, all calorimeter cells not associated with the electron within 0.8 units in ϕ and pseudo-rapidity η are summed. This energy must be less than 5 GeV if the electron is to be considered isolated. This cut is illustrated in Figure 4.2.

Electrons with $\theta > 15°$ are required to have a track with $P > 5$ GeV that extrapolates to within 10 cm of the electron. To avoid removing very high Q^2 events, electrons with $\theta < 15°$ are not required to have a track, but instead must have $p_t > 25$ GeV because fake electrons tend to have low p_t. Combined with the isolation requirement, these cuts are essential to suppress photoproduction background (Figure 4.3).

The cut on δ assures that the event is longitudinally contained and removes pho-

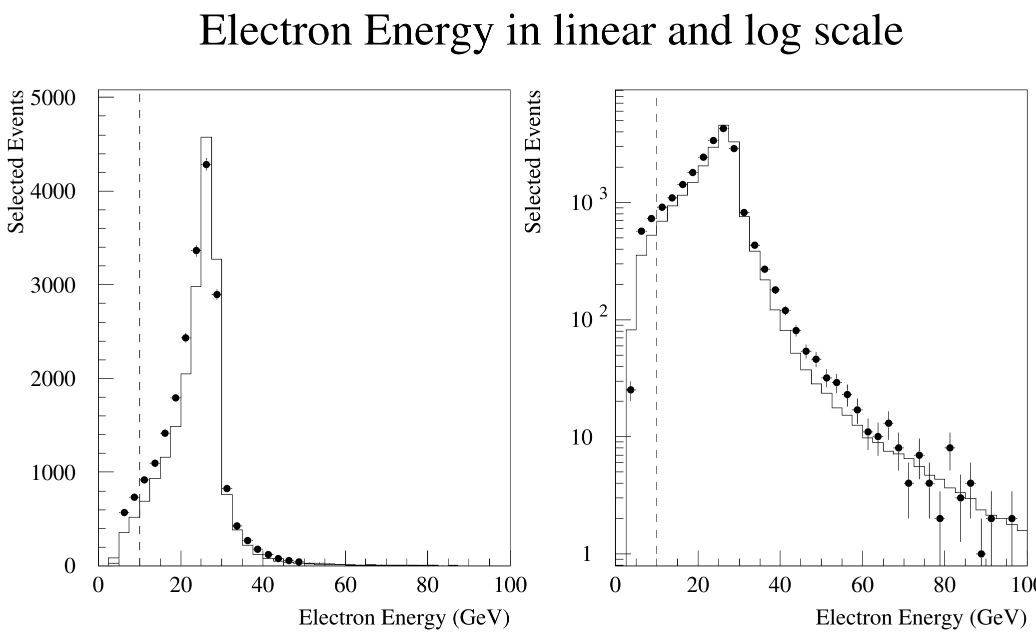

Figure 4.1: Electron energy before selection. Shown in both (a) linear and (b) log scales are data (points) and MC (histogram) for events passing all but the minimum electron energy cut (dashed line). Disagreement is seen in the energy scale and resolution.

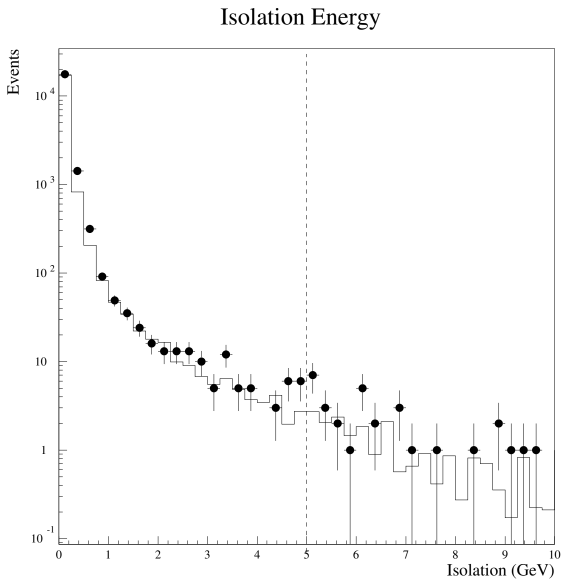

Figure 4.2: Electron isolation cut. Plotted are electron isolation energies in a cone for data (points) and MC (histogram). The dashed line is the cut.

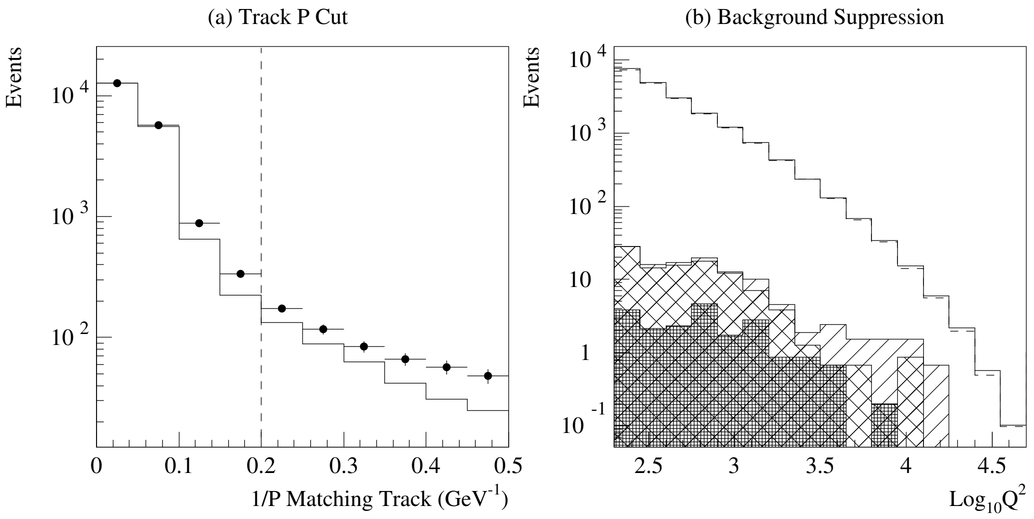

Figure 4.3: Electron track matching. (a) The inverse momentum $1/P$ of tracks that extrapolate within 10 cm of the electron, for data (points) and Monte Carlo (histogram). The cuts are shown as a dashed line. (b) According to Monte Carlo, NC DIS without tracking and isolation cuts (solid histogram) contains, as much as 10% background from photoproduction (single hash). If isolation is required, this is reduced by small factor (double hash). With the addition of track matching, little background remains (heavy hash). The dashed histogram shows the NC DIS after applying the same isolation and tracking cuts.

toproduction background in which the electron is lost down the rear beam hole. The cut in the z position of the vertex is to avoid situations where angles reconstructed in the calorimeter become poorly defined or where cracks between the endcap and barrel calorimeters begin to appear. The upper limit is large enough to include the satellite peak. These two cuts are shown in Figure 4.4.

After selection, 5% of the events that pass all cuts have more than one electron candidates, as shown in Figure 4.5. In these cases, the electron with a higher $DrakeProb$ as stated in the selecting algorithm of EM finder is chosen.

Two types of backgrounds are associated with multiple electron candidates. The first, contamination from low Q^2 DIS, is removed by rejecting any event with an isolated electron with $\theta > 170°$, outside of full CTD efficiency. The second background, elastic Compton events, are removed by rejecting any event with no more than 10 GeV of calorimeter energy remaining after the two electrons are removed. (Inelastic Compton events are simulated by the Monte Carlo as part of the radiative-corrected cross section.)

After all these cuts, only one significant background remains: cosmic rays that travel through the detector, produce a track, and deposit energy consistent with a electron in the calorimeter. To remove this background, a cut of $p_t/\sqrt{E_t} < 3$ GeV$^{1/2}$ is applied (Figure 4.6). For a traversed cosmic ray, the energy deposit is consistent with that of a minimum ionization particle. The p_t of the two parts are small, and nearly balance each other. Another possible cut is to take the difference between the calorimeter times in the top and bottom of the calorimeter, and remove any events with large negative values. This cut, however, is not found to be as effective.

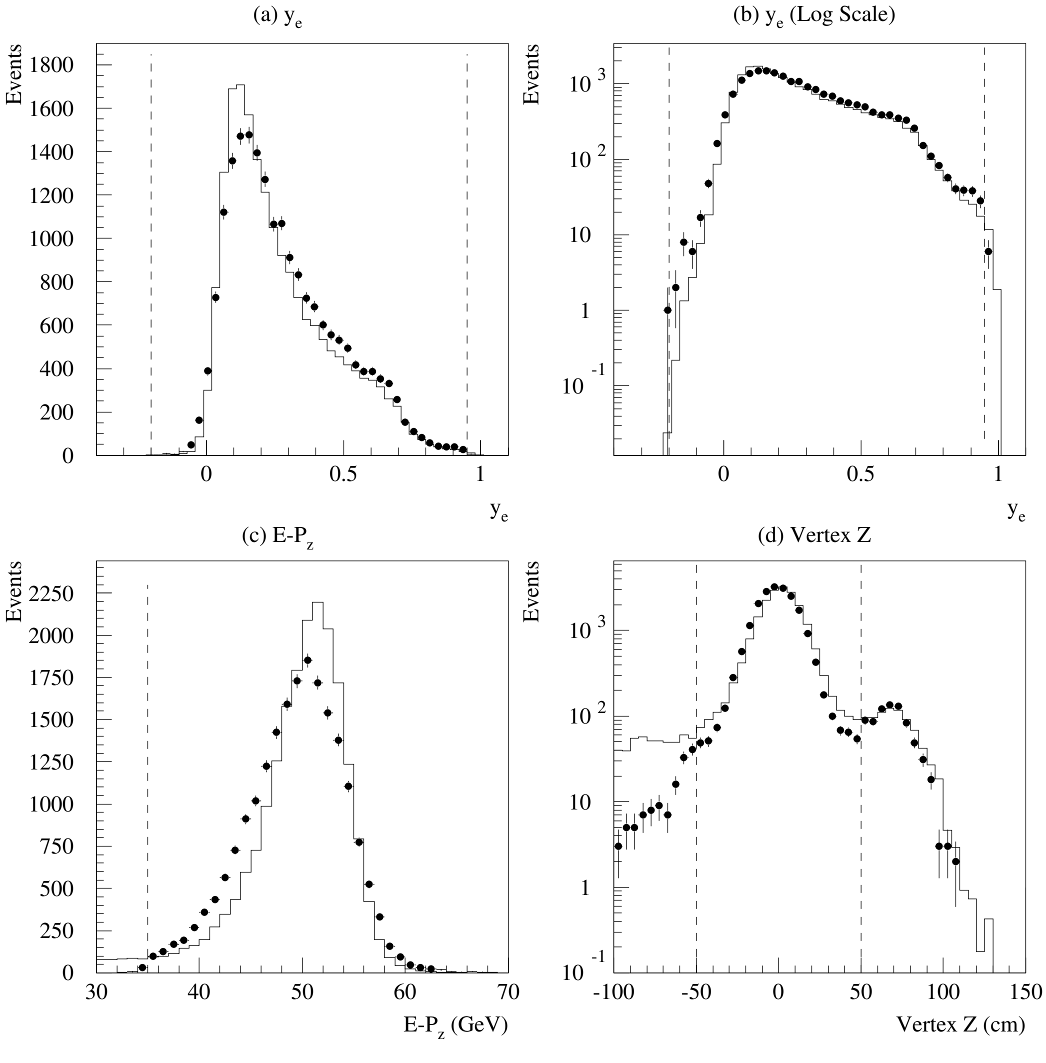

Figure 4.4: Event Selection Cuts. (a)(b) Two cuts are placed on y_e. (c) A lower cut on $E - P_z$ is for rejecting photoproduction background. This distribution also shows one of the more evident disagreements between data and MC. (d) Loose cuts in the vertex z position are needed to avoid a hole in coverage and awkward electron angles.

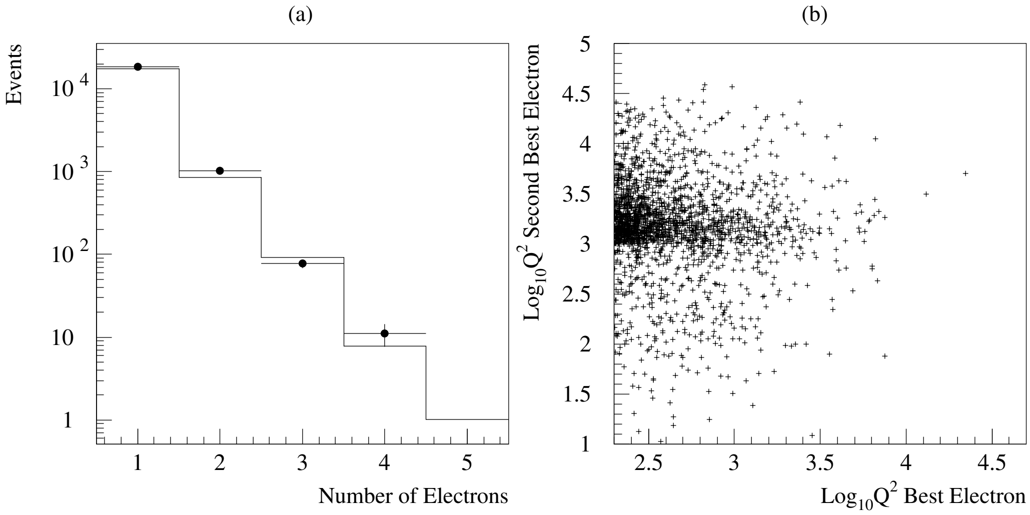

Figure 4.5: Two electron events. (a) 5% of events have more than one identified electron. (b) The second electron often has an effective Q^2 that is high, and would present a significant background if mistakenly chosen. Plotted is the Q_e^2 of the best and second best electrons in the data.

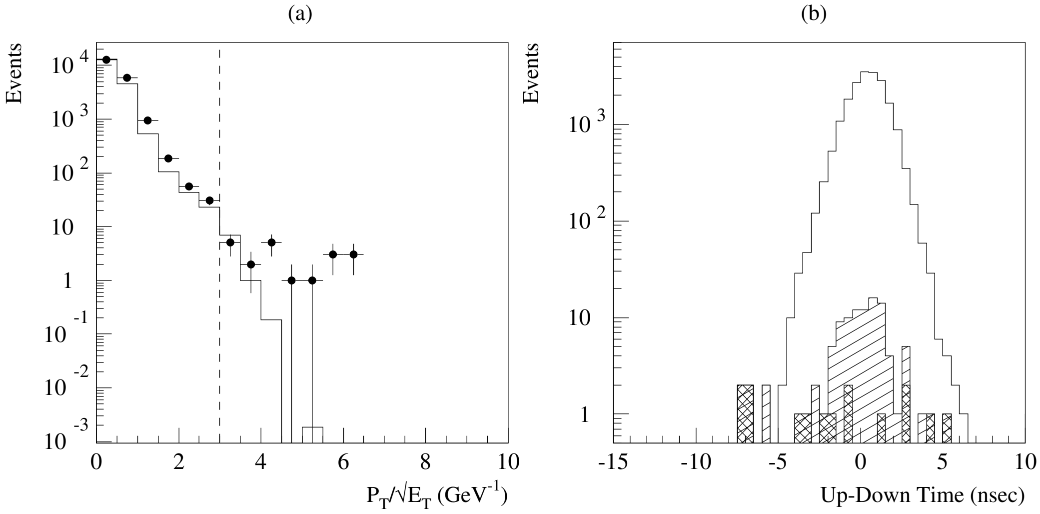

Figure 4.6: Cosmic ray suppression. (a) A cut of $p_t/\sqrt{E_t} > 3$ is applied to the data to remove cosmic rays. (b) Cosmic rays will usually (but not always) show an earlier time in the top of the detector relative to the bottom. Plotted is the up-down times for all events without the cut in $p_t/\sqrt{E_t}$ (white histogram), with the standard cut of 3 (double hash), and with a harder cut of 2 (single hash).

The MC calculated efficiency[4] of all cuts is 80% for $Q^2 > 200$ GeV^2. A breakdown of the efficiency of each cut is listed in Table 4.2. Shown in Figure 4.7 is the efficiency versus Q^2 and x. The efficiency at very high Q^2 drops slightly, primarily due to falling CTD acceptance and resolution. The loss of efficiency at lower Q^2 and x is due to the cut on electron energy.

Photoproduction background levels were estimated using 46.5 pb^{-1} of HERWIG direct, 5.7 pb^{-1} of HERWIG resolved, and 8.3 pb^{-1} of PYTHIA resolved photoproduction Monte Carlo. Generator level cuts of $E_T > 10$ GeV and $E - p_z > 30$ were used in order to reduce the photoproduction cross section so that sufficient Monte Carlo statistics (integrated luminosity) could be produced.

The photoproduction Monte Carlo is passed through the high Q^2 NC DIS event selection in order to estimate the size of the background. The result, shown in Figure 4.8, is approximately one event on average expected for 94–97 e^+p luminosity for the first 8 out of 16 $\log Q^2$ bins, and no events in the upper four bins. This produces a background that peaks at 1% at $Q^2 = 10000$ GeV^2.

Various distributions are shown in Figure 4.9 for selected events in Monte Carlo and data. Reasonable agreement is seen.

The x and y distributions in each of the Q^2 bins are shown in Figure 4.10 and Figure 4.11.

[4]Efficiency is defined as the ratio of number of events remaining after the cuts over before the cuts

Table 4.2: Event Selection inefficiencies. Listed are the fraction of events for $Q^2 > 200$ GeV^2 that do not pass each cut as predicted by Monte Carlo and as seen in the data. Listed are the number of events remaining after each cut and the fraction of events removed by each cut. For Monte Carlo, the number of events has been scaled by luminosity. Because of the manner in which the data is analyzed, values before a Q^2 cut are unavailable.

	Data		Monte Carlo	
Selection Cut	Events Passing	Fraction Removed	Events Passing	Fraction Removed
DST bit selection	unavailable		213179.2	49.96%
EM electron	unavailable		209152.4	0.95%
$Q^2 > 200$ GeV^2	188070.0	–	118277.8	21.33%[a]
Electron $E > 10$ GeV	127888.0	32.00%	110710.5	1.78%
Electron Isolation	123956.0	2.09%	110518.0	0.045%
Track or p_t requirement	111519.0	6.61%	107243.6	0.77%
$-0.2 < y_e < 0.95$	110880.0	0.34%	107160.0	0.020%
$E - P_z > 35$ GeV	110290.0	0.31%	106511.4	0.15%
$-50 < Z_{vertex} < 50$	106828.0	1.84%	104623.6	0.44%
$p_t/sqrt(e_t) < 3.0$ GeV$^{-1/2}$	106768.0	0.032%	104557.5	0.016%
Compton cut	106099.0	0.36%	104391.2	0.039%
Low Q^2 cut	106099.0	0.00%	104391.2	0.00%

a. The Monte Carlo was generated from $Q^2 > 40$ GeV^2.

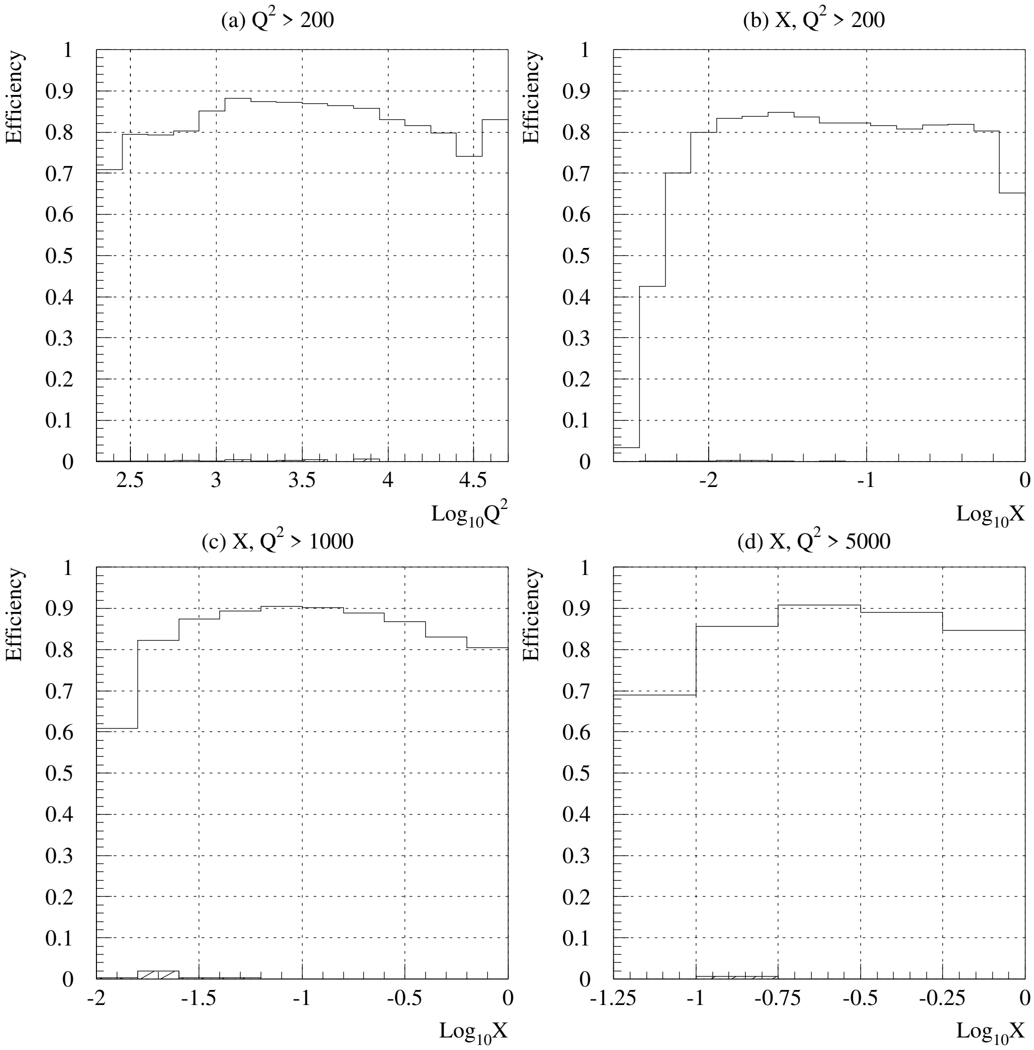

Figure 4.7: Event Selection Efficiency. Shown is the overall efficiency of selecting events plotted for (a) Q_h^2, (b) x_h with $Q_h^2 > 200$, (c) $Q_h^2 > 1000$, and (d) $Q_h^2 > 5000$ GeV^2. The hashed histogram is the predicted level of photoproduction background.

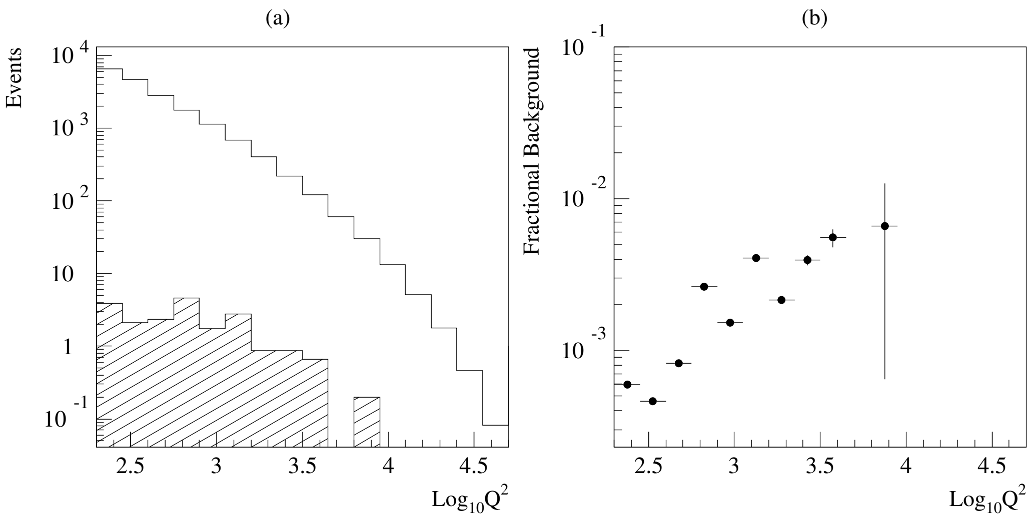

Figure 4.8: Predicted number of photoproduction events identified as NC DIS events after all cuts, compared to the expected number of NC DIS events. (a) The number of photoproduction background events averages to approximately one per $\log Q^2$ bin, up to $Q^2 = 10000$ GeV^2. (b) This corresponds to a relative background that peaks at 1%.

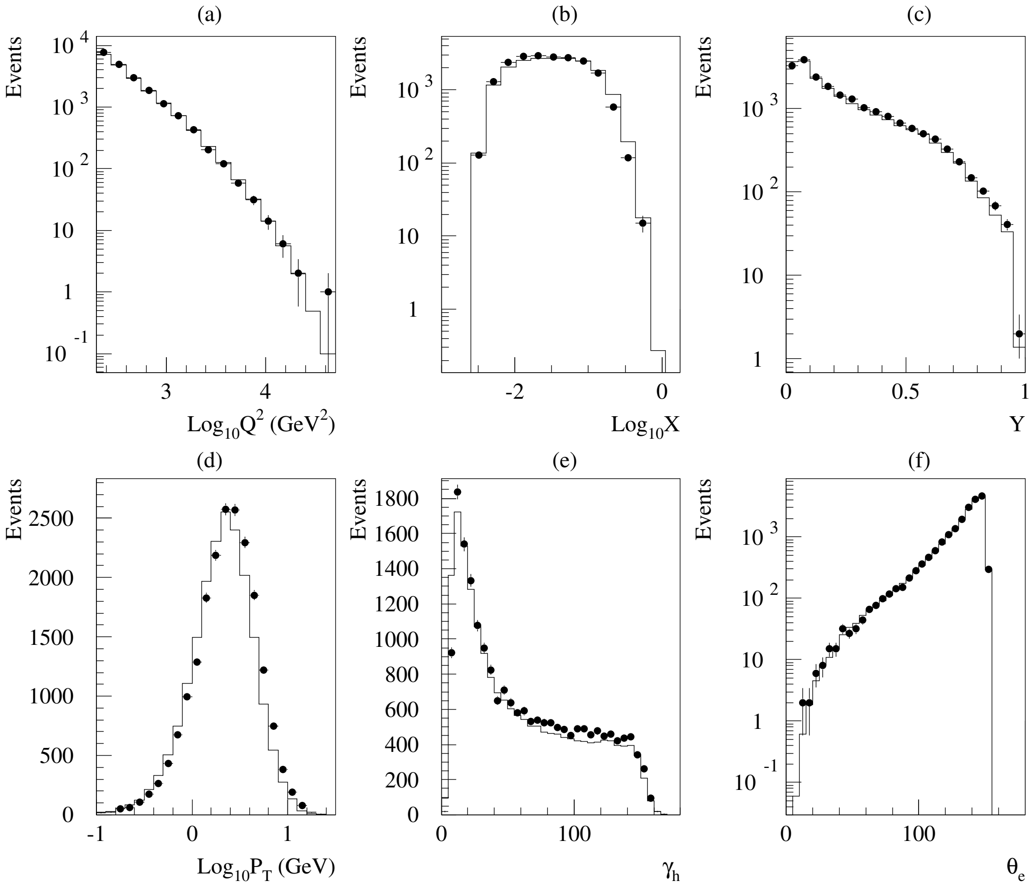

Figure 4.9: Comparison of data and Monte Carlo. Shown are data (points) and Monte Carlo (histogram) and event selection for (a) $\log_{10} Q^2_{DA}$, (b) $\log_{10} X_{DA}$, (c) Y_{DA}, (d) total calorimeter P_T, (e) hadron angle γ_h and (f) electron angle θ_e.

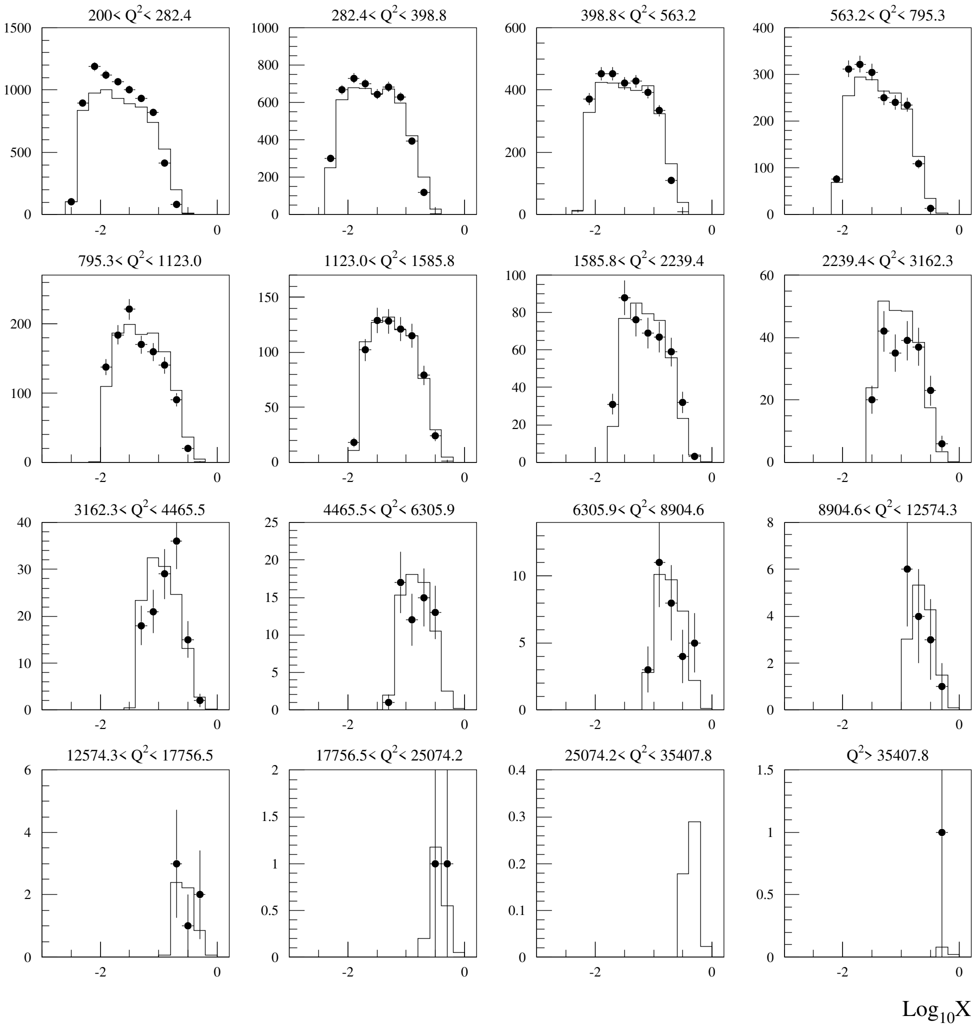

Figure 4.10: The uncorrected x distributions for data (points) and Monte Carlo (histograms) for each Q^2 bin.

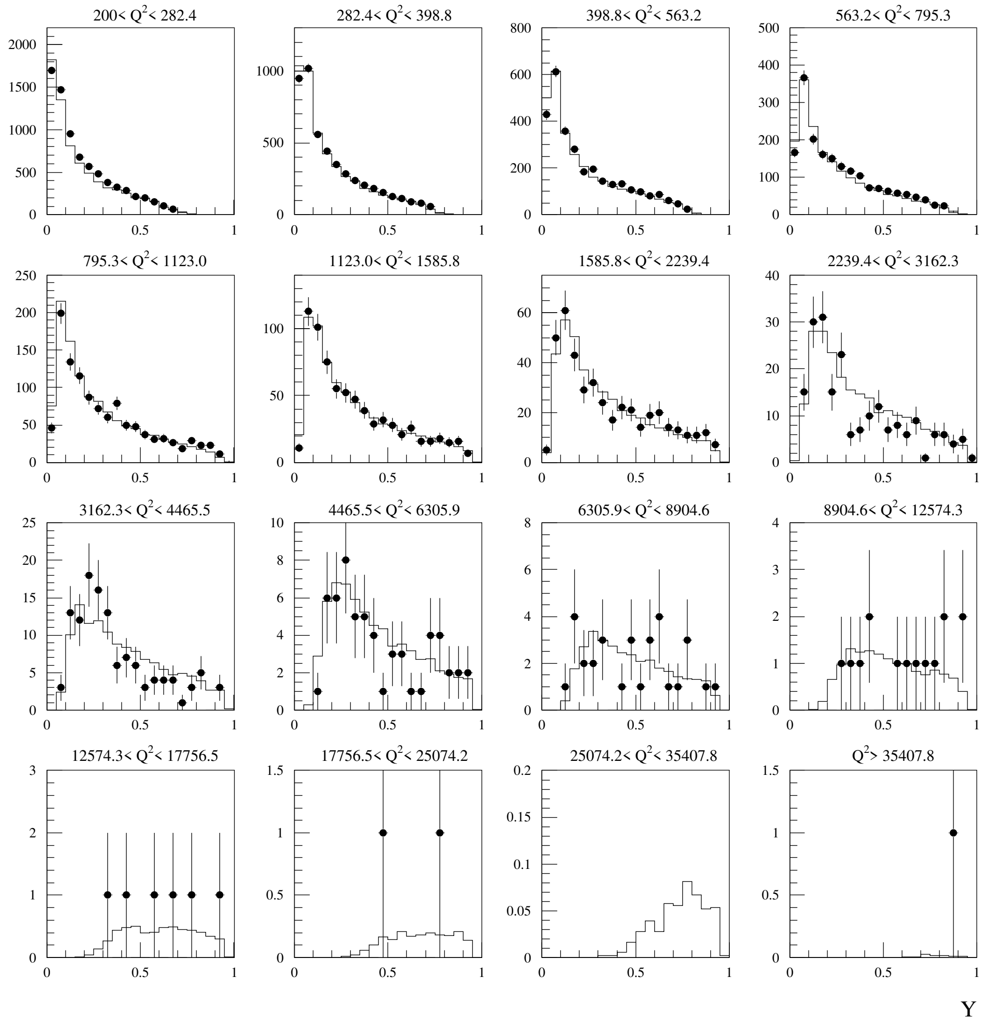

Figure 4.11: The uncorrected y distributions for data (points) and Monte Carlo (histograms) for each Q^2 bin.

Chapter 5

Kinematic Reconstruction

The ZEUS detector measures the energy and angle of both the electron (E_e, θ_e) and the hadronic systems (E_h, γ_h). The kinematic reconstruction of x and Q^2 requires measurement of only 2 of the 4 quantities E_e, θ_e, E_h and γ_h. That means we have a redundancy in the measurement of x and Q^2. We can use this additional information to perform cross checks. In this chapter, Double-Angle reconstruction method and its improved variant will be explained. Other methods will also be covered.

5.1 Standard Reconstruction Methods

The Electron-method uses scattered electron energy E_e and polar angle θ_e to reconstruct the kinematics:

$$Q^2_{el} = 2AE_e(1 + cos\theta_e) \tag{5.1}$$

$$y_{el} = 1 - \frac{E_e}{2A}(1 - cos\theta_e) \tag{5.2}$$

$$x_{el} = \frac{Q^2_{el}}{s\ y_{el}} \tag{5.3}$$

where A is the electron beam energy, s is the center-of-mass energy squared.

Jacquet-Blondel method uses the 4-momentum of the observed final state hadrons:

$$y_{jb} = \frac{\sum(E - p_z)_h}{2\ A} \tag{5.4}$$

$$Q^2_{jb} = \frac{(\sum p_x)^2_h + (\sum p_y)^2_h}{1 - y_{jb}} \tag{5.5}$$

$$x_{jb} = \frac{Q^2_{jb}}{s\ y_{jb}} \tag{5.6}$$

where the summation runs over all the observed hadronic deposits.

Double-Angle method uses the electron polar angle θ_e and the polar angle γ_h of the current (struck quark) hadron jet. Where γ_h is calculated from the 4-momentum of all observed hadronic final states:

$$cos\gamma_h = \frac{(\sum p_x)^2_h + (\sum p_y)^2_h - (\sum(E - p_z))^2_h}{(\sum p_x)^2_h + (\sum p_y)^2_h + (\sum(E - p_z))^2_h} \tag{5.7}$$

from θ and γ we can calculate:

$$Q^2_{DA} = 4A^2 \frac{sin\gamma_h\,(1 + cos\theta_e)}{sin\gamma_h + sin\theta_e - sin(\theta_e + \gamma_h)} \tag{5.8}$$

$$y_{DA} = \frac{sin\theta_e\,(1 - cos\gamma_h)}{sin\gamma_h + sin\theta_e - sin(\theta_e + \gamma_h)} \tag{5.9}$$

$$x_{DA} = \frac{Q^2_{DA}}{s\ y_{DA}} \tag{5.10}$$

This analysis uses the double-angle method. The advantage of the double-angle method is its high precision relative to other reconstruction methods at high Q^2[1] and a reduced sensitivity to errors in the absolute energy scale and effects of initial-state radiation because it uses hadronic system information as well.

5.2 Double Angle Reconstruction

As stated in the last section, the double-angle reconstruction method uses only the scattered electron angle and the angle of the current jet (final hadronic system), and is less sensitive to the absolute energy scale. However, the angle of the hadronic system γ_h is reconstructed using the transverse and longitudinal energies of all the hadronic final states. So, an acurate measurement and reconstruction of the angles is crucial to the validity and precision of this method. The error principally comes from the hadronic system angle reconstruction, and is more pronounced when hadrons are in the very forward direction. The reason is that forward hadronic jets have energy leakage through the beam pipe and do not deposit energy in the calorimeter, and also that some particles are scattered backwards from the face of FCAL, we will come to this point later. The angle γ_h is thus reconstructed larger than its true value, which in sequence affects x, y and Q^2 reconstruction, as shown in Figure 5.1 for γ_h, Figure 5.2 for x, Figure 5.3 for y and Figure 5.4 for Q^2, all of which uses the standard Zeus reconstruction method summing up energies cell by cell.

To improve the forward γ_h reconstruction, another reconstruction scheme called

[1] Electron method also has good precision at high Q^2 and high x, but depends strongly on electron energy scale.

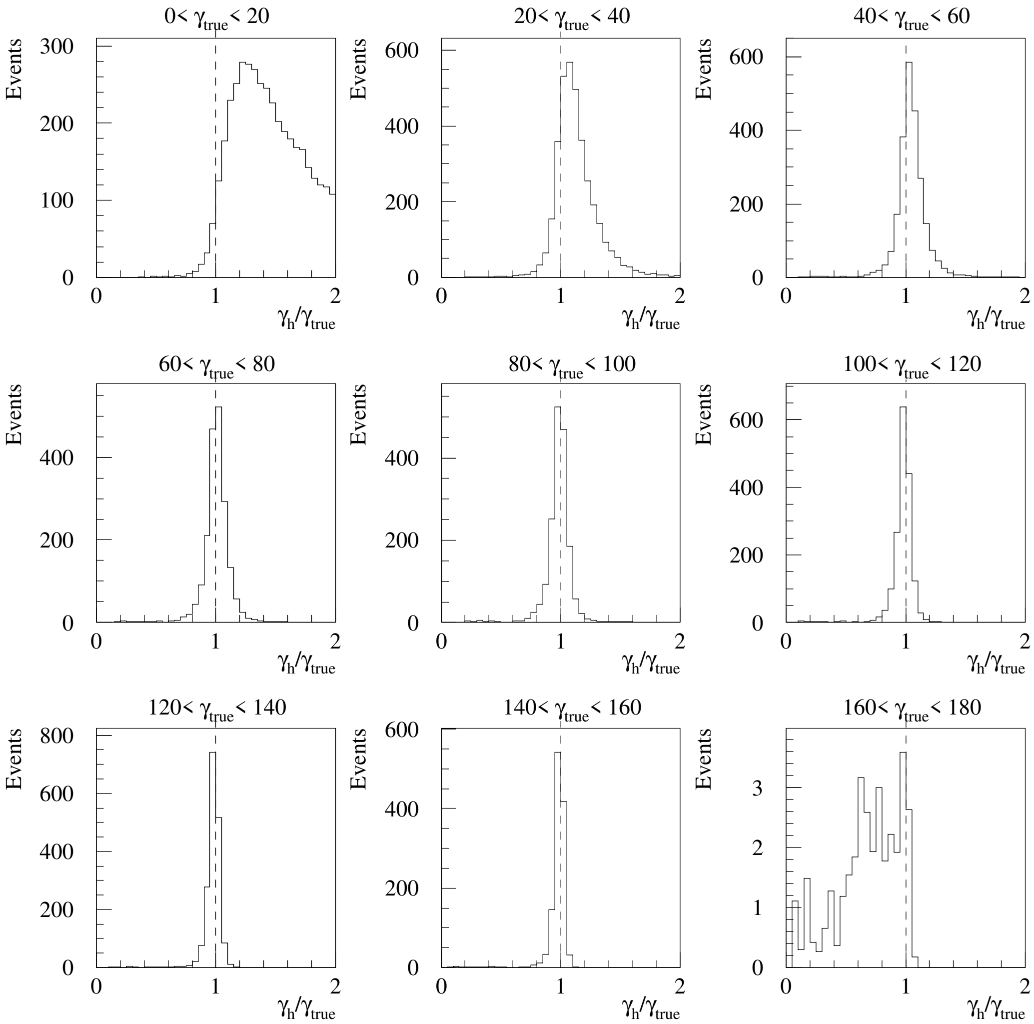

Figure 5.1: γ_h reconstruction, standard, summing energies cell by cell, with $Q^2 > 200$ GeV^2. Shown is γ_h/γ_{true} in different γ_{true} range. Note the poor reconstruction in forward γ, the first two bins. The dashed line means ideal reconstruction.

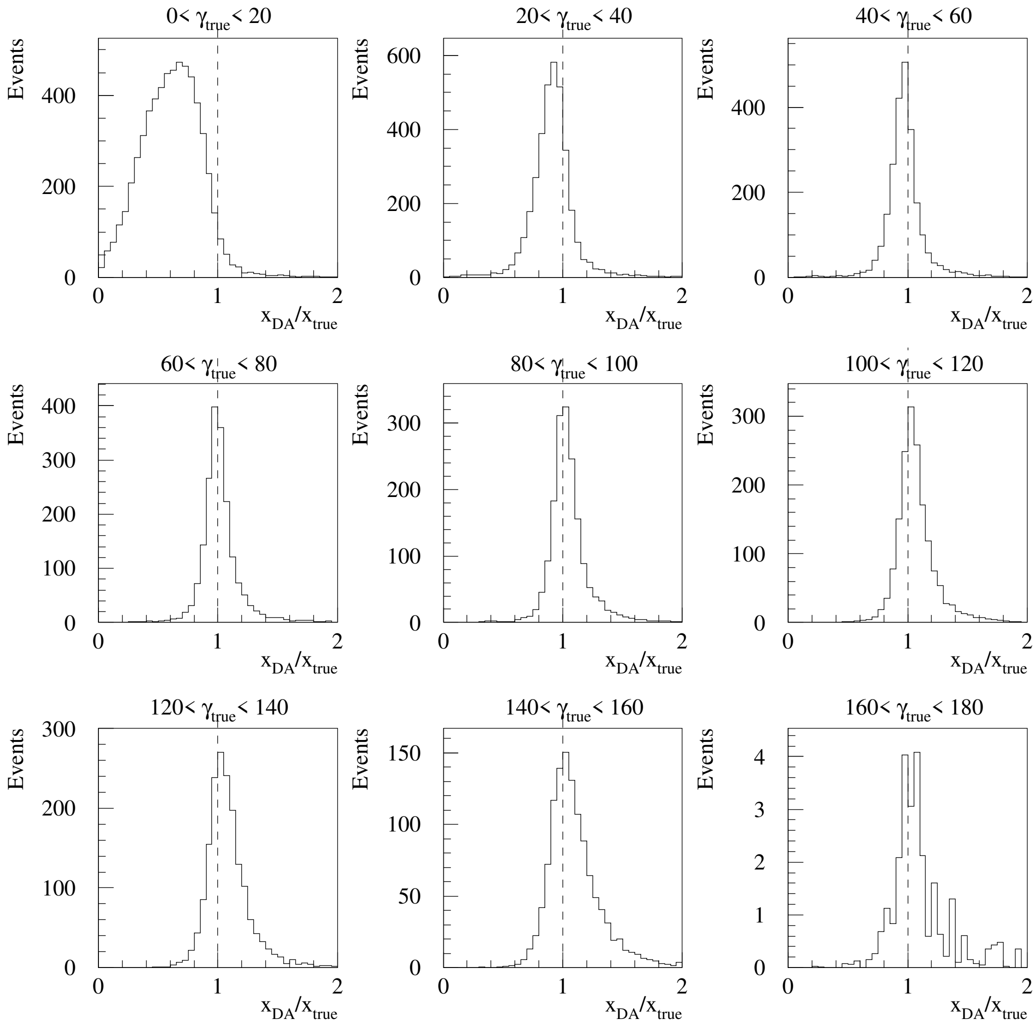

Figure 5.2: x_{DA} reconstruction, standard, summing energies cell by cell, with $Q^2 >$ 200 GeV^2. Shown is x_{DA}/x_{true} in different γ_{true} range. Note the poor reconstruction in forward γ, the first two bins. The dashed line means ideal reconstruction.

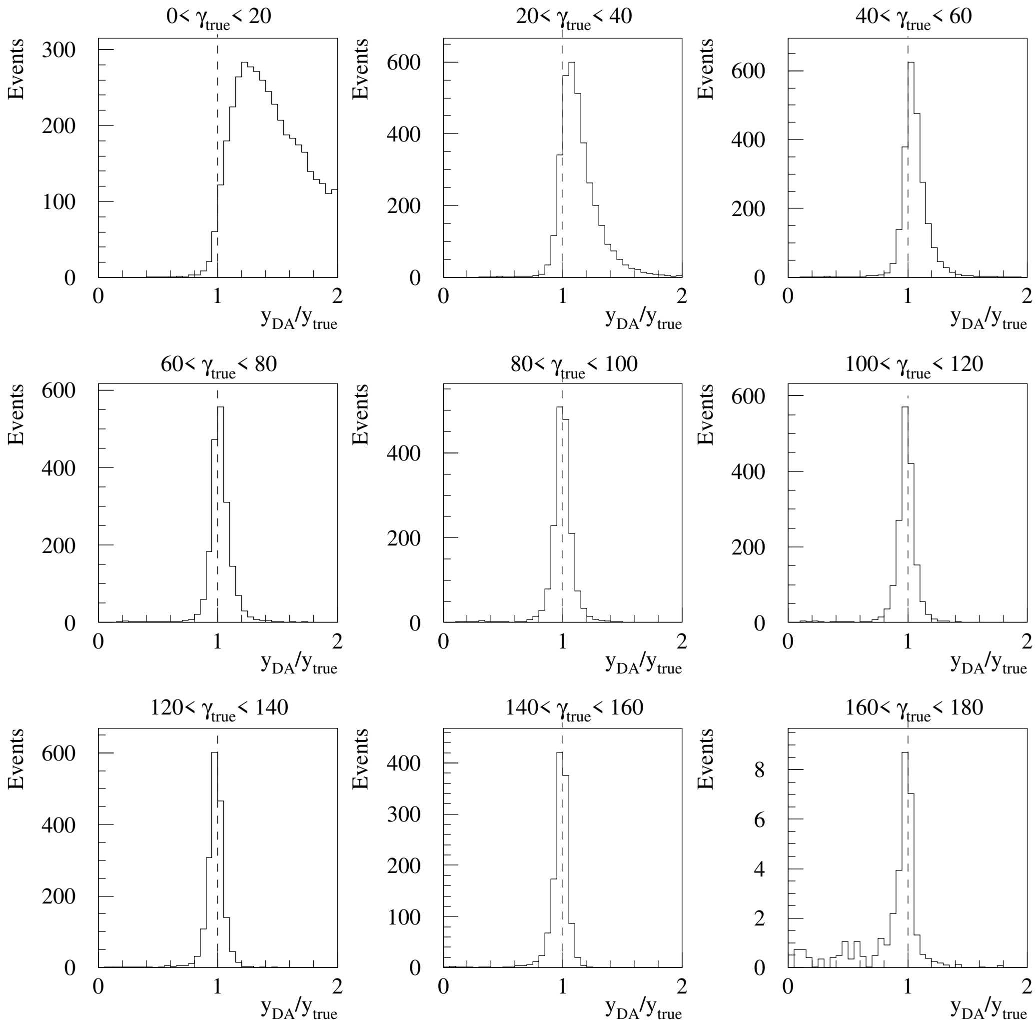

Figure 5.3: y_{DA} reconstruction, standard, summing energies cell by cell, with $Q^2 >$ 200 GeV^2. Shown is y_{DA}/y_{true} in different γ_{true} range. Note the poor reconstruction in forward γ, the first two bins. The dashed line means ideal reconstruction.

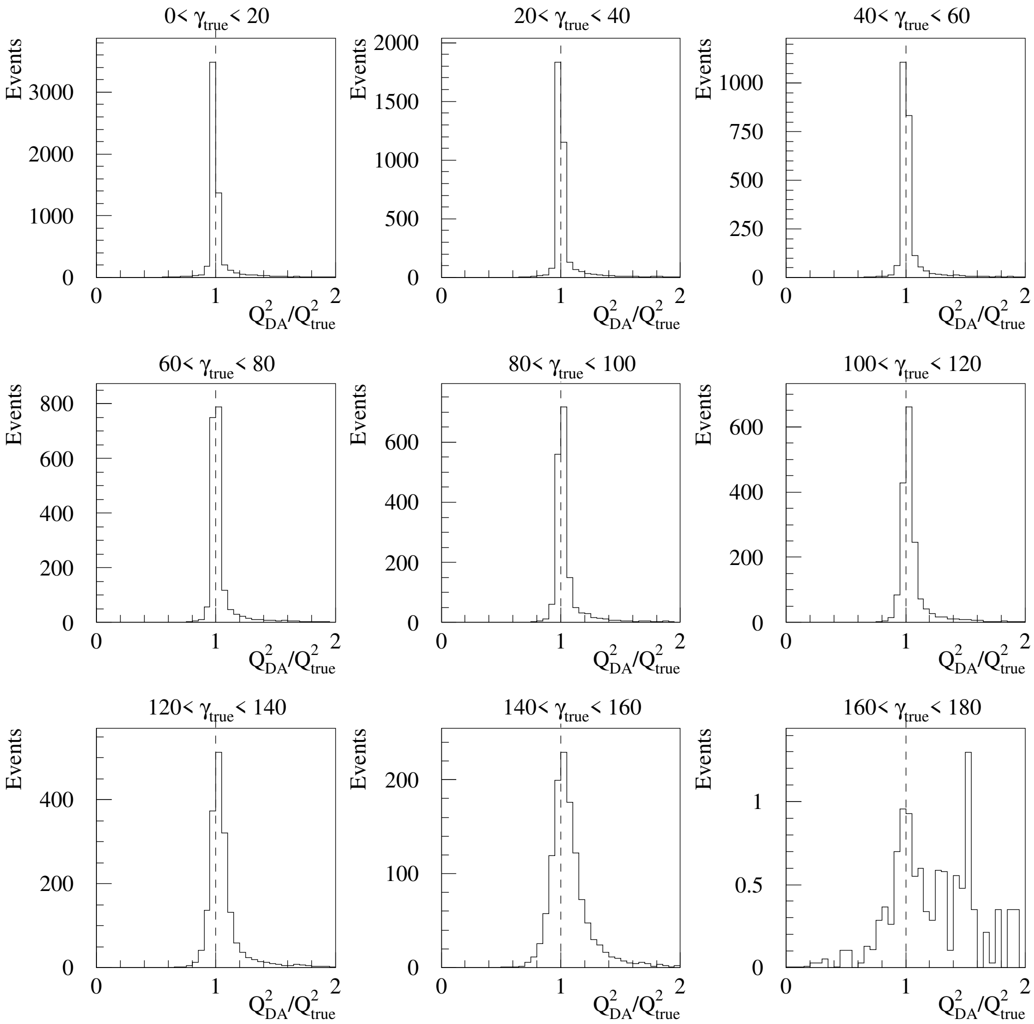

Figure 5.4: Q^2_{DA} reconstruction, standard, summing energies cell by cell, with $Q^2 >$ 200 GeV^2. Shown is Q^2_{DA}/Q^2_{true} in different γ_{true} range. Note the reconstruction in forward γ is as good as the other bins. The dashed line means ideal reconstruction.

Cone-Island[2] is used. In this Cone-Island scheme, instead of summing energies cell by cell and using cell center as the cell position, cells are grouped into cone-islands. In each cone-island, energy and position of this cone-island are calculated using the PMT imbalance information of each cell, and then energies are summed up cone-island by cone-island, the position is calculated accordingly using the cone-island energy weighted sum. The reconstruction improvement using this scheme is shown in Figure 5.5 for γ_h. We see a slight improvement in the forward γ_h.

To improve the forward γ_h reconstruction further more, an iterative procedure is employed in calculating the kinematics. Back scattering (albedo) is a factor that affects the precision of the hadronic reconstruction, especially when hadronic jets are in the forward direction. In this case, the backward hadronic activities in the calorimeter are not real, primary particles, they are in fact particles bounced off from the face of FCAL. To eliminate these artificial activities, an angular suppression mechanism is employed after exhaustly optimizing the angular cut. It is implemented as:

$$\Theta_{cut} = \gamma_h + 8 + \frac{(MAX(\gamma_h - 10, 0))^2}{20} \qquad (5.11)$$

The cutting angle Θ_{cut} is a function of first-time (0th iteration) calculated γ_h. If angle θ of any hadronic Cone-Island is bigger than Θ_{cut}, this hadronic Cone-Island will be ignored in the second-time (1st iteration) γ_h calculation. When γ_h reaches 58^o, Θ_{cut} reaches 180^o. That means if 0th iteration γ_h is above 58^o, no correction is made. The correction is made only if 0th order γ_h is less than 58^o, in the forward

[2]Cone-Island scheme was developed by Gennady Briskin of Univ. Tel Aviv

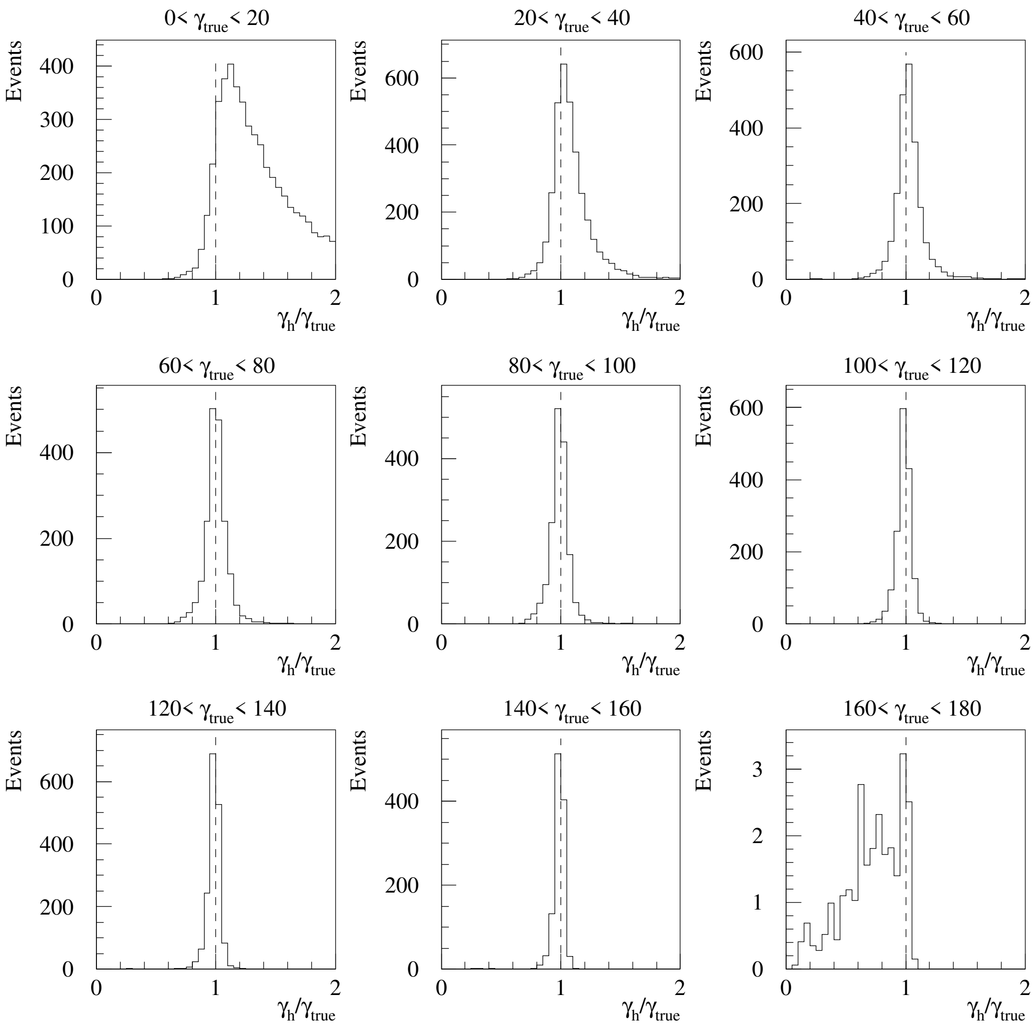

Figure 5.5: γ_h reconstruction, Cone-Island, summing energies cone-island by cone-island. Shown is γ_h/γ_{true} in different γ_{true} range. Note the slight improvement in forward γ, the first two bins. The dashed line is to guide the eye.

direction where back scattering happens most.

x_{DA}, y_{DA} and Q^2_{DA} will be recalculated accordingly. The justification for this procedure is that when γ_h is in the very forward direction, the hadronic jets are energetic and also in the very forward direction, the little energy deposit outside of Fcal only serves as back scattering or noise and tends to pull γ_h larger than it really is. The hadronic energy per cone-island outside of Fcal is typically less than 500 MeV, to ignore those little energies is safe. The reconstruction after this iteration, and the comparison with default DA method and Cone-Island method are shown in Figure 5.6 and Figure 5.7 for γ_h, Figure 5.8 and Figure 5.9 for x_{DA}, Figure 5.10 and Figure 5.11 for y_{DA}. Substantial improvement is seen in the forward hadronic angle γ_h region. The Q^2 reconstruction changes very little due to the fact that it depends mainly on scattered electron angle, while the correction technique employed does not touch scattered electron angle at all.

The comparison between three reconstruction methods is summarized in Table 5.2, Table 5.2, Table 5.2 and Table **??**. From the comparison, one can see that iterative method is the best among the three.

Another way to make the comparison is to plot the migration chart for the three reconstruction methods. Using Monte Carlo Migration from generated x_{true}, Q^2_{true} point to the reconstructed x_{rec}, Q^2_{rec} point can be established. The smallest migration indicates the best possible reconstruction method. Those migration charts are shown in Figure 5.12 for default DA method, Figure 5.13 for Cone-Island method, and Figure 5.14 for iterative method. The last one seems the best.

After iterative method had been established, the Q^2_{DA} vs. x_{DA} for the e^+p data

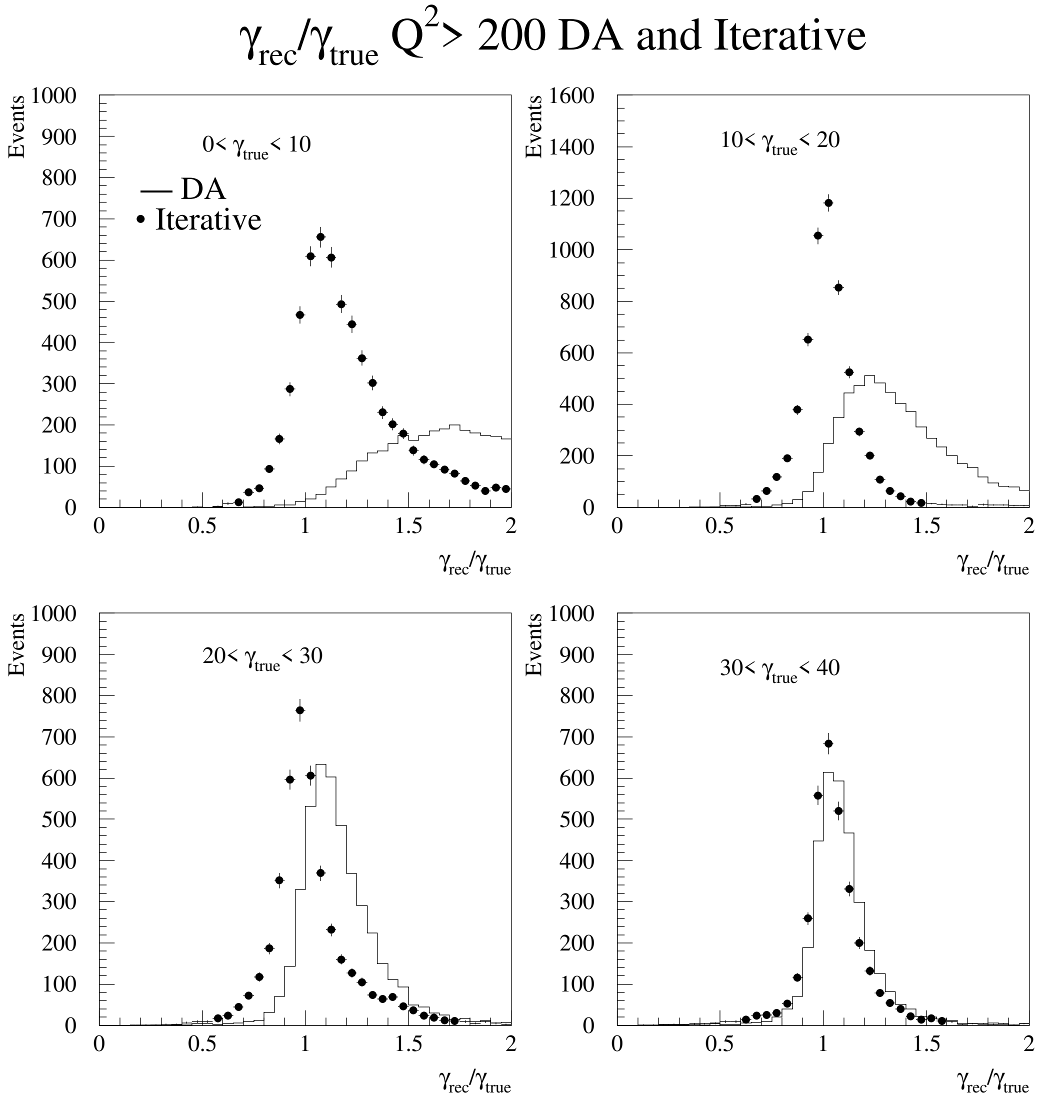

Figure 5.6: γ_h reconstruction, Cone-Island plus iterative procedure, compared to

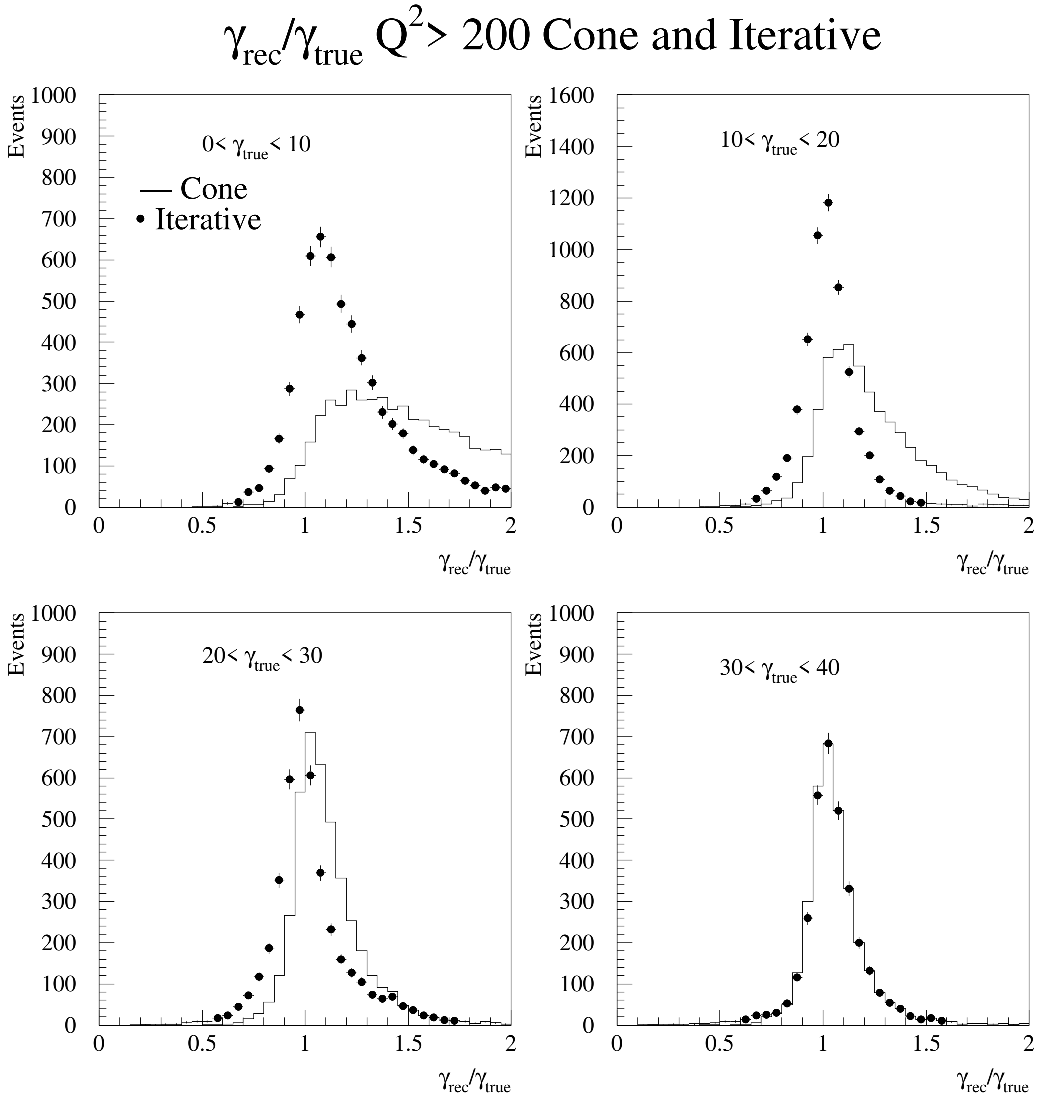

Figure 5.7: γ_h reconstruction, Cone-Island plus iterative procedure, compared to

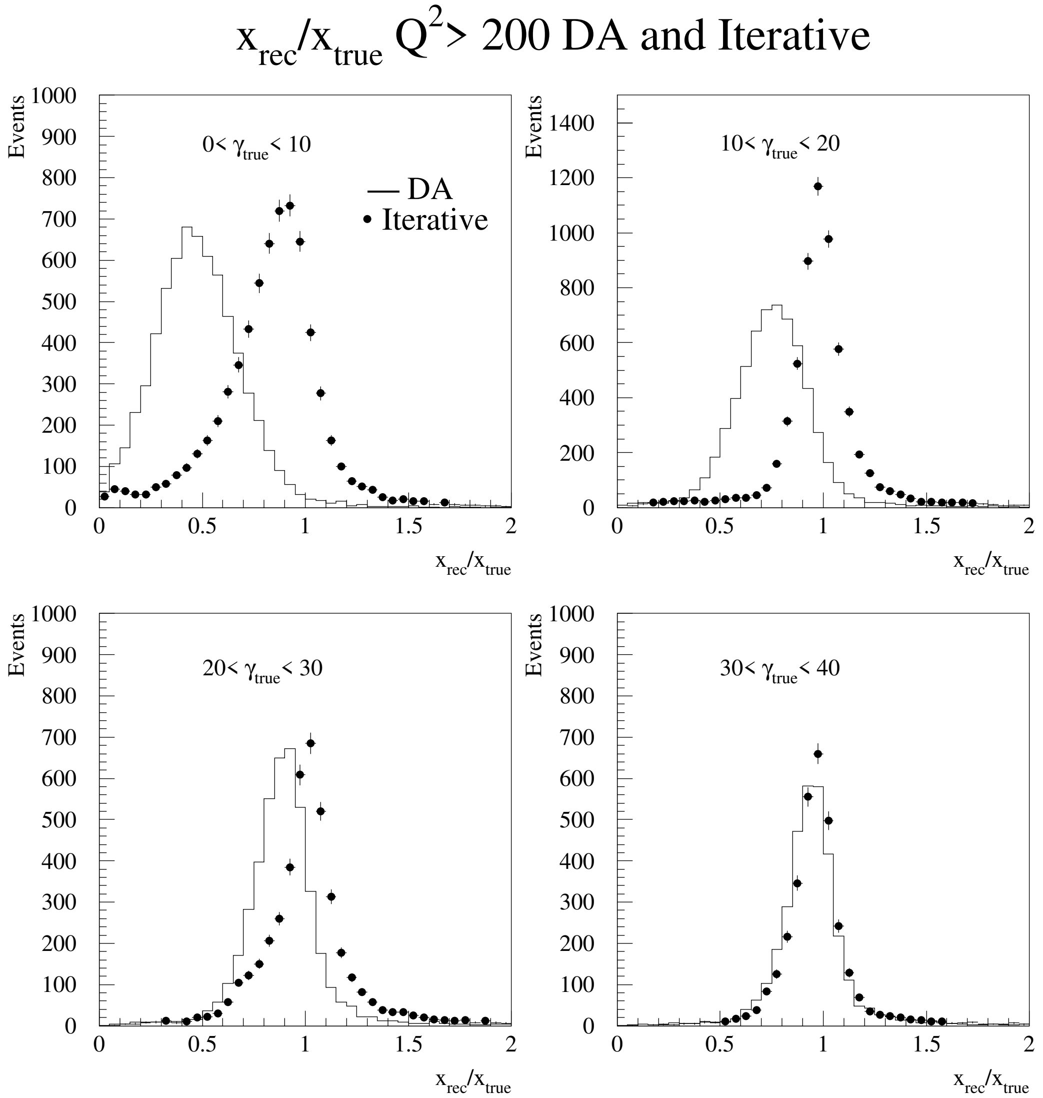

Figure 5.8: x reconstruction, Cone-Island plus iterative procedure, compared to de-

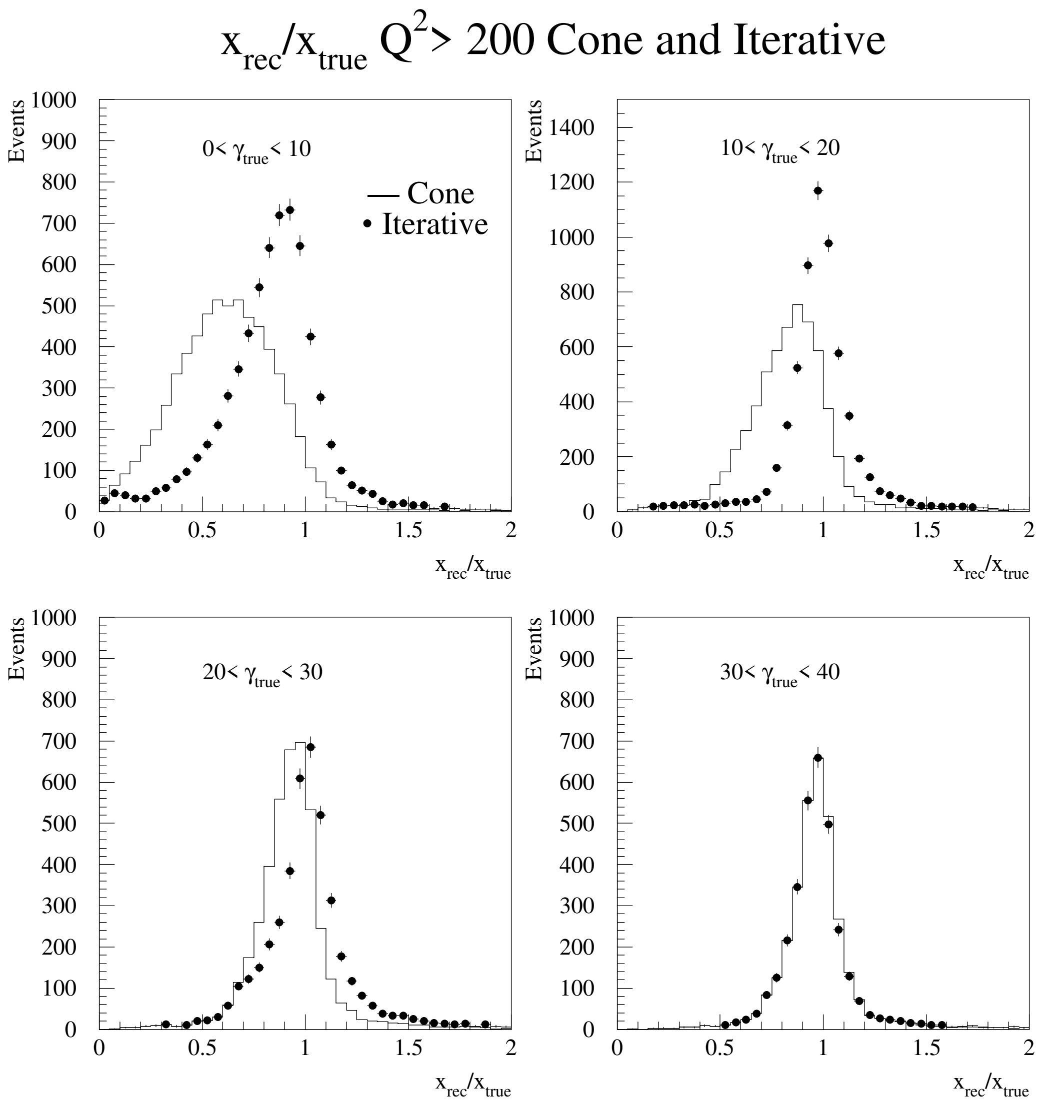

Figure 5.9: x reconstruction, Cone-Island plus iterative procedure, compared to Cone-

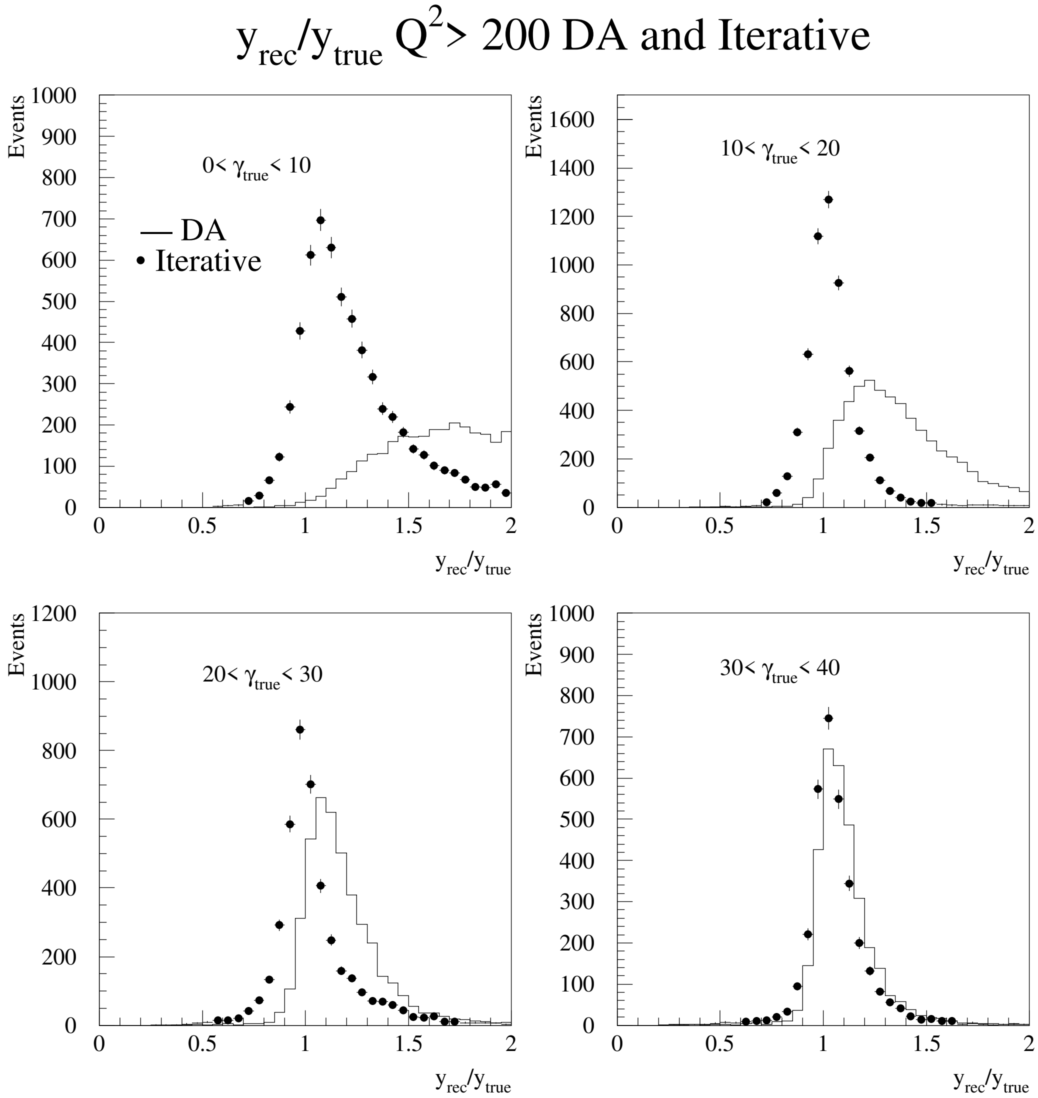

Figure 5.10: y reconstruction, Cone-Island plus iterative procedure, compared to

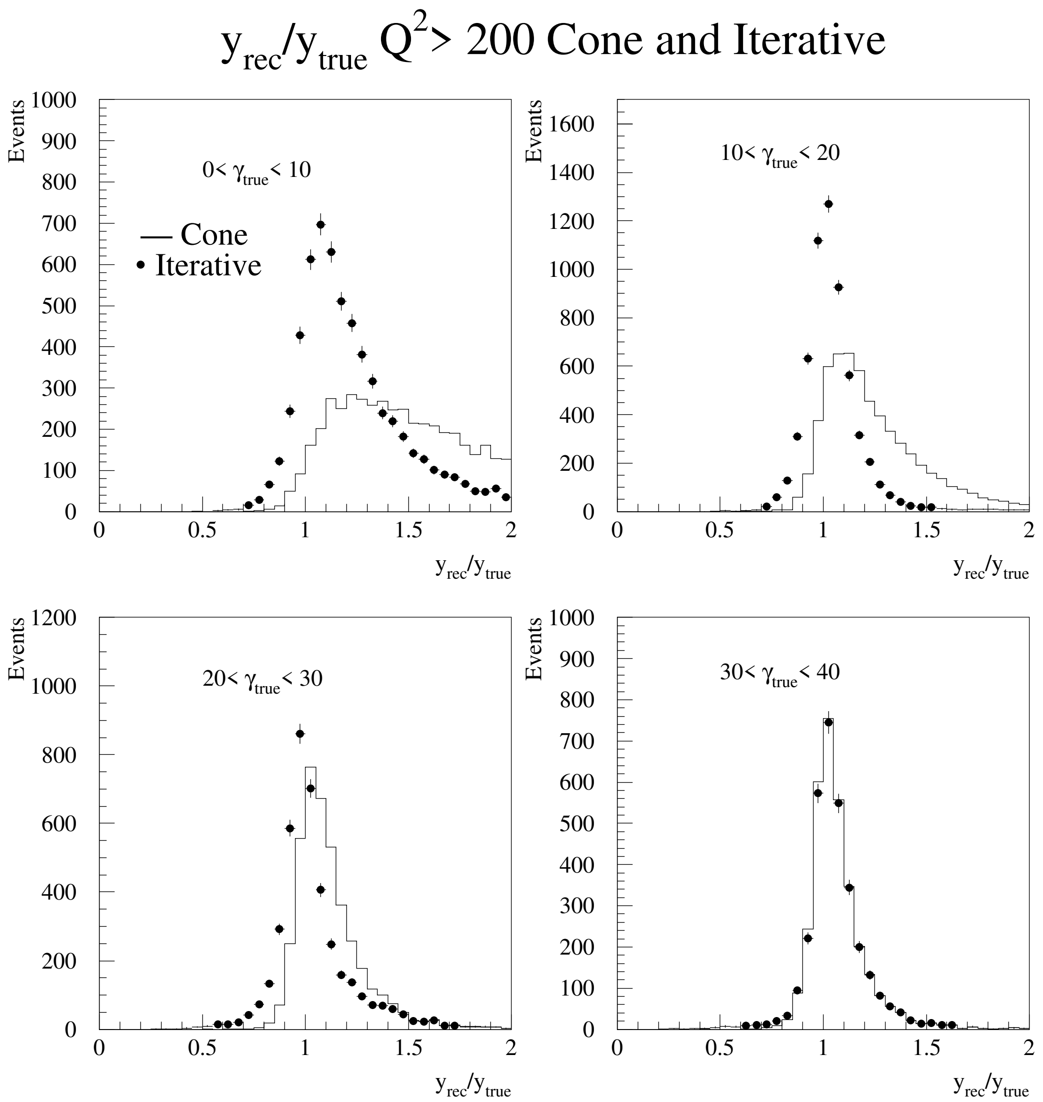

Figure 5.11: y reconstruction, Cone-Island plus iterative procedure, compared to

γ_h Reconstruction

Table 5.1: Comparison of γ_h reconstruction

Mean γ_h/γ_{true}			
γ_{true} range	Cell DA	Cone-Island	Iterative
$0 < \gamma_{true} < 20$	1.773	1.513	1.182
$20 < \gamma_{true} < 40$	1.150	1.107	1.059
$40 < \gamma_{true} < 60$	1.056	1.042	1.041
$60 < \gamma_{true} < 80$	1.007	1.006	1.006
$80 < \gamma_{true} < 100$	0.981	0.989	0.989
$100 < \gamma_{true} < 120$	0.968	0.980	0.980
$120 < \gamma_{true} < 140$	0.972	0.981	0.981
$140 < \gamma_{true} < 160$	0.973	0.981	0.981
$160 < \gamma_{true} < 180$	0.684	0.719	0.720
Resolution γ_h/γ_{true}			
γ_{true} range	Cell DA	Cone-Island	Iterative
$0 < \gamma_{true} < 20$	0.370	0.376	0.329
$20 < \gamma_{true} < 40$	0.224	0.231	0.259
$40 < \gamma_{true} < 60$	0.182	0.181	0.182
$60 < \gamma_{true} < 80$	0.139	0.124	0.124
$80 < \gamma_{true} < 100$	0.124	0.098	0.098
$100 < \gamma_{true} < 120$	0.115	0.078	0.078
$120 < \gamma_{true} < 140$	0.093	0.065	0.065
$140 < \gamma_{true} < 160$	0.098	0.065	0.066
$160 < \gamma_{true} < 180$	0.377	0.333	0.333

X Reconstruction

Table 5.2: Comparison of X reconstruction

Mean X/X_{true}			
γ_{true} range	Cell DA	Cone-Island	Iterative
$0 < \gamma_{true} < 20$	0.619	0.723	0.910
$20 < \gamma_{true} < 40$	0.924	0.948	0.994
$40 < \gamma_{true} < 60$	0.993	0.999	1.000
$60 < \gamma_{true} < 80$	1.041	1.033	1.033
$80 < \gamma_{true} < 100$	1.071	1.056	1.056
$100 < \gamma_{true} < 120$	1.091	1.075	1.075
$120 < \gamma_{true} < 140$	1.103	1.082	1.082
$140 < \gamma_{true} < 160$	1.124	1.099	1.099
$160 < \gamma_{true} < 180$	1.315	1.443	1.443
Resolution X/X_{true}			
γ_{true} range	Cell DA	Cone-Island	Iterative
$0 < \gamma_{true} < 20$	0.428	0.356	0.286
$20 < \gamma_{true} < 40$	0.257	0.201	0.260
$40 < \gamma_{true} < 60$	0.249	0.187	0.193
$60 < \gamma_{true} < 80$	0.256	0.189	0.189
$80 < \gamma_{true} < 100$	0.256	0.188	0.188
$100 < \gamma_{true} < 120$	0.232	0.188	0.188
$120 < \gamma_{true} < 140$	0.232	0.196	0.196
$140 < \gamma_{true} < 160$	0.269	0.224	0.224
$160 < \gamma_{true} < 180$	0.509	0.504	0.503

Y Reconstruction

Table 5.3: Comparison of Y reconstruction

Mean Y/Y_{true}			
γ_{true} range	Cell DA	Cone-Island	Iterative
$0 < \gamma_{true} < 20$	1.775	1.520	1.196
$20 < \gamma_{true} < 40$	1.160	1.116	1.069
$40 < \gamma_{true} < 60$	1.070	1.054	1.054
$60 < \gamma_{true} < 80$	1.027	1.026	1.026
$80 < \gamma_{true} < 100$	1.000	1.010	1.010
$100 < \gamma_{true} < 120$	0.980	0.993	0.993
$120 < \gamma_{true} < 140$	0.976	0.987	0.987
$140 < \gamma_{true} < 160$	0.973	0.983	0.983
$160 < \gamma_{true} < 180$	0.866	0.966	0.964
Resolution Y/Y_{true}			
γ_{true} range	Cell DA	Cone-Island	Iterative
$0 < \gamma_{true} < 20$	0.366	0.371	0.322
$20 < \gamma_{true} < 40$	0.215	0.216	0.240
$40 < \gamma_{true} < 60$	0.179	0.170	0.170
$60 < \gamma_{true} < 80$	0.162	0.151	0.150
$80 < \gamma_{true} < 100$	0.163	0.152	0.152
$100 < \gamma_{true} < 120$	0.138	0.108	0.107
$120 < \gamma_{true} < 140$	0.109	0.080	0.080
$140 < \gamma_{true} < 160$	0.114	0.080	0.080
$160 < \gamma_{true} < 180$	0.308	0.147	0.144

Q^2 Reconstruction

Table 5.4: Comparison of Q^2 reconstruction

Mean Q^2/Q^2_{true}			
γ_{true} range	Cell DA	Cone-Island	Iterative
$0 < \gamma_{true} < 20$	1.021	1.026	1.035
$20 < \gamma_{true} < 40$	1.027	1.030	1.033
$40 < \gamma_{true} < 60$	1.029	1.033	1.033
$60 < \gamma_{true} < 80$	1.036	1.039	1.039
$80 < \gamma_{true} < 100$	1.043	1.042	1.042
$100 < \gamma_{true} < 120$	1.052	1.048	1.048
$120 < \gamma_{true} < 140$	1.058	1.052	1.052
$140 < \gamma_{true} < 160$	1.068	1.063	1.063
$160 < \gamma_{true} < 180$	1.226	1.143	1.144
Resolution Q^2/Q^2_{true}			
γ_{true} range	Cell DA	Cone-Island	Iterative
$0 < \gamma_{true} < 20$	0.136	0.136	0.134
$20 < \gamma_{true} < 40$	0.131	0.128	0.127
$40 < \gamma_{true} < 60$	0.126	0.129	0.129
$60 < \gamma_{true} < 80$	0.130	0.133	0.133
$80 < \gamma_{true} < 100$	0.134	0.131	0.131
$100 < \gamma_{true} < 120$	0.133	0.132	0.132
$120 < \gamma_{true} < 140$	0.139	0.137	0.137
$140 < \gamma_{true} < 160$	0.159	0.153	0.153
$160 < \gamma_{true} < 180$	0.282	0.284	0.282

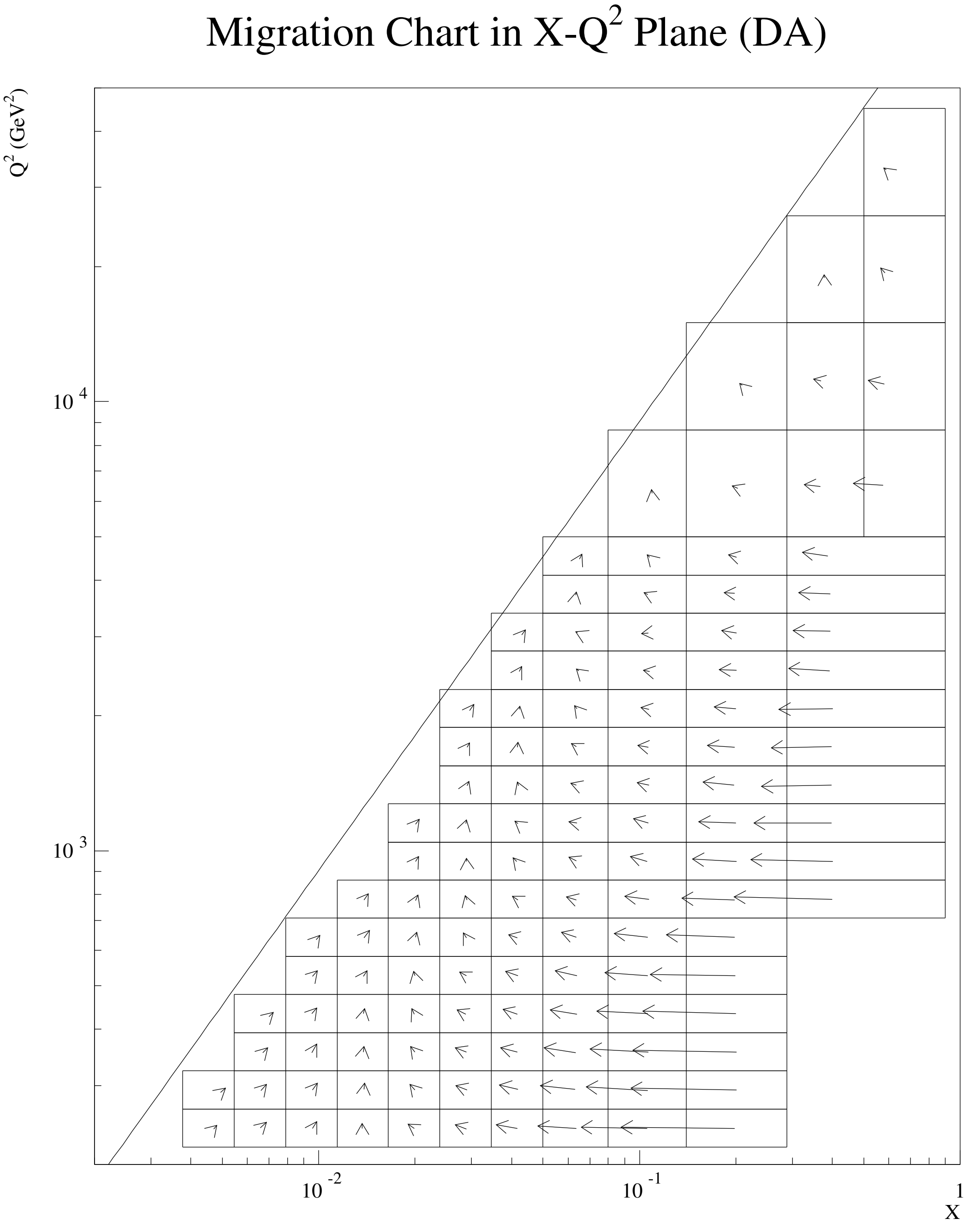

Figure 5.12: Migration chart for default DA method. The base of the arrow is the average generated kinematic position in a bin, the head is the average reconstructed kinematic position for that bin. Large migration can be seen at low y.

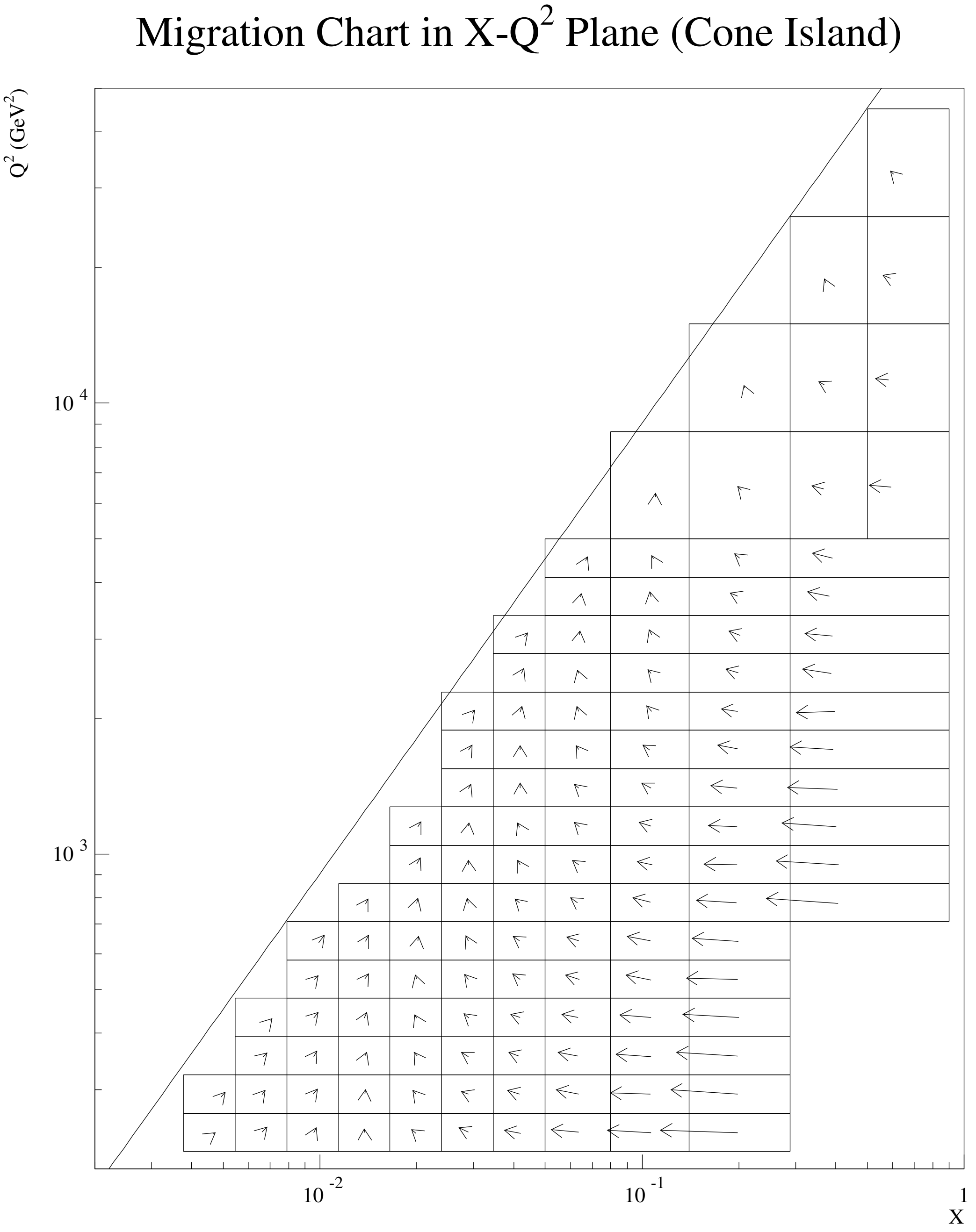

Figure 5.13: Migration chart for cone-island method. The base of the arrow is the average generated kinematic position in a bin, the head is the average reconstructed kinematic position for that bin. Large migration can be seen at low y, but slightly better.

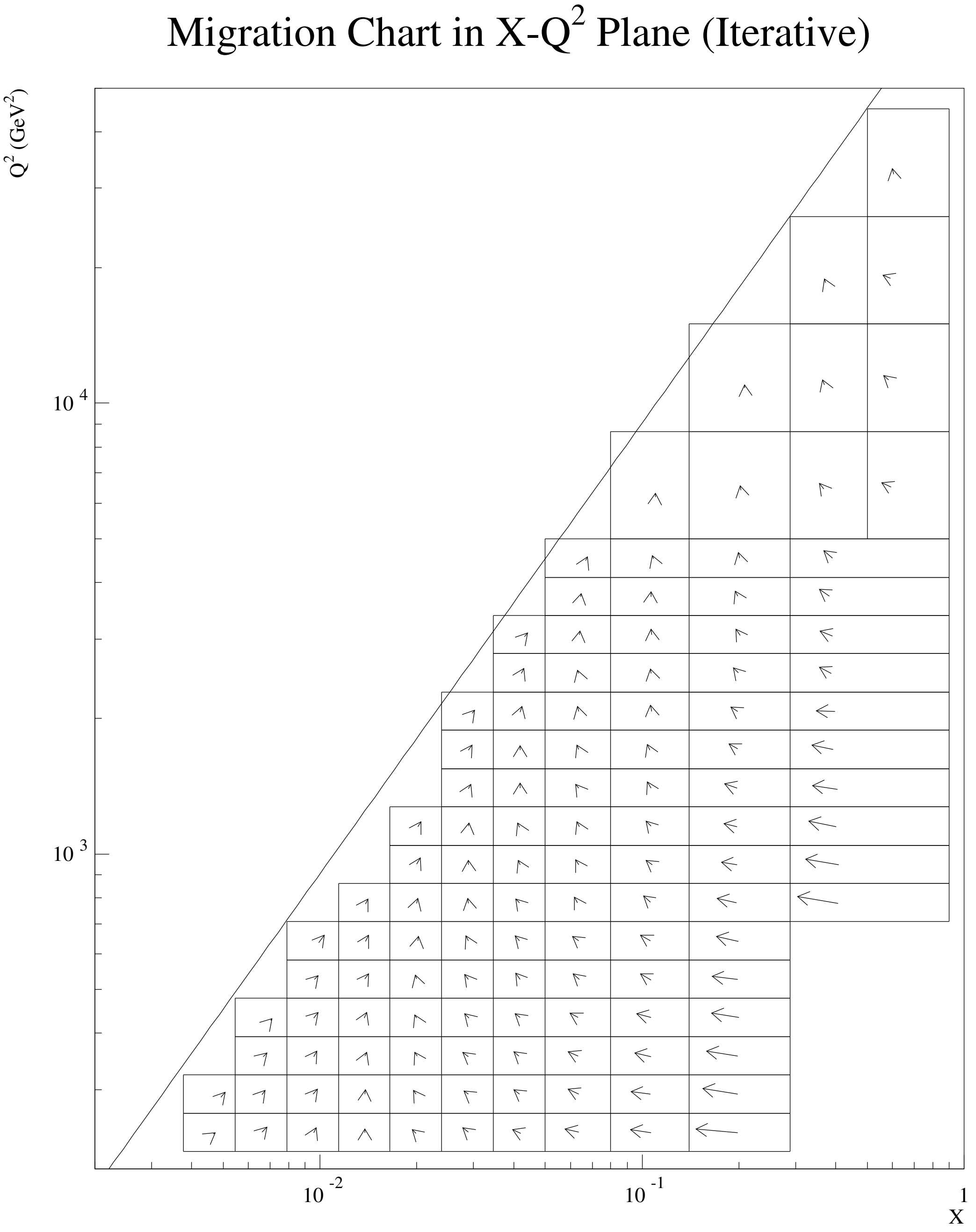

Figure 5.14: Migration chart for iterative method. The base of the arrow is the average generated kinematic position in a bin, the head is the average reconstructed kinematic position for that bin. Still some migration can be seen at low y, but reduced.

is plotted in Figure 5.15.

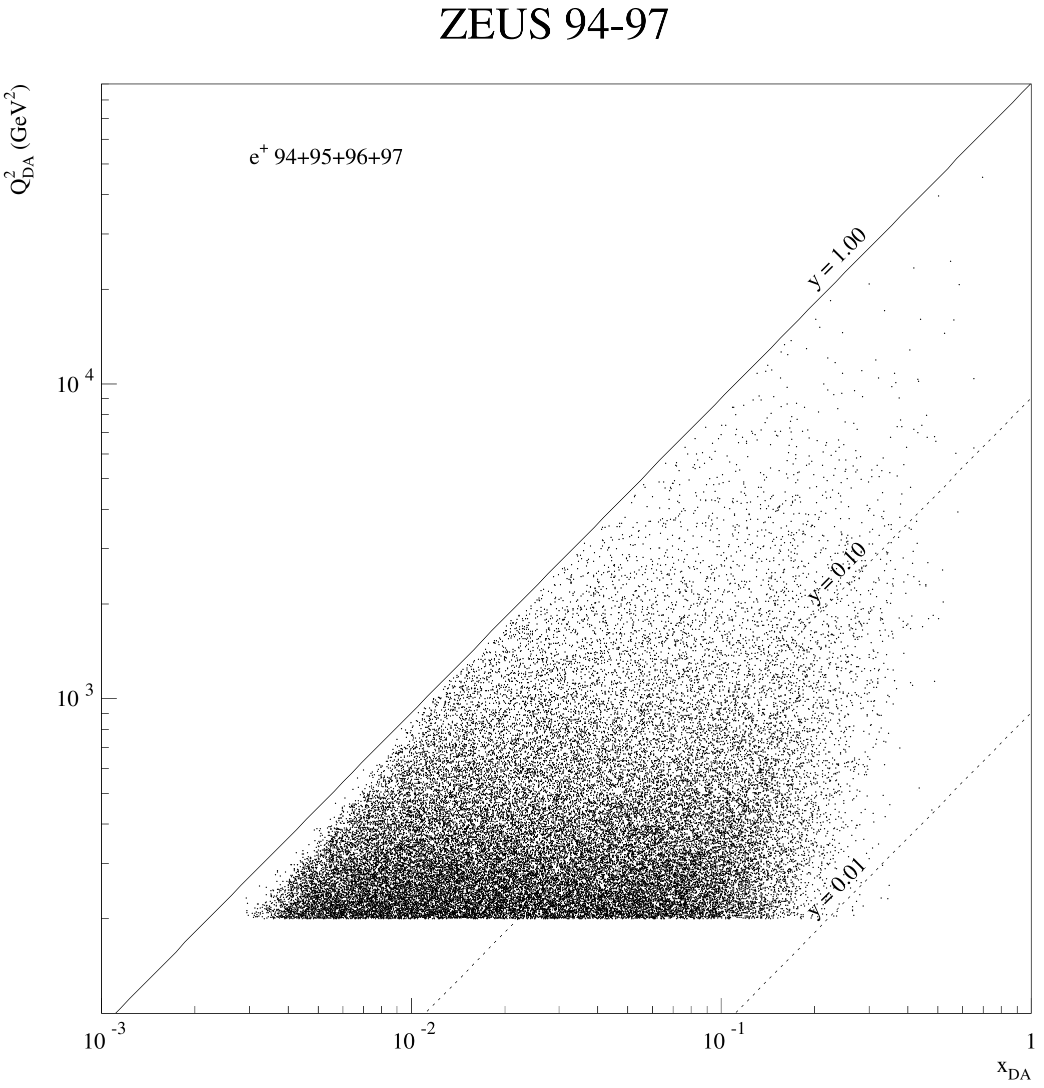

Figure 5.15: Q^2_{DA} vs x_{DA}, for the selected e^+p data sample.

Chapter 6

The Measurement of Double-differential cross section

In order to measure $d^2\sigma/\mathrm{d}x\mathrm{d}Q^2$, the number of events reconstructed in bins of x and Q^2 is compared with the MC prediction of a particular parton parameterization. A simple procedure is employed where the ratio of number of events in the data over that of Monte Carlo simulation is determined, this ratio is then multiplied by the input Monte Carlo theoretical double-differential cross section to obtain the measured value. The functional form of $d^2\sigma/\mathrm{d}x\mathrm{d}Q^2$ is not determined, rather a value for each bin is measured. Bins are chosen where kinematic quantities are well reconstructed so that the correction procedure applied is minimal.

6.1 Kinematic Region and Bin Selection

Bins in x and Q^2 are chosen such that the width of each bin is commensurate with the resolution of the x, Q^2 measurement of this bin, however, poor statistics at very high Q^2 demands bins at those regions much larger than the resolution of the x and

Q^2 reconstruction.

Efficiency and purity of each bin are defined as the bin quality factors E and P:

$$E = \frac{N_{GP}}{N_G} \tag{6.1}$$

$$P = \frac{N_{GR}}{N_R} \tag{6.2}$$

where

- N_G - Number of events generated in this bin.
- N_{GP} - Number of events generated in this bin that passed the selection cuts.
- N_R - Number of events reconstructed in this bin.
- N_{GR} - Number of events generated and reconstructed in this bin.

Bin of fair quality is defined by $E > 0.2$ and $P > 0.3$, while bin of good quality is defined by $E > 0.5$ and $P > 0.5$. Shown in Figure 6.1 is the bin quality for all chosen bins. We see that only two border bins at high y failed the fair quality definition, and only four border bins at high y failed the good quality definition. Also shown in Figure 6.2 is the migration chart in $x - Q^2$ plane for each bin. Only a few bins have comparably large migration.

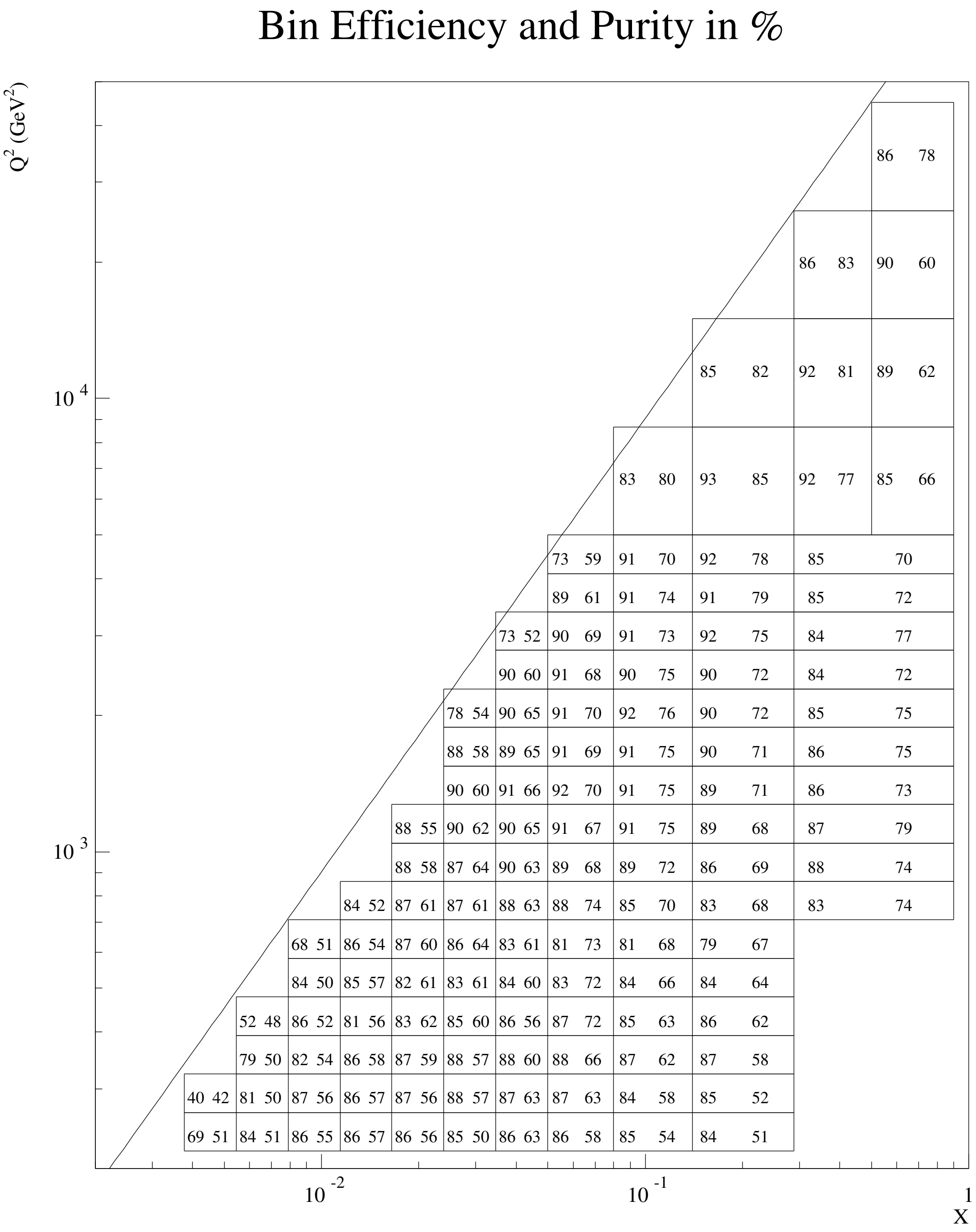

Figure 6.1: Bin efficiency and purity for all selected bins based on MC. Note only a few bins at high y do not meet the good quality criteria of $A > 0.5$ and $P > 0.5$.

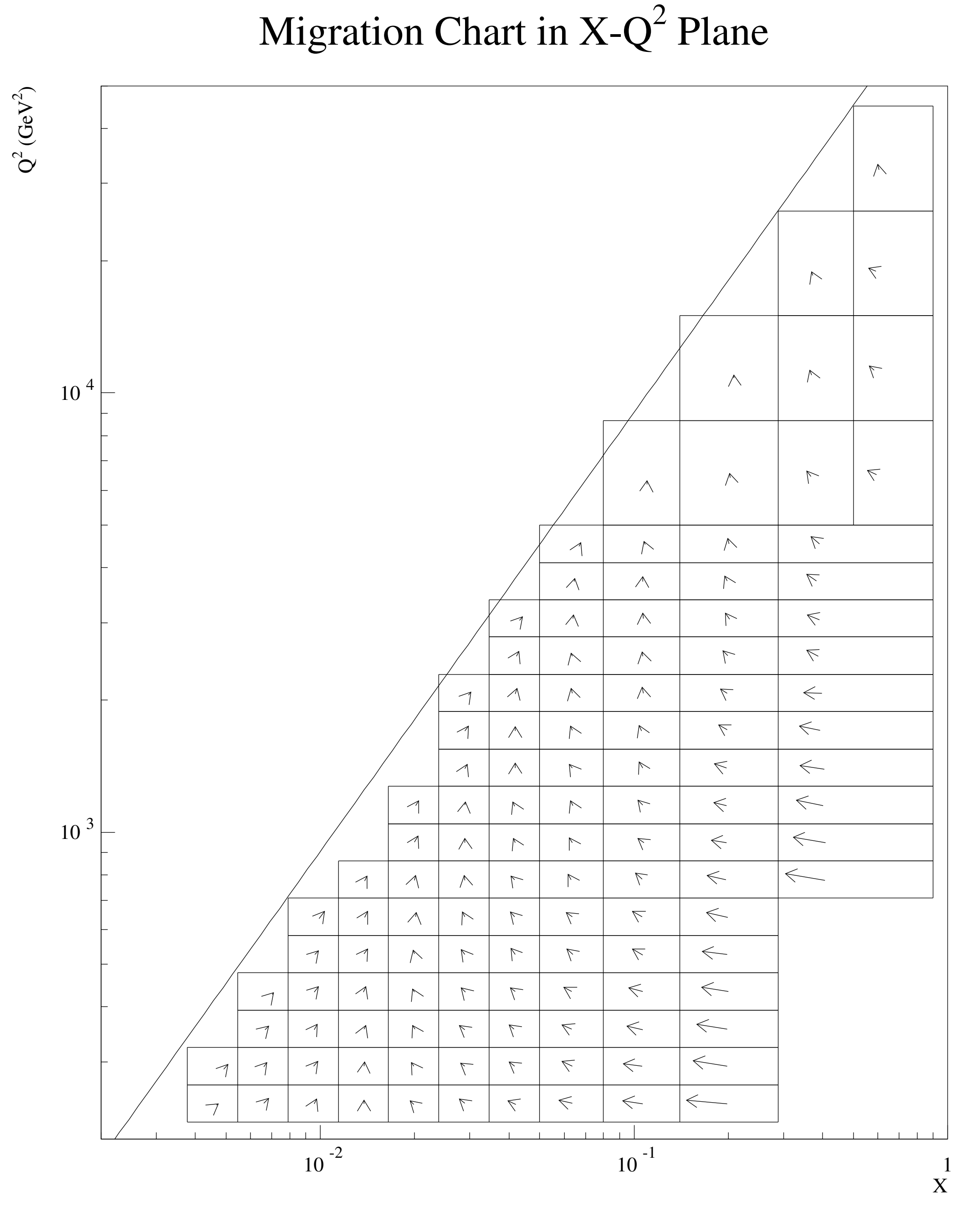

Figure 6.2: Migration Chart in x and Q^2 plane. The base of the arrow is at average Monte Carlo generated x_{true}, Q^2_{true} value for a bin, the head of the arrow is at average reconstructed x_{rec}, Q^2_{rec} value for that bin. Note that migration is more pronounced at low y.

6.2 Iterative Procedure to get $d^2\sigma/dxdQ^2$

We extract $d^2\sigma/dxdQ^2$ from the measured cross section in each bin in an iterative procedure. In each step of the iteration the double-differential cross section in each bin can be obtained by the ratio of observed events in the data to the number of events observed in the MC simulation and the MC double-differential cross section in that bin.

$$\frac{d^2\sigma}{dxdQ^2}^{Data}(\bar{x},\bar{Q^2})(bin) = \frac{N^{Data}(bin)}{\frac{L^{Data}}{L^{MC}} \cdot N^{MC}(bin)} \cdot \frac{d^2\sigma}{dxdQ^2}^{MC}(\bar{x},\bar{Q^2})(bin) \tag{6.3}$$

where $N^{Data}(bin)$ is the number of data events in each bin, $N^{MC}(bin)$ the number of MC events in that bin after full detector simulation, which is then weighted by the ratio of the luminosity of data to that of MC sample, L^{Data}/L^{MC}. The double-differential cross section $\frac{d^2\sigma}{dxdQ^2}^{MC}(\bar{x},\bar{Q^2})(bin)$ is evaluated at the mean values $\bar{x}$ and $\bar{Q^2}$ in each bin and is used in the MC simulation, adjusted in each step of the iteration.

In the first step the acceptance correction is taken from the MC simulation which uses the CTEQ4 parton distribution functions. The result of double- differential cross section from the first iteration is used for a QCD NLO fit. Then this QCD NLO fit is used to recalculate the MC cross sections, the MC events are reweighted by the ratio of this recalculated cross section and the old MC cross section. This reweighted MC is then used again to perform the acceptance correction to the data bin by bin, resulting in a new value of double-differential cross section, specified at the mean values of x and Q^2 in each bin. The procedure is repeated until the double- differential cross sections from two consective steps change by less than 1%. The final result is reached in 5 iterations. The functional form of the QCD NLO fit is used to quote the result of double-differential cross sections at x and Q^2 values of choice of convenience. The QCD NLO fit is used only as a means to obtain a stable and smooth acceptance correction.

The statistical errors of the double-differential cross sections are calculated from the number of data events measured in the bins, and the statistical errors from the MC simulation:

$$\frac{\sigma_{stat}(bin)}{double-differential(bin)} = \sqrt{(\frac{\sqrt{N^{Data}(bin)}}{N^{Data}(bin)})^2 + (\frac{\sqrt{N^{MC}(bin)}}{N^{MC}(bin)})^2} \tag{6.4}$$

where $N^{Data}(bin)$ and $N^{MC}(bin)$ are the same as before. The correlations of statistical errors between different bins are small given the relatively large MC sample used.

6.3 Results

The plots of double-differential cross sections are shown in Figure 6.3, Figure 6.4, Figure 6.5, Figure 6.6 and Figure 6.7. Please note that the plotted values are the double-differential cross sections taken out the kinematic factor $\frac{2\pi\alpha^2}{xQ^4}$, for easy plotting and comparison. The values of $\mathrm{d}^2\sigma/\mathrm{d}x\mathrm{d}Q^2$ are given in Table 6.3, Table 6.3, Table 6.3 and Table 6.3, together with systematic and statistical uncertainties. Also shown in the tables are the number of events and the estimated number of background events in each bin.

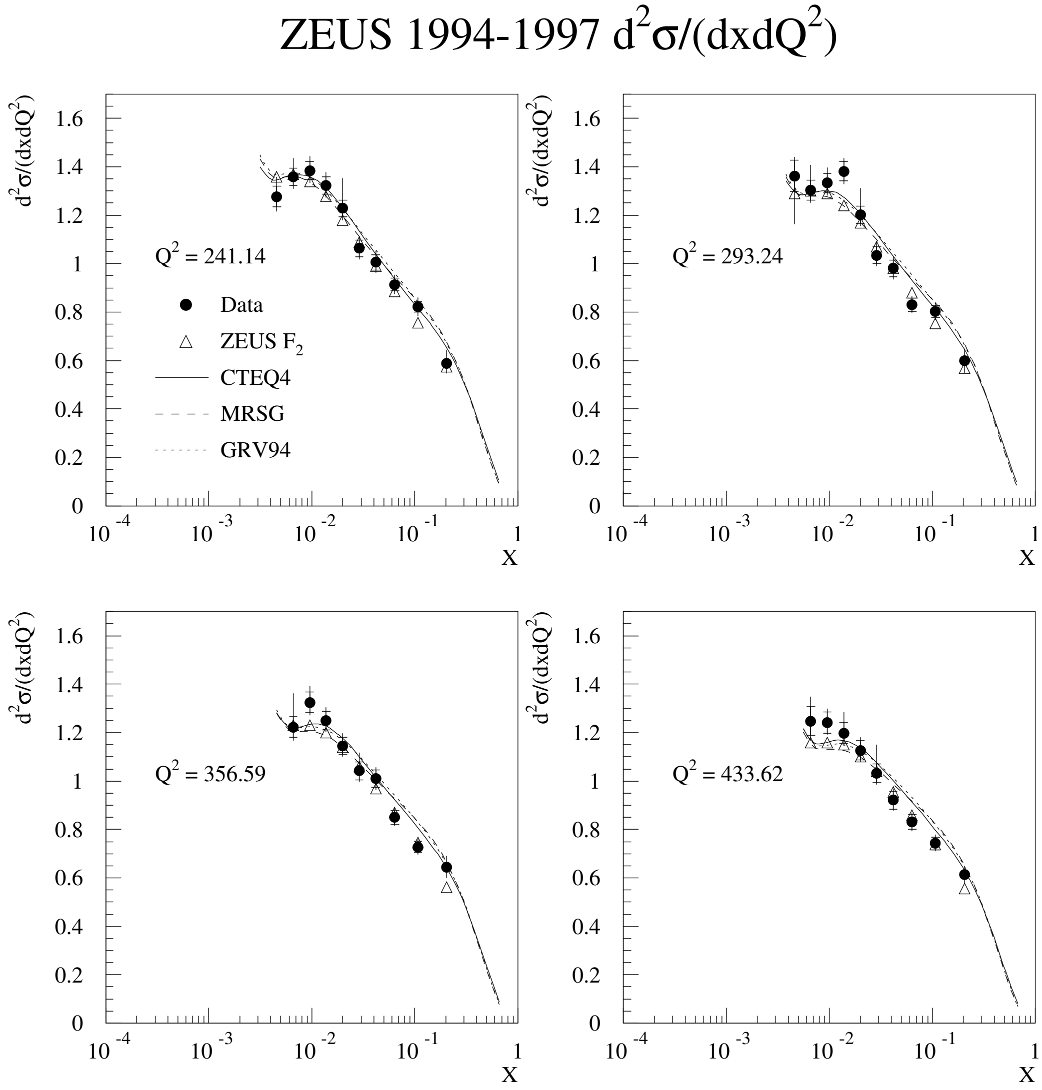

Figure 6.3: Double-differential cross section as a function of x in different Q^2 bins, the inner error bars being the statistical errors, while the whole error bars being the statistical and systematic errors added in quadrature. Also shown are theoretical curves from different parton distribution function parametrisations.

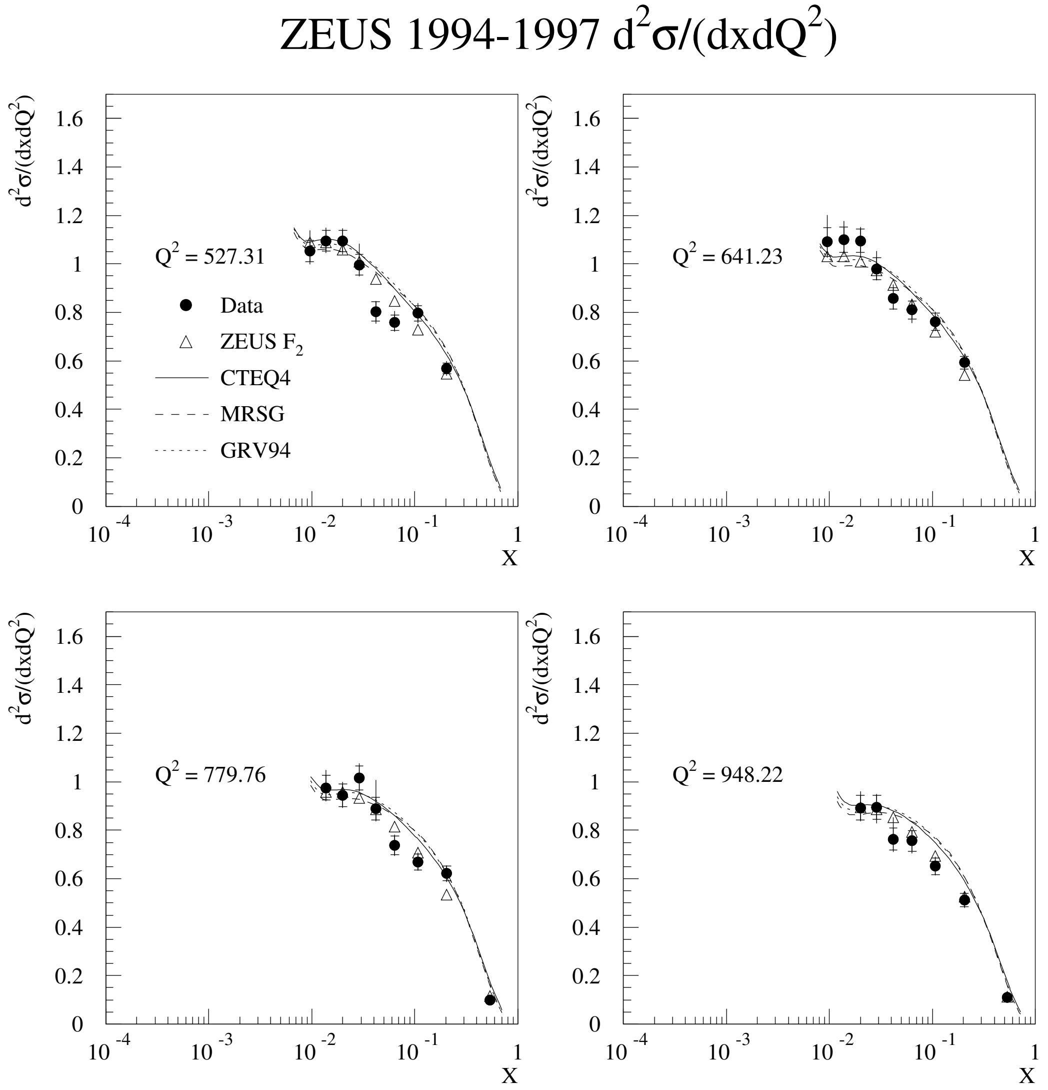

Figure 6.4: Double-differential cross section as a function of x in different Q^2 bins. Also shown are theoretical curves from different parton distribution function parametrisations.

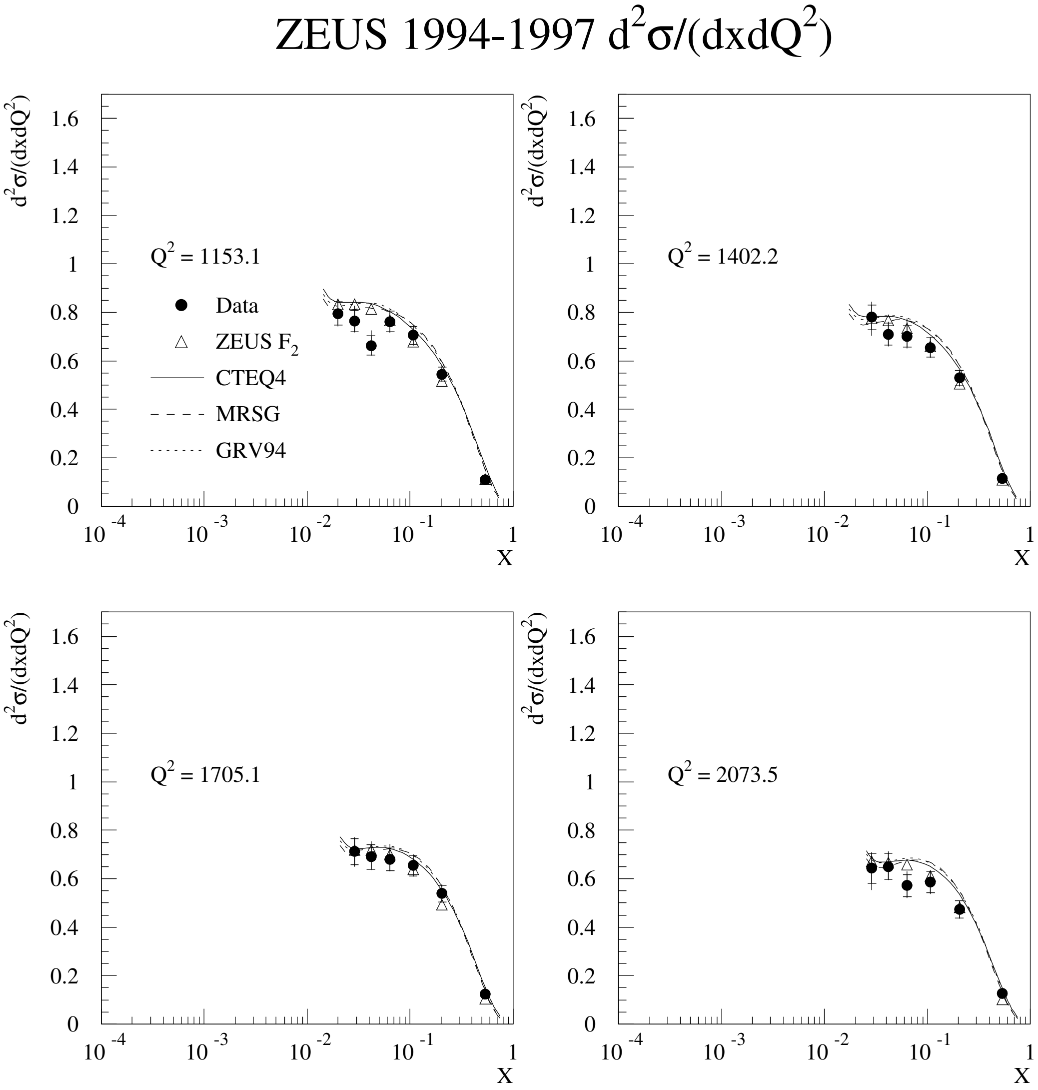

Figure 6.5: Double-differential cross section as a function of x in different Q^2 bins. Also shown are theoretical curves from different parton distribution function parametrisations.

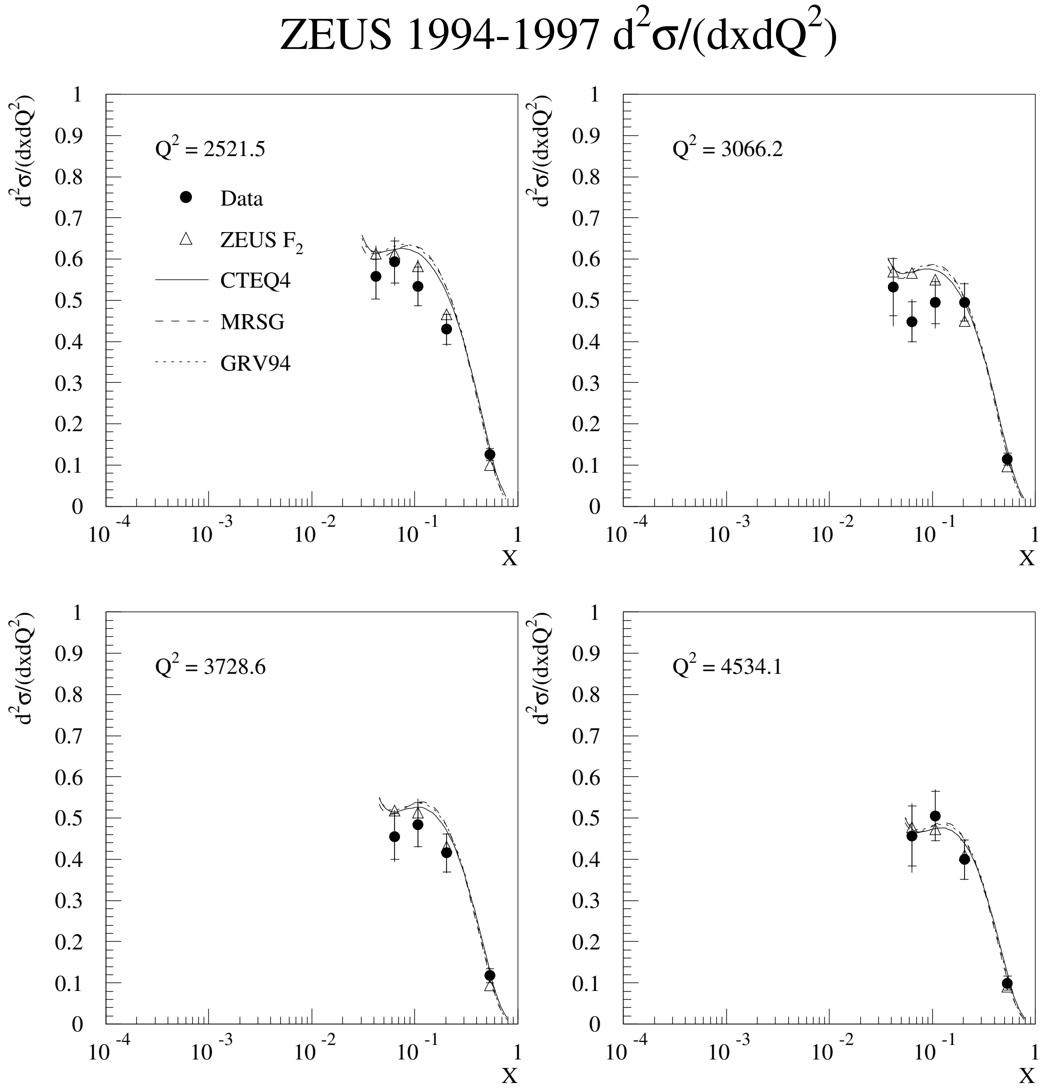

Figure 6.6: Double-differential cross section as a function of x in different Q^2 bins. Also shown are theoretical curves from different parton distribution function parametrisations.

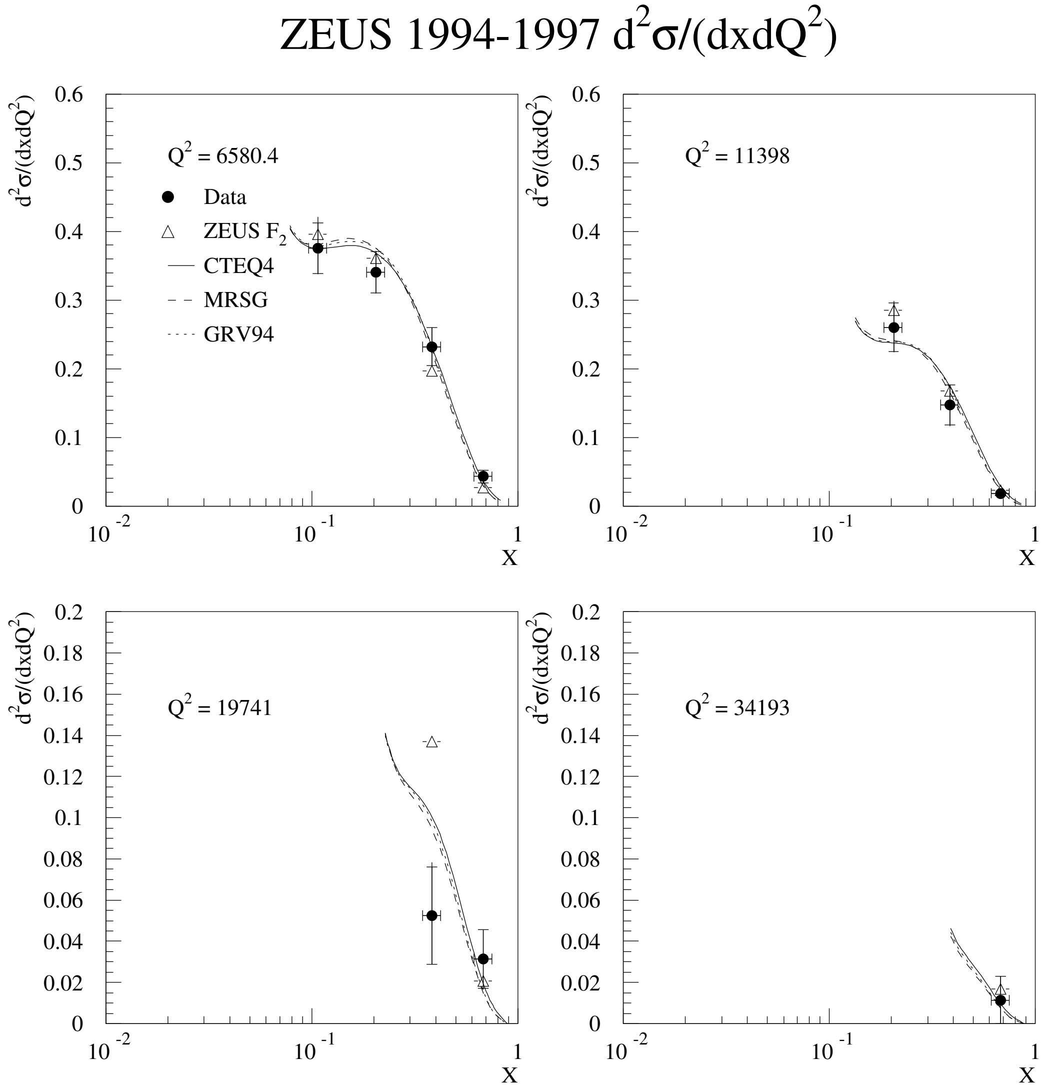

Figure 6.7: Double-differential cross section as a function of x in different Q^2 bins. Also shown are theoretical curves from different parton distribution function parametrisations.

To see the Bjorken scaling effect, the data are also plotted at fixed x as a function of Q^2. They are shown in Figure 6.8, Figure 6.9, Figure 6.10 and Figure 6.11.

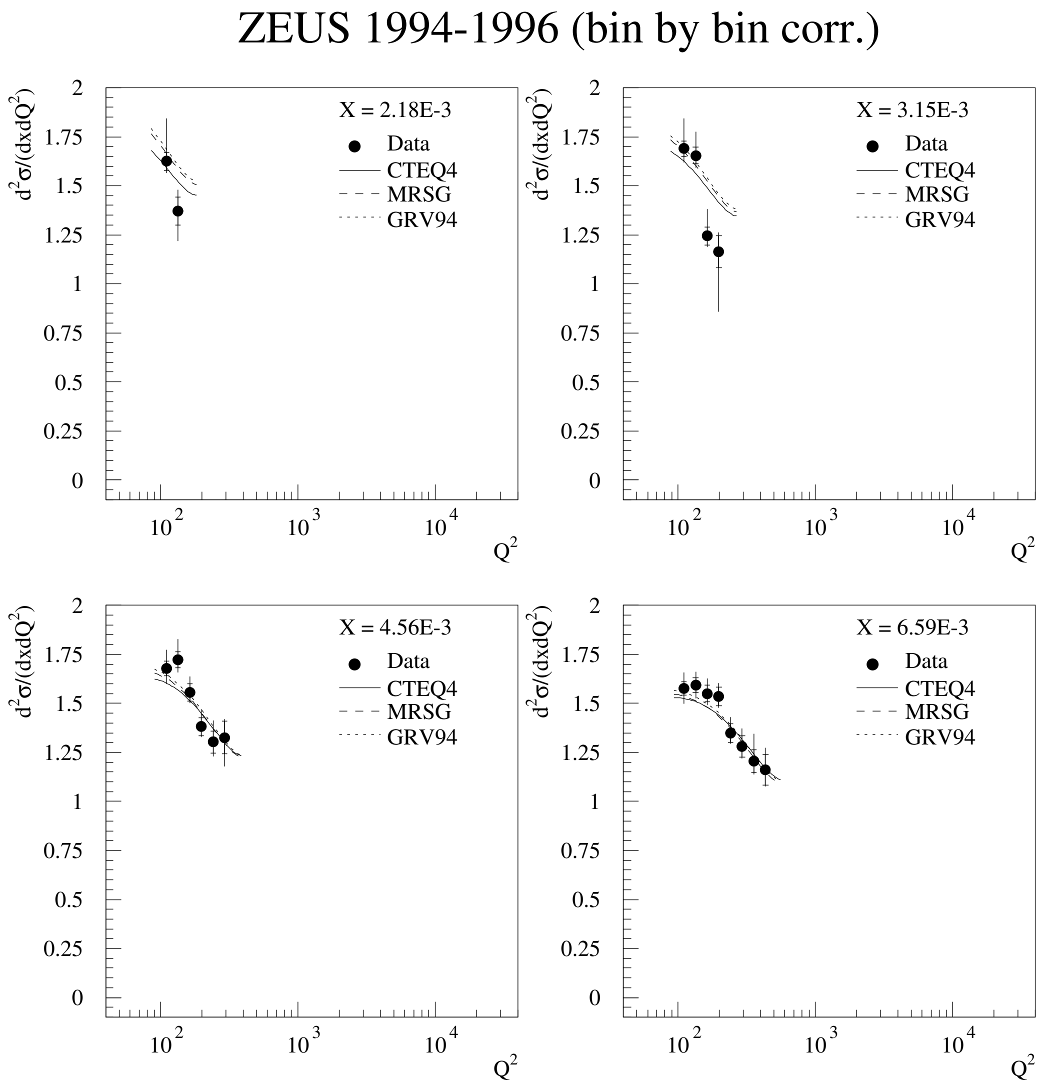

Figure 6.8: Double-differential cross section as a function of Q^2 in different x bins. Also shown are theoretical curves from different parton distribution function parametrisations.

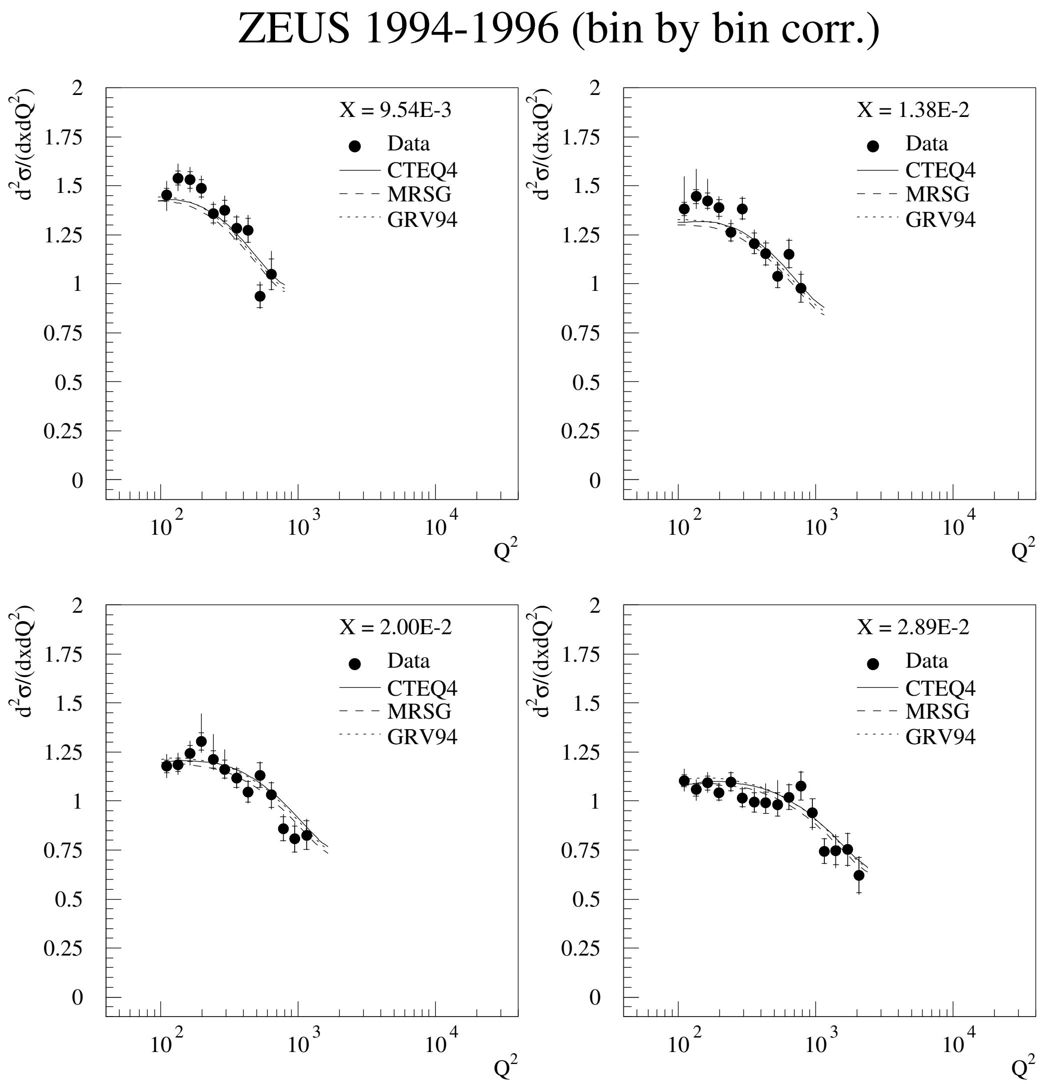

Figure 6.9: Double-differential cross section as a function of Q^2 in different x bins. Also shown are theoretical curves from different parton distribution function parametrisations.

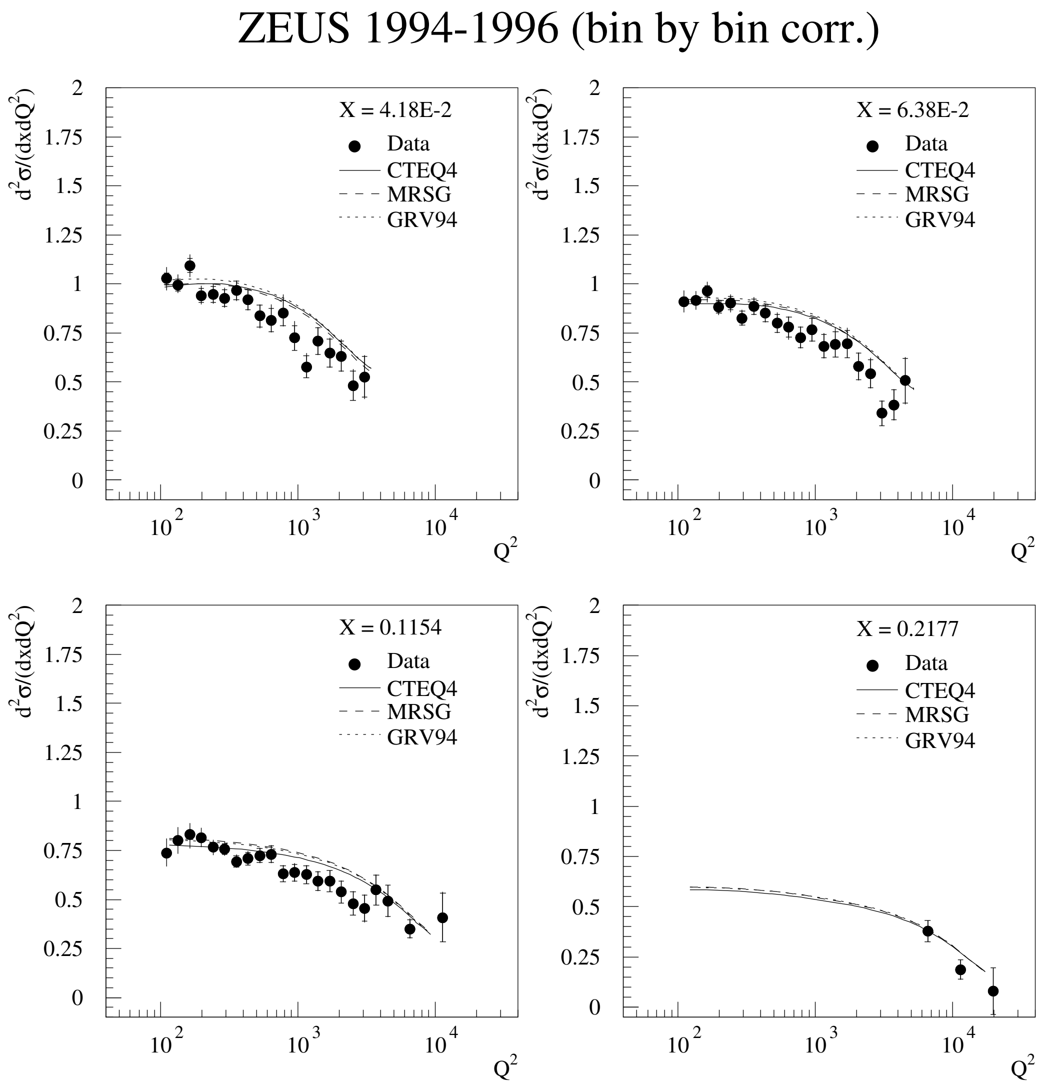

Figure 6.10: Double-differential cross section as a function of Q^2 in different x bins. Also shown are theoretical curves from different parton distribution function parametrisations.

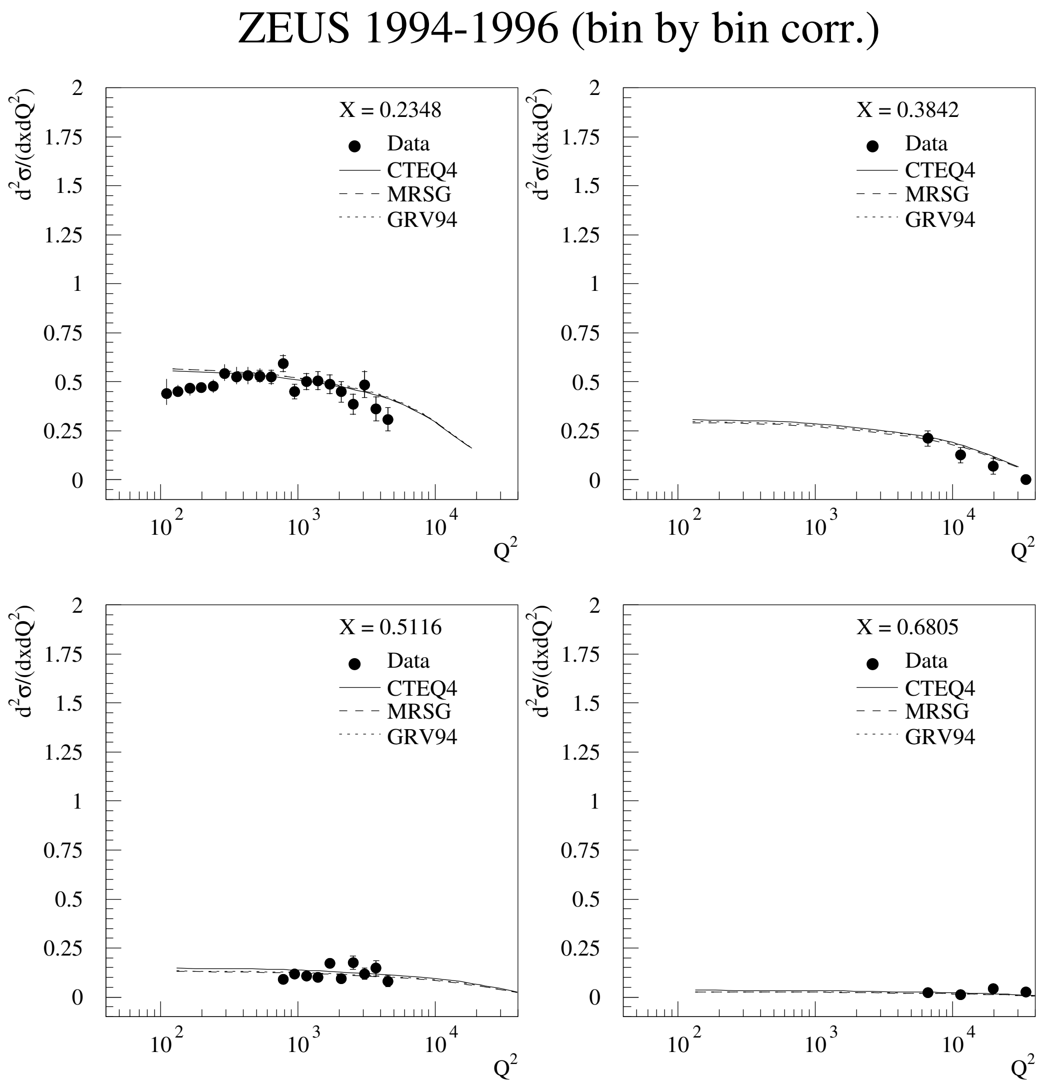

Figure 6.11: Double-differential cross section as a function of Q^2 in different x bins. Also shown are theoretical curves from different parton distribution function parametrisations.

Table 6.1: The measured $d^2\sigma/dxdQ^2$ values. The values of x and Q^2 at which $d^2\sigma/dxdQ^2$ is determined are shown outside the parenthesis, while the bin boundaries are shown inside the parenthesis. The number of events in each bin as well as the estimated number of background events are also given.

i_x	i_{Q^2}	x (range)	N_{ev}	N_{bg}	$d^2\sigma/dxdQ^2$ $\pm stat^{+sys}_{-sys}$
$Q^2 = 241.1$ (218.7 - 265.9)					
1	1	$4.56(3.77\text{-}5.45)10^{-3}$	????	??	$1.277 \pm 0.042^{+0.070}_{-0.046}$
2	1	$6.59(5.45\text{-}7.89)10^{-3}$	????	??	$1.359 \pm 0.036^{+0.066}_{-0.033}$
3	1	$9.54(7.89\text{-}11.4)10^{-3}$	????	??	$1.385 \pm 0.036^{+0.049}_{-0.035}$
4	1	$1.38(1.14\text{-}1.65)10^{-2}$	????	??	$1.323 \pm 0.035^{+0.044}_{-0.034}$
5	1	$2.00(1.65\text{-}2.39)10^{-2}$	????	??	$1.229 \pm 0.035^{+0.120}_{-0.035}$
6	1	$2.89(2.39\text{-}3.46)10^{-2}$	????	??	$1.063 \pm 0.034^{+0.033}_{-0.031}$
7	1	$4.18(3.46\text{-}5.00)10^{-2}$	????	??	$1.005 \pm 0.032^{+0.037}_{-0.029}$
8	1	$6.38(5.00\text{-}8.00)10^{-2}$	????	??	$0.913 \pm 0.026^{+0.033}_{-0.029}$
9	1	$1.07(0.80\text{-}1.40)10^{-1}$	????	??	$0.822 \pm 0.023^{+0.032}_{-0.033}$
10	1	$2.05(1.40\text{-}2.88)10^{-1}$	????	??	$0.589 \pm 0.016^{+0.053}_{-0.039}$
$Q^2 = 293.2$ (265.9 - 323.4)					
1	2	$4.56(3.77\text{-}5.45)10^{-3}$	????	??	$1.363 \pm 0.064^{+0.048}_{-0.189}$
2	2	$6.59(5.45\text{-}7.89)10^{-3}$	????	??	$1.303 \pm 0.041^{+0.098}_{-0.033}$
3	2	$9.54(7.89\text{-}11.4)10^{-3}$	????	??	$1.333 \pm 0.039^{+0.053}_{-0.034}$
4	2	$1.38(1.14\text{-}1.65)10^{-2}$	????	??	$1.381 \pm 0.040^{+0.039}_{-0.033}$
5	2	$2.00(1.65\text{-}2.39)10^{-2}$	????	??	$1.201 \pm 0.036^{+0.104}_{-0.027}$
6	2	$2.89(2.39\text{-}3.46)10^{-2}$	????	??	$1.035 \pm 0.035^{+0.041}_{-0.027}$
7	2	$4.18(3.46\text{-}5.00)10^{-2}$	????	??	$0.980 \pm 0.033^{+0.036}_{-0.031}$
8	2	$6.38(5.00\text{-}8.00)10^{-2}$	????	??	$0.830 \pm 0.027^{+0.025}_{-0.020}$
9	2	$1.07(0.80\text{-}1.40)10^{-1}$	????	??	$0.803 \pm 0.024^{+0.030}_{-0.026}$
10	2	$2.05(1.40\text{-}2.88)10^{-1}$	????	??	$0.598 \pm 0.017^{+0.047}_{-0.045}$
$Q^2 = 356.6$ (323.4 - 393.2)					
2	3	$6.59(5.45\text{-}7.89)10^{-3}$	????	??	$1.222 \pm 0.042^{+0.134}_{-0.035}$
3	3	$9.54(7.89\text{-}11.4)10^{-3}$	????	??	$1.324 \pm 0.042^{+0.055}_{-0.032}$
4	3	$1.38(1.14\text{-}1.65)10^{-2}$	????	??	$1.250 \pm 0.039^{+0.038}_{-0.028}$
5	3	$2.00(1.65\text{-}2.39)10^{-2}$	????	??	$1.146 \pm 0.036^{+0.037}_{-0.029}$
6	3	$2.89(2.39\text{-}3.46)10^{-2}$	????	??	$1.043 \pm 0.037^{+0.066}_{-0.026}$
7	3	$4.18(3.46\text{-}5.00)10^{-2}$	????	??	$1.010 \pm 0.036^{+0.029}_{-0.032}$
8	3	$6.38(5.00\text{-}8.00)10^{-2}$	????	??	$0.849 \pm 0.028^{+0.029}_{-0.019}$
9	3	$1.07(0.80\text{-}1.40)10^{-1}$	????	??	$0.728 \pm 0.024^{+0.024}_{-0.020}$
10	3	$2.05(1.40\text{-}2.88)10^{-1}$	????	??	$0.645 \pm 0.019^{+0.042}_{-0.042}$

Table 6.2: (continued) The measured $\mathrm{d}^2\sigma/\mathrm{d}x\mathrm{d}Q^2$ values.

i_x	i_{Q^2}	x (range)	N_{ev}	N_{bg}	$\mathrm{d}^2\sigma/\mathrm{d}x\mathrm{d}Q^2$ $\pm stat^{+sys}_{-sys}$
$Q^2 = 433.6$ (393.2 - 478.2)					
2	4	$6.59(5.45\text{-}7.89)10^{-3}$	????	??	$1.248 \pm 0.059^{+0.081}_{-0.057}$
3	4	$9.54(7.89\text{-}11.4)10^{-3}$	????	??	$1.242 \pm 0.044^{+0.038}_{-0.028}$
4	4	$1.38(1.14\text{-}1.65)10^{-2}$	????	??	$1.198 \pm 0.042^{+0.077}_{-0.033}$
5	4	$2.00(1.65\text{-}2.39)10^{-2}$	????	??	$1.126 \pm 0.040^{+0.037}_{-0.027}$
6	4	$2.89(2.39\text{-}3.46)10^{-2}$	????	??	$1.032 \pm 0.039^{+0.112}_{-0.023}$
7	4	$4.18(3.46\text{-}5.00)10^{-2}$	????	??	$0.921 \pm 0.037^{+0.031}_{-0.029}$
8	4	$6.38(5.00\text{-}8.00)10^{-2}$	????	??	$0.832 \pm 0.030^{+0.024}_{-0.024}$
9	4	$1.07(0.80\text{-}1.40)10^{-1}$	????	??	$0.742 \pm 0.026^{+0.025}_{-0.017}$
10	4	$2.05(1.40\text{-}2.88)10^{-1}$	????	??	$0.615 \pm 0.021^{+0.029}_{-0.029}$
$Q^2 = 527.3$ (478.2 - 581.5)					
3	5	$9.54(7.89\text{-}11.4)10^{-3}$	????	??	$1.054 \pm 0.044^{+0.072}_{-0.033}$
4	5	$1.38(1.14\text{-}1.65)10^{-2}$	????	??	$1.096 \pm 0.043^{+0.035}_{-0.028}$
5	5	$2.00(1.65\text{-}2.39)10^{-2}$	????	??	$1.094 \pm 0.044^{+0.028}_{-0.031}$
6	5	$2.89(2.39\text{-}3.46)10^{-2}$	????	??	$0.997 \pm 0.043^{+0.076}_{-0.022}$
7	5	$4.18(3.46\text{-}5.00)10^{-2}$	????	??	$0.804 \pm 0.039^{+0.020}_{-0.030}$
8	5	$6.38(5.00\text{-}8.00)10^{-2}$	????	??	$0.757 \pm 0.032^{+0.038}_{-0.019}$
9	5	$1.07(0.80\text{-}1.40)10^{-1}$	????	??	$0.797 \pm 0.031^{+0.026}_{-0.025}$
10	5	$2.05(1.40\text{-}2.88)10^{-1}$	????	??	$0.569 \pm 0.022^{+0.019}_{-0.020}$
$Q^2 = 641.2$ (581.5 - 707.1)					
3	6	$9.54(7.89\text{-}11.4)10^{-3}$	????	??	$1.090 \pm 0.058^{+0.096}_{-0.029}$
4	6	$1.38(1.14\text{-}1.65)10^{-2}$	????	??	$1.101 \pm 0.053^{+0.055}_{-0.029}$
5	6	$2.00(1.65\text{-}2.39)10^{-2}$	????	??	$1.095 \pm 0.047^{+0.031}_{-0.046}$
6	6	$2.89(2.39\text{-}3.46)10^{-2}$	????	??	$0.980 \pm 0.044^{+0.060}_{-0.021}$
7	6	$4.18(3.46\text{-}5.00)10^{-2}$	????	??	$0.858 \pm 0.044^{+0.038}_{-0.019}$
8	6	$6.38(5.00\text{-}8.00)10^{-2}$	????	??	$0.810 \pm 0.038^{+0.022}_{-0.038}$
9	6	$1.07(0.80\text{-}1.40)10^{-1}$	????	??	$0.761 \pm 0.035^{+0.025}_{-0.016}$
10	6	$2.05(1.40\text{-}2.88)10^{-1}$	????	??	$0.593 \pm 0.026^{+0.020}_{-0.016}$
$Q^2 = 779.8$ (707.1 - 859.9)					
4	7	$1.38(1.14\text{-}1.65)10^{-2}$	????	??	$0.975 \pm 0.051^{+0.054}_{-0.022}$
5	7	$2.00(1.65\text{-}2.39)10^{-2}$	????	??	$0.944 \pm 0.047^{+0.028}_{-0.021}$
6	7	$2.89(2.39\text{-}3.46)10^{-2}$	????	??	$1.015 \pm 0.050^{+0.034}_{-0.022}$
7	7	$4.18(3.46\text{-}5.00)10^{-2}$	????	??	$0.889 \pm 0.048^{+0.107}_{-0.020}$
8	7	$6.38(5.00\text{-}8.00)10^{-2}$	????	??	$0.737 \pm 0.038^{+0.022}_{-0.020}$
9	7	$1.07(0.80\text{-}1.40)10^{-1}$	????	??	$0.670 \pm 0.033^{+0.018}_{-0.015}$
10	7	$2.05(1.40\text{-}2.88)10^{-1}$	????	??	$0.621 \pm 0.030^{+0.016}_{-0.019}$
11	7	$5.37(2.88\text{-}9.00)10^{-1}$	????	??	$0.098 \pm 0.0082^{+0.0025}_{-0.0040}$

Table 6.3: (continued) The measured $\mathrm{d}^2\sigma/\mathrm{d}x\mathrm{d}Q^2$ values.

i_x	i_{Q^2}	x (range)	N_{ev}	N_{bg}	$\mathrm{d}^2\sigma/\mathrm{d}x\mathrm{d}Q^2$ $\pm stat^{+sys}_{-sys}$
Q^2 = 948.2 (859.9 - 1045.6)					
5	8	$2.00(1.65\text{-}2.39)10^{-2}$	????	??	$0.893\ \pm 0.051^{+0.045}_{-0.027}$
6	8	$2.89(2.39\text{-}3.46)10^{-2}$	????	??	$0.895\ \pm 0.050^{+0.020}_{-0.043}$
7	8	$4.18(3.46\text{-}5.00)10^{-2}$	????	??	$0.763\ \pm 0.045^{+0.079}_{-0.026}$
8	8	$6.38(5.00\text{-}8.00)10^{-2}$	????	??	$0.756\ \pm 0.042^{+0.017}_{-0.028}$
9	8	$1.07(0.80\text{-}1.40)10^{-1}$	????	??	$0.652\ \pm 0.035^{+0.021}_{-0.017}$
10	8	$2.05(1.40\text{-}2.88)10^{-1}$	????	??	$0.511\ \pm 0.028^{+0.017}_{-0.014}$
11	8	$5.37(2.88\text{-}9.00)10^{-1}$	????	??	$0.111\ \pm 0.0089^{+0.0033}_{-0.0052}$
Q^2 = 1153.1 (1045.6 - 1271.5)					
5	9	$2.00(1.65\text{-}2.39)10^{-2}$	????	??	$0.796\ \pm 0.048^{+0.037}_{-0.025}$
6	9	$2.89(2.39\text{-}3.46)10^{-2}$	????	??	$0.765\ \pm 0.044^{+0.046}_{-0.017}$
7	9	$4.18(3.46\text{-}5.00)10^{-2}$	????	??	$0.663\ \pm 0.040^{+0.047}_{-0.014}$
8	9	$6.38(5.00\text{-}8.00)10^{-2}$	????	??	$0.762\ \pm 0.042^{+0.025}_{-0.024}$
9	9	$1.07(0.80\text{-}1.40)10^{-1}$	????	??	$0.705\ \pm 0.037^{+0.020}_{-0.020}$
10	9	$2.05(1.40\text{-}2.88)10^{-1}$	????	??	$0.545\ \pm 0.029^{+0.023}_{-0.011}$
11	9	$5.37(2.88\text{-}9.00)10^{-1}$	????	??	$0.109\ \pm 0.0091^{+0.0027}_{-0.0055}$
Q^2 = 1402.2 (1271.5 - 1546.3)					
6	10	$2.89(2.39\text{-}3.46)10^{-2}$	????	??	$0.780\ \pm 0.050^{+0.040}_{-0.059}$
7	10	$4.18(3.46\text{-}5.00)10^{-2}$	????	??	$0.710\ \pm 0.046^{+0.021}_{-0.023}$
8	10	$6.38(5.00\text{-}8.00)10^{-2}$	????	??	$0.700\ \pm 0.044^{+0.061}_{-0.022}$
9	10	$1.07(0.80\text{-}1.40)10^{-1}$	????	??	$0.655\ \pm 0.039^{+0.020}_{-0.016}$
10	10	$2.05(1.40\text{-}2.88)10^{-1}$	????	??	$0.529\ \pm 0.031^{+0.015}_{-0.014}$
11	10	$5.37(2.88\text{-}9.00)10^{-1}$	????	??	$0.114\ \pm 0.010^{+0.0029}_{-0.0050}$
Q^2 = 1705.1 (1546.3 - 1880.3)					
6	11	$2.89(2.39\text{-}3.46)10^{-2}$	????	??	$0.712\ \pm 0.054^{+0.022}_{-0.034}$
7	11	$4.18(3.46\text{-}5.00)10^{-2}$	????	??	$0.690\ \pm 0.051^{+0.040}_{-0.016}$
8	11	$6.38(5.00\text{-}8.00)10^{-2}$	????	??	$0.679\ \pm 0.047^{+0.042}_{-0.017}$
9	11	$1.07(0.80\text{-}1.40)10^{-1}$	????	??	$0.654\ \pm 0.042^{+0.020}_{-0.014}$
10	11	$2.05(1.40\text{-}2.88)10^{-1}$	????	??	$0.539\ \pm 0.035^{+0.016}_{-0.018}$
11	11	$5.37(2.88\text{-}9.00)10^{-1}$	????	??	$0.123\ \pm 0.011^{+0.0056}_{-0.0032}$
Q^2 = 2073.5 (1880.3 - 2286.5)					
6	12	$2.89(2.39\text{-}3.46)10^{-2}$	????	??	$0.643\ \pm 0.061^{+0.025}_{-0.066}$
7	12	$4.18(3.46\text{-}5.00)10^{-2}$	????	??	$0.650\ \pm 0.053^{+0.034}_{-0.019}$
8	12	$6.38(5.00\text{-}8.00)10^{-2}$	????	??	$0.571\ \pm 0.045^{+0.039}_{-0.024}$
9	12	$1.07(0.80\text{-}1.40)10^{-1}$	????	??	$0.586\ \pm 0.045^{+0.017}_{-0.018}$
10	12	$2.05(1.40\text{-}2.88)10^{-1}$	????	??	$0.473\ \pm 0.035^{+0.011}_{-0.014}$
11	12	$5.37(2.88\text{-}9.00)10^{-1}$	????	??	$0.126\ \pm 0.013^{+0.0032}_{-0.0070}$

Table 6.4: (continued) The measured $\mathrm{d}^2\sigma/\mathrm{d}x\mathrm{d}Q^2$ values.

i_x	i_{Q^2}	x (range)	N_{ev}	N_{bg}	$\mathrm{d}^2\sigma/\mathrm{d}x\mathrm{d}Q^2 \pm stat^{+sys}_{-sys}$
$Q^2 = 2521.5$ (2286.5 - 2780.5)					
7	13	$4.18(3.46\text{-}5.00)10^{-2}$	????	??	$0.558 \pm 0.054^{+0.052}_{-0.013}$
8	13	$6.38(5.00\text{-}8.00)10^{-2}$	????	??	$0.593 \pm 0.051^{+0.032}_{-0.028}$
9	13	$1.07(0.80\text{-}1.40)10^{-1}$	????	??	$0.534 \pm 0.047^{+0.043}_{-0.011}$
10	13	$2.05(1.40\text{-}2.88)10^{-1}$	????	??	$0.429 \pm 0.037^{+0.013}_{-0.012}$
11	13	$5.37(2.88\text{-}9.00)10^{-1}$	????	??	$0.126 \pm 0.015^{+0.0029}_{-0.0073}$
$Q^2 = 3066.2$ (2780.5 - 3381.2)					
7	14	$4.18(3.46\text{-}5.00)10^{-2}$	????	??	$0.532 \pm 0.070^{+0.016}_{-0.066}$
8	14	$6.38(5.00\text{-}8.00)10^{-2}$	????	??	$0.448 \pm 0.048^{+0.025}_{-0.014}$
9	14	$1.07(0.80\text{-}1.40)10^{-1}$	????	??	$0.495 \pm 0.051^{+0.029}_{-0.036}$
10	14	$2.05(1.40\text{-}2.88)10^{-1}$	????	??	$0.495 \pm 0.045^{+0.021}_{-0.010}$
11	14	$5.37(2.88\text{-}9.00)10^{-1}$	????	??	$0.114 \pm 0.015^{+0.0027}_{-0.0079}$
$Q^2 = 3728.6$ (3381.2 - 4111.7)					
8	15	$6.38(5.00\text{-}8.00)10^{-2}$	????	??	$0.456 \pm 0.056^{+0.033}_{-0.027}$
9	15	$1.07(0.80\text{-}1.40)10^{-1}$	????	??	$0.484 \pm 0.054^{+0.032}_{-0.013}$
10	15	$2.05(1.40\text{-}2.88)10^{-1}$	????	??	$0.415 \pm 0.046^{+0.013}_{-0.018}$
11	15	$5.37(2.88\text{-}9.00)10^{-1}$	????	??	$0.118 \pm 0.017^{+0.0030}_{-0.0039}$
$Q^2 = 4534.1$ (4111.7 - 5000.0)					
8	16	$6.38(5.00\text{-}8.00)10^{-2}$	????	??	$0.456 \pm 0.073^{+0.029}_{-0.052}$
9	16	$1.07(0.80\text{-}1.40)10^{-1}$	????	??	$0.505 \pm 0.060^{+0.025}_{-0.011}$
10	16	$2.05(1.40\text{-}2.88)10^{-1}$	????	??	$0.399 \pm 0.047^{+0.015}_{-0.014}$
11	16	$5.37(2.88\text{-}9.00)10^{-1}$	????	??	$0.099 \pm 0.017^{+0.0037}_{-0.0028}$
$Q^2 = 6580.4$ (5000.0 - 8660.3)					
9	17	$1.07(0.80\text{-}1.40)10^{-1}$	????	??	$0.375 \pm 0.037^{+0.027}_{-0.009}$
10	17	$2.05(1.40\text{-}2.88)10^{-1}$	????	??	$0.341 \pm 0.030^{+0.0088}_{-0.0080}$
12	17	$3.84(2.88\text{-}5.00)10^{-1}$	????	??	$0.232 \pm 0.028^{+0.0063}_{-0.0049}$
13	17	$6.81(5.00\text{-}9.00)10^{-1}$	????	??	$0.043 \pm 0.0093^{+0.0017}_{-0.0039}$
$Q^2 = 11398.0$ (8660.3 - 15000.0)					
10	18	$2.05(1.40\text{-}2.88)10^{-1}$	????	??	$0.260 \pm 0.035^{+0.016}_{-0.0065}$
12	18	$3.84(2.88\text{-}5.00)10^{-1}$	????	??	$0.147 \pm 0.029^{+0.0040}_{-0.0091}$
13	18	$6.81(5.00\text{-}9.00)10^{-1}$	????	??	$0.019 \pm 0.0076^{+0.0005}_{-0.0028}$
$Q^2 = 19741.0$ (15000.0 - 25980.8)					
12	19	$3.84(2.88\text{-}5.00)10^{-1}$	????	??	$0.0526 \pm 0.024^{+0.0104}_{-0.0016}$
13	19	$6.81(5.00\text{-}9.00)10^{-1}$	????	??	$0.0315 \pm 0.014^{+0.0011}_{-0.0048}$
$Q^2 = 19741.0$ (25980.8 - 45000.0)					
13	20	$6.81(5.00\text{-}9.00)10^{-1}$	????	??	$0.0115 \pm 0.0115^{+0.0012}_{-0.0004}$

6.4 Systematic Errors

The systematic errors for the high Q^2 double-differential cross-section are calculated for the following 10 effects:

1. Luminosity.
2. Electron energy scale.
3. Hadronic angle γ_h resolution.
4. Electron angle θ_e resolution.
5. Electron identification inefficiency.
6. Tracking inefficiency.
7. Tracking momentum resolution.
8. Tracking and calorimeter alignment.
9. Calorimeter total p_T resolution.
10. Photoproduction background levels.

6.4.1 Luminosity

The error on the 1994 luminosity values as reported by the luminosity group is 1.5%, for 1995 luminosity it is 2%, and for 1996 luminosity it is 4%, for 1997 luminosity it is 1.5%. An error of 1.5% is assumed here for all 1994-1997 electron data.

6.4.2 Electron energy scale

It has been reported that the ZEUS calorimeter energy response to electrons is off by a few percent in the MC simulation, presumably due to missing dead material and/or overal calibration. This does not pose a serious problem to this analysis because the double-angle method is used to determine x and Q^2. However, it does cause a bias through the event selection (from the electron energy, $E - p_z$, and p_T cuts). To estimate this bias requires some estimate of the error in the simulation.

One method to estimate the error in the simulation of electron energy response is to compare the electron energy measured and the calculated electron energy back from double-angle x and Q^2. Suppose that the double-angle method is unbiased, this can produce a measure of how biased the electron energy measurement is in both data and Monte Carlo:

$$\delta E = E - E_{DA} = E - \frac{Q^2_{DA}}{2A(1+cos\theta)} \tag{6.5}$$

where A is the electron beam energy and θ the electron angle.

A comparison of δE between data and MC for various parts of the calorimeter does indeed show a discrepency. The size of the discrepancy varies according to three major portions of the calorimeter:

- RCAL, radius < 110 cm. Smearing the measured electron energy in MC by 2.5% is required to match the data (Figure 6.12).

- RCAL, radius > 110 cm. Multipling the measured electron energy in MC by 0.99 and smearing it by 4% are required to match the data (Figure 6.13).
- BCAL. Multipling the measured electron energy in MC by 1.015 and smearing it by 4% are requred to match the data (Figure 6.14).
- FCAL. Multipling the measured electron energy in MC by 0.95 is required to match the data (Figure 6.15).

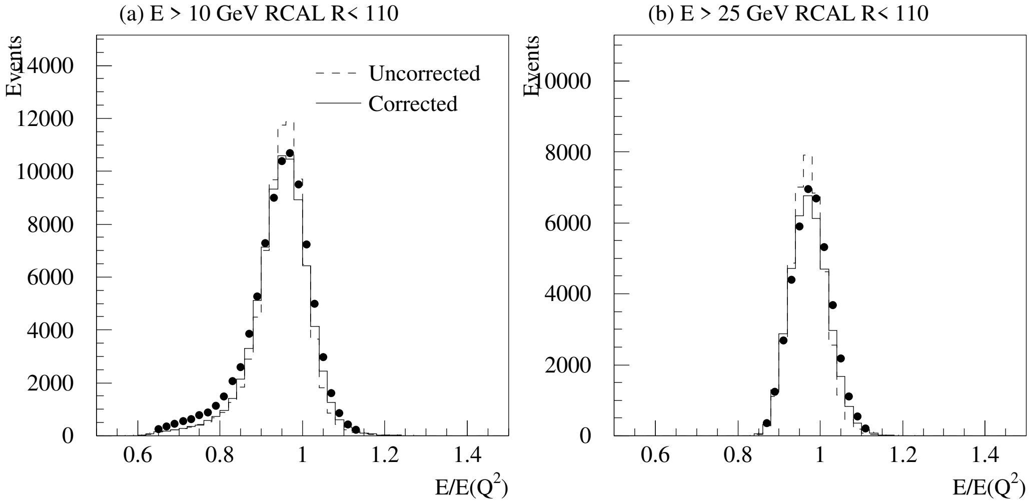

Figure 6.12: Correcting the simulation of electron energy response in the inner portion of the RCAL. Shown are results for (a) electron energy above 10 GeV and (b) electron energy above 25 GeV that impact in the RCAL with $R < 110$ cm. Plotted in points are data, in solid lines are corrected MC, and in dashed lines uncorrected MC.

Correcting the disagreement repairs not only Q_e^2, but also much of the discrepency in the electron energies and $E - p_z$ as shown in Figure 6.16. When applied before event selection, it results in a systematic error less than 1% for almost all the bins (Figure 6.17).

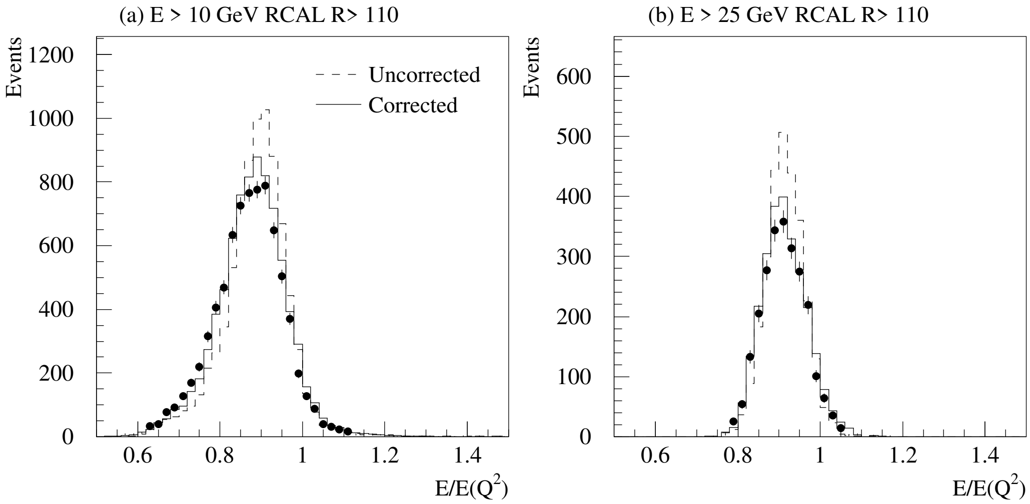

Figure 6.13: Correcting the simulation of electron energy response in the outer portion of the RCAL. Shown are results for (a) electron energy above 10 GeV and (b) electron energy above 25 GeV that impact in the RCAL with $R > 110$ cm. Plotted in points are data, in solid lines are corrected MC, and in dashed lines uncorrected MC.

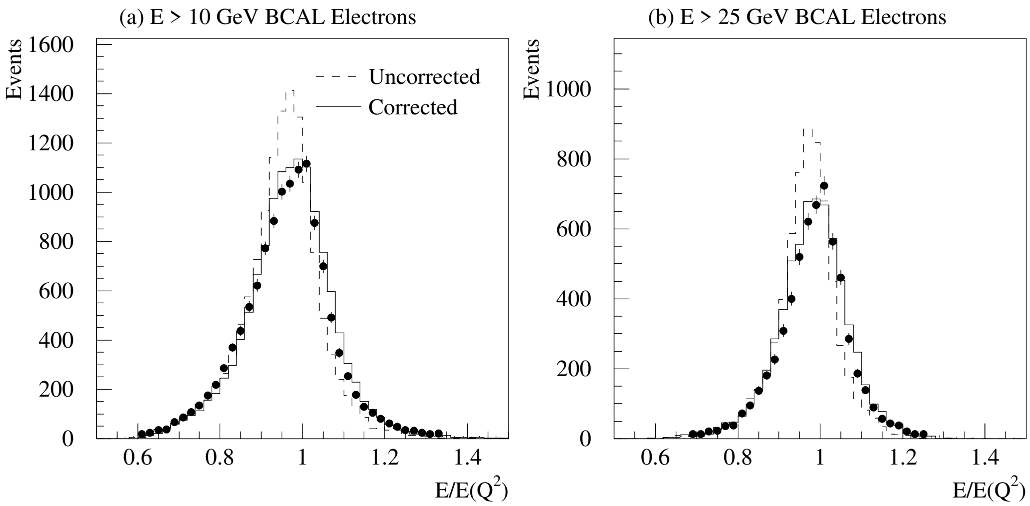

Figure 6.14: Correcting the simulation of electron energy response in the BCAL. Shown are results for (a) electron energy above 10 GeV and (b) electron energy above 25 GeV that impact in the BCAL. Plotted in points are data, in solid lines are corrected MC, and in dashed lines uncorrected MC.

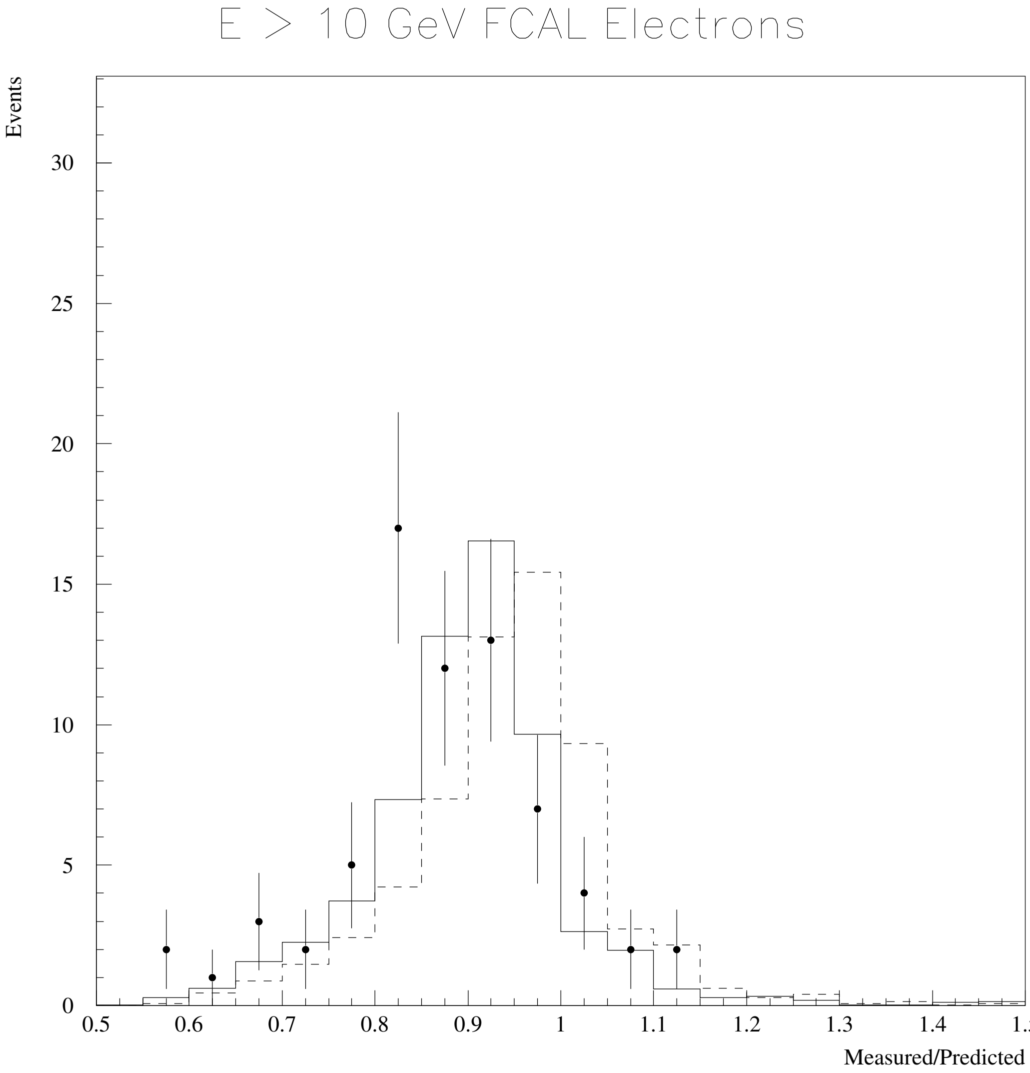

Figure 6.15: Correcting the simulation of electron energy response in the FCAL. Shown are results for electron energy above 10 GeV that impact in the FCAL. Plotted in points are data, in solid lines are corrected MC, and in dashed lines uncorrected MC.

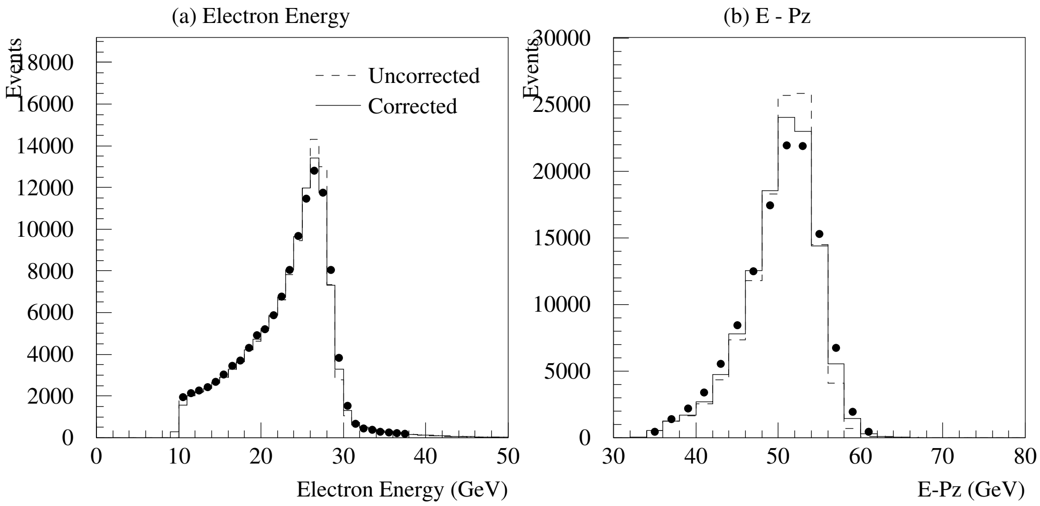

Figure 6.16: Results of correcting Monte Carlo electron energy response. Shown are (a) electron energy and (b) $E - p_z$ of all selected events. Plotted in points are data, in solid lines are corrected MC, and in dashed lines uncorrected MC.

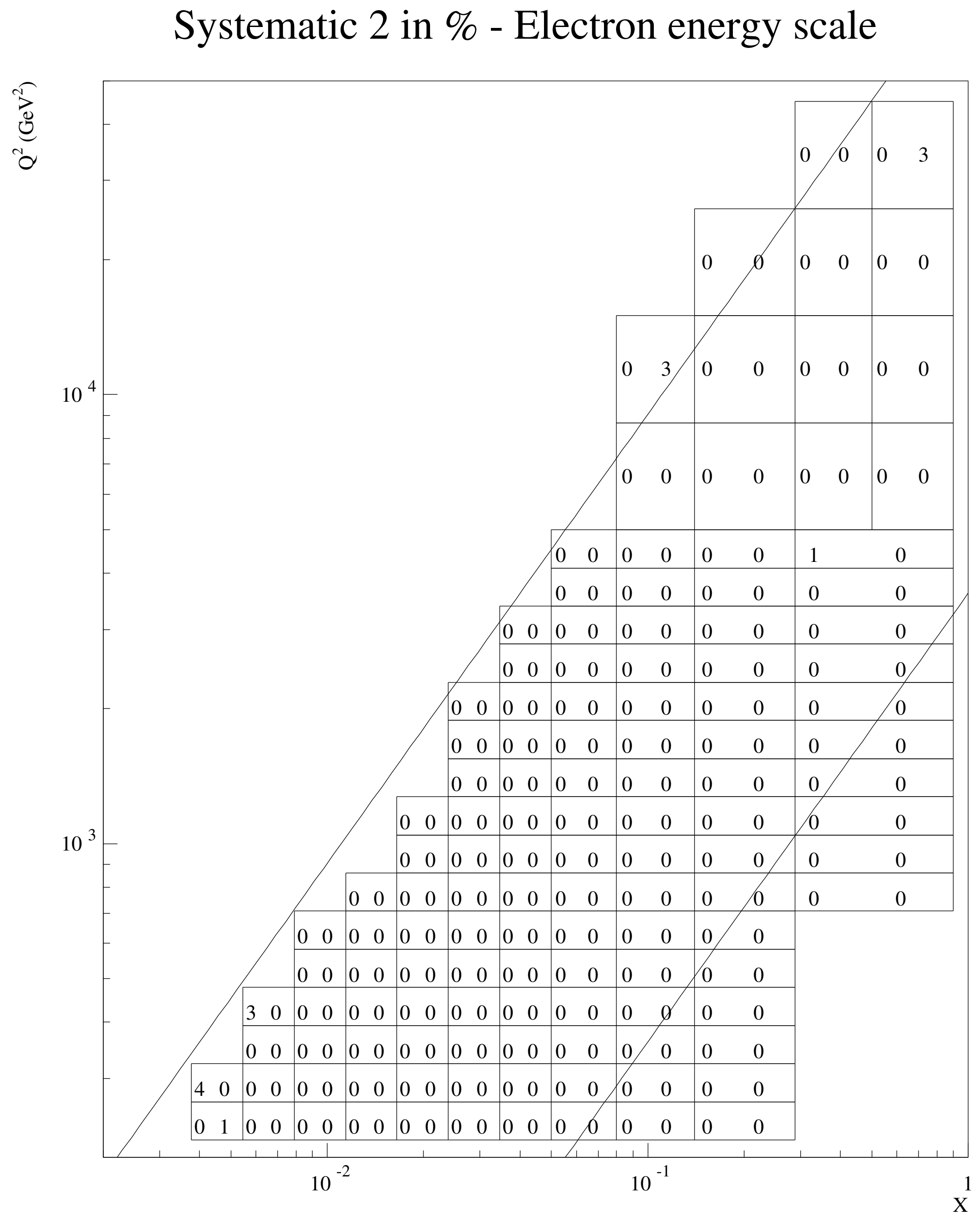

Figure 6.17: Systematic error for electron energy scale in each bin. Left number is negative, right number is positive. The numbers are in percentage.

6.4.3 Hadronic angle γ_h resolution

The kinematic variables of this analysis, are derived from the electron angle θ_e and hadron angle γ_h. Errors in the simulation of these angles, therefore, are a direct source of systematic error.

Three variations are used to estimate the systematic uncertainty in the simulation of the γ_h measurement:

- The effect of shifts in energy scales of RCAL (Figure 6.18), BCAL (Figure 6.19) and FCAL (Figure 6.20).
- The effect of 15% energy variation in the first ring of FCAL (Figure 6.21).
- The effect of smearing γ_h (Figure 6.22).

The last item was found to be by far the largest effect on the systematic error of γ_h measurement. The total systematic error for hadronic angle resolution in each bin is shown in Figure 6.23.

6.4.4 Electron angle θ_e resolution

Just like hadron angle γ_h, error in the simulation of electron angle γ_h is a direct source of systematic error. This was estimated by doubling the error observed event by event in the Monte Carlo. Because the electron angle is more precisely measured, the effect of this systematic error is less than 1% overall (Figure 6.25). The error doubling effect is shown in Figure 6.24.

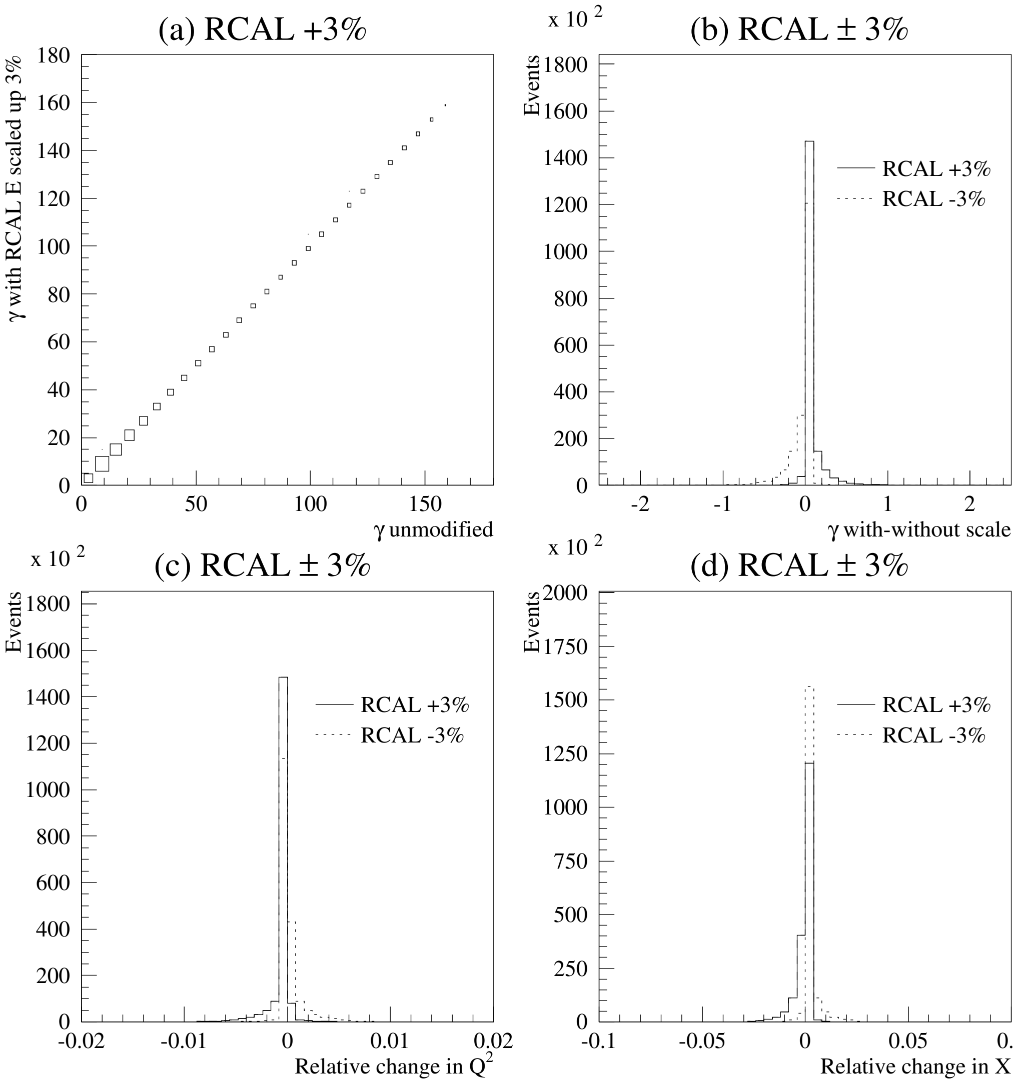

Figure 6.18: Difference in measurement of γ_h after scaling RCAL energy. A scaling of 3% is chosen to quote ZEUS official findings of RCAL energy scale uncertainty. Shown are (a) Adding 3% to the energy scale of all RCAL cells produces a small change in γ_h. (b) Change in γ_h on $\pm 3\%$ change in RCAL energy scale. (c) Consequence in x. (d) Consequence in Q^2.

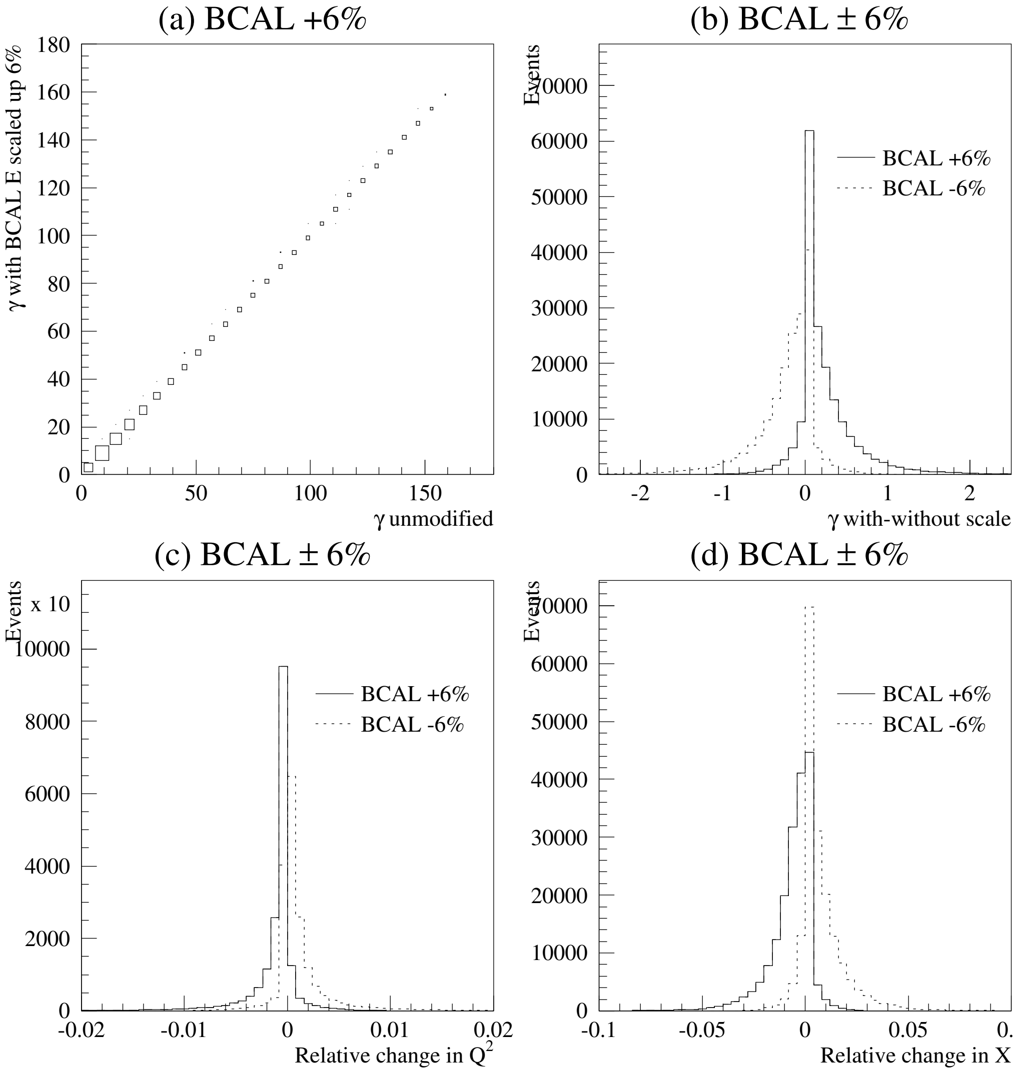

Figure 6.19: Difference in measurement of γ_h after scaling BCAL energy. A scaling of 6% is chosen to quote ZEUS official findings of BCAL energy scale uncertainty. Shown are (a) Adding 6% to the energy scale of all RCAL cells produces a small change in γ_h. (b) Change in γ_h on $\pm 6\%$ change in BCAL energy scale. (c) Consequence in x. (d) Consequence in Q^2.

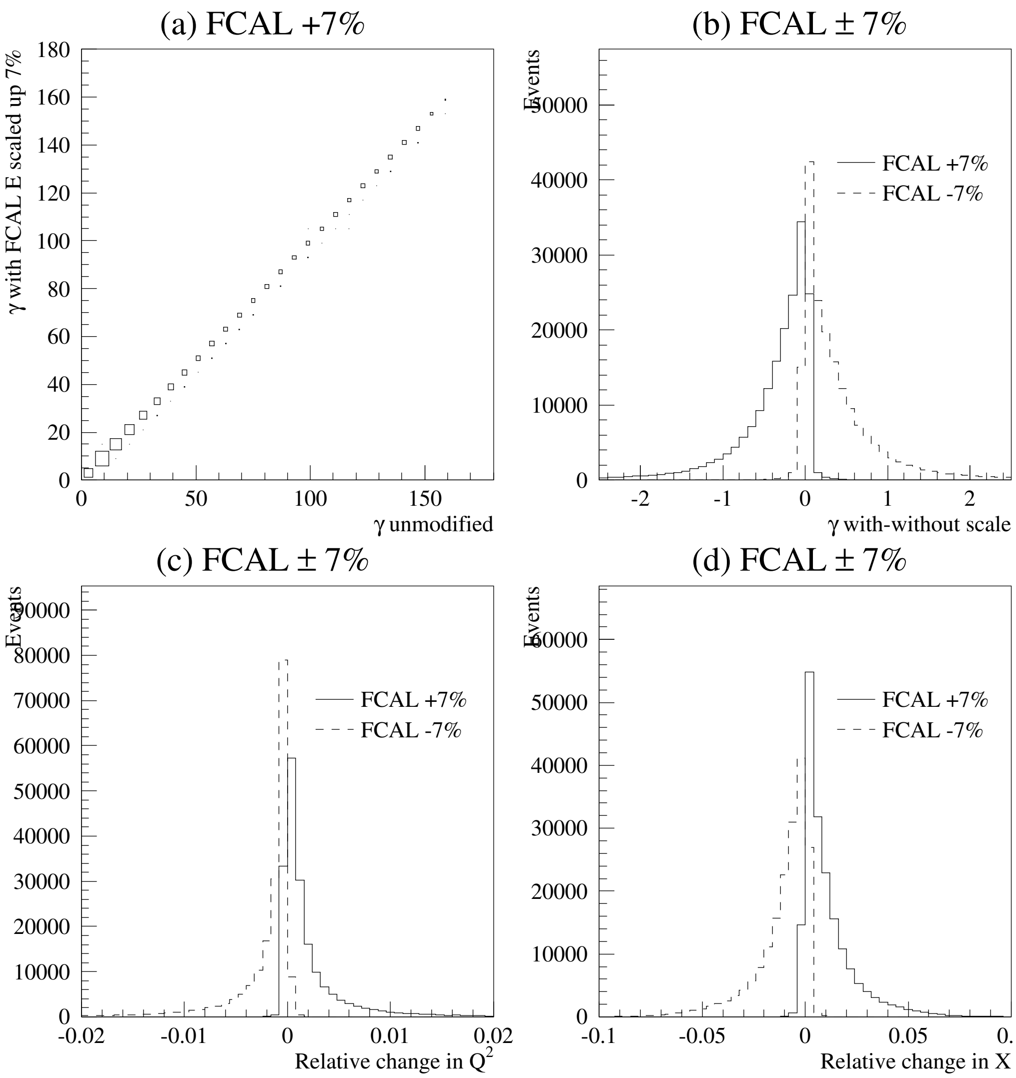

Figure 6.20: Difference in measurement of γ_h after scaling FCAL energy. A scaling of 7% is chosen to quote ZEUS official findings of FCAL energy scale uncertainty. Shown are (a) Adding 7% to the energy scale of all FCAL cells produces a small change in γ_h. (b) Change in γ_h on $\pm 7\%$ change in FCAL energy scale. (c) Consequence in x. (d) Consequence in Q^2.

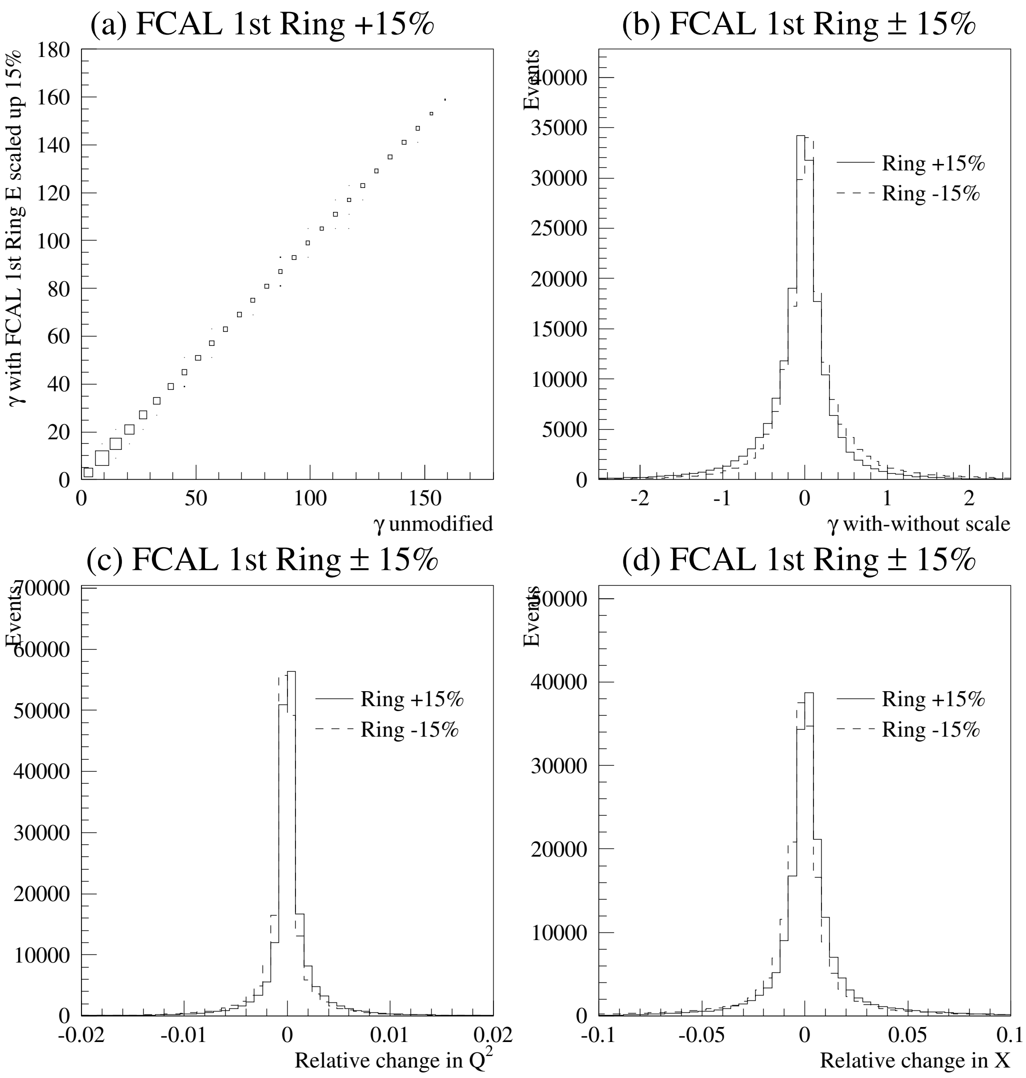

Figure 6.21: Difference in measurement of γ_h after scaling FCAL first ring energy. A scaling of 15% is chosen to assess FCAL first ring energy scale uncertainty. Shown are (a) Adding 15% to the energy scale of all FCAL cells produces a small change in γ_h. (b) Change in γ_h on $\pm15\%$ change in FCAL first ring energy scale. (c) Consequence in x. (d) Consequence in Q^2.

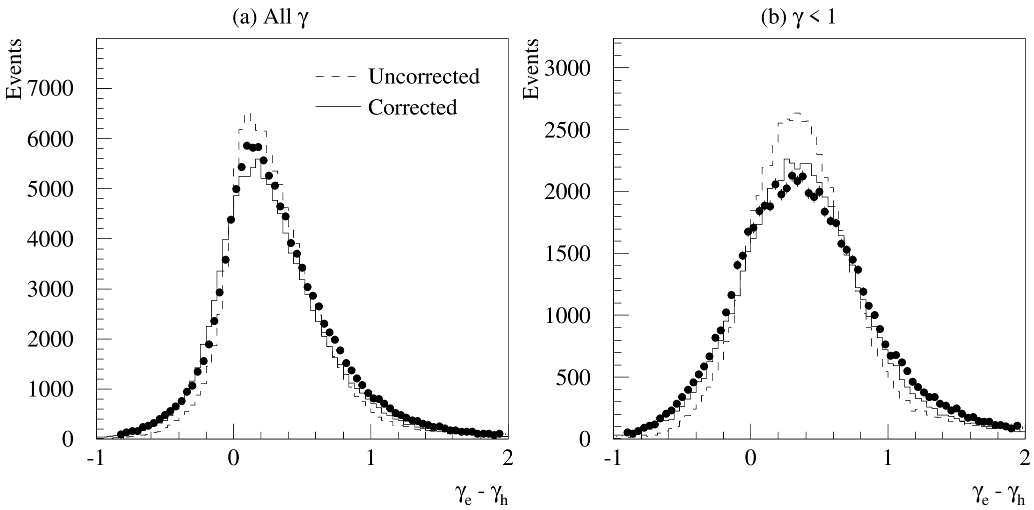

Figure 6.22: Difference in measurement of γ_h after smearing γ_h. γ_h is smeared by 5% so that $\gamma_e - \gamma_h$ in MC simulation matches that of data.

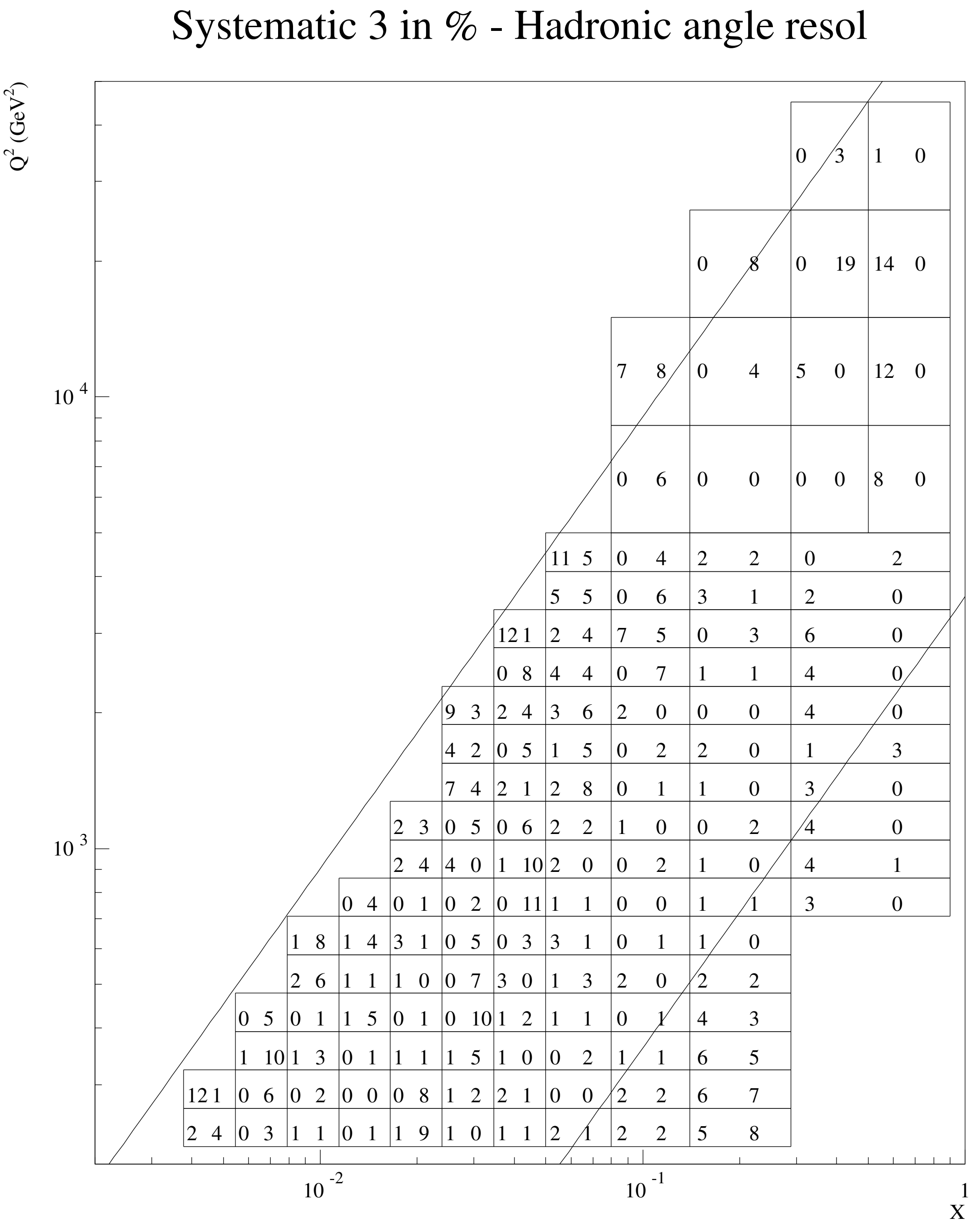

Figure 6.23: Systematic error for hadronic angle resolution in each bin. Left number is negative, right number is positive. The numbers are in percentage.

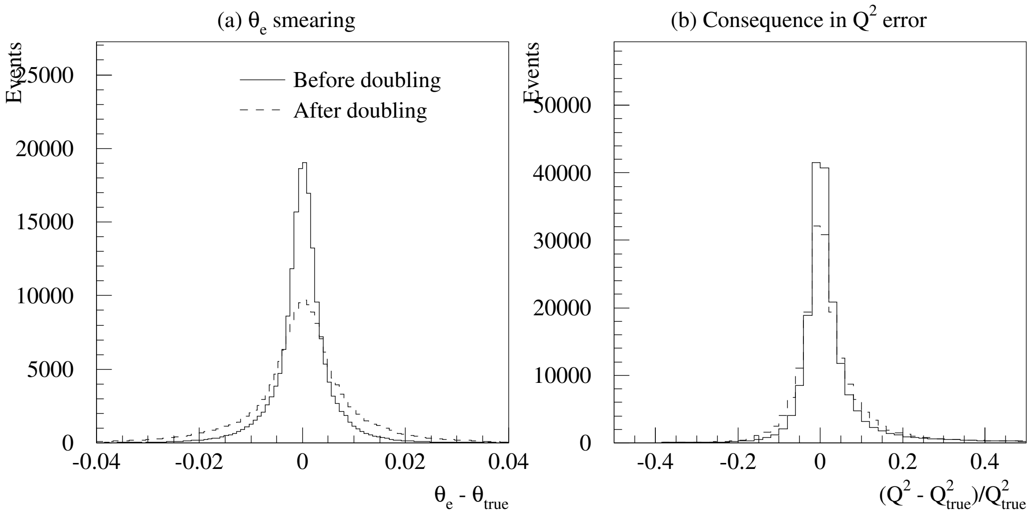

Figure 6.24: Systematic error due to electron angle θ_e resolution. Shown are (a) $\theta_e - \theta_t rue$ in the Monte Carlo and the doubling of this error. (b) Consequence in Q^2.

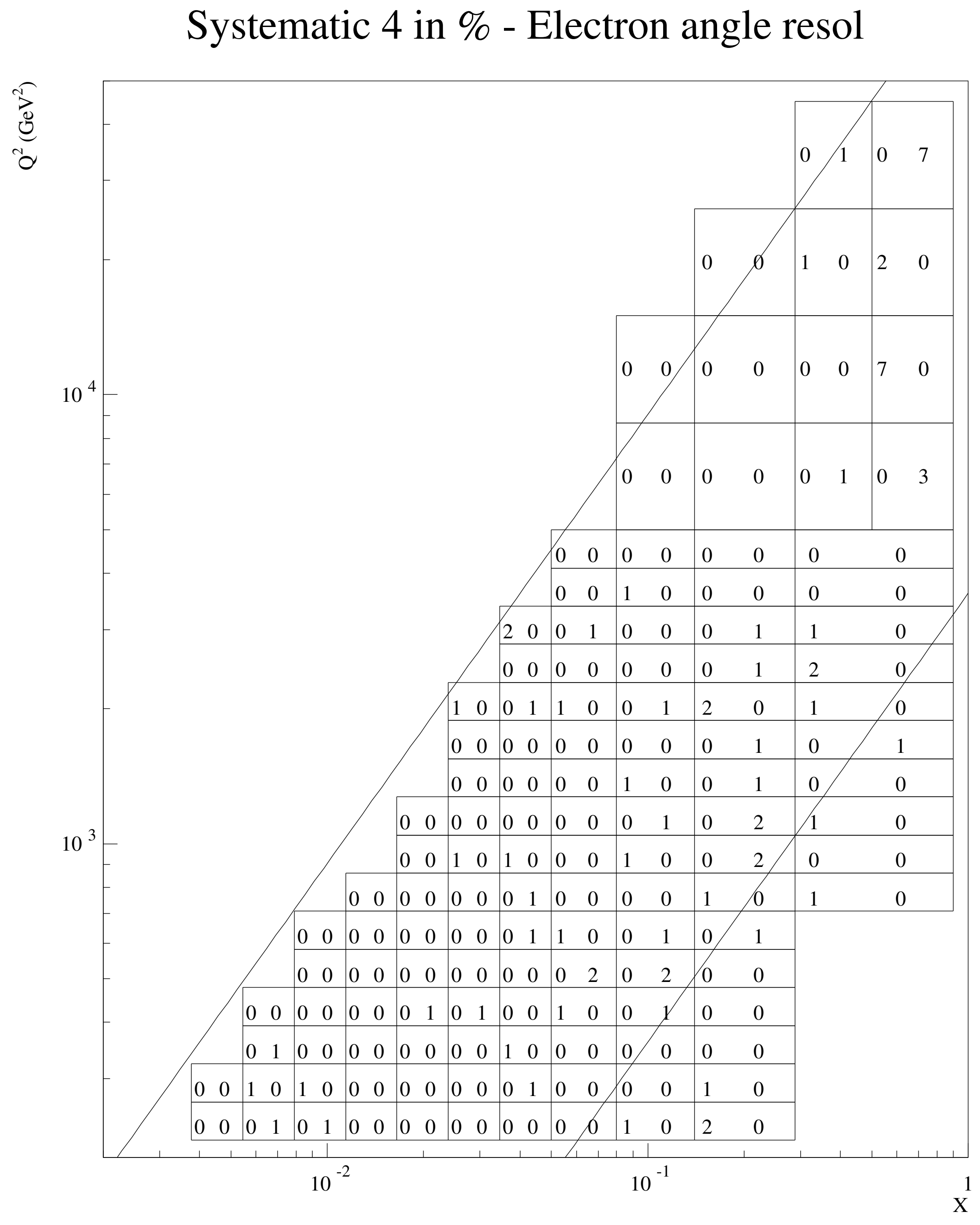

Figure 6.25: Systematic error for electron angle resolution in each bin. Left number is negative, right number is positive. The numbers are in percentage.

6.4.5 Electron identification inefficiency

Systematic error due to electron identification inefficiency in the Monte Carlo simulation can be naturally estimated by doubling the simulated inefficiency, parameterized as a function of energy (Figure 6.26). The size of this systematic error is shown in Figure 6.27.

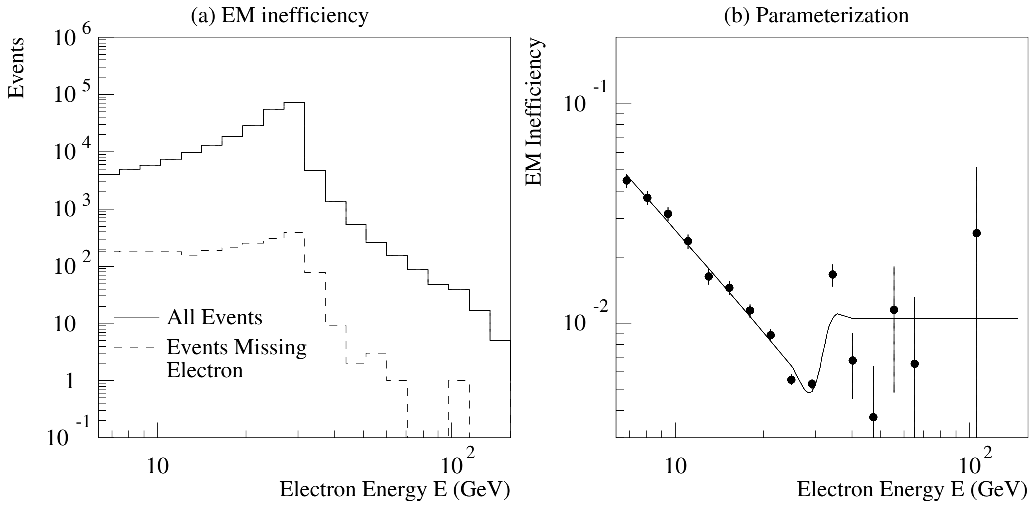

Figure 6.26: EM inefficiency according to Monte Carlo. (a) Monte Carlo predicts that EM efficiency slowly turns on as a function of energy, becoming nearly 99% efficient above 20 GeV. (b) The inefficiency is parameterized as a function of energy so that a systematic error can be estimated.

6.4.6 Tracking inefficiency

Since the majority of electrons are required to have a matching track, the tracking inefficiency is an additional systematic error. The efficiency is expected to be nearly

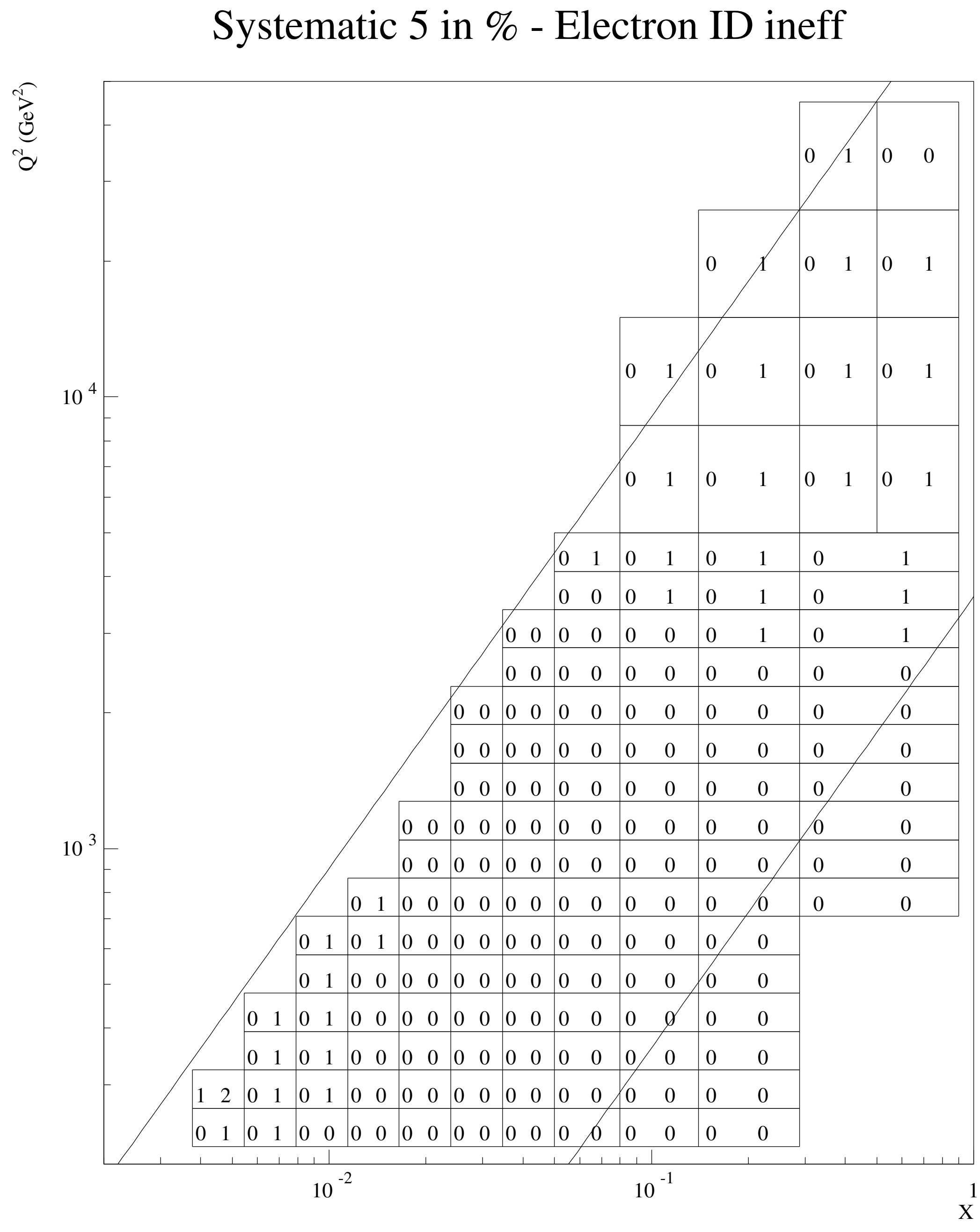

Figure 6.27: Systematic error for electron ID inefficiency in each bin. Left number is negative, right number is positive. The numbers are in percentage.

100% inside the acceptance of the CTD, minimizing this systematic error. For forward tracks, however, efficiency can be expected to drop, primarily because of less CTD superlayers traversed and the requirements that the tracks have at least 2 GeV and extrapolate to within 10 cm of the calorimeter deposit.

To estimate the systematic error, the tracking inefficiency simulated in the Monte Carlo is fitted to a polynomial and the resulting function is used to double the inefficiency (Figure 6.28). The size of this systematic error is shown in Figure 6.29.

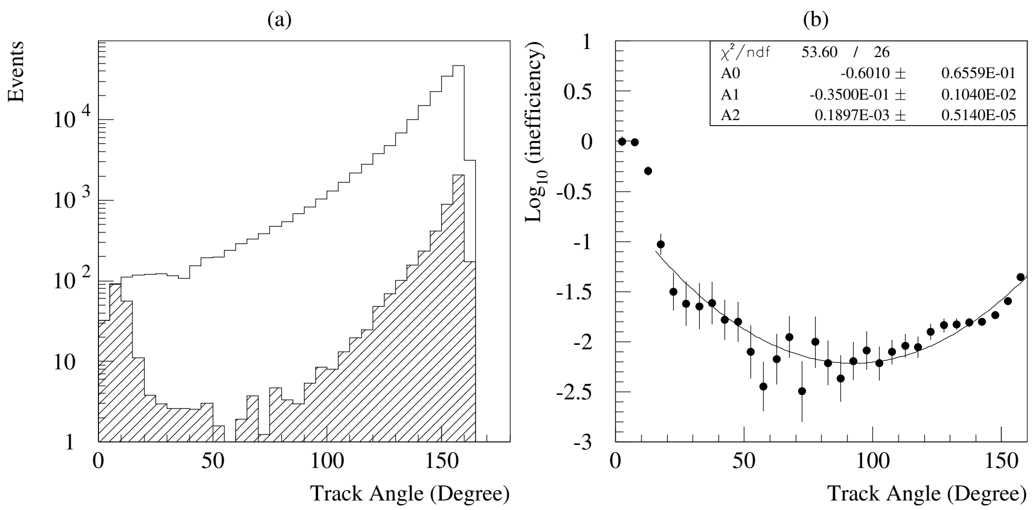

Figure 6.28: Tracking inefficiency as simulated in Monte Carlo. (a) The white histogram are all Monte Carlo events, weighted to the 94-96 electron luminosity, that pass all event selection cuts except those requiring a track. Events at large and small angles (shaded histogram), however, are missing a track of at least 2 GeV. (b) The inefficiency is shown in log scale versus track angle and the parameterization is used in the estimation of systematic errors.

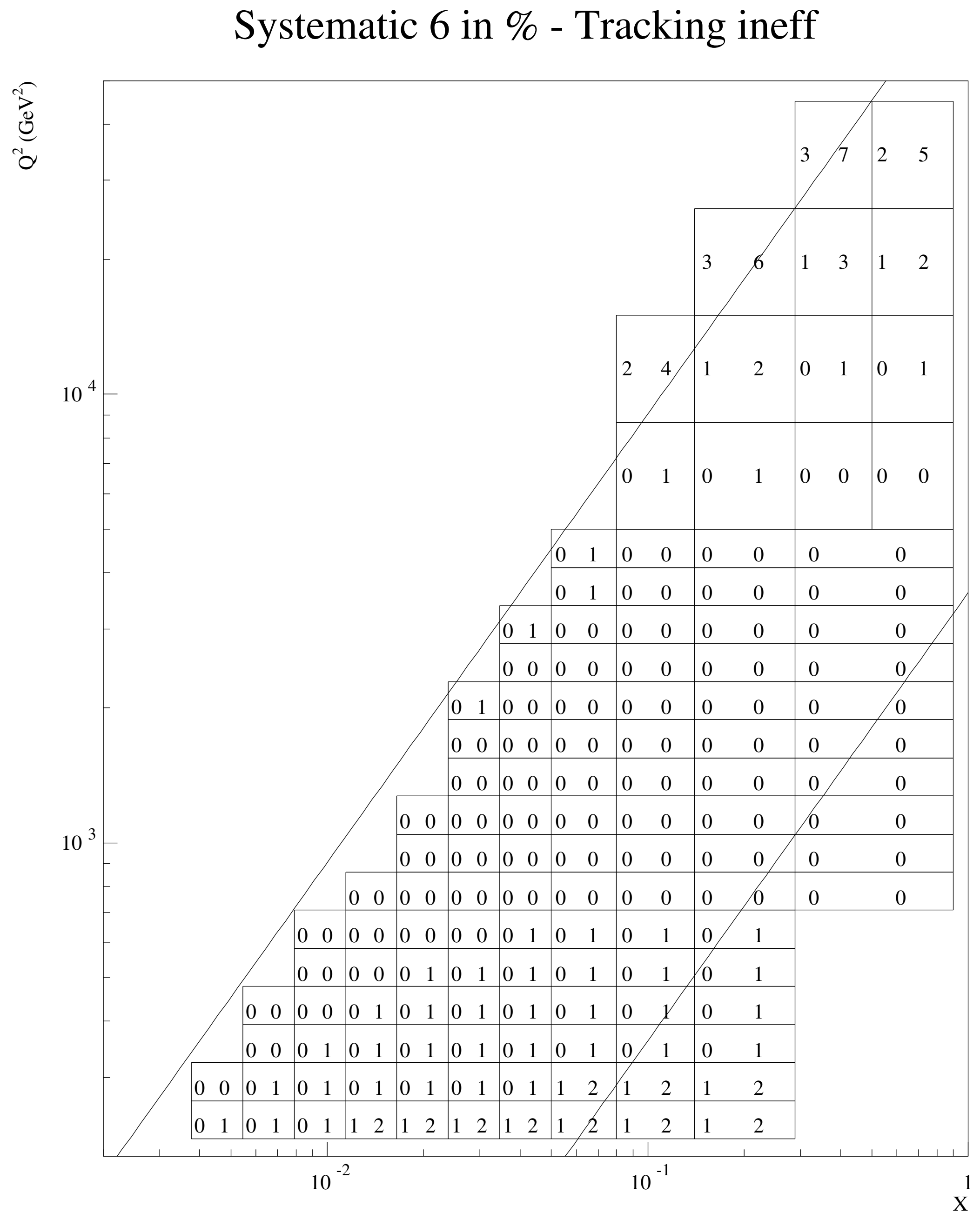

Figure 6.29: Systematic error for tracking inefficiency in each bin. Left number is negative, right number is positive. The numbers are in percentage.

6.4.7 Tracking momentum resolution

Since tracks that match electrons are required to have a momentum greater than 2 GeV, tracking momentum resolution or bias is a potential systematic error. The simulation of the CTD tracking is expected to reproduce the momentum resolution of measured tracks.

Momentum resolution, quantified by the error in $1/p_t$ of a track, is expected to remain independent of θ until tracks begin to fall outside of the CTD acceptance and traverse less superlayers. To measure this, the θ angle and z vertex position is used event by event to calculate the number of CTD superlayers a electron passes through in the Monte Carlo. The difference in measured and generated $1/p_t$ is then plotted and fitted versus number of superlayers for tracks that pass through. The result is shown in Figure 6.30.

The $1/p_t$ errors shown in Figure 6.30 appear to have a linear dependence on the number of CTD superlayers traversed. This linear dependence is used to add an additional smear to the Monte Carlo in order to estimate the systematic error from the uncertainty in the simulation. The size of this systematic error is shown in Figure 6.31.

6.4.8 Tracking and calorimeter alignment

To estimate the effect on event selection, the following tracking-CAL alignment problem was simulated:

- RCAL smear in z by 1 cm.

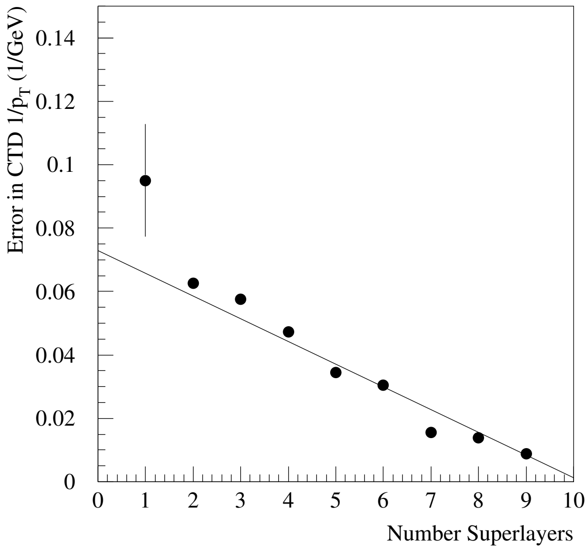

Figure 6.30: The inverse transverse momentum $(1/p_T)$ distributions for events that pass all selection cuts except the 2 GeV minimum track momentum requirement, versus the number of CTD superlayers traversed. The line is the linear fit that is used as an additional smear in the Monte Carlo to estimate the systematic error due to uncertainty in the simulation of $1/p_T$ resolution.

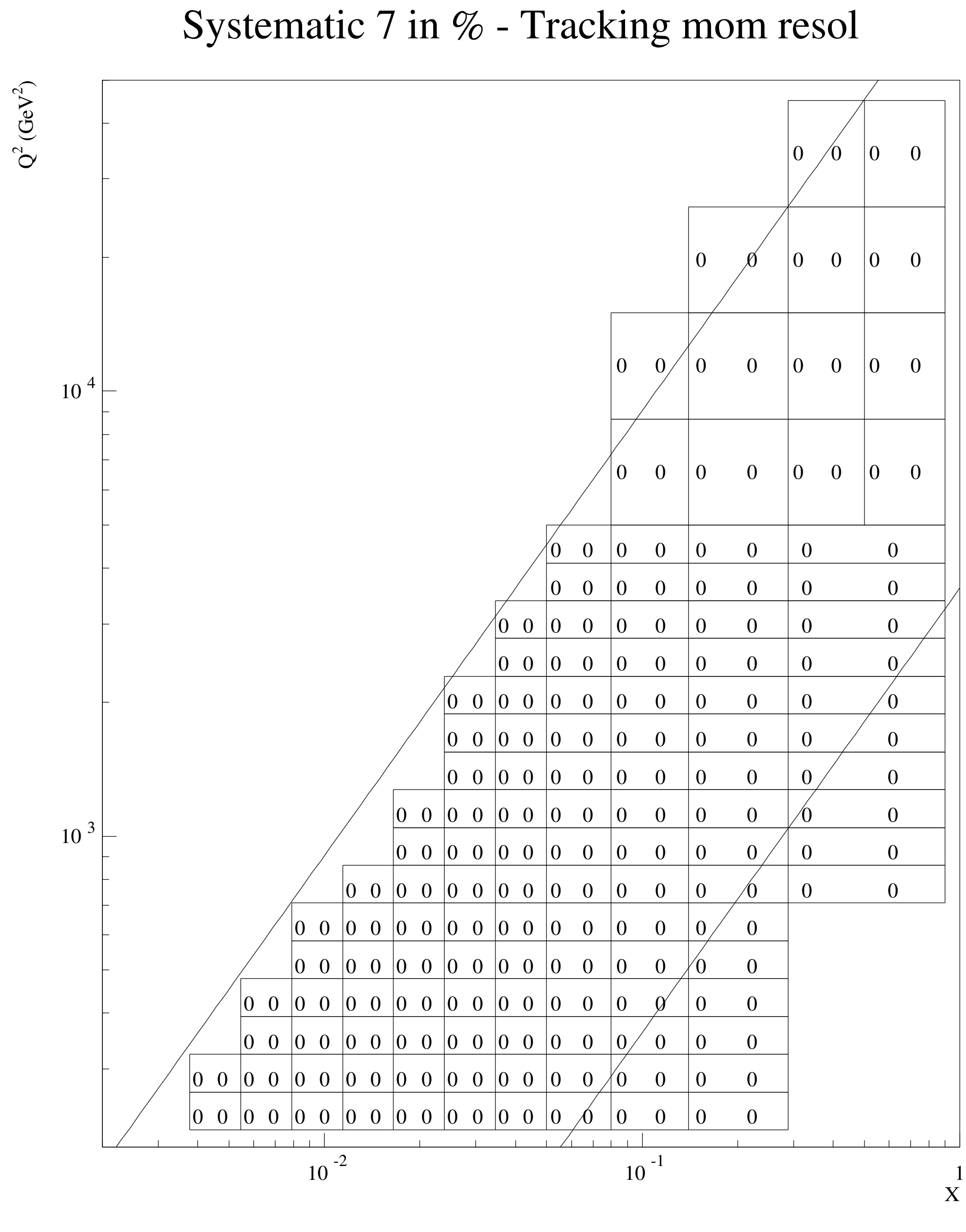

Figure 6.31: Systematic error for tracking momentum resolution in each bin. Left number is negative, right number is positive. The numbers are in percentage.

- RCAL smear in x by 1 cm and y by 1 cm.
- BCAL smear in $r\phi$ direction by 1 cm.

Although these effects are more than large enough to be measured, they have little effect on the distance of 10 cm (the cut used in this analysis), as seen in Figure 6.32. The resulting systematic errors are less than 0.15% (Figure 6.33).

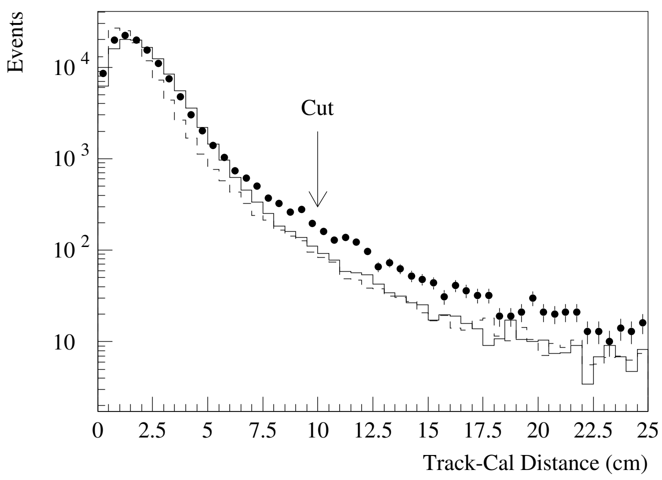

Figure 6.32: The distance between the extrapolated track position and the calorimeter position of the electron. Shown are data (points), unsmeared Monte Carlo (dashed histogram) and smeared Monte Carlo (solid histogram).

6.4.9 Calorimeter total p_T resolution

The anti-cosmic ray cut in $p_T/\sqrt{E_T}$ can produce a systematic error if the p_T resolution is not correctly simulated. When the Monte Carlo and data are compared,

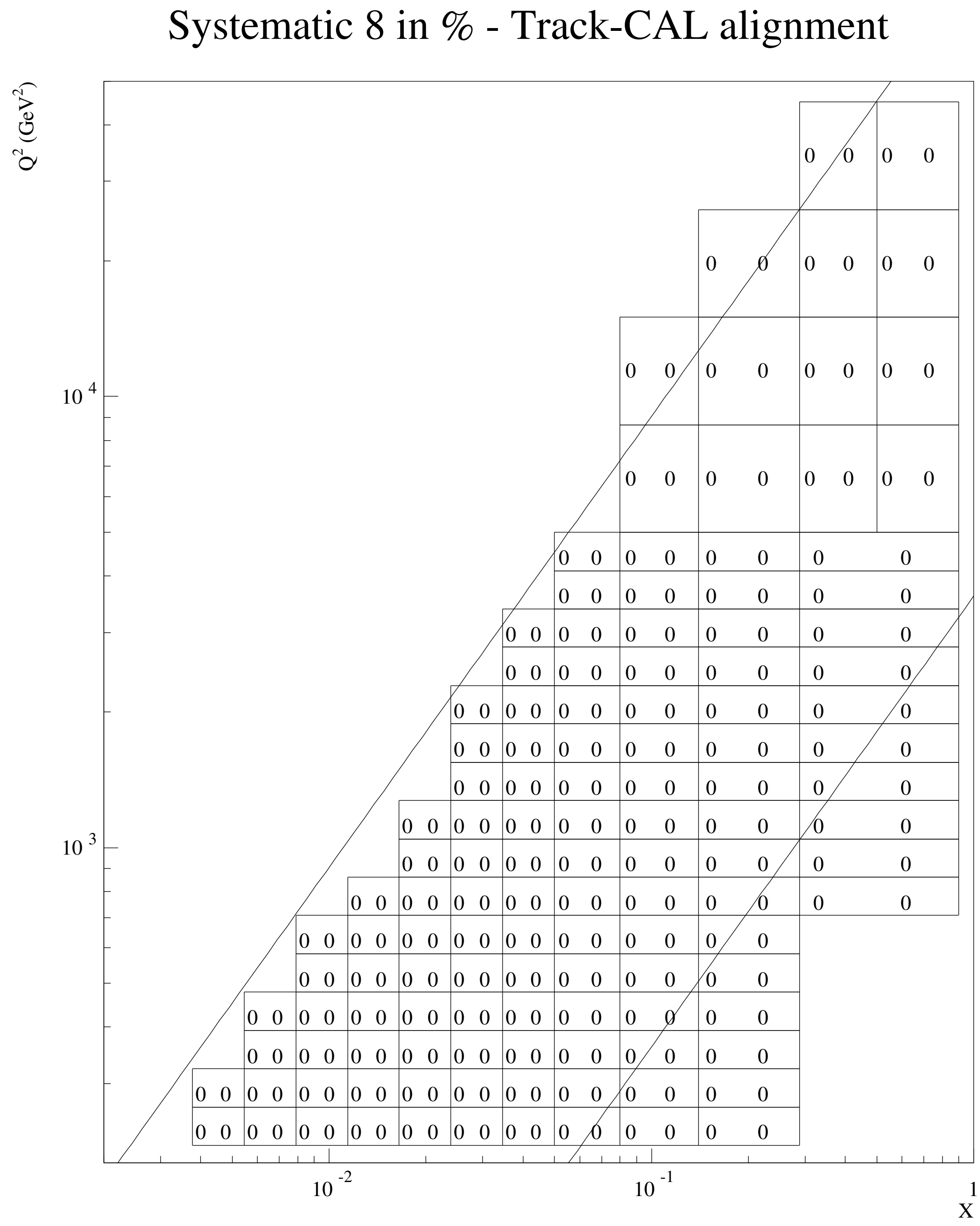

Figure 6.33: Systematic error for track-calorimeter alignment in each bin. Left number is negative, right number is positive. The numbers are in percentage.

indeed, a small disagreement is visible as shown in Figure 6.34. Much of the disagreement can be repaired by smearing p_T in the following way:

$$p'_T = \sqrt{(p_T + 0.1\delta_1)^2 + (0.1\delta_2)^2} \tag{6.6}$$

where δ_1 and δ_2 are two independent random Gaussian numbers. The result is also shown in Figure 6.34. Since the cut of $p_T/\sqrt{E_T} < 3$ is conservative, the systematic effect of smearing p_T is small (Figure 6.35).

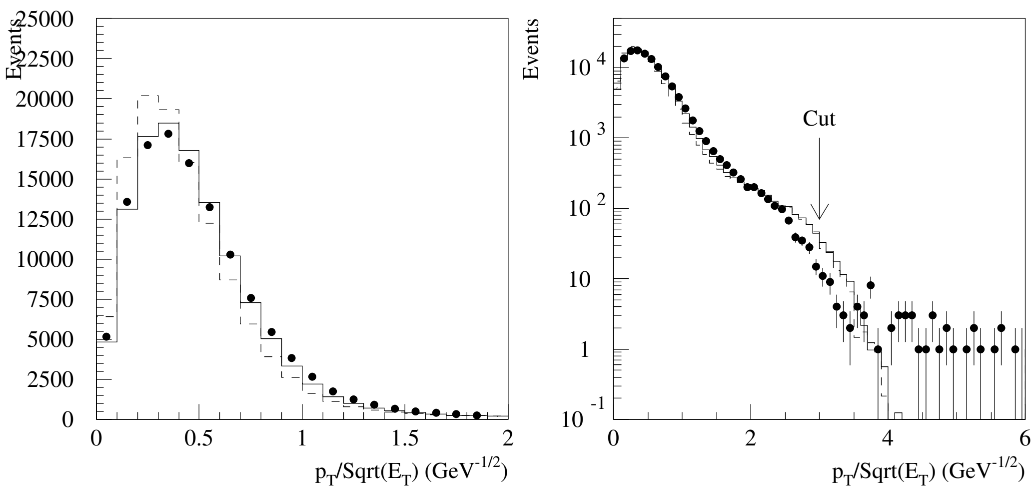

Figure 6.34: The quantity p_T divided by square root of E_T for events that pass all selection cuts except the one on this quantity itself. Shown are data (points), unsmeared Monte Carlo (dashed histogram) and smeared Monte Carlo (solid histogram)

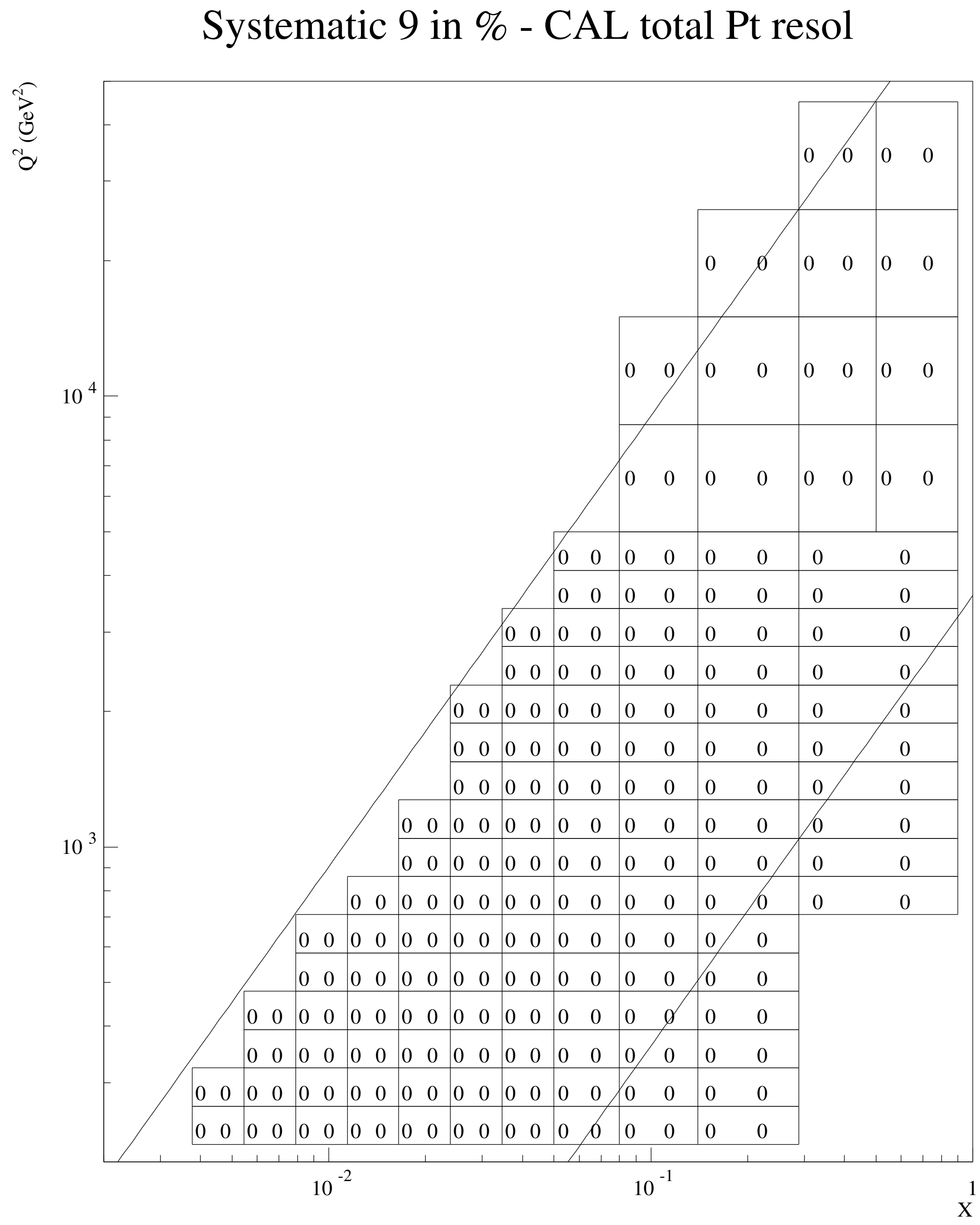

Figure 6.35: Systematic error for calorimeter total p_T resolution in each bin. Left number is negative, right number is positive. The numbers are in percentage.

6.4.10 Photoproduction background levels

The systematic uncertainty due to estimates of photoproduction background is calculated by varying the background estimate by $\pm 100\%$. The photoproduction background estimate is shown in Figure 6.36. The size of this systematic error is small (Figure 6.37).

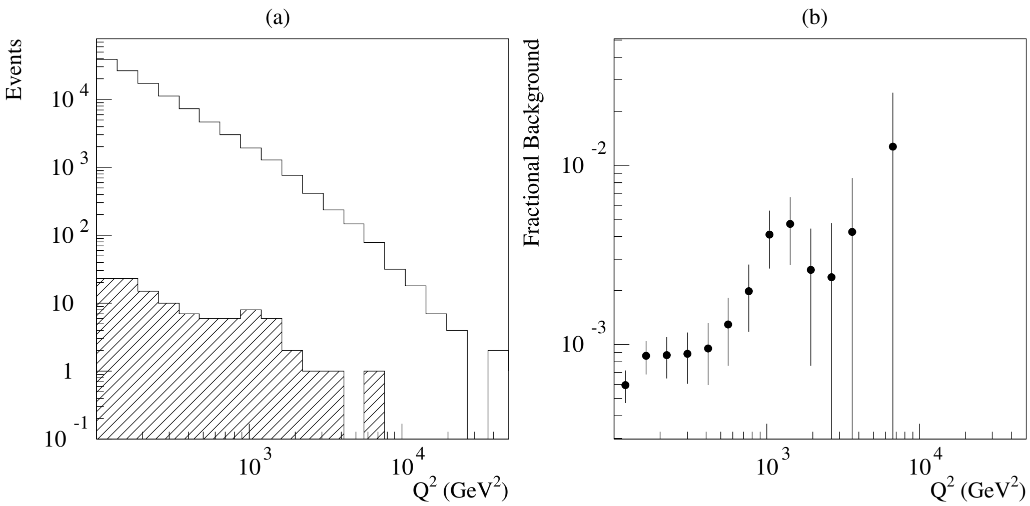

Figure 6.36: The photoproduction background estimate from Monte Carlo as a function of Q^2. (a) All events that pass the selection cuts (white histogram), photoproduction background as estimated from MC (hashed histogram). (b) Photoproduction background level in percentage as a function of Q^2.

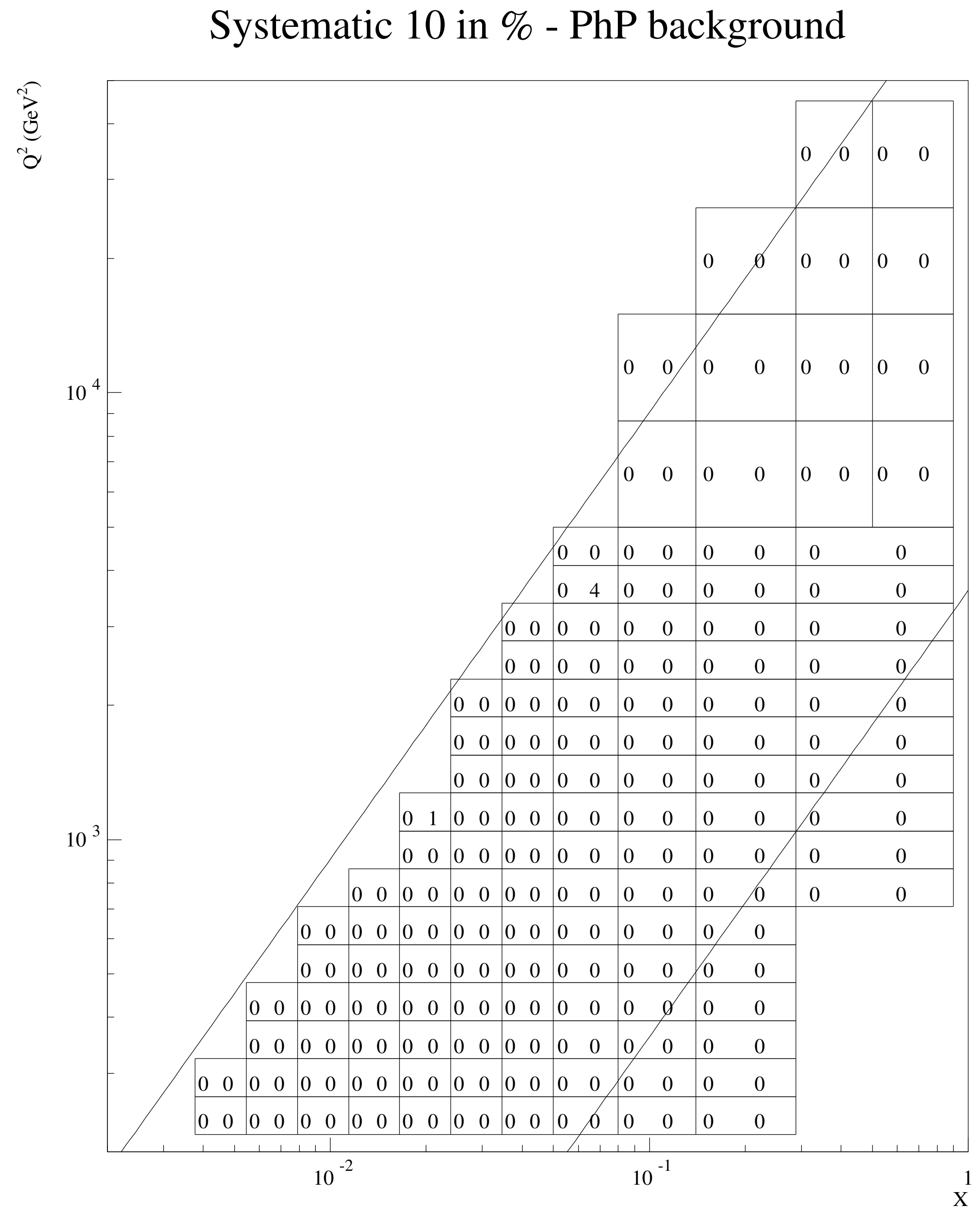

Figure 6.37: Systematic error for photoproduction background level in each bin. Left number is negative, right number is positive. The numbers are in percentage.

Chapter 7

The extraction of xF_3

7.1 The effect of xF_3

From chapter 1, the quark parton model section, we know:

$$\begin{aligned}
\frac{d^2\sigma(e^{\pm}p)}{dxdQ^2} &= \frac{2\pi\alpha^2}{xQ^4}\left[Y^+F_2(x,Q^2) \mp Y^- xF_3(x,Q^2) - y^2F_L(x,Q^2)\right], \qquad (7.1)\\
Y^{\pm} &= 1 \pm (1-y)^2\\
F_2 &= \sum_{flavor}[xq(x,Q^2) + x\bar{q}(x,Q^2)]A_f(Q^2)\\
xF_3 &= \sum_{flavor}[xq(x,Q^2) - x\bar{q}(x,Q^2)]B_f(Q^2)
\end{aligned}$$

where $q(x,Q^2)$ and $\bar{q}(x,Q^2)$ are the quark and anti-quark distribution functions and the top (bottom) sign is for positrons (electrons).

If we have measured the double-differential cross section, F_2 structure function, and calculated the tiny F_L contribution, we may be able to infer the structure function xF_3. This xF_3 effect may also be seen by plotting the ratio of $\mathrm{d}^2\sigma/\mathrm{d}x\mathrm{d}Q^2$

over $\mathrm{d}^2\sigma/\mathrm{d}x\mathrm{d}Q^2$ (electromagnetic part). This ratio is shown in Figure 7.1, Figure 7.2, Figure 7.3 and Figure 7.4.

However, the size of the errors on the structure function xF_3 may be much bigger than the values of xF_3 itself, making it difficult to interpret the values of xF_3. Nevertheless, that is the course to be taken. The structure function F_2 values are taken from the published ZEUS F_2 data, with a QCD evolution to high Q^2. F_L contribution is also calculated by QCD evolution from ZEUS F_2 data. The results of the structure function xF_3 are shown in Figure 7.5, Figure 7.6, Figure 7.7, Figure 7.8 and Figure 7.9.

7.2 The cumulative effect of xF_3

From the discussion in last section, we see that xF_3 effect is marginal. However, we can accumulate this effect by integrating $\mathrm{d}^2\sigma/\mathrm{d}x\mathrm{d}Q^2$ over the whole x phase space. In another word, we can measure the single-differential cross section $\mathrm{d}\sigma/\mathrm{d}Q^2$ and compare it to the theoretical predictions. The biggest deviation from electromagnetic single- differential cross section can also be calculated. The results are shown in Figure 7.10 and Figure 7.11. We can see that the largest deviation is about 2 or 3 σ effect.

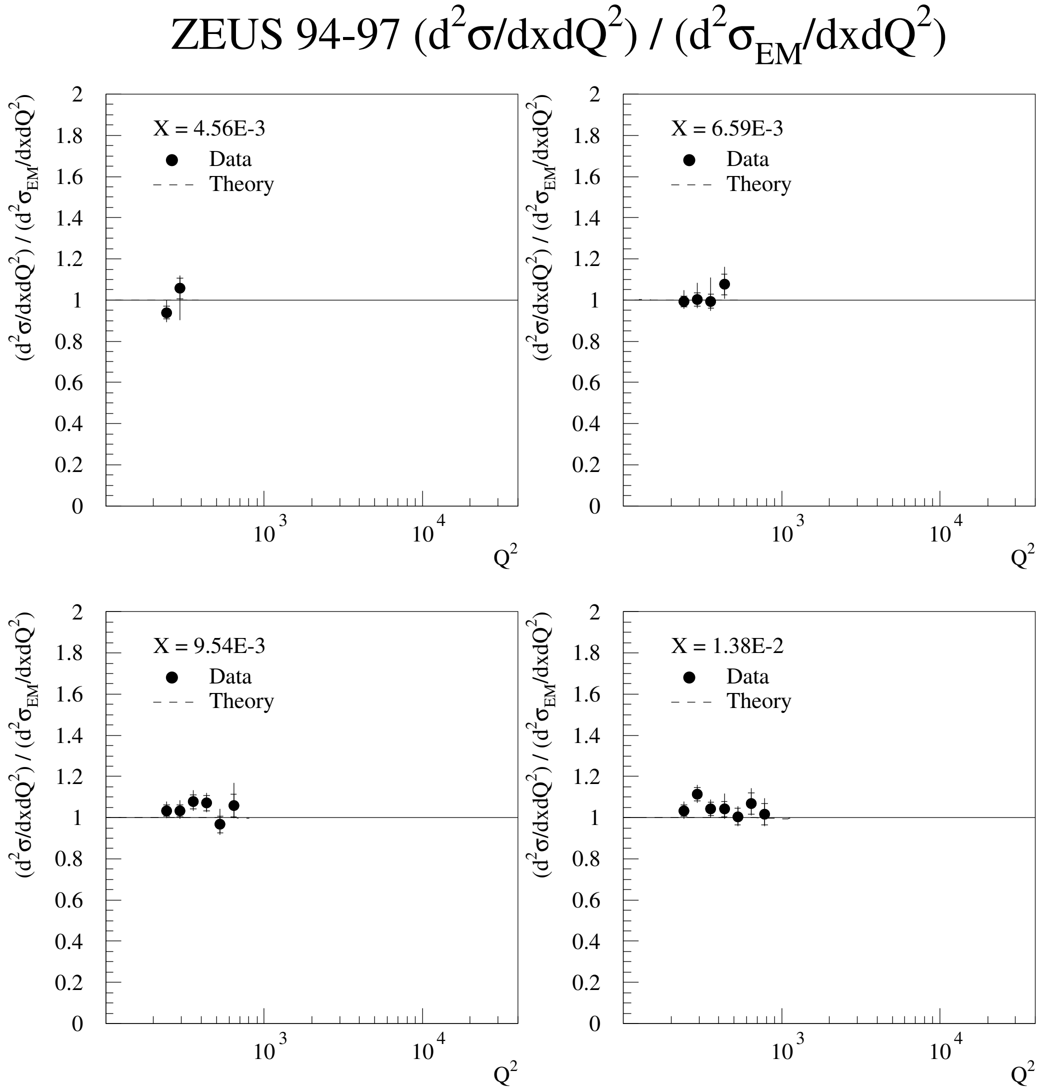

Figure 7.1: Ratio of double-differential cross section over its electromagnetic part, set 1. Also shown are the theoretical predictions from CTEQ4.

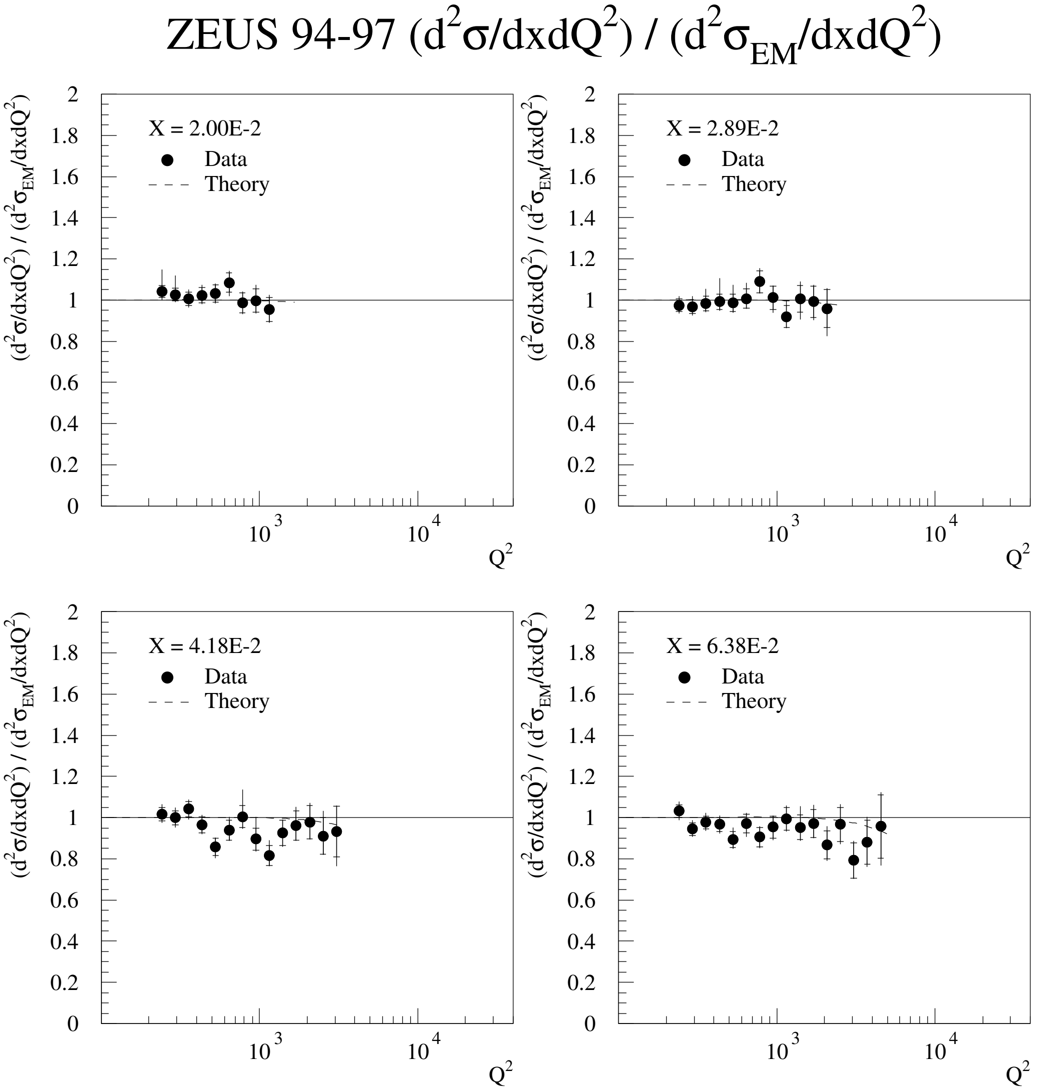

Figure 7.2: Ratio of double-differential cross section over its electromagnetic part, set 2. Also shown are the theoretical predictions from CTEQ4.

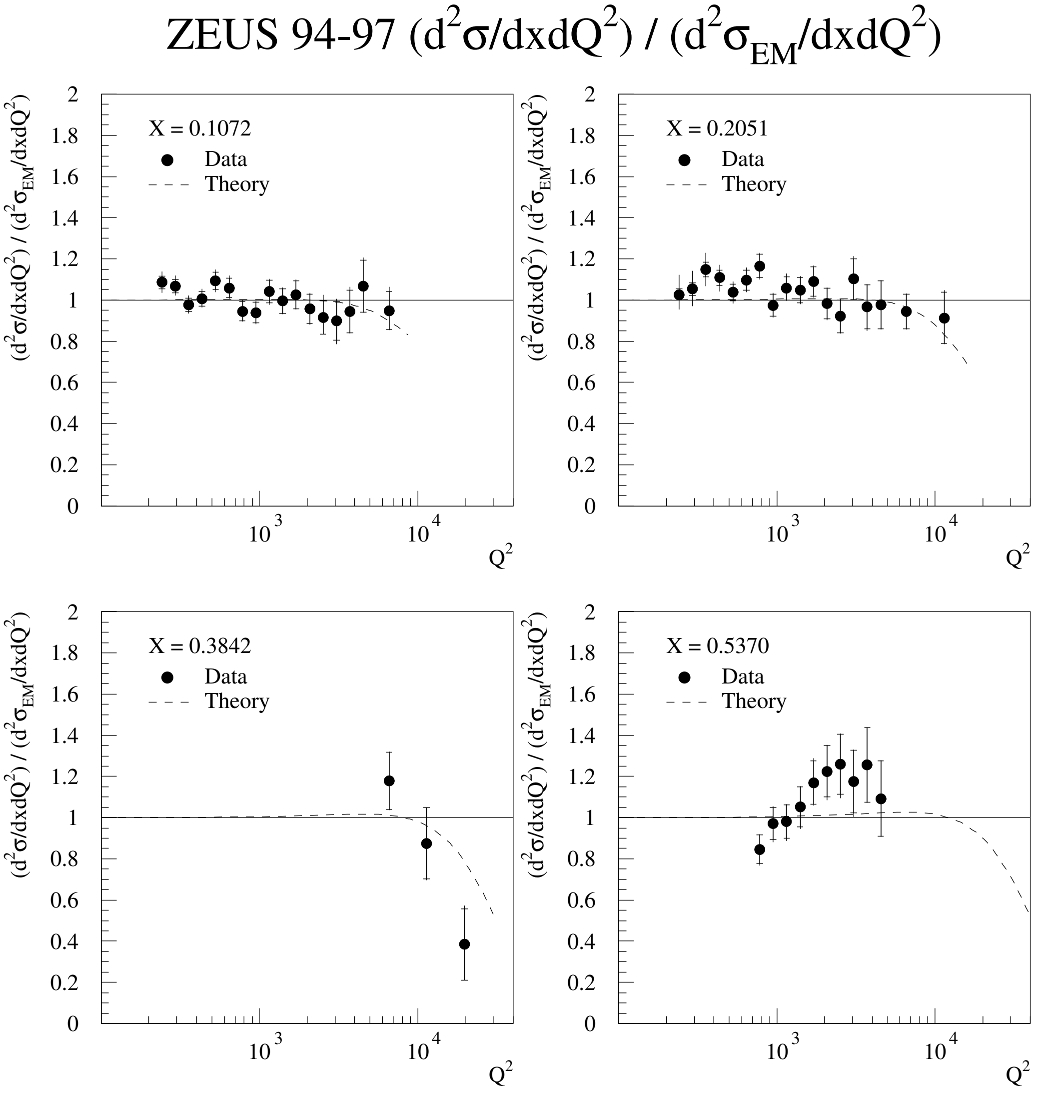

Figure 7.3: Ratio of double-differential cross section over its electromagnetic part, set 3. Also shown are the theoretical predictions from CTEQ4.

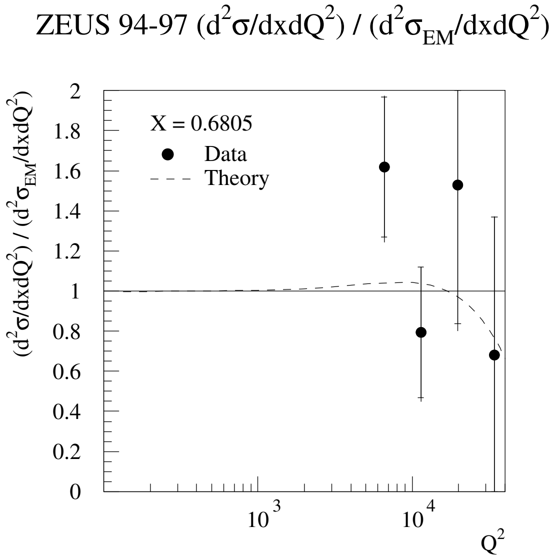

Figure 7.4: Ratio of double-differential cross section over its electromagnetic part, set 4. Also shown are the theoretical predictions from CTEQ4.

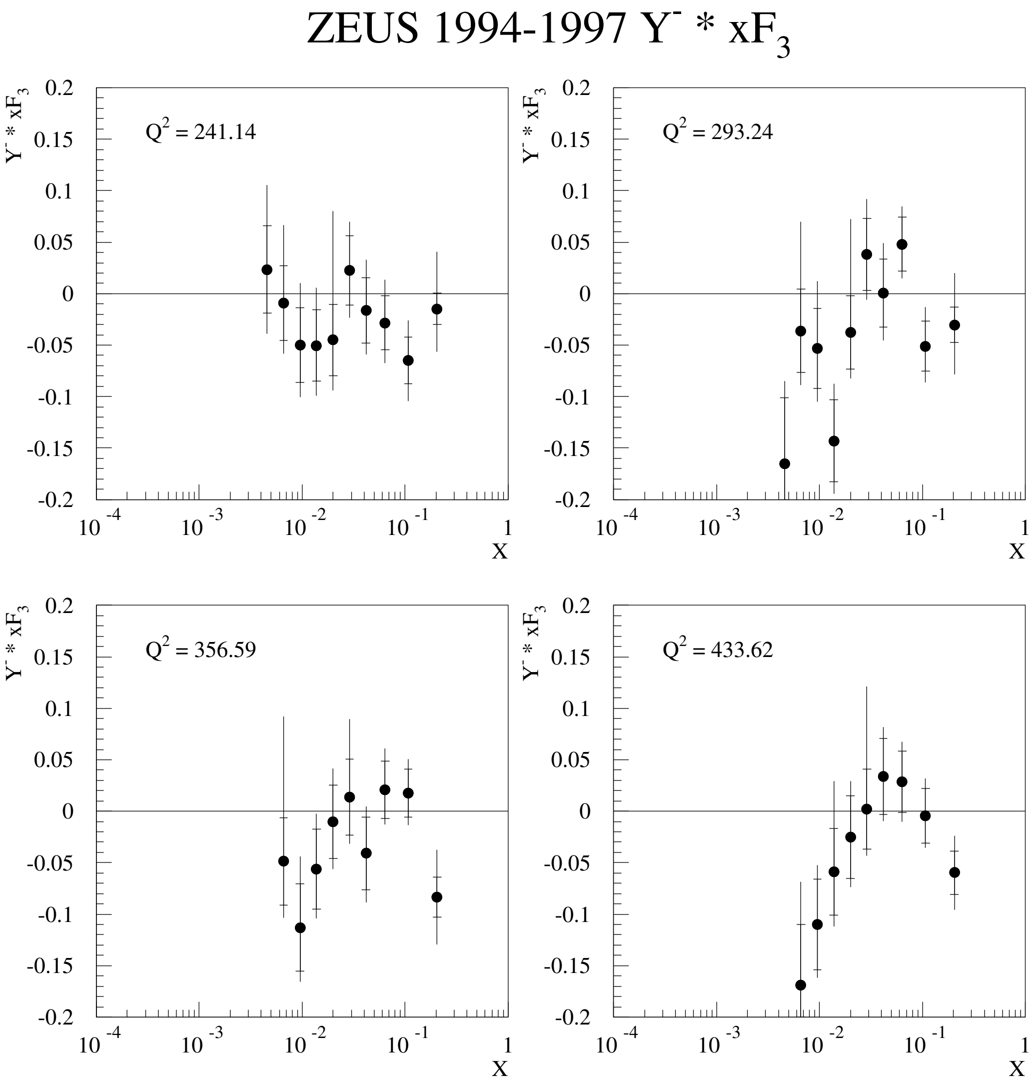

Figure 7.5: Inferred xF_3 as a function of X at fixed Q^2, set 1. The inner error bars are statistical, while the whole error bars are statistical and systematic errors added in quadrature.

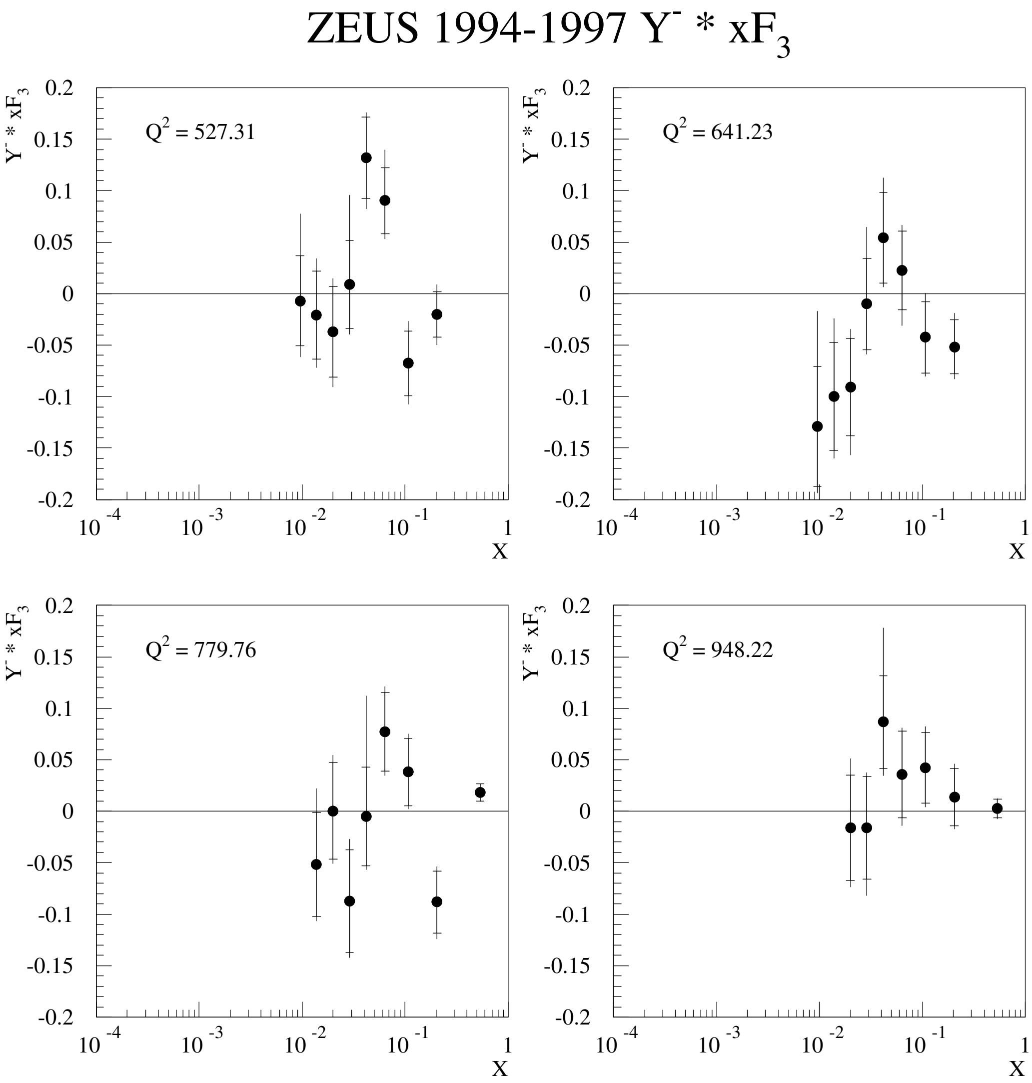

Figure 7.6: Inferred xF_3 as a function of X at fixed Q^2, set 2. The inner error bars are statistical, while the whole error bars are statistical and systematic errors added in quadrature.

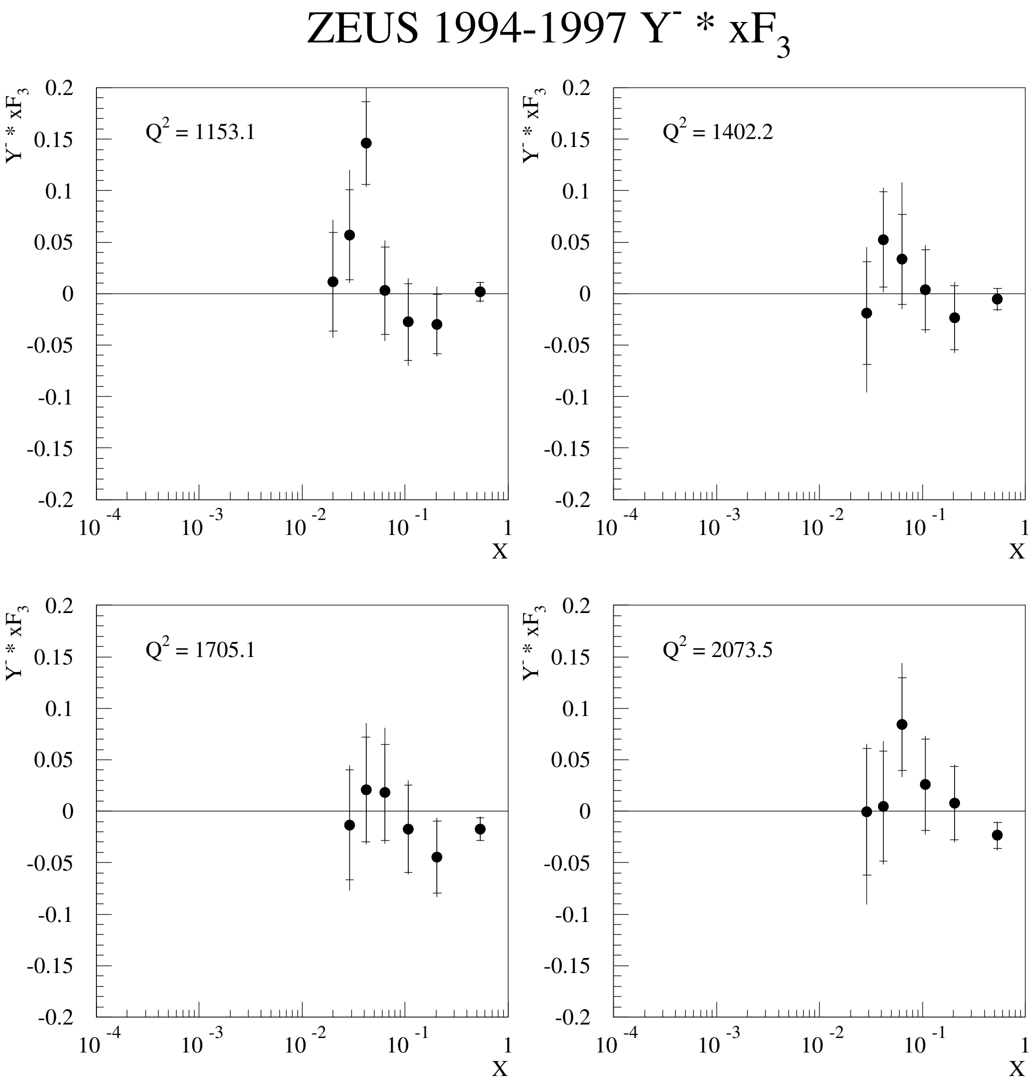

Figure 7.7: Inferred xF_3 as a function of X at fixed Q^2, set 3. The inner error bars are statistical, while the whole error bars are statistical and systematic errors added in quadrature.

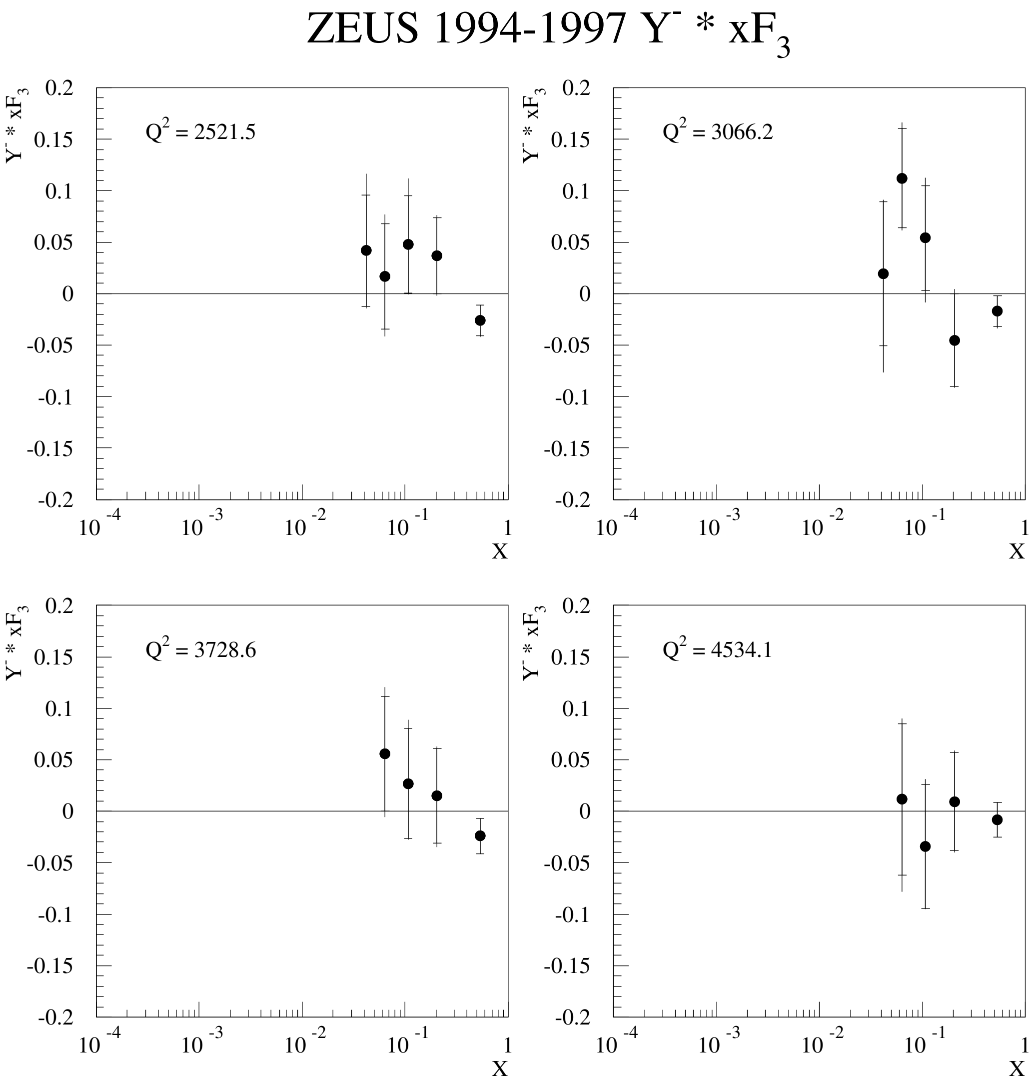

Figure 7.8: Inferred xF_3 as a function of X at fixed Q^2, set 4. The inner error bars are statistical, while the whole error bars are statistical and systematic errors added in quadrature.

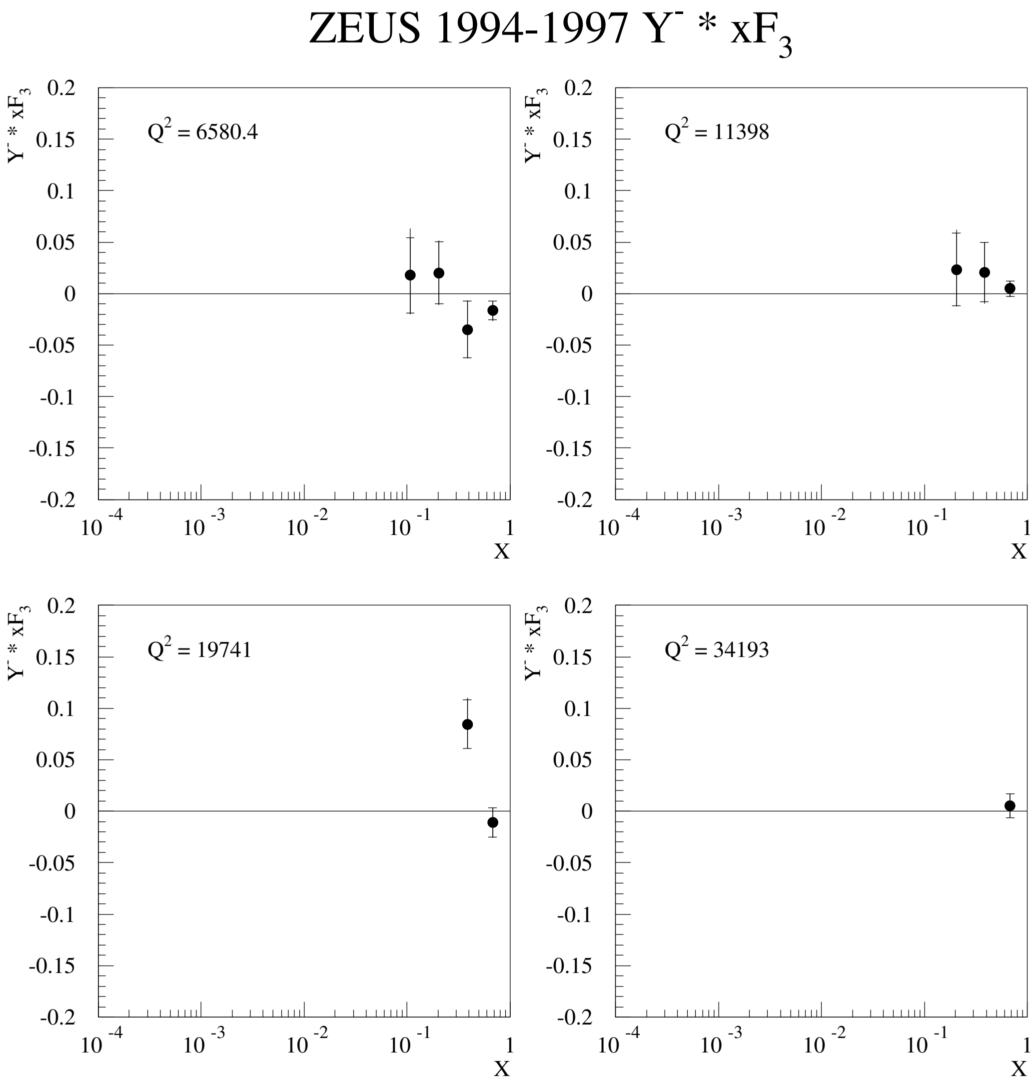

Figure 7.9: Inferred xF_3 as a function of X at fixed Q^2, set 5. The inner error bars are statistical, while the whole error bars are statistical and systematic errors added in quadrature.

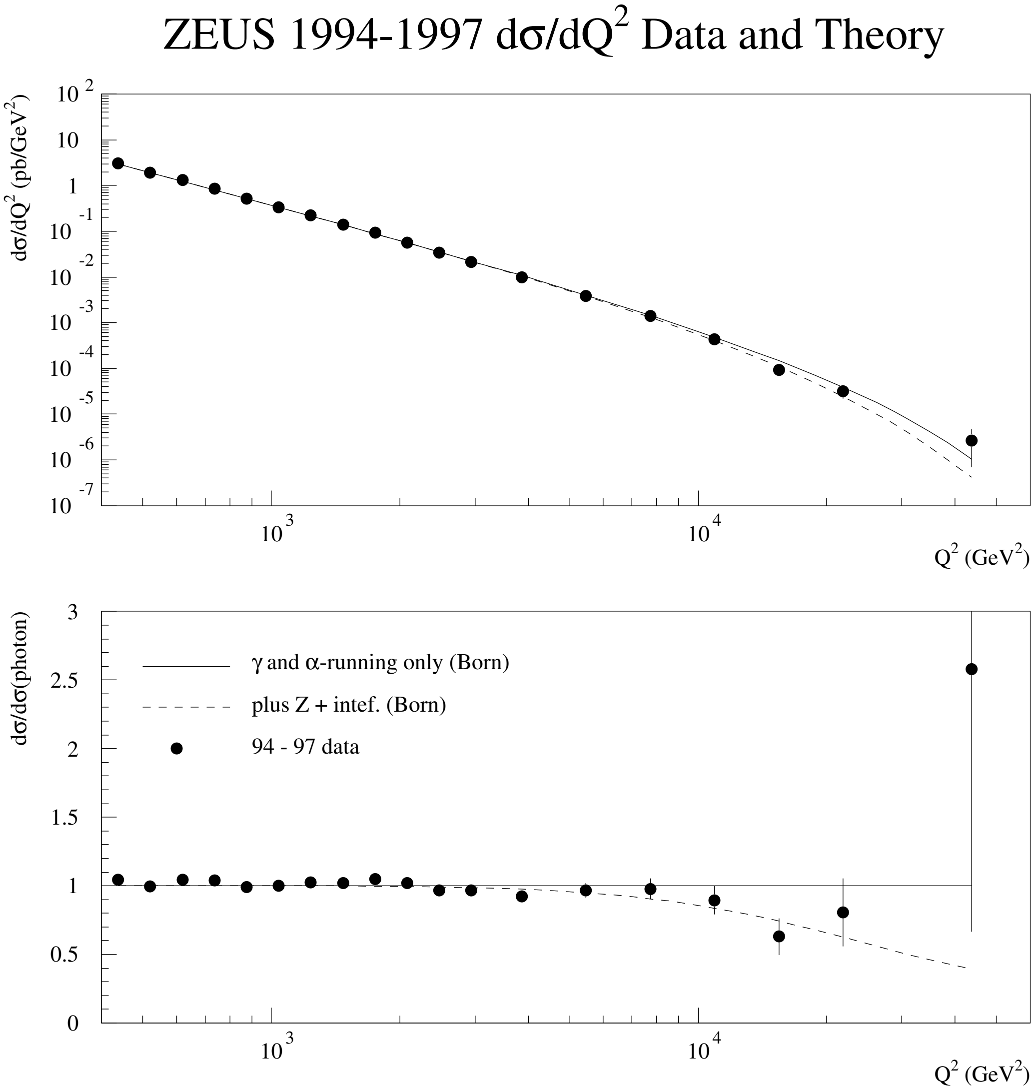

Figure 7.10: The measured $\mathrm{d}\sigma/\mathrm{d}Q^2$ and the comparison to theoretical predictions. The solid circles are data, the curves are CTEQ4 predictions. The bottom plot gives the ratio of $\mathrm{d}\sigma/\mathrm{d}Q^2$ over its electromagnetic part.

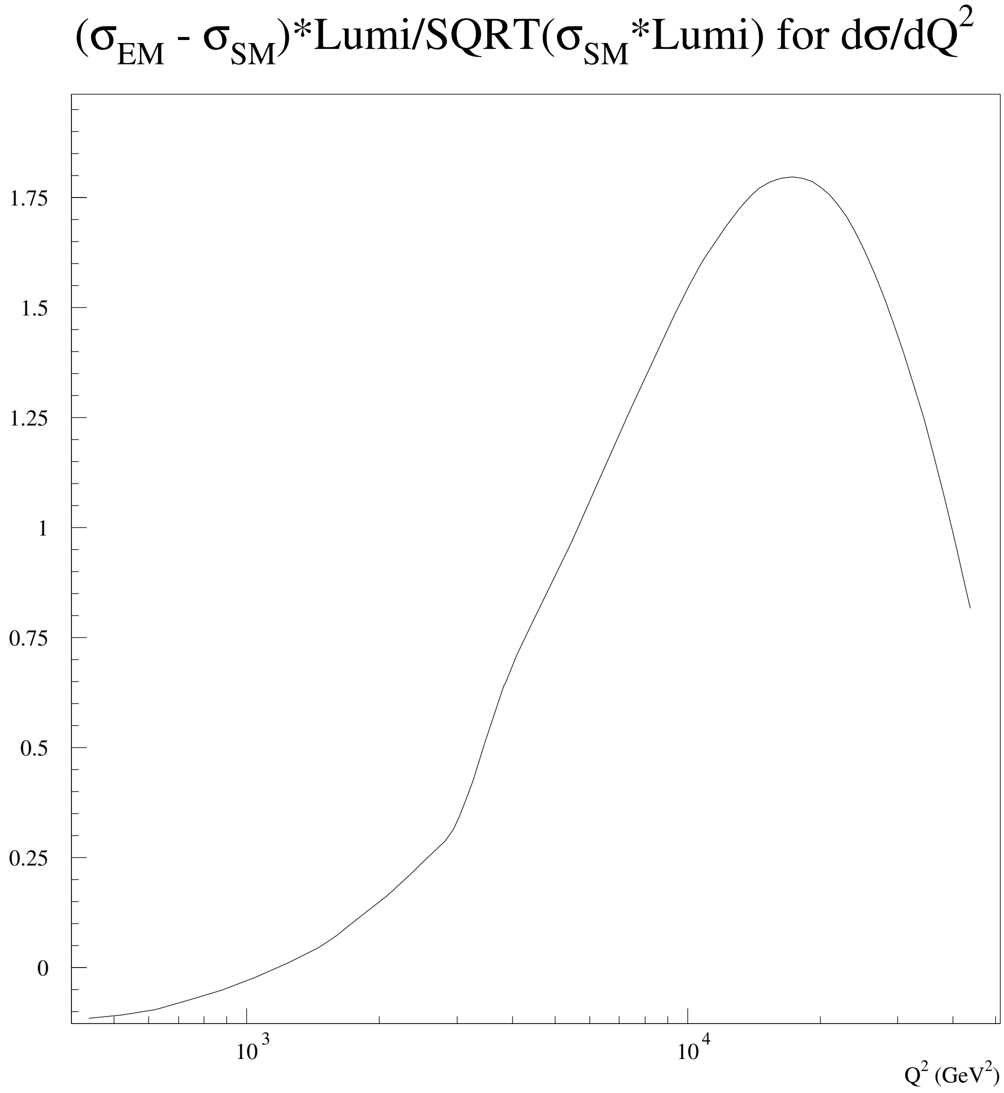

Figure 7.11: The deviation of $\mathrm{d}\sigma/\mathrm{d}Q^2$ from its electromagnetic part. The maximum deviation is about 2.5 σ, it occurs at about $Q^2 = 10000$.

Chapter 8

Conclusions

We have measured the double-differential cross section $\mathrm{d}^2\sigma/\mathrm{d}x\mathrm{d}Q^2$ for $Q^2 > 200$ GeV^2. The agreement with the Standard Model prediction is observed. At Q^2 above 10000 GeV^2, some eccess over Standard Model is also observed. It could be due to statistical fluctuations, however, speculation about new physics at this very high Q^2 has been considered by people at ZEUS and elsewhere. Confirmation of new physics requires more data in the near future. We expect to have three times more statistics at ZEUS by the end of the century.

The attempt to infer xF_3 from cross section measurement is also made. Little success has been obtained due to large statistical error bars, which makes the interpretation of the inferred xF_3 obscure. If more efforts are made in this direction in the near future, the measurement of xF_3 may be worth the endeavor.

Bibliography

[1] J. Chadwick, *Proc. Roy. Soc. (London)* **A136**, 692 (1932).

[2] E. Fermi, *Nuovo Cimento* **11**, 1 (1934), *Z. Phys.* **88**, 161 (1934).

[3] S. Weinberg, *Phys. Rev. Lett.* **19**, 1264 (1967), A. Salam and J.C. Ward, *Phys. Lett.* **13**, 168 (1964).

[4] J.C. Maxwell, *Phil. Trans. R. Soc.* **155**, 459 (1864).

[5] J.D. Bjorken, *Phys. Rev.* **179**, 1547 (1969).

[6] C.G. Callan and D. Gross, *Phys. Rev. Lett.* **22**, 156 (1969).

[7] R.P. Feynman, *Phys. Rev. Lett.* **23**, 1415 (1969).

[8] R.G. Roberts, *The structure of the proton* **Ch5**, 29 (1990), Cambridge University Press.

[9] ZEUS Collaboration, *The ZEUS Detector* **Status Report**, 1 (1989).

[10] ZEUS Collaboration, *The ZEUS Detector* **Ch5**, 5-2 (1989).

[11] ZEUS Collaboration, *The ZEUS Detector* **Ch5**, 5-63 (1989).

[12] A. Bamberger et al., *ZEUS Note* **95**, 095 (1995).

[13] ZEUS Collaboration, *The ZEUS Detector* **Ch11**, 11-1 (1989).